

**Synthesis and Modifications of 2D Nanomaterials
for Sensing Applications**

Thesis

Submitted to

DELHI TECHNOLOGICAL UNIVERSITY

for the award of the degree of

DOCTOR OF PHILOSOPHY

in

Applied Physics

by

Ritika Khatri

(2K17/Ph.D./AP/01)

Under the supervision of

Prof. Nitin K. Puri



Delhi Technological University

Delhi-110042, India

July 2022

©Delhi Technological University-2022
All rights reserved.

DECLARATION

I would like to declare that the Ph.D. thesis entitled “Synthesis and Modifications of 2D Nanomaterials for Sensing Applications” submitted to Delhi Technological University (DTU) for the award of the degree of “**Doctor of Philosophy**” in Applied Physics is a record of bonafide work carried out by me under the guidance and supervision of **Prof. Nitin K. Puri** at Nanomaterials Research Laboratory, and Advanced Sensor Laboratory, Department of Applied Physics, DTU and has fulfilled the requirements for the submission of this thesis. The results contained in this thesis are original and have not been submitted to any other University/Institution for the award of any degree or diploma.

Date: **29-07-2022**

Place: **Delhi**



Ritika Khatri

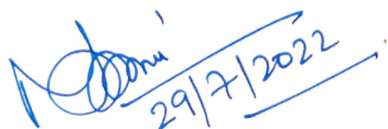
(Reg. No.: 2K17/Ph.D./AP/01)



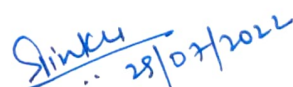
DELHI TECHNOLOGICAL UNIVERSITY
(Govt. of National Capital Territory of Delhi)
BAWANA ROAD, DELHI – 110042

CERTIFICATE

This is to certify that the thesis entitled “Synthesis and Modifications of 2D Nanomaterials for Sensing Applications” submitted by **Ritika Khatri (Roll No. - 2K17/Ph.D/AP/01)** to Delhi Technological University is for the award of the Degree of Philosophy in Department of Applied Physics. The work embodied in this thesis is a record of bonafide research work carried out by her under the supervision of **Prof. Nitin K. Puri**, Professor, Department of Applied Physics, Delhi Technological University, Delhi, India. It is further certified this work is based on original research and has not been submitted in full or in part for any other diploma or degree of any University.


29/7/2022

(Prof. Nitin K. Puri)
Department of Applied Physics
Delhi Technological University


29/07/2022

HOD
Department of Applied Physics
Delhi Technological University

ACKNOWLEDGMENTS

Researching at Delhi Technological University (DTU) has been a life-changing experience for me. Today when I sit to pen down my gratitude, I feel blessed to have countless people who contributed to me achieving my goal.

First and foremost I am thankful to **almighty God** for making me capable enough to reach this level of studies. Getting the right help at the required time has further enhanced my faith in God during my tenure of Ph.D.

I am fully indebted to my supervisor, **Prof. Nitin K. Puri** for his guidance, wisdom, and motivation, and for pushing me up to the limits, I never thought I could reach. His unwavering enthusiasm kept me headstrong throughout the journey toward the attainment of this degree. Further, his good humor and cheerful nature are an aspect that always kept the atmosphere full of positivity and made this time enjoyable. My appreciation also extends to the pedagogy that he proffers to his students, which is an important attribute to survive in the world after the attainment of a Ph.D. Under his guidance, I could achieve all my goals against all the odds. I couldn't have imagined a better supervisor than him for my Ph.D.

I stand obliged to **Hon'ble Vice Chancellor, DTU** for creating a marvelous research environment and for the requisite infrastructure. My heartfelt recognition to **Prof. Rinku Sharma**, HOD Applied Physics, and **Prof. S.C. Sharma**, DRC Chairman for their guidance, suggestions, and support during my Ph.D. work. I am also thankful to **Prof. Rishu Chaujar** for her insightful discussions. I would also like to thank all the other faculty members of the Department of Applied Physics for their assistance during my tenure of research at DTU. Further, I would like to express my sincere thanks to the **Department of Applied Physics, DTU** for allowing me to pursue my research here.

No words can express my gratitude towards my labmates **Ms. Nikita Jain, Mr. Saroj Kumar Jha, Mr. Hemant Kumar Arora, Mr. Sunil Kumar, Ms. Ashi Mittal,** and **Mr. Anmol Aggarwal** who were continuously there with me like pillars of support during both my ups and downs. I will always cherish the joyous moments we had together which will make me miss this place even more. I am also thankful to other members of my lab and my colleagues **Ms. Kanika Sharma, Mr. Sandeep Sarpal, and Mr. Anurag Bhandari** for their cooperation. I would also like to acknowledge my appreciation to my friends in DTU like **Mr. Mukesh Kumar Sahu, Dr. Prateek Sharma, Ms. Suman Dahiya, Ms. Ritika Ranga, Ms. Renu, Dr. Shankar Subramanian, Dr. Harpreet Kaur, Mr. Abhishek Bhardwaj, Ms. Shivangi Rajput, Ms. Reetu Yadav, Ms. Manjot Kaur, Mr. Owais Jalil, Ms. Sakshi Verma, Ms. Deeksha Thakur, Mr. Himansh Goel, Mr. Tarun Narayan, Ms. Niharika Gupta, Mr. Vishal Singh, Ms. Shilpa Rana, Ms. Komal** for all their technical help, suggestions, and support during this time.

I would like to thank **Prof. Kondepudy Sreenivas**, Delhi University (DU), and Late **Prof. Vinay Gupta**, DU who gave me exposure to the field of research, by allowing me to work in their respective research labs during my post-graduation studies at DU.

I would like to express my heartfelt gratitude to **Dr. Mukesh Kumari**, Postdoctoral researcher, University of California, Berkeley, the United States of America (USA) for her always positive approach. I will always be indebted to her for the valuable time that she gave me for scientific and technical discussions. I am grateful to **Dr. Saurabh Srivastava**, Assistant Professor, Rajkiya Engineering College, Ambedkar Nagar, Uttar Pradesh, India for giving me the direction in the field of biosensing. I am thankful to my seniors **Dr. Deepika Sandil** and **Dr. Kamal Arora** and **Dr. Vikash Sharma** for showing me the direction of research and for being available for valuable discussions. I would like to extend my gratitude to **Dr. Archit Dhingra**

for his valuable time and for having interesting discussions related to the topic of research. I would also like to extend my thanks to my friends in other Universities like **Ms. Nidhi Dhull** (DU), **Ms. Ravina Panwar** (DU), **Mr. Gaurav Gupta** (DU), **Mr. Sudhanshu** (DU), **Ms. Nitika Dahiya** (SRM University) **Ms. Vandana Nagal** (Jamia Millia Islamia) for all their help with scientific discussions.

I am very grateful to my family (**Mr. Premchand** - My Father, **Mrs. Neelam** - My mother, and my brother - **Mr. Shivam Khatri**) for their continuous support and motivation during this entire journey which became to be stressful and tiring. They were always there with a sense of positive hope which filled me with energy and desire to complete my work and attain the degree. There were times when I was left with no hope, but it was through their support that I could accomplish my work with untiring perseverance. I would like to thank my aunt **Dr. Rajani Mandhyan** for helping and guiding me with the biological part of my research. I would like to extend my thanks to all the other family members on my maternal and paternal sides for having faith in me. Striking a work-life balance is important which couldn't have been possible without my friends **Ms. Artee Chugh**, **Ms. Diksha Malik**, **Ms. Shweta Sahu**, and **Mr. Karan Rajwar**. Also, their unconditional moral support and persuasion kept on reminding me of my ultimate goal. I would like to extend my gratitude and love to my cute little nephews **Kaveer Arora** and **Gurveer Arora** for being my stress busters during this period.


Ritika Khatri
(2K17/Ph.D./AP/01)

Abstract

Synthesis and Modifications of 2D Nanomaterials for Sensing Applications

Unique surface features and physicochemical properties possessed by 2 dimensional (2D) nanomaterials have made them attract tremendous recognition for a vast multitude of applications. 2D nanomaterials like transition metal dichalcogenides (TMDs), black phosphorus, transition metal carbides, nitrides, etc are being widely explored in the field of sensing. Particularly, the large surface area makes 2D nanomaterials ideal platforms for loading more and more entities for sensitive detection of the target analyte. Amongst various 2D nanomaterials, molybdenum disulfide (MoS_2) has displayed a substantial potential for further exploration owing to its vast number of intriguing properties. To name a few, large surface area, good absorption coefficient, high heterogeneous electron transfer rate, chemical stability, and biocompatibility makes it an ideal candidate for fabricating a sensing platform. Further, the synergistic effect of MoS_2 offers a strategic and rational approach, to overcome its intrinsic shortcomings and modify it in innumerable ways.

In this work, we have synthesized MoS_2 nanostructures using a simple and cost-effective hydrothermal method with a large yield and reproducibility. For harnessing the potential of synthesized nanostructures for the welfare of society, we employed them in the fabrication of biosensors. Biosensors are analytical devices that integrate a biological element, transducer, and immobilization matrix. Different types of biological elements and transducing mechanisms can be utilized in the construction of biosensors. Based on careful consideration of various types, we finalized antibodies as the biological element and the electrochemical method as the transducing mechanism in our case. Therefore, in the present study, we have kept our focus on developing a stable and low-cost immobilization matrix, which is

biocompatible, reproducible, and favors maximum immobilization of chosen biological elements i.e. antibodies. The biological element can be immobilized on the immobilization matrix using physical or chemical techniques. But covalent binding which is a chemical method is more favorable when testings are done in buffer solutions and repeated measurements are to be recorded. Therefore, we modified MoS₂ nanostructures using reduced graphene oxide (rGO) and chitosan (CS), to anchor functional groups on the matrix for covalent attachment of antibodies on the immobilization matrix.

Cancer is a major threat to the socio-economic development of society pertaining to the rising incidence of cases of different types of cancers in human beings. Amongst various types, lung cancer tops the list of mortalities caused due to cancer. The survival rate after five years of its diagnosis is quite poor, and the weak general health condition of people in developing nations makes the situation even more gruesome in countries like India. Lung cancer is silent at its initial stage and symptoms like shortness of breath and coughing are highly non-specific. Conventional techniques used for detecting lung cancer are time-consuming, expensive, cumbersome, and require trained personnel for operation. Biomarker-based detection of diseases has become quite popular these days since tumor growth directly changes the concentration of proteins. Therefore, biomarkers can serve as an efficient indicator for the rapid, sensitive, and specific diagnosis of a disease. Neuron-specific enolase (NSE) is a biomarker released in high concentration in the case of a person suffering from small cell lung cancer (SCLC) and is highly specific for SCLC. Therefore, we have used NSE as the target analyte for testing the performance of our biosensor.

The findings of the research work conducted for achieving the above-mentioned objectives have been divided into 6 chapters. *Chapter 1* begins with a brief introduction to nanoscience and nanotechnology, gradually followed by intriguing properties of 2D

nanomaterials, a discussion about biosensors and their components, choice of MoS₂ as an immobilization matrix, based on a comprehensive literature review. The importance of rapid, specific, and sensitive detection of lung cancer and the choice of NSE as a target biomarker is also emphasized. The chapter then elucidates the motivation to pursue this work and the objectives of the present thesis work. **Chapter 2** describes in detail the methods chosen for the synthesis of MoS₂ and modified nanostructures and the technique used for film formation. This is succeeded by a discussion on all the characterization techniques which have been used in the present thesis work for confirmation of the formation of desired nanostructures and testing the biosensing performance of the fabricated platform. **Chapter 3** examines the dependence of electrochemical performance on the morphology of synthesized MoS₂ nanostructures. **Chapter 4** and **Chapter 5** present the results of studies related to the modification of synthesized MoS₂ nanostructures using rGO and CS respectively. The two matrices are analyzed using various characterization tools and then the biosensing performance of the two platforms is also reported for detection of NSE. **Chapter 6** summarizes the results of all the above chapters and concludes that the surface chemistry of modified MoS₂ nanostructures plays a huge role in determining the analytical performance of the biosensor. This chapter winds up with prospects of this research work.

LIST OF PUBLICATIONS

Included in Ph.D. Thesis

1. **Ritika Khatri** and Nitin K. Puri. "*Electrochemical study of hydrothermally synthesised reduced MoS₂ layered nanosheets.*" Vacuum (Elsevier) 175 (2020): 109250. (Impact Factor – 4.11)
 2. **Ritika Khatri** and Nitin K. Puri. "*Electrochemical biosensor utilizing dual-mode output for detection of lung cancer biomarker based on reduced graphene oxide-modified reduced-molybdenum disulfide multi-layered nanosheets.*" Journal of Materials Research (Springer) 37 (8), (2022): 1451-1463. (Impact Factor – 3.089)*
- *As per licence agreement “Reproduced with permission from Springer Nature”
3. **Ritika Khatri** and Nitin K. Puri. "*Electrochemical studies of biofunctionalized MoS₂ matrix for highly stable immobilization of antibodies and detection of lung cancer protein biomarker.*" New Journal of Chemistry (Royal Society of Chemistry) 46 (16) (2022): 7477-7489. (Impact Factor – 3.925)

Not Included in Ph.D. Thesis

4. Deepika Sandil, Saurabh Srivastava, **Ritika Khatri**, Kanika Sharma, and Nitin K. Puri. "*Synthesis and fabrication of 2D Tungsten trioxide nanosheets based platform for impedimetric sensing of cardiac biomarker.*" Sensing and Bio-Sensing Research (Elsevier) 32 (2021): 100423.
5. Shreya, Anukool Yadav, **Ritika Khatri**, Nikita Jain, Anurag Bhandari, Nitin K. Puri. "*Double Zone Thermal CVD and Plasma Enhanced CVD Systems for Deposition of*

Films/Coatings with Eminent Conformal Coverage.” Lecture Notes in Mechanical Engineering, **2021** (Scopus indexed publication of springer nature).

6. **Ritika Khatri**, Nitin K. Puri. “*Potentialities of Carbon Dots for Bio-Imaging Applications*”. Carbon Dots: Next Generation Material for Biomedical Applications, **2022** (Published as a book chapter in IOP Publishing)

LIST OF CONFERENCES

1. **Ritika Khatri**, Nitin K. Puri, “*Synthesis and fabrication of ZnO-MoS₂ nanocomposite thin film for hydrogen sensing application*”, 17th International Meeting on Chemical Sensors (**IMCS 2018**) held at the University of Vienna, Vienna, Austria from 15th - 19th July **2018**.
2. **Ritika Khatri**, Nitin K. Puri, “*Role of reducing agents on hydrothermally synthesised MoS₂ nanosheets and their electrochemical studies for sensing applications*”, International Conference on Advanced Materials (**ICAM 2019**) held at Jamia Millia Islamia, Delhi, India from 6th - 7th March **2019**.
3. **Ritika Khatri**, Nitin K. Puri, “*Synthesis of Functionalised Reduced MoS₂ Nanostructures for Early Detection of Cancer*”, 5th International Conference on Emerging Electronics held at Indian Institute of Technology Delhi [IIT-D], (**IEEE-ICEE 2020**) from 26th - 28th November **2020**.

LIST OF WEBINARS, TALKS, AND WORKSHOPS ATTENDED

1. Participated in the workshop “E-Resources: A Gateway for Research, 2017” organized by Central Library, Delhi Technological University, held from 4th - 8th September **2017**.
2. Attended TEQIP-III sponsored one-week faculty development program on “Recent Trends in Material Science and Engineering” organized by the Department of Applied Physics, Delhi Technological University from 17th - 21st September **2018**.
3. Attended Indian Nanoelectronics Users Program (INUP **2019**, 14th - 16th May **2019**), held at CENSE, IISC Bangalore, India.
4. Attended workshop on “Advanced Spectroscopy Techniques for FTIR and FTNIR” held at JNU from 25th -26th July **2019**.
5. One Day National Seminar on “Recent Trends in Applied Physics and Engineering (RTAPE-2020)” by Shanti Swarup Bhatnagar (SSB) Awardees organized by the Department of Applied Physics on 10th February **2020**.
6. Attended a webinar series on “Role of Science, Technology, and Innovation in the Current Scenario” organized by Guru Gobind Singh Indraprastha University from 26th - 29th May **2020** using the CISCO-Webex platform.
7. Attended a session on “How to write a great research paper and get it accepted by a good journal” by Elsevier on 3rd June **2020**.
8. Participated in online training/lecture on the topic “Prospects of Nanomaterials Modified Conducting Paper-Based Biosensors for Cancer Detection” by Professor B.D. Malhotra, DTU, on 12th June **2020**.
9. Attended the virtual workshop on “Basics of Combined Confocal Raman AFM System and its Research Applications” organized jointly by AIRF- JNU & Toshniwal Brother (SR) Pvt. Ltd. on 29th - 30th December **2020** at AIRF, JNU, New Delhi.

10. Attended a one-week e-workshop on “Materials and Their Characterization” organized by the Department of Physics, School of Basic and Applied Sciences, Maharaja Agrasen University, from 14th - 19th June **2021**.

LIST OF FIGURES

Figure No.	Title of Figure	Page No.
Fig. 1.1	Schematic illustrating the increase in surface area to volume ratio on going from a (i) larger dimension to a (ii) smaller dimension.	2
Fig. 1.2	Classification of nanostructured materials based on dimensions	3
Fig. 1.3	Schematic diagram showing the components of a biosensor with various types of its constituent elements	6
Fig. 1.4	Structure of Ab showing a 'Y' shaped protein with 2 heavy and 2 light chains	11
Fig. 1.5	Shows various techniques for immobilization of biological elements on the immobilization matrix	12
Fig. 1.6	Schematic showing 2H and 1T structure of MoS ₂	17
Fig. 1.7	Properties of MoS ₂ favorable for biosensing in a schematic diagram	19
Fig. 2.1	Setup of Teflon-lined stainless-steel autoclave used for hydrothermal synthesis	33
Fig. 2.2	Mortar and pestle used for grinding in solid-state method	35
Fig. 2.3	An insight into EPD setup	36
Fig. 2.4	Schematic diagram showing grating-like crystal structure and the diffraction of incident X-rays obeying Bragg's law	38
Fig. 2.5	Schematic representation of basic SEM components	40
Fig. 2.6	Schematic diagram of TEM	43
Fig. 2.7	Profile data acquisition by stylus type surface profilometer	48
Fig. 2.8	Block diagram of FTIR spectroscopy	50
Fig. 2.9	Simplified block diagram of Raman spectrometer	51
Fig. 2.10	Typical AFM force vs distance curve	53
Fig. 2.11	Schematic diagram of basic working principle of AFM	54
Fig. 2.12	Block diagram of TGA	55
Fig. 2.13	Nyquist plot obtained by EIS technique	57
Fig. 2.14	A typical cyclic voltammogram curve	59
Fig. 2.15	(a) Input signal in DPV (b) Output voltammogram in DPV	60
Fig. 3.1	Dispersion solution of (a) MoS ₂ HH in DI water (b) MoS ₂ CA in DI water (c) MoS ₂ HH in acetone (d) MoS ₂ CA in acetone (e) MoS ₂ HH in ethanol (f) MoS ₂ CA in ethanol (g) MoS ₂ HH in acetonitrile (h) MoS ₂ CA in acetonitrile.	70
Fig. 3.2	XRD patterns of as-prepared MoS ₂ , MoS ₂ HH, and MoS ₂ CA	73
Fig. 3.3	FESEM image of MoS ₂ nanostructures (a, b, c) MoS ₂ HH (d, e, f) MoS ₂ CA	74
Fig. 3.4	Raman Spectra of MoS ₂ HH and MoS ₂ CA	75
Fig. 3.5	TEM image (a) MoS ₂ HH at 100 nm (b) MoS ₂ CA at 100 nm (c) MoS ₂ HH at 20 nm (d) MoS ₂ CA at 20 nm	77

Fig. 3.6	Nyquist plot of MoS ₂ HH_ITO and MoS ₂ CA_ITO using EIS technique	79
Fig. 3.7	Cyclic Voltammogram of MoS ₂ HH_ITO and MoS ₂ CA_ITO	82
Fig. 3.8	Scan rate study of (a) MoS ₂ HH_ITO and (b) MoS ₂ CA_ITO at scan rate varying from 10 mV s ⁻¹ – 150 mV s ⁻¹	82
Fig. 3.9	Variation of <i>i</i> _{pa} and <i>i</i> _{pc} with under root of scan rate (a) MoS ₂ HH_ITO (b) MoS ₂ CA_ITO	83
Fig. 3.10	Differential pulse voltammograms of MoS ₂ HH_ITO and MoS ₂ CA_ITO	83
Fig. 4.1	XRD pattern of GO and rGO modified MoS ₂	98
Fig. 4.2	Raman spectra of GO and rGO/MoS ₂	99
Fig. 4.3	FTIR spectra of GO and rGO/MoS ₂	100
Fig. 4.4	(a) SEM image of GO and (b, c, d, e) SEM images of rGO modified MoS ₂ multilayered nanosheets (f) Histogram of length distribution of rGO in rGO/MoS ₂	101
Fig. 4.5	The selected area of (a) GO and (b, c) rGO modified MoS ₂ multi-layered nanosheets for elemental analysis using EDX.	102
Fig. 4.6	TGA curves of GO, MoS ₂ , and rGO/MoS ₂	104
Fig. 4.7	Topographical images taken using AFM of (a) rGO/MoS ₂ /ITO (b) anti-NSE/rGO/MoS ₂ /ITO (c) BSA/anti-NSE/rGO/MoS ₂ /ITO electrode	105
Fig. 4.8	(a)Variation of CV peak current with the concentration of antibody attached on rGO/MoS ₂ /ITO electrode (b)Variation of peak current with the incubation time of antigen NSE over BSA/anti-NSE/rGO/MoS ₂ /ITO	106
Fig. 4.9	(a)Electrochemical response of rGO/MoS ₂ /ITO, anti-NSE/rGO/MoS ₂ /ITO and BSA/Anti-NSE/rGO/MoS ₂ /ITO electrodes, (b) Stability study of BSA/antiNSE/rGO/MoS ₂ /ITO bioelectrode with 50 continuous CV cycles at scan rate 50 mV s ⁻¹ (c) Plot of anodic peak current (<i>i</i> _{pa}) with respect to CV cycles	107
Fig. 4.10	Scan rate dependent plot of BSA/anti-NSE/rGO/MoS ₂ /ITO bioelectrode, inset shows the variation of <i>i</i> _{pa} of BSA/anti-NSE/rGO/MoS ₂ /ITO bioelectrode with under root of scan rate	109
Fig. 4.11	Response of BSA/anti-NSE/rGO/MoS ₂ /ITO bioelectrode as a function of the concentration of NSE (a) using EIS (c) using CV; Calibration plot BSA/anti-NSE/rGO/MoS ₂ /ITO bioelectrode (b) using EIS (d) Using CV	112
Fig. 4.12	Reproducibility check of BSA/anti-NSE/rGO/MoS ₂ /ITO bioelectrode by preparing 4 different bioelectrodes under similar conditions using dual modes (a) EIS (b) CV	113
Fig. 4.13	Specificity Study of BSA/anti-NSE/rGO/MoS ₂ /ITO bioelectrode against other interferents present in human serum using dual modes (a) EIS (b) CV	114

Fig. 5.1	XRD pattern of CS, MoS ₂ , and, CS/MoS ₂	128
Fig. 5.2	(a) Raman spectra of CS and CS/MoS ₂ (b) Raman spectrum of CS/MoS ₂ in the range 250 to 500 cm ⁻¹ showing A _{1g} and E _{2g} ¹ modes of MoS ₂ in CS/MoS ₂	130
Fig. 5.3	TGA curves of CS, MoS ₂ , and CS/MoS ₂	131
Fig. 5.4	FTIR curves of (a) CS and (b) CS/MoS ₂	132
Fig. 5.5	SEM micrographs of (a, b) MoS ₂ (c) CS (d) CS/MoS ₂	133
Fig. 5.6	(a) Current response with varying concentration of anti-NSE (b) Current response with variation in incubation time of NSE on BSA/anti-NSE/CS/MoS ₂ /ITO bioelectrode	134
Fig. 5.7	(a) CV curves of (i) CS/MoS ₂ /ITO (ii) anti-NSE/CS/MoS ₂ /ITO (iii) BSA/anti-NSE/CS/MoS ₂ /ITO (b) EIS curves of (i) CS/MoS ₂ /ITO (ii) anti-NSE/CS/MoS ₂ /ITO (iii) BSA/anti-NSE/CS/MoS ₂ /ITO. The inset shows the magnified Nyquist plots (in the range of 25 to 250 Ω)	135
Fig. 5.8	(a) Scan Rate Study of bioelectrode BSA/anti-NSE/CS/MoS ₂ /ITO by varying scan rate from 10 to 100 mV s ⁻¹ and recording CV profiles (b) Variation of peak anodic current (i _{pa}) and peak cathodic current (i _{pc}) with under root of scan rate.	136
Fig. 5.9	(a) Consecutive scans of bioelectrode (BSA/anti-NSE/CS/MoS ₂ /ITO) for 50 CV cycles (b) Variation of peak anodic (i _{pa}) and peak cathodic current (i _{pc}) with no. of CV cycles	138
Fig. 5.10	(a) Electrochemical detection of NSE studied using CV with variation in concentration of NSE from 0.1 ng mL ⁻¹ to 200 ng mL ⁻¹ in PBS 7.4 containing 50 mM [Fe(CN) ₆] ^{3-/4-} (b) Calibration plot between CV peak current and concentration of NSE (c) Response of control electrode (CS/MoS ₂ /ITO) towards varying concentrations of NSE from 0.1 to 100 ng mL ⁻¹	140
Fig. 5.11	(a) Reproducibility study of 5 different bioelectrodes prepared under similar conditions (b) Specificity study of bioelectrode towards various interferents commonly present in human serum (c) Specificity study of bioelectrode towards NSE in the simultaneous presence of various other interferents	141
Fig. 5.12	(a) Shelf-life study of fabricated bioelectrode (b) Regeneration study of prepared bioelectrode	142

LIST OF TABLES

Table No.	Title of Table	Page No.
Table 3.1	Lattice parameters of two samples calculated using X-Powder software	74
Table 3.2	The elemental composition of MoS ₂ HH and MoS ₂ CA determined using EDXRF and CHNS elemental analysis	78
Table 4.1	Atomic percentages for different elements present in GO and rGO modified MoS ₂ multi-layered nanosheets	103
Table 4.2	Electrochemical parameters calculated for the prepared bioelectrode and its comparison to other electrochemical sensors reported in the literature	110
Table 4.3	Some previous works reported in the literature for the detection of NSE	115-116
Table 5.1	Comparison of the analytical performance of bioelectrode proposed in this study with other bioelectrodes reported earlier for detection of NSE	143-144
Table 6.1	Comparison table of electrochemical parameters of our bioelectrodes with previously reported electrochemical bioelectrodes	154-155

LIST OF SCHEMES

Scheme No.	Title of Scheme	Page No.
Scheme 4.1	Pictorial representation of layers of MoS ₂ bridged by rGO	93
Scheme 4.2	Pictorial representation of the hydrothermal synthesis of rGO-modified MoS ₂ multi-layered nanosheets	95
Scheme 4.3	Step-by-step preparation of BSA/anti-NSE/rGO/MoS ₂ /ITO bioelectrode and detection of NSE	96
Scheme 5.1	Schematic diagram illustrating the synthesis of CS/MoS ₂ matrix and fabrication of BSA/anti-NSE/CS/MoS ₂ /ITO bioelectrode for detection of NSE	127

LIST OF SYMBOLS AND ACRONYMS

0D	Zero Dimension
1D	One Dimension
2D	Two Dimension
3D	Three Dimension
g-C ₃ N ₄	Graphitic carbon nitride
hBN	Hexagonal boron nitride
S	Sulphur (S)
Se	Selenium
Te	Tellurium
nm	nanometer
mm	millimeter
cm	centimeter
mA	milli Ampere
mg	milligram
mL	milliliter
kHz	kilohertz
ev	Electron volt
KV	Kilo Volt
NPs	Nanoparticles
NS	Nanosheet
NFs	Nanoflowers
CNTs	Carbon nanotubes
Fig	Figure
TMD	Transition metal dichalcogenides
JCPDS	Joint committee on powder diffraction standards
GO	Graphene oxide
rGO	reduced Graphene oxide
MoS ₂	Molybdenum disulfide
pH	Potential of Hydrogen
SPR	Surface plasmons resonance
BSA	Bovine Serum Albumin
ISFET	Ion-sensitive field effect transistor
FET	Field effect transistor
CMRR	Common mode rejection ratio
DI	Deionized water
IPA	Isopropanol
PANI	Polyaniline
APTES	(3-aminopropyl) triethoxysilane
EpCAM	Epithelial cell adhesion molecule
CML	Chronic myelogenous leukemia
CEA	Carcinoembryonic antigen

NSCLC	Non-small cell lung cancer
SCLC	Small cell lung cancer
MRI	Magnetic resonance imaging
CAT	Computerized axial tomography
CA	Carbohydrate antigen
NSE	Neuron-specific enolase
Au	Gold
Ag	Silver
Ni	Nickel
Cu	Copper
Pt	Platinum
LD	Limited stage
ED	Extensive stage
HH	Hydrazine hydrate
CA	Citric acid
CS	Chitosan
AMT	Ammonium molybdate tetrahydrate
ITO	Indium Tin oxide
RSD	Relative standard deviation
HET	Heterogenous electron transfer
HER	Hydrogen evolution reaction
GCE	Glassy carbon electrode
RE	Reference electrode
CE	Counter electrode
WE	Working electrode
IR	Infrared radiation
S/N	Signal-to-noise ratio
MCA	Multichannel analyser
GUI	Graphical user interface
CCD	Charge-coupled devices
BSE	Backscattered electron
FWHM	Full width at half maximum
XRD	X-Ray Diffraction
SEM	Scanning electron microscope
TGA	Thermogravimetric analysis
AFM	Atomic force microscopy
FTIR	Fourier transform infrared spectroscopy
EDXRF	Energy dispersive X-Ray fluorescence
EDAX	Energy dispersive X-Ray analysis
Å	Angstrom
CV	Cyclic Voltammetry
EIS	Electrochemical Impedance spectroscopy
DPV	Differential pulse voltammetry

EPD	Electrophoretic deposition
PET	Positron emission tomography
AFP	Alpha-fetoprotein
Ab	Antibody
-NH ₂	Amino group
-COOH	Carboxyl group
CYFRA-21-1	Cytokeratin fragment 21-1
Pd	Palladium
Ppy	polypyrrole
PEDOT	poly (3,4-ethylenedioxythiophene)
MWCNTs	Multi-walled carbon nanotubes
AMP	Ampicillin
H ₂ O ₂	Hydrogen peroxide
DC	Direct current
μm	micrometer
CT	Computed tomography
i _{pa}	Anodic peak current
EA	Ethanolamine
CTnI	Cardiac troponin
WO ₃	Tungsten trioxide
NRs	Nanorods
VD	Vitamin-D
Fe ₃ O ₄	Iron oxide
PANnFs	Polyacrylonitrile nanofibers
nYZR	yttria-doped zirconia-reduced graphene oxide
SPE	Screen printed electrode
PPD	Polyphenylenediamine
NAs	Nanoassemblies
Ap	Alkaline phosphatase
Ag	Antigen
Fc-g	Ferrocene grafted
BBY	Bismarck Brown Y
Thi	Thionine

TABLE OF CONTENTS

Title	Page No.
Acknowledgments	<i>v</i>
Abstract	<i>viii</i>
List of Publications	<i>xi</i>
List of Conferences	<i>xiii</i>
List of Webinars, Talks and Workshops attended	<i>xiv</i>
List of Figures	<i>xvi</i>
List of Tables	<i>xix</i>
List of Schemes	<i>xx</i>
List of Symbols and Acronyms	<i>xxi</i>
Chapter 1: Introduction to 2D Nanomaterials and Scientific Motivation	1 – 30
1.1 Introduction	2
1.1.1 Nanoscience and nanotechnology	2
1.1.2 Classification of nanostructured materials based upon dimensionality	3
1.2 Biosensors and their important components	5
1.2.1 Classification of biosensors based upon transducing mechanism	6
1.2.2 Classification of biosensors based upon the biological element	9
1.2.3 Immobilization matrix	11
1.2.4 Important parameters of a biosensor on which its performance is evaluated	14
1.3 Various functional materials have been explored for the fabrication of immobilization matrices previously	15
1.4 Properties of MoS ₂ and its selection for the fabrication of immobilization matrix	16
1.4.1 Structure of MoS ₂	16
1.4.2 Properties of MoS ₂ which make it a favorable candidate for the fabrication of immobilization matrix	18
1.4.3 Utilization of bare MoS ₂ as an immobilization matrix	19
1.4.4 Modification of MoS ₂ by composite formation for fabrication of immobilization matrix	21
1.5 Cancer and the importance of its rapid and sensitive detection	22
1.6 Importance of choosing an appropriate immobilization matrix and the motivation for this work	23
1.7 Objectives of the present work	25
References	26
Chapter 2: Methodologies: Synthesis, Film Fabrication and Characterization Techniques	31 – 62
2.1 Synthesis and modifications of MoS ₂ nanostructures	32
2.1.1 Hydrothermal method of synthesis	33
2.1.2 Improved Hummer's Method	34
2.1.3 Solid-state method	35
2.2 Method of film fabrication for MoS ₂ and modified nanostructures	35

	2.2.1 Electrophoretic deposition (EPD) technique	35
2.3	Characterization techniques used for structural, morphological, topographical, and spectroscopic investigation of MoS ₂ and modified nanostructures	36
	2.3.1 X-ray diffraction (XRD) for structural investigations	37
	2.3.2 Scanning electron microscopy (SEM) and field emission scanning electron microscopy (FESEM) for morphological investigations	39
	2.3.3 Transmission electron microscopy (TEM) for morphological and crystallographic investigations	42
	2.3.4 Energy dispersive X-ray analysis (EDAX) for elemental analysis	44
	2.3.5 Energy dispersive X-ray fluorescence (EDXRF) spectroscopy for elemental analysis	45
	2.3.6 CHNS for elemental analysis	46
	2.3.7 Surface profilometer for thickness measurement of films	47
	2.3.8 Fourier transform infrared spectroscopy (FTIR) for identification of functional groups	48
	2.3.9 Raman spectroscopy	50
	2.3.10 Atomic force microscopy (AFM) for topographical analysis	52
	2.3.11 Thermogravimetric analysis (TGA) for thermal analysis	54
2.4	Electrochemical Techniques	56
	2.4.1 Electrochemical impedance spectroscopy (EIS)	56
	2.4.2 Cyclic voltammetry (CV)	58
	2.4.3 Differential pulse voltammetry (DPV)	59
	References	60
	Chapter 3: Electrochemical Study of Hydrothermally Synthesised MoS₂ Layered Nanosheets	63 - 88
3.1	Introduction	64
3.2	Experimental Details	67
	3.2.1 Materials and Solutions	67
	3.2.2 Preparation of MoS ₂ Nanostructures	67
	3.2.2.1 Preparation of MoS ₂ without using reducing agents	67
	3.2.2.2 Preparation using HH as a reducing agent (MoS ₂ HH)	68
	3.2.2.3 Preparation using CA as a reducing agent (MoS ₂ CA)	68
	3.2.3 Preparation of MoS ₂ -based electrode for electrochemical Studies	69
3.3	Results and Discussion	71
	3.3.1 Characterization of samples and instrumentation	71
	3.3.2 Structural study of MoS ₂ nanostructures using XRD	72
	3.3.3 Morphological investigations using FESEM	74
	3.3.4 Qualitative analysis of the layered structure using Raman spectroscopy	75
	3.3.5 Morphological investigations using TEM	76
	3.3.6 EDXRF	77
	3.3.7 CHNS	78
	3.3.8 Electrochemical Studies	78
	3.3.8.1 Electrochemical analysis using EIS and determination of HET rate constant	79
	3.3.8.2 Electrochemical analysis using CV and determination of the electroactive surface area	80

	3.3.8.3 Electrochemical analysis using DPV	83
3.4 Conclusion		85
References		86
Chapter 4: Electrochemical Study of reduced graphene oxide (rGO) Modified MoS₂ Layered Nanosheets for Detection of Lung Cancer Biomarker		89 - 120
4.1 Introduction		90
4.2 Experimental Details		94
	4.2.1 Materials and solutions	94
	4.2.2 In-situ preparation of rGO modified MoS ₂ multi-layered nanosheets	94
	4.2.3 Preparation of electrochemical immuno-sensing platform for detection of lung cancer biomarker	96
4.3 Results and Discussion		97
	4.3.1 Characterization of Samples and Instrumentation	97
	4.3.2 Results of characterization studies of the samples	98
	4.3.2.1 Structural study of synthesized nanostructures using XRD	98
	4.3.2.2 Confirmation of layered structure using Raman spectroscopy	99
	4.3.2.3 Identification of functional groups using FTIR	100
	4.3.2.4 Morphological study of modified nanostructures using SEM	101
	4.3.2.5 Elemental analysis using EDX	102
	4.3.2.6 Thermal Analysis using TGA	103
	4.3.2.7 Analysis of various steps of preparation of bioelectrode using AFM	104
	4.3.3 Electrochemical studies	105
	4.3.3.1 Optimization of biosensing parameters	105
	4.3.3.2 Electrochemical characterization and stability study of the modified electrode	107
	4.3.3.3 Analytical performance of bioelectrode towards detection of NSE	111
	4.3.3.4 Reproducibility check of the bioelectrode	113
	4.3.3.5 Specificity study of the bioelectrode	113
4.4 Conclusions		116
References		117
Chapter 5: Electrochemical Study of Chitosan (CS) Modified MoS₂ Layered Nanosheets for Detection of Lung Cancer Biomarker		121 - 148
5.1 Introduction		122
5.2 Experimental Details		124
	5.2.1 Chemicals and reagents used for synthesis, cleaning, and biosensing	124
	5.2.2 Synthesis of CS/MoS ₂ nanostructures	125
	5.2.3 Fabrication of bioelectrode	126
5.3 Results and Discussion		128
	5.3.1 Characterization Equipment and Facilities	128
	5.3.2 Characterization study of synthesized nanostructures	128
	5.3.2.1 Crystallographic study of CS/MoS ₂ matrix using XRD	128
	5.3.2.2 Study of vibrational modes and qualitative information about layered structure and functionalization using Raman spectroscopy	129

	5.3.2.3 Thermogravimetric analysis using TGA of CS/MoS ₂ matrix	130
	5.3.2.4 Study of functional groups attached on CS/MoS ₂ matrix using FTIR	131
	5.3.2.5 Study of surface morphology of CS/MoS ₂ matrix using SEM	132
	5.3.3 Electrochemical performance of bioelectrode prepared using CS/MoS ₂ matrix	133
	5.3.3.1 Optimization of biosensing parameters	133
	5.3.3.2 Electrochemical study of the various steps of fabrication of bioelectrode	134
	5.3.3.3 Stability study of prepared bioelectrode	138
	5.3.3.4 Electrochemical performance of bioelectrode (BSA/anti-NSE/CS/MoS ₂ /ITO) and control electrode (CS/MoS ₂ /ITO) towards detection of NSE	139
	5.3.3.5 Investigation of reproducibility and specificity of prepared bioelectrode towards NSE	140
	5.3.3.6 Shelf life and regeneration study of prepared bioelectrode	142
	5.4 Conclusions	144
	References	145
	Chapter 6: Summary, Conclusions, and Future Scope of Work	149 - 156
	6.1 Summary of research work	150
	6.2 Conclusions and major takeaways from the research work	153
	6.3 Prospects of this work	155
	References	156

Reprints of journal publications

Chapter 1

Introduction to 2D Nanomaterials and Scientific Motivation

This chapter begins with a brief discussion of nanoscience and nanotechnology, followed by a categorization of nanomaterials based on their dimensionality. Special emphasis is given to 2D nanomaterials owing to their attractive and intriguing properties possessed by them, which make them highly favorable for various applications. Further, this chapter discusses biosensors, their prime components namely transducer, biological element, their parts, and the immobilization matrix. The choice of Molybdenum disulfide (MoS_2) as material for the fabrication of the immobilization matrix of biosensor has been discussed in detail, with a special focus on its versatile properties and the previous literature on MoS_2 and other functional materials. The chapter continues to discuss lung cancer and the importance of its quick and sensitive detection by fabricating a biosensor based on a specific biomarker. The chapter culminates with the motivation for this work with the realization that the fabrication of a stable and low-cost immobilization matrix is one of the most important components to focus on to make a biosensor for clinical application.

1.1 Introduction

1.1.1 Nanoscience and nanotechnology

The realm of nanoscience and nanotechnology has been expanding explosively because of its potential to revolutionize the industrial and commercial market. Nanostructured materials are the backbone of this exponentially growing domain. Nanostructured materials have at least one dimension of less than 100 nm and have properties in between the bulk materials and atoms [1, 2]. An increase in relative surface area and the emergence of new quantum effects lead to distinct properties of nanomaterials from bulk or atom counterparts. An escalated surface-to-volume ratio enhances their chemical reactivity, as more fractions of atoms at the surface are available [1, 3]. Fig. 1.1 shows a schematic illustrating the increase in surface area to volume ratio as we go to a smaller dimension (ii) from a larger dimension (i). Since the size is in the nanoscale and is comparable to length, therefore properties of the whole material are much more dependent on the surface. While the quantum effects arise from spatial confinement in nanoscale dimensions.

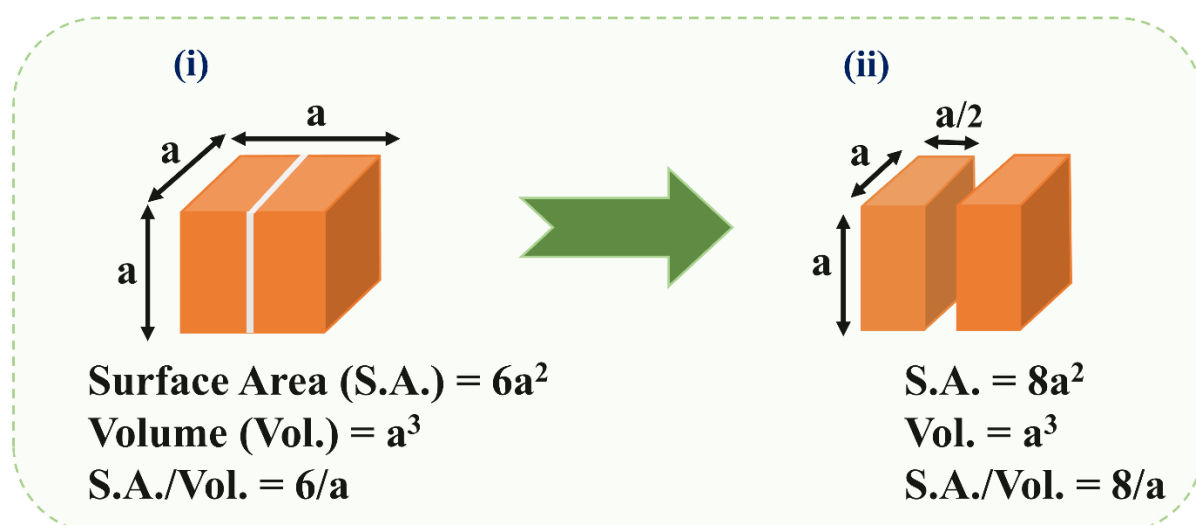


Fig. 1.1: Schematic illustrating the increase in surface area to volume ratio on going from a (i) larger dimension to a (ii) smaller dimension

1.1.2 Classification of nanostructured materials based upon dimensionality

Nanostructured materials can be categorized as 0 dimensional (0D), 1 dimensional (1D), 2 dimensional (2D) and 3 dimensional (3D) materials. In 0D materials, all three dimensions are in the nanoscale (i.e., <100 nm), for example: quantum dots, nanoparticles (NPs), etc. In 1D, any one of the dimensions cannot be measured on the nanoscale, examples include nanorods, nanowires, nanotubes, etc. In 2D nanomaterials, any of the two dimensions are outside the nanoscale, some examples include nanosheets, nanoplates, etc. In 3D, all three dimensions are outside the nanoscale, for example in bulk powders. **Fig. 1.2** shows the dimensions-based classification of nanomaterials.

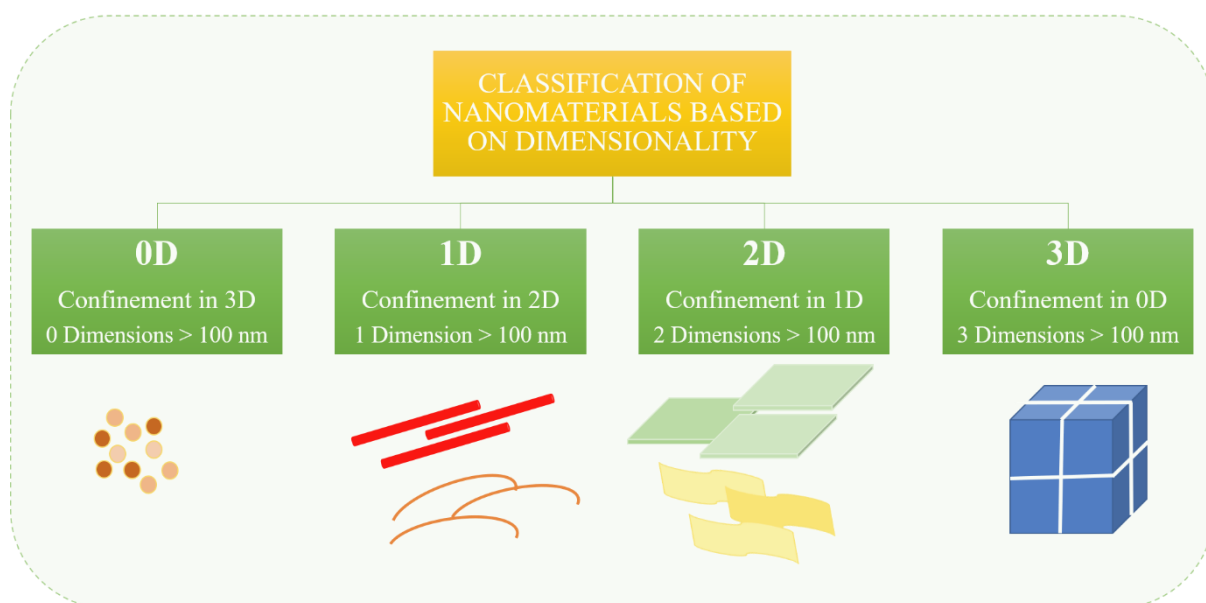


Fig. 1.2: Classification of nanostructured materials based on dimensions.

Amongst various dimensionalities, the research endeavor toward 2D nanomaterials has been particularly blooming since the discovery of outstanding properties of graphene in 2004 [2]. The vast variety of structural and chemical properties of 2D nanomaterials are dictated by their dimensionality which offers their utilization in diverse applications. Affluence in

electronic and optical properties of 2D nanomaterials, with further feasibility of engineering the properties with functionalization, escalates their appeal in many applications [1]. 2D nanomaterials can be easily functionalized owing to a large number of exposed atoms present on the surface which facilitates easy interaction with other materials [4]. 2D nanomaterials possess marvelous mechanical properties also like flexibility, and light-weight, along with robustness which can be highly favorable for the emergence of wearable and portable sensors [2]. Graphene, transition metal dichalcogenides (TMDs), hexagonal boron nitride (hBN), graphitic carbon nitride (g-C₃N₄), Mxene, and phosphorene are some of the materials which belong to this class. The most exploited 2D nanomaterial for various applications is graphene owing to a large number of fascinating properties like being a single atom thick with zero bandgaps, being highly conductive along with a large surface area. However, producing high-quality graphene for industrial applications with high yield and low cost remains to be a significant challenge. Thus, a large amount of graphene is produced by the reduction of graphene oxide (GO) as this method is cheap as well as scalable [5]. Reduced graphene oxide (rGO) is not as conductive as graphene and has a fair number of functional groups on its surface but that is highly favorable for sensing applications where functional groups are required for covalent attachment [2, 6]. The synthesis techniques of various 2D materials like black phosphorus, MXene, etc. are still in the stage of infancy, which makes it difficult to exert control on their yield, size, and surface properties [7]. TMDs are another class of 2D materials that are most studied alongside graphene. TMDs are represented by a general formula MX₂ where M corresponds to groups 4, 5, and 10 transition metals in the periodic table, whereas X is the chalcogen like sulfur (S), selenium (Se), tellurium (Te). Amidst various TMDs, Molybdenum disulfide (MoS₂) is the most investigated one due to an abundance of physicochemical properties like a fast electron transfer rate, easy functionalization, facile synthesis, a large number of routes available for synthesis, scalable yield, easy dispersion in

various solvents, tunable morphologies and synergistic effect with various materials which promotes composite formation [6, 8]. Driven by the large number of properties possessed by MoS₂, it finds application in a vast variety of fields including batteries [9], supercapacitors [10], hydrogen evolution reaction (HER) [11], electronic devices [12], sensors [13], etc. The unprecedented integration of high surface area and ease of functionalization makes MoS₂ highly favorable for applications in biosensors also [14]. MoS₂ can be synthesized using both top-down and bottom-up approaches as a result of which precise control over its morphology and surface functionalities can be achieved which makes its utilization highly favorable for biosensing applications [7].

1.2 Biosensors and their important components

A biosensor is an analytical device that integrates a biological element, a transducer, and an immobilization matrix. The biological element may be an enzyme, antibody, tissue, or a living cell that creates a specific recognition event on reaction with the target analyte, which is converted by the physical element (transducer) into a readable signal [14]. The first-ever biosensor was introduced by Clark and Lyons in 1962 when they fabricated a glucose biosensor to directly determine the concentration of glucose in a sample [15, 16]. They developed an enzymatic sensor by using glucose oxidase enzyme which converted glucose to gluconic acid, in turn increasing the pH of the solution which was directly correlated with the concentration of glucose. This enabled the detection of glucose in blood samples in place of urine. This was a major milestone in medicine as glucose levels in the blood could be measured instantaneously using this glucose oxidase-based biosensor [16]. Since then biosensors also found their utility in various applications like biotechnology, medicine, agriculture, military, and the detection and prevention of bioterrorism owing to their specificity, practical usability, and short response time [15, 17]. The biosensors can be used to detect a wide range of signals, however, most of

the time the concentration of the target species is determined. The fabrication of a biosensor requires the selection of an appropriate biological element, the transducer, and an immobilization matrix. **Fig. 1.3** shows important components of a biosensor along with their types, schematically.

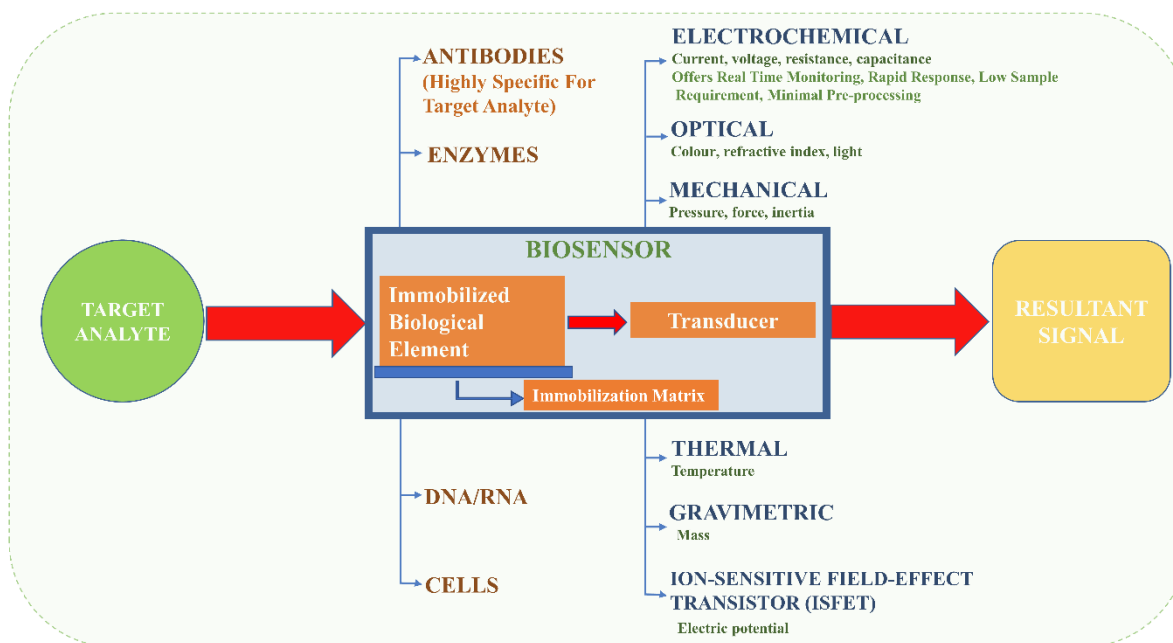


Fig. 1.3: Schematic diagram showing the components of a biosensor with various types of its constituent elements

1.2.1 Classification of biosensors based upon transducing mechanism

Based on transducing mechanism used, a biosensor can be classified as an electrochemical biosensor, optical biosensor, thermal biosensor, mechanical, gravimetric, and ion-sensitive field-effect transistor (ISFET) biosensor [17].

a) **Optical biosensors** – An optical biosensor is an analytical device containing an integrated biological element recognition system and an optical transducer [18]. The biological element could be an enzyme, antibody, or DNA/RNA. The optical transducer can be a waveguide, grating, resonator, interferometer, refractometer, and surface plasmon resonance

(SPR). In an optical biosensor, an optical field like an evanescent field (a field whose strength decreases with distance because it has entered a region where it cannot propagate) recognizes the interaction between the biological element and the target analyte [18]. The advantage of using an optical biosensor is that the evanescent field decays with distance, which prevents non-specific binding, thus promising for the detection of target analyte in complex samples [19]. But, optical sensors are also susceptible to physical damage and prone to interference from the environment, which makes them unsuitable for the choice of transducing mechanism [20].

b) **Thermal biosensors** – A thermal biosensor employs a flow injection method, by utilization of an immobilized enzyme reactor coupled with a thermal transducer which measures the differential temperature across the immobilized enzyme reactor [21]. The biological reactions are either endothermic or exothermic, and this heat energy released or absorbed during the reaction is directly proportional to the total number of molecules produced during biological reactions which are utilized to construct thermal biosensors [21]. The thermal transducer could be a thermistor, thermopile, or thermocouple. The advantage of using a differential measurement system is that the common-mode rejection ratio (CMRR) is high which alleviates the fluctuations due to environmental temperature, thus making the sensor specific to temperature changes due to enzyme catalysis only [21]. The calorimetric biosensor is an example of a thermal sensor since it utilizes the change in heat as a parameter to monitor the structural dynamics of biological elements. However, thermal biosensors suffer from a low response time, low stability, and accuracy which impedes their utilization [20].

c) **Mechanical biosensors** – mechanical biosensors measure the change in force, mass, or displacement caused by the binding of the analyte with the immobilized biological element on the recognition layer immobilized on the surface of a cantilever. The cantilever is the central element of mechanical biosensors. With the binding of the target analyte with an immobilized

biological element, surface stress is created due to the steric interactions or electrostatic attractive and repulsive forces which causes a deflection in the cantilever. To measure the deflection of the cantilever a reflected laser beam is generally used [22, 23]. The cantilevers are sensitive to temperature changes and can expand or contract with the variation in temperature which results to strain induction. This calls for regular calibration to compensate for the strain-induced effects, making their utilization less favorable [20].

d) **Gravimetric biosensors** – when an antibody or any other protein is attached to the immobilization matrix fabricated using a piezoelectric crystal, then the associated change in mass of the binding protein results in a specific vibration frequency of the crystal, generating a measurable signal. Therefore, gravimetric sensors rely on the change in mass upon the attachment of the target analyte [21]. The gravimetric method is meticulously time-consuming with limits its utility.

e) **Ion-sensitive field-effect transistor (ISFET) biosensor**- ISFET biosensor is used mainly for pH detection as it can measure the concentration of H^+ and OH^- ions in a solution, resulting in the change in interface potential at the gate of field-effect transistor (FET) [17, 24]. ISFET biosensors are generally not preferred due to their short life span, hysteresis, and long-term drift which hampers their utilization as a transducing mechanism [20].

f) **Electrochemical biosensors** – In an electrochemical biosensor, the interaction between the target analyte and immobilized biological element results in the production of ions or electrons which causes a change in the electrical properties of the solution. The resultant electrical parameters that change could be voltage, current, resistance, or capacitance [17, 21]. The intensity of the generated electrochemical signal can be directly or inversely proportional to the analyte concentration [15]. Based on the measured parameter like the current, voltage, or resistance electrochemical sensors can further be categorized as amperometric, potentiometric, or conductimetric [17]. Due to a large number of advantages proffered by

electrochemical biosensors like low cost, small dimensions, simple design, and rapid detection, a high signal-to-noise ratio, electrochemical is the most preferred transducing mechanism and we have also chosen this for our work [15, 25].

1.2.2 Classification of biosensors based upon the biological element

Various types of biological elements can be immobilized on the transducing matrix for the fabrication of biosensors. The classification of biosensors based on the biological element is given as follows:

(a) **Enzyme-based biosensor** – enzymes are the most common types of biological elements which are used in fabricating biosensors. Enzymes are the proteins that act as a catalyst in the chemical reaction, but themselves remain unchanged. Enzymes are highly specific making the fabrication of enzymatic biosensors the most preferable one [17]. Glucose and urea biosensors are the most common enzyme-based biosensors. The sensitivity of the enzyme structure makes it difficult to enhance the stability and sensitivity of the biosensor [21]. Since analytes are often consumed in these sensors, due to the reaction between enzyme and analyte, therefore regeneration of enzymatic biosensors is not possible [26]. Also, the large size of enzymes hinders electron transport and the active site is not readily available, therefore enzymes as a biological element are less preferred in the construction of biosensors [27].

(b) **Aptamer-based biosensor** – Aptamers are sequences of DNA or RNA which can selectively bind to the target molecules. Depending upon the requirement, they can be folded in 2D or 3D structures [21]. Being nucleic acids, aptamers can retain their structures and functionality even in extreme temperatures which makes their long-term storage quite feasible [21]. Aptamers are stable in a wide pH range of 2-12 and can also be synthesized chemically which makes their usage favorable for the fabrication of biosensors [21]. However, the aptamer

selection process is tricky, and the orientation and folding of aptamers are also difficult to control on gold (Au) and other electrodes [27].

(c) **Whole cell-based biosensors** – cell-based biosensors are constructed by using microbes like fungi, algae, protozoa, bacteria, viruses, etc as the biological element. Whole cell-based biosensors offer easy handling and they can proliferate by self-replication which diminishes the need for the production of recognition elements by extraction or purification [21]. Whole cell-based biosensors offer high sensitivity and high selectivity due to which they find their utility in food analysis, environmental monitoring, drug screening, detection of organic contaminants, etc [21]. But, poor shelf life due to extreme storage conditions, difficulty in regeneration, high interference, and a soaring maintenance cost are some of the issues to be addressed before the utilization of cells as the biological element for the fabrication of biosensors [28].

(d) **Affinity-based biosensors** - The biosensors which utilize antibodies as the biological element are called affinity-based sensors and are advantageous over other types since the target analyte can now be detected on a localized surface [29]. This reduces the challenge of biosensors from detecting the analyte in the whole of the solution in turn improving the sensitivity and selectivity of the sensor. Also, a stable complex is formed between the immobilized antibody (Ab) and the target antigen, which is bound to happen once the target antigen comes in close vicinity of the antibody, due to their affinity and specificity. Therefore affinity-based sensors hold a bright future since only this thermodynamic equilibrium needs to be detected. Due to the upper hand provided by affinity-based sensors, we have chosen antibodies as the biological element to fabricate our biosensor. **Fig. 1.4** shows the structure of the Ab, a 'Y' shaped protein having Fab and Fc regions [30]. The Fc region has a COOH group on its tail, while the Fab region has an NH₂ group on its head. The underlying principle of the type of biosensor fabricated in this work is that when the analyte of interest comes in contact

with the immobilized biomolecule (Ab here), there is a change in the electrical parameter like resistance or current which can be calibrated against the concentration of the analyte [17].

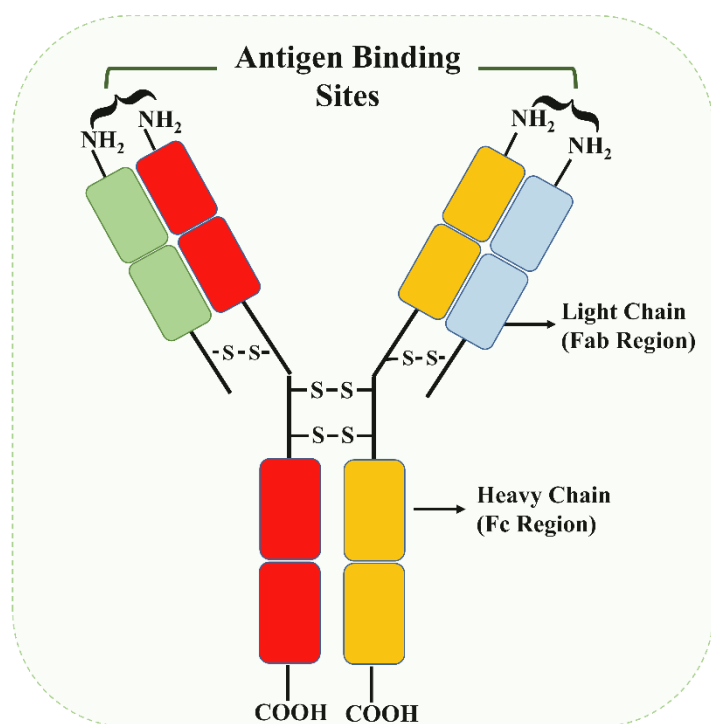


Fig. 1.4: Structure of Ab showing a ‘Y’ shaped protein with 2 heavy and 2 light chains

1.2.3 Immobilization matrix

The choice of a suitable immobilization matrix holds paramount importance in the fabrication of biosensors. The immobilization matrix is the one that holds the biological element onto it and forms the interface between the transducer and the immobilized biological element. An ideal immobilization matrix is one, that can preserve the native activity of the immobilized biological element, is stable in repeated cycles of measurement, and is non-interferent to the detection of the target analyte. Besides this, it should be reproducible, biocompatible, non-toxic, and should have a high surface area for larger immobilization of biomolecules. Initially, the only purpose of immobilization matrices was to provide a native environment to the immobilized biological element to preserve its activity. However, with the evolution of biosensors, the immobilization matrices took the central stage by getting directly involved in

escalating the performance of biosensors by strengthening the capability of the transducer. Thus, it should also act as electron-conducting channels, in such a way that the matrix surface is not passivated [31, 32].

Therefore, after the selection of an appropriate biological element and the transducing technique, it is of utmost importance to identify a suitable immobilization matrix for the fabrication of a biosensor. Stable immobilization of the biological element is pivotal to ensure that the biological activity is conserved during the repeated use of the sensor. The biological element can be coupled with the surface of the biosensor (immobilization matrix) using various techniques which can be broadly compartmentalized into physical and chemical methods (**Fig. 1.5**) [15, 17, 21].

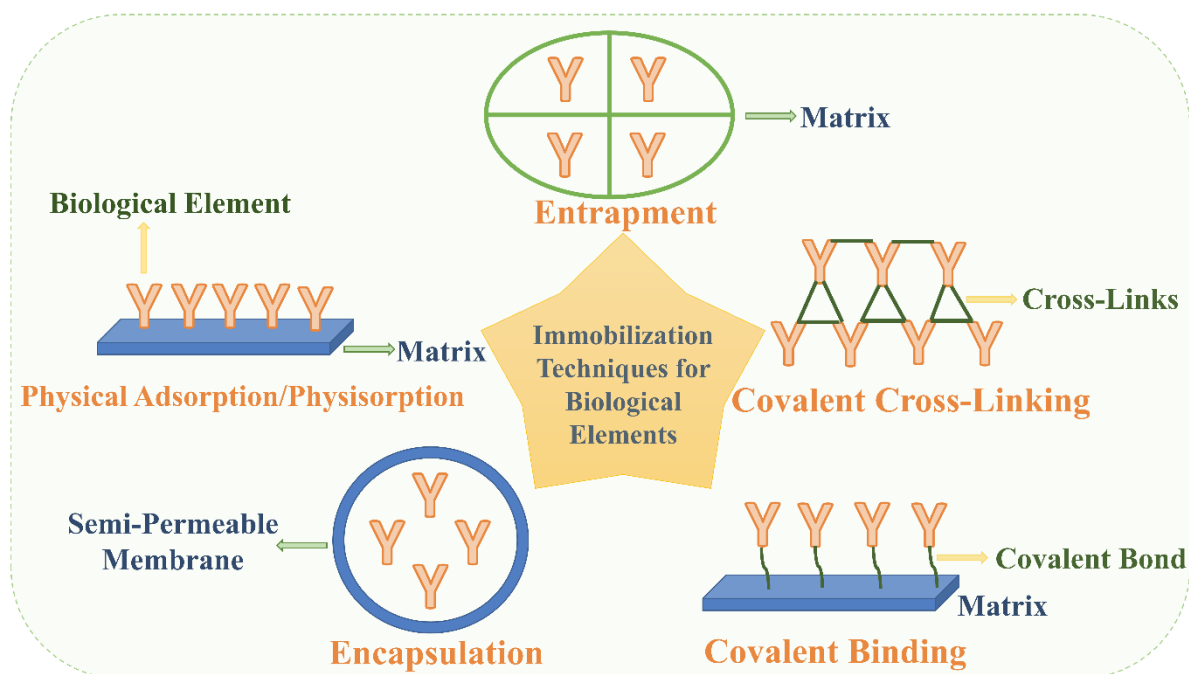


Fig. 1.5 Shows various techniques for immobilization of biological elements on the immobilization matrix

- (i) **Physical method of immobilization of biological element on the immobilization matrix:** The physical method of attachment is usually reversible. Physical methods are suitable

when real-time monitoring involving fast response and recovery is desired, but these weak linkages are not favorable when testings are done in buffer solutions like in the case of electrochemical measurements [2]. Adsorption, entrapment, and encapsulation are some examples of physical methods.

(a) **Physical adsorption or physisorption** – in this method the biological element gets attached to the immobilization matrix using weak interactive forces like electrostatic interaction, Van Der Waals forces, hydrophobic interactions, hydrogen or ionic bonding, etc. This method is uncomplicated and economical, however, due to weak bonding the shelf life is small and the sensor is susceptible to temperature and pH changes. This method is usually employed in enzymatic sensors [15, 21].

(b) **Physical entrapment** – in this method, the biological element is entrapped in a polymer matrix which is then cast onto the working electrode. Conductive polymers like Nafion, polyaniline, or starch gels are used as matrices for entrapment [15].

(c) **Encapsulation** – in this method an inert membrane is used to encapsulate the biological element on the working electrode [15]. This way the biomolecules are confined in a limited space. Since an inert membrane is used, thus the biomolecules do not interact with the membrane which prevents their denaturation and provides a stable matrix. Glutaraldehyde, Nafion, collagen, and cellulose acetate are some of the commonly used membranes [15].

(ii) **Chemical method of immobilization of biological element on the immobilization matrix:** The chemical method is irreversible and primarily includes covalent bonding and covalent crosslinking. Such a method is more desirable when testings are done in buffer saline solution, involving repeated interaction with the redox media [2].

(a) **Covalent cross-linking** – this technique involves the usage of a linker molecule to form the bond between the immobilization matrix and the biological element. Inert proteins like

bovine serum albumin (BSA), or linkers like glutaraldehyde or (3-aminopropyl)triethoxysilane (APTES) are used linkers. A stronger chemical binding ensures less leakage, however, sometimes the linkages occur between protein molecules themselves, instead of linkage between the matrix and the biological element, which causes a loss of activity of the biological element [15].

(b) **Covalent binding** – In this case of the covalent immobilization of biomolecules, a covalent bond is formed between the matrix and the biological element using functional groups like carboxyl (-COOH) and amino (-NH₂). Covalent binding is particularly favorable because the covalent connection between the biological element and the immobilization matrix ensures that the biological element is not released upon repeated usage [15]. This technique is extensively used for the immobilization of biomolecules and we have also chosen this method of immobilization of antibodies on the immobilization matrix.

1.2.4 Important parameters of a biosensor on which its performance is evaluated

1. **Sensitivity** – the change in the output response of the biosensor per unit change in the analyte's concentration is termed the sensitivity of the biosensor.
2. **Specificity** – the ability of the sensor to identify the target analyte independently from other species by giving an analytical response only for the target analyte is termed specificity. The biological element plays a vital role in making the sensor-specific. For example, in affinity-based sensors, antibodies are particularly specific to their analyte.
3. **Reproducibility** – a biosensor is termed to be reproducible if, various identical biosensors fabricated under similar conditions give identical responses.
4. **Stability** – a biosensor is termed to be stable if it can give a similar response for repeated cycles of measurement. The immobilization matrix and attachment of biological element to it plays a significant role in establishing the stability of the biosensor.

5. **Shelf Life** – shelf life is the time duration for which the biosensor gives the same response for a particular concentration of the target analyte.
6. **Linearity** – linearity is defined as the range in which the biosensor displays a linear relationship between its response and the concentration of the analyte.
7. **Reusability/Regenerability** – the number of times the binding sites of the biosensor can be regenerated for the interrogation of the same level of the analyte. This is useful to remove sensor-to-sensor variance [26].

1.3 Various functional materials have been explored for the fabrication of immobilization matrices previously

Functional nanomaterials like graphene, metallic NPs, polymers, etc can prove to be an innovative method for the fabrication of biosensors with high analytical performance. Metallic NPs are usually employed as the immobilization matrix, to provide smooth conduction and biocompatibility [33], however, they suffer from complex immobilization procedures. Au NPs particularly have the capability of self-assembling and providing excellent conductivity, but they are expensive which limits their utilization. Using metallic NPs alone is not sufficient and requires a comprehensive methodology, also they are susceptible to salt concentration which may lead to their aggregation [34]. Sol-gel-derived silica-based matrices have been tremendously explored for the fabrication of immobilization platforms [35, 36]. Even though they offer various multifaceted advantages, their brittleness proves to be a major obstacle in their widespread utilization for fabricating biosensors [37]. Also, sol-gel materials are less conductive and offer poor resistance to interference [37]. Being chemically stable, highly conductive, and having high tensile strength, carbon nanotubes (CNTs), are been extensively used for fabricating biosensors [38-40]. But, their insolubility, non-uniformity, low control over the manufacturing process, and aggregation limit their utility in the fabrication of

immobilization matrix [34]. Another popular carbon-based material is graphene, which has various favorable characteristics for the fabrication of biosensors, but insolubility in water calls for its modification or composite formation [34]. Nanowires of different materials show excellent potential for the fabrication of immobilization matrices because of their electronic characteristics, compact size, and high width-to-length ratio [41]. But nanowires have an inherent limitation, that is an exponential decay of the electrostatic potential which arises due to the charge of the analyte with the increasing length [34]. Polymers also offer numerous merits like tunable conductivity, no requirement for purification, and low-temperature synthesis [42]. But polymer materials alone suffer from low stability, poor conductivity of electrons, and a randomly oriented morphology of nanofibers which renders a low analytical performance to the biosensors [34]. The practical utility of the biosensors, is possible only if the immobilization matrix is highly stable, conductive, has large surface area for maximum attachment and immobilization of biomolecules, and is synergistic with other materials for the enhancement of the performance of biosensors. Therefore, 2D nanomaterials and particularly MoS₂, are becoming increasingly popular and widely explored for the immobilization of enzymes, antibodies and other biological elements, pertaining to the innumerable favourable properties for construction of biosensors.

1.4 Properties of MoS₂ and its selection for the fabrication of immobilization matrix

1.4.1 Structure of MoS₂

Primarily MoS₂ can exist in two phases, one is the trigonal prismatic, and the other is octahedral coordination of Mo atoms [43]. The 2H and 3R forms of MoS₂ correspond to trigonal prismatic coordination, while the 1T form corresponds to the octahedral phase [43-45]. Most of the

studies use the dominant and more stable 2H phase, in which each unit cell has two layers of Mo and S atoms covalently bonded to each other, arranged in a hexagonal symmetry. In the 3R phase, three such layers are present, stacked in a rhombohedral symmetry. 3R phase is not stable and gets transformed into the 2H phase just on heating. These layers have weak Van der Waals interactions amongst themselves.

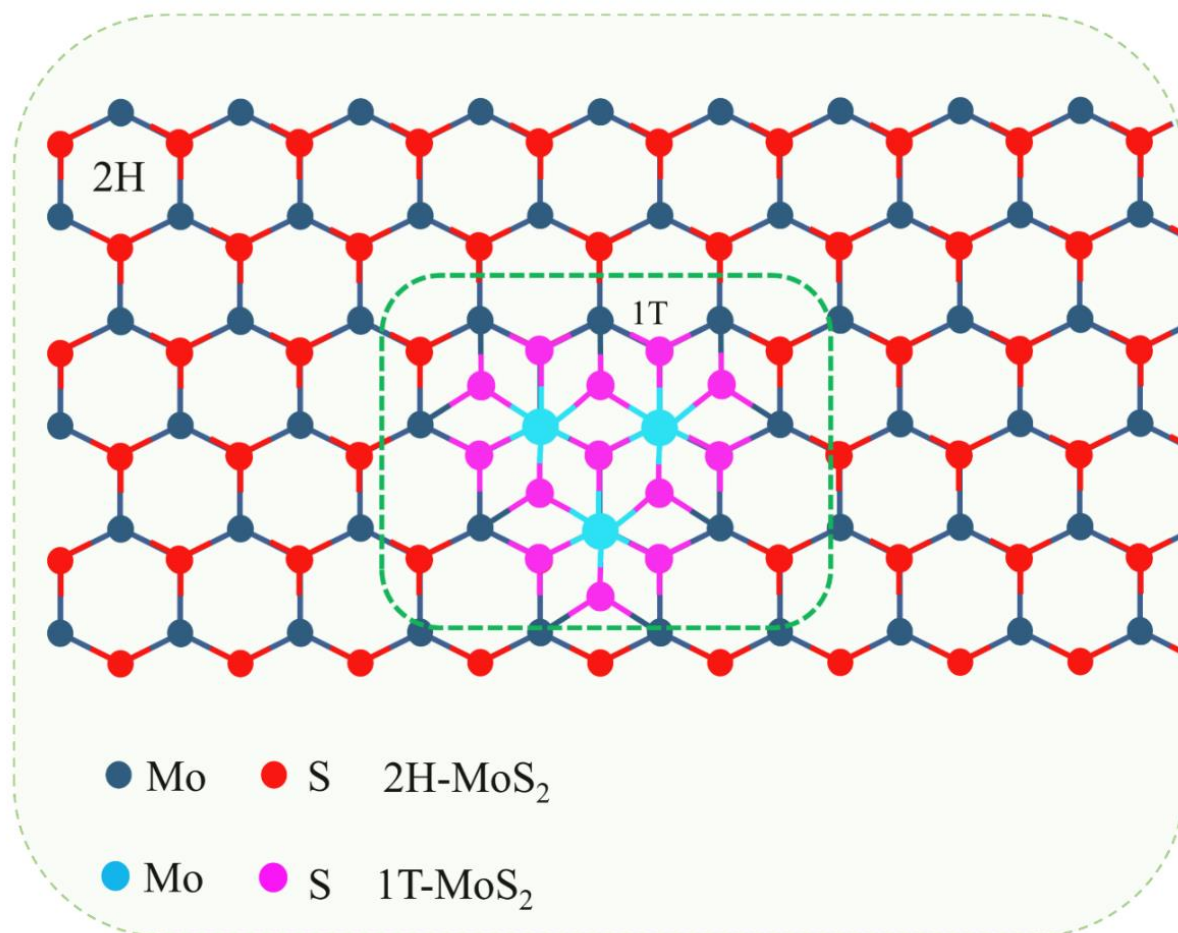


Fig. 1.6: Schematic showing 2H and 1T structure of MoS₂

Being the stable phase 2H-MoS₂ is used to extract mono or few-layer MoS₂ by exfoliation method, as a consequence of the weak van der Waals forces of interaction between the layers. The octahedral coordination of Mo atoms results in trigonal symmetry and this phase is termed 1T, which is metallic [43]. Since the p-orbital of S atoms lies much below the fermi level therefore the filling of the d-orbitals determines the physical and chemical properties of

different phases of MoS₂ [43]. Completely filled d-orbitals give rise to the semiconducting nature of the 2H phase, while partially filled d-orbitals lead to the metallic 1T phase [43]. **Fig. 1.6** shows the 2H and 1T phases of MoS₂.

1.4.2 Properties of MoS₂ which make it a favorable candidate for the fabrication of immobilization matrix

Being a 2D nanomaterial, MoS₂ is bestowed with a high surface area [46]. The relevance of high surface area comes from the fact that more biological elements can be immobilized implying a larger number of attachment sites for the analyte, thus preventing the saturation of the biosensor. This facilitates the detection of a large range of the target analyte, increasing the linear detection range of the device and conferring an enriched shelf life [47]. A large electroactive surface area and biocompatibility are also highly favorable for the fabrication of biosensors [46]. MoS₂ is characterized by strong covalent interaction between Mo and S, whereas the S atoms are bonded to each other via weak Van der Waals interactions [48].

Layered MoS₂ has a lot of active sites due to unsaturated S atoms at the surface sites which are available for coordination [8, 49]. The surface functionalization of MoS₂ is important to lessen the non-specific dangling bonds [47]. Further, surface functionalization of MoS₂ is important to introduce functional groups on its surface for covalent attachment of the biological element. Further, MoS₂ furnishes a high dispersibility in various solvents like ethanol, acetone, acetonitrile, de-ionized (DI) water, isopropanol (IPA), etc which makes its film fabrication quite convenient [7, 50]. The abundance of MoS₂ in nature as molybdenite makes it find its utility in plentiful applications [51]. MoS₂ can efficiently adsorb different types of biological elements ranging from proteins, drugs, nucleic acids, enzymes, etc through covalent and non-covalent interactions [7]. **Fig. 1.7** shows all these properties highlighted in a schematic diagram.

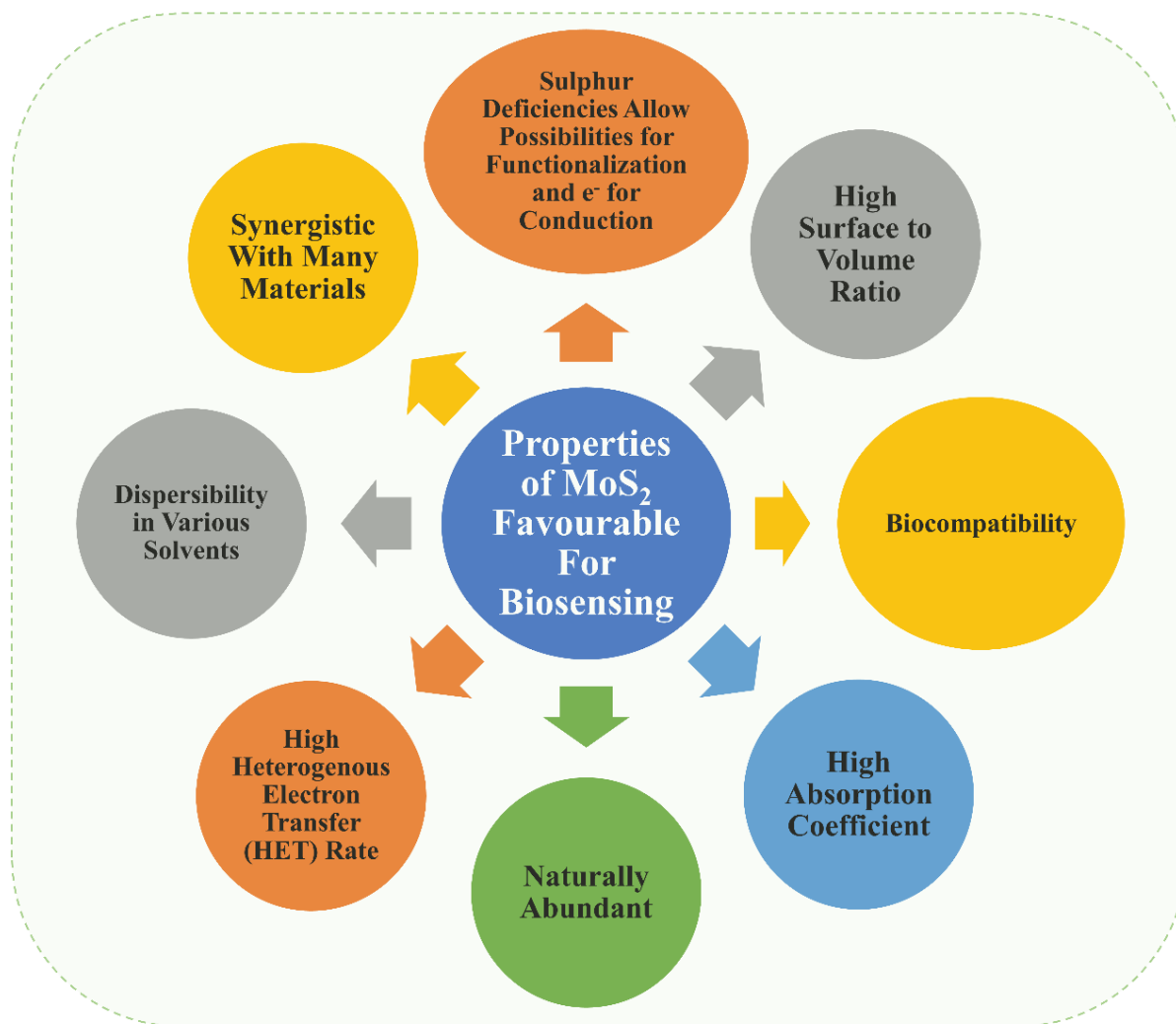


Fig. 1.7: Properties of MoS₂ favorable for biosensing in a schematic diagram

1.4.3 Utilization of bare MoS₂ as an immobilization matrix

Recent reports have unveiled that MoS₂ can be used as the immobilization matrix for the immobilization of different types of biological elements. For instance, a recent work reports the utilization of MoS₂ nanoflowers (NFs) in the fabrication of immobilization matrix for the electrochemical detection of tumor necrosis factor- α (TNF- α) in serum of cancer patients [47]. The immobilization of anti-TNF- α antibodies on MoS₂-NFs is achieved using a physical adsorption technique to avoid the use of any linker molecule. The biosensor is found to be promising due to its high sensitivity, wide linear detection range, high selectivity, the shelf life

of 4 weeks, and low limit of detection. MoS₂ is found to be a promising material due to its elevated surface area to volume ratio which promotes the physical adsorption of anti-TNF- α antibodies on its surface. In another work, Yadav, and co-workers utilized MoS₂ NPs for the fabrication of an immobilization matrix for the electrochemical detection of ampicillin (AMP), an antibiotic [52]. MoS₂ is used due to its high chemical stability, elevated surface-to-volume ratio, biocompatibility, high electron transfer ability, and easy functionalization. MoS₂ NPs-based sensor is found to have a high sensitivity, a wide linear detection range, good specificity excellent recovery along with a low detection limit. APTES is used as the linker molecule for anchoring the amino (-NH₂) group on the immobilization matrix for bonding with the carboxyl group (-COOH) of the antibody. Singhal et al utilized MoS₂ nanosheets (NS) for the immobilization of chikungunya probe DNA for the electrochemical detection of the chikungunya virus [46]. MoS₂ is utilized to dispense biocompatibility to the immobilized biological element after its immobilization. The basal planes of MoS₂ NS can adsorb single-stranded DNA by van der Waals forces acting between nucleobases of DNA and basal planes of MoS₂. The MoS₂ NS-based sensor is found to be sensitive, repeatable, and specific, with a wide linear detection range and low limit of detection. Wang et al utilized MoS₂ NPs for the detection of trace levels of hydrogen peroxide (H₂O₂), which is a byproduct of various cellular processes [13]. They could get a highly sensitive and selective sensor due to the high activity of MoS₂ NPs along with a low limit of detection.

MoS₂ has been widely explored for enzyme-based sensors also. Like Tuan et al synthesized three different morphologies of MoS₂ namely NFs, NPs, and nanoplatelets for fabricating an immobilization matrix for the detection of glucose [53]. All three morphologies of MoS₂ presented a low detection limit, good sensitivity, high specificity, stability, and reproducibility. The outstanding performance of these MoS₂ nanostructures is owed to their biocompatibility, high surface area, high electrochemical catalytic activity, and electron

transfer abilities. Various other reports are available in which MoS₂ has been used as an immobilization matrix for different biological elements owing to its biocompatibility, fast electron transfer, and large surface area [54-58].

1.4.4 Modification of MoS₂ by composite formation for fabrication of immobilization matrix

Owing to the synergistic effect of MoS₂ with other materials like metal NPs [Gold (Au), Silver (Ag), Nickel (Ni), Copper (Cu), etc.], graphene, polymers, metal oxides, etc., composite is usually formed to enhance the property of the final blend [59, 60]. For instance, Owais et al fabricated an ultrasensitive sensor based on rGO-MoS₂ for the detection of epithelial cell adhesion molecules (EpCAM), a cancer biomarker [61]. The sensor is found to exhibit a wide linear detection range, low detection limit, colossal stability, remarkable specificity, and reproducibility. The excellent analytical performance of the biosensor is owed to the synergistic effect between rGO and MoS₂ where rGO prevents stacking of MoS₂ layers, in turn restoring the active sites for immobilization along with ensuring the mobility of charge carriers. Soni and co-workers composited MoS₂ with polyaniline (PANI) for the fabrication of an immobilization matrix for the electrochemical detection of chronic myelogenous leukemia (CML) [62]. PANI is used to anchor protonated active sites, along with enhancing the stability of the MoS₂ structure during repeated cycles of charge and discharge. PANI itself has poor insolubility, low mechanical strength, and difficult processing. Therefore, the compositing overcomes the individual drawbacks of MoS₂ and PANI. The resultant biosensor is found to have a high value of electrochemical parameters like electroactive surface area, fast transfer of electrons, a broad linear detection range, low limit of detection, the shelf life of 42 days, and capability of regeneration. Solanki et al [63] decorated MoS₂ nanosheets with Au NPs to escalate the charge transfer process for the electrochemical detection of dengue and to prevent

restacking of MoS₂ nanosheets. The as-prepared biosensor is found to be highly sensitive, and reproducible, with a low detection limit and broad linear detection range. Su and co-workers utilized Au decorated thionine-MoS₂ composite for electrochemically detecting carcinoembryonic antigen (CEA) [64]. The biosensor presents excellent selectivity, low detection limit, remarkable reproducibility, and high stability with promising results in real human sera samples. Numerous other reports are also available which provide clear evidence that compositing MoS₂ with other materials can greatly enhance the properties of the immobilization matrix in turn escalating the performance of the biosensor [65-68].

1.5 Cancer and the importance of its rapid and sensitive detection

Cancer is one of the deadliest diseases and thus a prime cause of mortality these days [69]. Unregulated growth of cells in any part of the human body causes cancer [70]. An increase in population and socio-economic development has a direct correlation with the escalating number of cases of cancer incidence and mortality [69]. Amongst various types of cancers, lung cancer constitutes to be the leading cause of death related to cancer [69]. Tobacco smoking and inhalation of hazardous industrial emissions such as asbestos, arsenic, and radon are the primary causes of lung cancer [70]. Lung cancer severely impacts the quality of life since the oxygenation levels are reduced and the chances of metastasis are higher [32]. Therefore, timely detection of lung cancer can enhance the survival time of the patient, along with ensuring effective treatment and elevating the quality of life. Based on the clinical behavior and response to radio- and chemotherapy, lung cancer can be divided into two types namely non-small cell lung cancer (NSCLC) and small cell lung cancer (SCLC) [71]. Conventionally used techniques for the detection of lung cancer include magnetic resonance imaging (MRI), computerized axial tomography (CAT), positron emission tomography (PET),

biopsy, chest radiography, sputum cytology, chest x-ray, and bone scans [6, 32]. However, their limited availability, high cost, the expertise required to operate the instruments, repeated scanning, and heavy machinery make their utilization challenging [6, 72]. This calls for a device that can be used for quick, specific, and sensitive detection of lung cancer. Overexpression of protein biomarkers as a result of the growth of cancer cells can be utilized for the detection of lung cancer [6]. For various subtypes of lung cancer, different biomarkers with varied sensitivities and specificities are used like CEA, cytokeratin 19 fragment (CYFRA-21-1), alpha-fetoprotein (AFP), serum carbohydrate antigen – 125 (CA-125), ferritin, CA – 19.9, and neuron-specific enolase (NSE) [72]. NSE is regarded as a highly sensitive and specific biomarker for small cell lung cancer (SCLC) and is found to have a concentration $> 12 \text{ ng mL}^{-1}$, in 69% of cases diagnosed with SCLC [6]. NSE can be used in both diagnosis and prognosis of SCLC and also as an indicator of treatment efficacy for SCLC. There are two clinical stages of SCLC named limited-stage (LD) and extensive-stage disease (ED) [73]. NSE can be used for diagnosis of both these stages since serum NSE level rises to 13 ng mL^{-1} and 59 ng mL^{-1} in case of patients suffering from LD and ED respectively [74]. Therefore, NSE has been chosen as the target analyte for testing fabricated biosensors, due to its high specificity, sensitivity, and higher concentration found in serum samples of a patient suffering from SCLC.

1.6 Importance of choosing an appropriate immobilization matrix and the motivation for this work

Emerging technologies and the exploration of the outshining properties of nanostructured materials can significantly enhance the electrochemical performance of biosensors for the detection of SCLC. Enormous efforts are being put into the investigation of strategies for the

fabrication of immobilization matrices and their biofunctionalization since the immobilization matrix plays a pivotal role in the sensitive detection of the target analyte. In comparison to planar electrodes, nanostructured electrodes are being pursued, due to their high surface area, high loading capacity, and facile electron transfer which escalates the sensitivity and accuracy of the biosensor [75]. A good immobilization matrix provides maximum immobilization sites for the attachment of biological elements along with complete conservation of their bioactivity to ensure stability and regeneration [19]. Various immobilization matrices have been explored previously for the electrochemical detection of NSE. For instance, Han et al utilized a graphene-based biosensor functionalized using Au NPs for the electrochemical detection of NSE [76]. Yin and co-workers employed Au and palladium (Pd) metal NPs with multi-walled carbon nanotubes (MWCNTs) owing to their synergistic effect, for the electrochemical detection of NSE [77]. Zhang et al reported the use of Au electrode modified with rGO and polyaniline (PANI) for fabricating electrochemical biosensors for detecting NSE [71]. Wang et al modified a glassy carbon electrode (GCE) with a nanocomposite of Au NPs, platinum (Pt) NPs, and polyresorcinol to enhance the conductivity of the platform and immobilize antibodies without using any coupling agent for amperometric detection of NSE [25]. Fu and co-workers utilized Pt nanoflowers (NFs) as nano labels for anti-NSE antibodies for fabricating a sandwich-type immunoassay for electrochemical detection of NSE [78]. Tang and co-workers utilized polypyrrole (Ppy) and poly(3,4-ethylenedioxythiophene) (PEDOT) nanotubes coupled with Au NPs to escalate conductivity, and interfacial electron transfer rate, and ensure bioactivity of immobilized biomolecules. A stable sensing environment could be provided for 30 cycles of CV [79]. Yu and co-workers fabricated a sandwich-type immunosensor utilizing hollow balls of carbon supporting graphene as an immobilization matrix and found it to be stable for 30 CV cycles [80]. Mo and co-workers fabricated a sensor utilizing Au and Pt NPs for detecting NSE and CYFRA21-1 simultaneously and observed a stable trend for 15 CV

cycles only. However, we found that still a considerable amount of work has to be done on two prospects

- 1) large costs of gold/platinum electrodes and metallic NPs like Au, Pt, or Pd used for the fabrication of biosensors, which retards their commercial realization
- 2) Maintaining the response of the signal along with ensuring that the bioactivity of the biosensor is retained even after repeated cycles of measurement.

Therefore, in this work, MoS₂ is synthesized using a facile and low-cost hydrothermal method and is tested for its electrochemical performance (discussed in chapter 3). Then it is modified using rGO and chitosan (CS) to anchor functional groups on MoS₂ and tested for electrochemical performance by choosing NSE as the target analyte owing to its high specificity and sensitivity for the detection of SCLC (discussed in chapters 4 and 5 respectively). The performance of both the immobilization matrices is discussed by determining the important parameters of a biosensor like sensitivity, specificity, reproducibility, stability, electroactive surface area (A_e), and heterogenous rate transfer constant (K_o). It is found that the direction of immobilization of antibodies plays a direct role in determining the stability of the matrix.

1.7 Objectives of the present work

- Literature review and identification of suitable 2D nanomaterial and biomarkers as target analytes for biosensors.
- Synthesis of 2D nanomaterials using different methods to attain optimum structure with enhanced properties.
- Film fabrication of 2D nanomaterials using spin coating/electrophoretic deposition/dip coating/drop-casting.

- Modification of 2D nanomaterials via composite formation/doping/functionalization for sensing applications.
- Immobilization of biomolecules (anti-body) over the 2D nanomaterial prepared matrix and studies related to biosensing or adsorption of gases for studying gas sensing.

References

- [1] Edelstein, Alan S., and R. C. Cammarata. *Nanomaterials: synthesis, properties and applications*. CRC press, 1998.
- [2] Anichini, Cosimo, Włodzimierz Czepa, Dawid Pakulski, Alessandro Aliprandi, Artur Ciesielski, and Paolo Samori. "Chemical sensing with 2D materials." *Chemical Society Reviews* 47, no. 13 (2018): 4860-4908.
- [3] Malhotra, Bansi Dhar, and Md Azahar Ali. "Nanomaterials in biosensors: Fundamentals and applications." *Nanomaterials for biosensors* (2018): 1.
- [4]. Zhang, Hua, Hui-Ming Cheng, and Peide Ye. "2D nanomaterials: beyond graphene and transition metal dichalcogenides." *Chemical Society Reviews* 47, no. 16 (2018): 6009-6012.
- [5] Zhu, Yanwu, Shanthi Murali, Weiwei Cai, Xuesong Li, Ji Won Suk, Jeffrey R. Potts, and Rodney S. Ruoff. "Graphene and graphene oxide: synthesis, properties, and applications." *Advanced materials* 22, no. 35 (2010): 3906-3924.
- [6] Khatri, Ritika, and Nitin K. Puri. "Electrochemical biosensor utilizing dual-mode output for detection of lung cancer biomarker based on reduced graphene oxide-modified reduced-molybdenum disulfide multi-layered nanosheets." *Journal of Materials Research* 37, no. 8 (2022): 1451-1463.
- [7] Wang, Jianling, Lihua Sui, Jia Huang, Lu Miao, Yubing Nie, Kuansong Wang, Zhichun Yang et al. "MoS₂-based nanocomposites for cancer diagnosis and therapy." *Bioactive Materials* 6, no. 11 (2021): 4209-4242.
- [8] Sinha, Ankita, Bing Tan, Yujin Huang, Huimin Zhao, Xueming Dang, Jiping Chen, and Rajeev Jain. "MoS₂ nanostructures for electrochemical sensing of multidisciplinary targets: A review." *TrAC Trends in Analytical Chemistry* 102 (2018): 75-90.
- [9] Zhao, Yanyan, Long Kuai, Yanguo Liu, Pengpeng Wang, Hamidreza Arandiyani, Sufeng Cao, Jie Zhang et al. "Well-constructed single-layer molybdenum disulfide nanorose cross-linked by three dimensional-reduced graphene oxide network for superior water splitting and lithium storage property." *Scientific reports* 5, no. 1 (2015): 1-10.
- [10] Wang, Lina, Ying Ma, Min Yang, and Yanxing Qi. "Hierarchical hollow MoS₂ nanospheres with enhanced electrochemical properties used as an electrode in supercapacitor." *Electrochimica Acta* 186 (2015): 391-396.
- [11] Li, Zhongcheng, Jiaojiao Ma, Ying Zhou, Zhengmao Yin, Yubao Tang, Yinxue Ma, and Debao Wang. "Synthesis of sulfur-rich MoS₂ nanoflowers for enhanced hydrogen evolution reaction performance." *Electrochimica Acta* 283 (2018): 306-312.
- [12] Di Bartolomeo, Antonio, Alessandro Grillo, Francesca Urban, Laura Iemmo, Filippo Giubileo, Giuseppe Luongo, Giampiero Amato et al. "Asymmetric Schottky contacts in bilayer MoS₂ field effect transistors." *Advanced Functional Materials* 28, no. 28 (2018): 1800657.
- [13] Wang, Tanyuan, Haichuan Zhu, Junqiao Zhuo, Zhiwei Zhu, Pagona Papakonstantinou, Gennady Lubarsky, Jian Lin, and Meixian Li. "Biosensor based on ultras-small MoS₂ nanoparticles for electrochemical detection of H₂O₂ released by cells at the nanomolar level." *Analytical chemistry* 85, no. 21 (2013): 10289-10295.

- [14] Wang, Lu, Qirong Xiong, Fei Xiao, and Hongwei Duan. "2D nanomaterials based electrochemical biosensors for cancer diagnosis." *Biosensors and Bioelectronics* 89 (2017): 136-151.
- [15] Koyun, Ahmet, E. Ahlatcolu, Y. Koca, and S. Kara. "Biosensors and their principles." *A Roadmap of Biomedical Engineers and Milestones* (2012): 117-142.
- [16] Chalklen, Thomas, Qingshen Jing, and Sohini Kar-Narayan. "Biosensors based on mechanical and electrical detection techniques." *Sensors* 20, no. 19 (2020): 5605.
- [17] Mohanty, Saraju P., and Elias Kougiianos. "Biosensors: A tutorial review." *Ieee Potentials* 25, no. 2 (2006): 35-40.
- [18] Damborský, Pavel, Juraj Švitel, and Jaroslav Katrlík. "Optical biosensors." *Essays in biochemistry* 60, no. 1 (2016): 91-100.
- [19] Chen, Chen, and Junsheng Wang. "Optical biosensors: An exhaustive and comprehensive review." *Analyst* 145, no. 5 (2020): 1605-1628.
- [20] McGrath, Michael J., and Cliodhna Ní Scanaill. "Sensing and sensor fundamentals." In *Sensor technologies*, pp. 15-50. Apress, Berkeley, CA, 2013.
- [21] Naresh, Varnakavi, and Nohyun Lee. "A review on biosensors and recent development of nanostructured materials-enabled biosensors." *Sensors* 21, no. 4 (2021): 1109.
- [22] Tamayo, Javier, Priscila M. Kosaka, José J. Ruz, Álvaro San Paulo, and Montserrat Calleja. "Biosensors based on nanomechanical systems." *Chemical Society Reviews* 42, no. 3 (2013): 1287-1311.
- [23] Arlett, J. L., E. B. Myers, and M. L. Roukes. "Comparative advantages of mechanical biosensors." *Nature nanotechnology* 6, no. 4 (2011): 203-215.
- [24] Lee, Chang-Soo, Sang Kyu Kim, and Moonil Kim. "Ion-sensitive field-effect transistor for biological sensing." *Sensors* 9, no. 9 (2009): 7111-7131.
- [25] H. Wang, Z.J.M.A. Ma, Amperometric immunoassay for the tumor marker neuron-specific enolase using a glassy carbon electrode modified with a nanocomposite consisting of polyresorcinol and of gold and platinum nanoparticles, 184(9) (2017) 3247-3253.
- [26] Goode, J. A., J. V. H. Rushworth, and P. A. Millner. "Biosensor regeneration: a review of common techniques and outcomes." *Langmuir* 31, no. 23 (2015): 6267-6276.
- [27] Rozenblum, Guido T., Ivan G. Pollitzer, and Martin Radrizzani. "Challenges in electrochemical aptasensors and current sensing architectures using flat gold surfaces." *Chemosensors* 7, no. 4 (2019): 57.
- [28] Gupta, Niharika, Venkatesan Renugopalakrishnan, Dorian Liepmann, Ramasamy Paulmurugan, and Bansi D. Malhotra. "Cell-based biosensors: Recent trends, challenges and future perspectives." *Biosensors and Bioelectronics* 141 (2019): 111435.
- [29] Daniels, Jonathan S., and Nader Pourmand. "Label-free impedance biosensors: Opportunities and challenges." *Electroanalysis: An International Journal Devoted to Fundamental and Practical Aspects of Electroanalysis* 19, no. 12 (2007): 1239-1257.
- [30] Beenhouwer, David O. "Molecular basis of diseases of immunity." In *Molecular Pathology*, pp. 329-345. Academic Press, 2018.
- [31] Khatri, Ritika, and Nitin K. Puri. "Electrochemical studies of biofunctionalized MoS₂ matrix for highly stable immobilization of antibodies and detection of lung cancer protein biomarker." *New Journal of Chemistry* 46, no. 16 (2022): 7477-7489.
- [32] Arya, Sunil K., and Shekhar Bhansali. "Lung cancer and its early detection using biomarker-based biosensors." *Chemical reviews* 111, no. 11 (2011): 6783-6809.
- [33] Chang, Honghong, Haochun Zhang, Jia Lv, Bing Zhang, Wenlong Wei, and Jingang Guo. "Pt NPs and DNAzyme functionalized polymer nanospheres as triple signal amplification strategy for highly sensitive electrochemical immunosensor of tumour marker." *Biosensors and Bioelectronics* 86 (2016): 156-163.
- [34] Cho, Il-Hoon, Dong Hyung Kim, and Sangsoo Park. "Electrochemical biosensors: Perspective on functional nanomaterials for on-site analysis." *Biomaterials research* 24, no. 1 (2020): 1-12.
- [35] Wang, Joseph. "Sol-gel materials for electrochemical biosensors." *Analytica Chimica Acta* 399, no. 1-2 (1999): 21-27.
- [36] Jin, Wen, and John D. Brennan. "Properties and applications of proteins encapsulated within sol-gel derived materials." *Analytica Chimica Acta* 461, no. 1 (2002): 1-36.

- [37] Xu, Zhihai, Xu Chen, and Shaojun Dong. "Electrochemical biosensors based on advanced bioimmobilization matrices." *TrAC Trends in Analytical Chemistry* 25, no. 9 (2006): 899-908.
- [38] Guo, Xuefeng. "Single-molecule electrical biosensors based on single-walled carbon nanotubes." *Advanced Materials* 25, no. 25 (2013): 3397-3408.
- [39] Zhang, Xian, Chao-Rui Li, Wei-Cheng Wang, Jian Xue, Ya-Ling Huang, Xian-Xian Yang, Bin Tan et al. "A novel electrochemical immunosensor for highly sensitive detection of aflatoxin B1 in corn using single-walled carbon nanotubes/chitosan." *Food chemistry* 192 (2016): 197-202.
- [40] Gutierrez, Fabiana A., Jose Miguel Gonzalez-Dominguez, Alejandro Ansón-Casaos, Javier Hernández-Ferrer, María D. Rubianes, María T. Martínez, and Gustavo Rivas. "Single-walled carbon nanotubes covalently functionalized with cysteine: A new alternative for the highly sensitive and selective Cd (II) quantification." *Sensors and Actuators B: Chemical* 249 (2017): 506-514.
- [41] He, Bo, Thomas J. Morrow, and Christine D. Keating. "Nanowire sensors for multiplexed detection of biomolecules." *Current opinion in chemical biology* 12, no. 5 (2008): 522-528.
- [42] Chang, Haixin, Ying Yuan, Nanlin Shi, and Yifu Guan. "Electrochemical DNA biosensor based on conducting polyaniline nanotube array." *Analytical chemistry* 79, no. 13 (2007): 5111-5115.
- [43] Zhang, Gong, Huijuan Liu, Jiahui Qu, and Jinghong Li. "Two-dimensional layered MoS₂: rational design, properties and electrochemical applications." *Energy & Environmental Science* 9, no. 4 (2016): 1190-1209.
- [44] Beal, A. R., J. C. Knights, and W. Y. Liang. "Transmission spectra of some transition metal dichalcogenides. II. Group VIA: trigonal prismatic coordination." *Journal of Physics C: Solid State Physics* 5, no. 24 (1972): 3540.
- [45] Xu, Guanchen, Xinsheng Wang, Yupeng Sun, Xiao Chen, Jingying Zheng, Lifei Sun, Liying Jiao, and Jinghong Li. "Metallic and ferromagnetic MoS₂ nanobelts with vertically aligned edges." *Nano Research* 8, no. 9 (2015): 2946-2953.
- [46] Singhal, Chaitali, Manika Khanuja, Nahid Chaudhary, C. S. Pundir, and Jagriti Narang. "Detection of chikungunya virus DNA using two-dimensional MoS₂ nanosheets based disposable biosensor." *Scientific reports* 8, no. 1 (2018): 1-11.
- [47] Sri, Smriti, Deepika Chauhan, G. B. V. S. Lakshmi, Alok Thakar, and Pratima R. Solanki. "MoS₂ nanoflower based electrochemical biosensor for TNF alpha detection in cancer patients." *Electrochimica Acta* 405 (2022): 139736.
- [48] Zhu, Changbao, Xiaoke Mu, Peter A. van Aken, Yan Yu, and Joachim Maier. "Single-layered ultrasmall nanoplates of MoS₂ embedded in carbon nanofibers with excellent electrochemical performance for lithium and sodium storage." *Angewandte chemie* 126, no. 8 (2014): 2184-2188.
- [49] Deng, Jiao, Haobo Li, Jianping Xiao, Yunchuan Tu, Dehui Deng, Huaixin Yang, Huanfang Tian, Jianqi Li, Pengju Ren, and Xinhe Bao. "Triggering the electrocatalytic hydrogen evolution activity of the inert two-dimensional MoS₂ surface via single-atom metal doping." *Energy & environmental science* 8, no. 5 (2015): 1594-1601.
- [50] Chou, Stanley S., Bryan Kaehr, Jaemyung Kim, Brian M. Foley, Mrinmoy De, Patrick E. Hopkins, Jiaying Huang, C. Jeffrey Brinker, and Vinayak P. Dravid. "Chemically exfoliated MoS₂ as near-infrared photothermal agents." *Angewandte Chemie International Edition* 52, no. 15 (2013): 4160-4164.
- [51] Khatri, Ritika, and Nitin K. Puri. "Electrochemical study of hydrothermally synthesised reduced MoS₂ layered nanosheets." *Vacuum* 175 (2020): 109250.
- [52] Yadav, Amit K., Damini Verma, G. B. V. S. Lakshmi, Sergei Eremin, and Pratima R. Solanki. "Fabrication of label-free and ultrasensitive electrochemical immunosensor based on molybdenum disulfide nanoparticles modified disposable ITO: An analytical platform for antibiotic detection in food samples." *Food Chemistry* 363 (2021): 130245.
- [53] Van Tuan, Dinh, Dang Thi Thuy Ngan, Nguyen Thi Thuy, Hoang Lan, Nguyen Thi Nguyet, Vu Van Thu, Vuong-Pham Hung, and Phuong Dinh Tam. "Effect of nanostructured MoS₂ morphology on the glucose sensing of electrochemical biosensors." *Current Applied Physics* 20, no. 9 (2020): 1090-1096.
- [54] Parra-Alfambra, Ana María, Elena Casero, Luis Vázquez, Carmen Quintana, María del Pozo, and María Dolores Petit-Domínguez. "MoS₂ nanosheets for improving analytical performance of lactate biosensors." *Sensors and Actuators B: Chemical* 274 (2018): 310-317.

- [55] Zhai, Y. J., J. H. Li, X. Y. Chu, M. Z. Xu, F. J. Jin, X. Li, X. Fang, Z. P. Wei, and X. H. Wang. "MoS₂ microflowers based electrochemical sensing platform for non-enzymatic glucose detection." *Journal of Alloys and Compounds* 672 (2016): 600-608.
- [56] Sha, Rinky, Nandimalla Vishnu, and Sushmee Badhulika. "MoS₂ based ultra-low-cost, flexible, non-enzymatic and non-invasive electrochemical sensor for highly selective detection of uric acid in human urine samples." *Sensors and Actuators B: Chemical* 279 (2019): 53-60.
- [57] Rubio-Govea, Rodrigo, David P. Hickey, Raul Garcia-Morales, Melissa Rodriguez-Delgado, Mario A. Dominguez-Rovira, Shelley D. Minter, Nancy Ornelas-Soto, and Alejandra Garcia-Garcia. "MoS₂ nanostructured materials for electrode modification in the development of a laccase based amperometric biosensor for non-invasive dopamine detection." *Microchemical Journal* 155 (2020): 104792.
- [58] Narayanan, Tharangattu N., Chiranjeevi SR Vusa, and Subbiah Alwarappan. "Selective and efficient electrochemical biosensing of ultrathin molybdenum disulfide sheets." *Nanotechnology* 25, no. 33 (2014): 335702.
- [59] Wang, Xiaocheng, Yunru Yu, Chaoyu Yang, Changmin Shao, Keqing Shi, Luoran Shang, Fangfu Ye, and Yuanjin Zhao. "Microfluidic 3D printing responsive scaffolds with biomimetic enrichment channels for bone regeneration." *Advanced Functional Materials* 31, no. 40 (2021): 2105190.
- [60] Yadav, Varnika, Shounak Roy, Prem Singh, Ziyauddin Khan, and Amit Jaiswal. "2D MoS₂-based nanomaterials for therapeutic, bioimaging, and biosensing applications." *Small* 15, no. 1 (2019): 1803706.
- [61] Jalil, Owais, Chandra Mouli Pandey, and Devendra Kumar. "Highly sensitive electrochemical detection of cancer biomarker based on anti-EpCAM conjugated molybdenum disulfide grafted reduced graphene oxide nanohybrid." *Bioelectrochemistry* 138 (2021): 107733.
- [62] Soni, Amrita, Chandra Mouli Pandey, Manoj Kumar Pandey, and Gajjala Sumana. "Highly efficient Polyaniline-MoS₂ hybrid nanostructures based biosensor for cancer biomarker detection." *Analytica chimica acta* 1055 (2019): 26-35.
- [63] Solanki, Shipra, Amrita Soni, M. K. Pandey, Ashok Biradar, and Gajjala Sumana. "Langmuir-Blodgett nanoassemblies of the MoS₂-Au composite at the air-water interface for dengue detection." *ACS applied materials & interfaces* 10, no. 3 (2018): 3020-3028.
- [64] Su, Shao, Min Zou, He Zhao, Chengfeng Yuan, Yanan Xu, Chi Zhang, Lihua Wang, Chunhai Fan, and Lianhui Wang. "Shape-controlled gold nanoparticles supported on MoS₂ nanosheets: Synergistic effect of thionine and MoS₂ and their application for electrochemical label-free immunosensing." *Nanoscale* 7, no. 45 (2015): 19129-19135.
- [65] Wang, Xiu, Chengchao Chu, Lei Shen, Wenping Deng, Mei Yan, Shengguang Ge, Jinghua Yu, and Xianrang Song. "An ultrasensitive electrochemical immunosensor based on the catalytic activity of MoS₂-Au composite using Ag nanospheres as labels." *Sensors and Actuators B: Chemical* 206 (2015): 30-36.
- [66] Yoon, Jinho, Jae-Wook Shin, Joungpyo Lim, Mohsen Mohammadniaei, G. Bharate Bapurao, Taek Lee, and Jeong-Woo Choi. "Electrochemical nitric oxide biosensor based on amine-modified MoS₂/graphene oxide/myoglobin hybrid." *Colloids and Surfaces B: Biointerfaces* 159 (2017): 729-736.
- [67] Su, Shao, Haofan Sun, Wenfang Cao, Jie Chao, Hongzhen Peng, Xiaolei Zuo, Lihui Yuwen, Chunhai Fan, and Lianhui Wang. "Dual-target electrochemical biosensing based on DNA structural switching on gold nanoparticle-decorated MoS₂ nanosheets." *ACS applied materials & interfaces* 8, no. 11 (2016): 6826-6833.
- [68] Su, Shao, Wenfang Cao, Wei Liu, Zaiwei Lu, Dan Zhu, Jie Chao, Lixing Weng, Lihua Wang, Chunhai Fan, and Lianhui Wang. "Dual-mode electrochemical analysis of microRNA-21 using gold nanoparticle-decorated MoS₂ nanosheet." *Biosensors and Bioelectronics* 94 (2017): 552-559.
- [69] Sung, Hyuna, Jacques Ferlay, Rebecca L. Siegel, Mathieu Laversanne, Isabelle Soerjomataram, Ahmedin Jemal, and Freddie Bray. "Global cancer statistics 2020: GLOBOCAN estimates of incidence and mortality worldwide for 36 cancers in 185 countries." *CA: a cancer journal for clinicians* 71, no. 3 (2021): 209-249.
- [70] Amani, Jafar, Mehdi Maleki, Alireza Khoshroo, Ali Sobhani-Nasab, and Mehdi Rahimi-Nasrabadi. "An electrochemical immunosensor based on poly p-phenylenediamine and graphene nanocomposite

for detection of neuron-specific enolase via electrochemically amplified detection." *Analytical biochemistry* 548 (2018): 53-59.

[71] Zhang, Qi, Xiaoyan Li, Chunhua Qian, Li Dou, Feng Cui, and Xiaojun Chen. "Label-free electrochemical immunoassay for neuron specific enolase based on 3D macroporous reduced graphene oxide/polyaniline film." *Analytical biochemistry* 540 (2018): 1-8.

[72] Li, X., T. Asmitananda, L. Gao, D. Gai, Z. Song, Y. Zhang, H. Ren, T. Yang, T. Chen, and M. Chen. "Biomarkers in the lung cancer diagnosis: a clinical perspective." *Neoplasma* 59, no. 5 (2012): 500-507.

[73] Xu, Cai-Ming, Ya-Lan Luo, Shuai Li, Zhao-Xia Li, Liu Jiang, Gui-Xin Zhang, Lawrence Owusu, and Hai-Long Chen. "Multifunctional neuron-specific enolase: its role in lung diseases." *Bioscience reports* 39, no. 11 (2019).

[74] Carney, Desmond N, Daniel C Ihde, Martin H Cohen, Paul J Marangos, Paul A Bunn JR, John D Minna, and Adi F Gazdar. "Serum neuron-specific enolase: a marker for disease extent and response to therapy of small-cell lung cancer." *The Lancet* 319, no. 8272 (1982): 583-585.

[75] Schröper, Florian, Dorothea Brüggemann, Yulia Mourzina, Bernhard Wolfrum, Andreas Offenhäusser, and Dirk Mayer. "Analyzing the electroactive surface of gold nanopillars by electrochemical methods for electrode miniaturization." *Electrochimica acta* 53, no. 21 (2008): 6265-6272.

[76] Han, Jing, Ying Zhuo, Ya-Qin Chai, Ya-Li Yuan, and Ruo Yuan. "Novel electrochemical catalysis as signal amplified strategy for label-free detection of neuron-specific enolase." *Biosensors and Bioelectronics* 31, no. 1 (2012): 399-405.

[77] Yin, Shuang, Lihua Zhao, and Zhanfang Ma. "Label-free electrochemical immunosensor for ultrasensitive detection of neuron-specific enolase based on enzyme-free catalytic amplification." *Analytical and bioanalytical chemistry* 410, no. 4 (2018): 1279-1286.

[78] Fu, Xiaohong, Rong Huang, Jiexue Wang, and Xueru Feng. "Platinum nanoflower-based catalysts for an enzyme-free electrochemical immunoassay of neuron-specific enolase." *Analytical Methods* 5, no. 16 (2013): 3803-3806.

[79] Tang, Chunyuan, Ping Wang, Kaiwei Zhou, Jie Ren, Shujun Wang, Feng Tang, Yueyun Li, Qing Liu, and Li Xue. "Electrochemical immunosensor based on hollow porous Pt skin AgPt alloy/NGR as a dual signal amplification strategy for sensitive detection of Neuron-specific enolase." *Biosensors and Bioelectronics* 197 (2022): 113779.

[80] Yu, Xiaodong, Yueyun Li, Yueyuan Li, Shanghua Liu, Zhanglei Wu, Hui Dong, Zhen Xu, Xinjin Li, and Qing Liu. "An electrochemical amplification strategy based on the ferrocene functionalized cuprous oxide superparticles for the detection of NSE." *Talanta* 236 (2022): 122865.

Chapter 2

Methodologies: Synthesis, Film Fabrication and Characterization Techniques

***Chapter 2** puts light on synthesis methods that are used for the synthesis and modifications of MoS₂ nanostructures, the method used for fabricating its films, characterization techniques used for confirming the formation of nanostructures along with different electrochemical techniques used for biosensing application. The formation of MoS₂ nanostructures and its subsequent modifications is examined using various characterization techniques like X-ray diffraction (XRD), Raman spectroscopy, scanning electron microscopy (SEM), thermogravimetric analysis (TGA), Fourier transform infrared spectroscopy (FTIR), transmission electron microscopy (TEM), atomic force microscopy (AFM), energy dispersive X-ray fluorescence (EDXRF), energy dispersive X-ray analysis (EDAX), carbon, hydrogen nitrogen, sulfur (CHNS) analysis, surface profilometer. All these characterization techniques are described in this chapter. Further, for the biosensing studies, a galvanostat/potentiostat Autolab is used and electrochemical characterization studies of fabricated films of MoS₂ nanostructures and subsequently modified nanostructures are done using cyclic voltammetry (CV), electrochemical impedance spectroscopy (EIS), and differential pulse voltammetry (DPV). All these techniques are also read up on in brief in this chapter.*

2.1 Synthesis and modifications of MoS₂ nanostructures

The synthesis and modification of MoS₂ can be done using a vast multitude of techniques to obtain desirous structures and properties to suit various applications. These methods are broadly categorized into two categories, namely 1) Top-down and 2) Bottom-up. In the Top-down technique, the material in bulk form is exfoliated to layers by overcoming the weak binding forces between the layers like Van der Waals forces, by using the mechanical, chemical, or ultrasonic method. While in the bottom-up method, the nanosheets are assembled from individual atoms only. That is, the precursors containing molybdenum (Mo) and sulfur (S) atoms are decomposed first and then the Mo and S atoms are assembled to form MoS₂. Deciding an efficient synthesis route is of utmost importance before the investigation of properties and using the material for desirous applications. Also, to achieve ultimate commercialization and industrialization, it is utterly important to synthesize a high yield of these 2D nanomaterials with satisfactory quality [1]. In our work, we have used a simple and environmentally friendly hydrothermal method for the synthesis of MoS₂ nanostructures. Further, the modification of MoS₂ nanostructures is done with

(i) **reduced graphene oxide (rGO):** graphene oxide [(GO), prepared using improved Hummer's method] is added in the process of synthesis of MoS₂ by hydrothermal method only. Thus, GO is reduced to rGO to modify MoS₂ nanostructures in an in-situ way.

(ii) **chitosan (CS):** CS is added to synthesized MoS₂ nanostructures by an ionic liquid (IL) assisted solid-state grinding method.

All the three methods used for synthesis have been discussed in brief in the following sections and the details of synthesis have been discussed consequently in chapters 3, 4, and 5 respectively.

2.1.1 Hydrothermal method of synthesis

It was in 1845 when the first report on hydrothermal growth of crystals was reported by Karl Emil von Schafhäütl a German geologist. Since then, various scientists and researchers working around the globe have contributed to developing this technique. Hydrothermal synthesis refers to the synthesis of nanomaterials by chemical reactions occurring inside a sealed Teflon-lined stainless-steel autoclave, filled with water-dissolved reagents under certain temperature and pressure conditions. The optimum amount of aqueous reagents is filled in Teflon to create enough pressure so that nanomaterials of desired morphology and phase are obtained. Also, it must be ensured that Teflon should not overflow during the reaction process. Optimization of temperature, pressure and time for which autoclave is kept in a high-temperature oven leads to a high yield of nanomaterials of good crystallinity [2]. **Fig. 2.1** shows the setup of the hydrothermal autoclave used in hydrothermal synthesis.

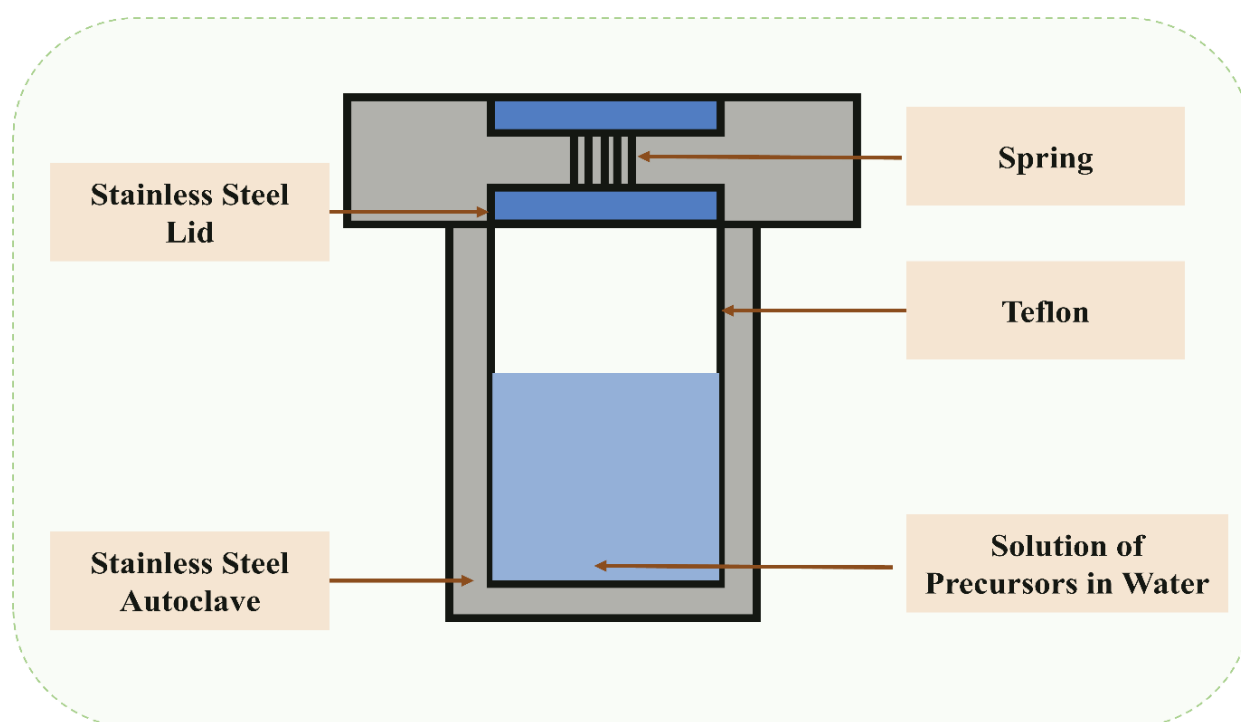


Fig. 2.1: Setup of Teflon-lined stainless-steel autoclave used for hydrothermal synthesis

The components of the hydrothermal reaction are listed below:

- 1. Precursors:** These are the reactants that react in the presence of suitable solvents to give the final product.
- 2. Mineralizers and other Additives:** Various acids and bases are added during the reaction to attain a particular pH. These are known as mineralizers. Additives include reducing, chelating, capping, and stabilizing agents which are required to attain a certain morphology.

The advantages of the Hydrothermal method are as follows:

- 1.** The method is highly feasible for the inexpensive and large-scale production of nanomaterials.
- 2.** Control over the morphology and size of nanomaterials also adds up in favor of this method.
- 3.** The method can be integrated with other methods like sonochemical and electrochemical microwave synthesis techniques which extends the horizon of synthesis techniques of new nanomaterials.
- 4.** Lastly, the experimental setup is very convenient and simple. Once installed, it can be used several times for the synthesis of nanomaterials.

2.1.2 Improved Hummer's Method

The improved hummer's method is a procedure used to synthesize GO under the presence of strong oxidizing agents like potassium permanganate (KMnO_4), potassium chlorate (KClO_3), etc. The conventional hummer's method was modified by William S. Hummers and Richard E. Offerman. The method is fast, non-hazardous, use low temperatures, as well as maintains a high C/O ratio [3].

2.1.3 Solid-state method

The solid-state synthesis method is a versatile technique used to make a wide range of nanomaterials including metal oxides, sulfides, nitrides, and nanocomposites as well. This method requires control of a few parameters like grinding time, annealing temperature, etc. In this method, the desired quantities of the precursors are weighed and ground in mortar and pestle for a certain time. The time may vary from a few hours to a few weeks, depending on the type of sample to be prepared. After grinding, the powder so obtained is heated for a few hours to obtain the desired product. In some cases, high-temperature heating is required which may decompose the desired compound. Also, it requires a lot of energy and time [4]. **Fig. 2.2** shows the mortar and pestle required to grind the precursors.



Fig. 2.2: Mortar and pestle used for grinding in solid-state method

2.2 Method of film fabrication for MoS₂ and modified nanostructures

2.2.1 Electrophoretic deposition (EPD) technique

EPD is a technique by which homogeneous films are produced when an electric field is applied to the charged particles suspended in liquid like de-ionized water, ethanol, isopropanol, etc. It is a cost-efficient and versatile technique to produce films. The EPD cell is a glass beaker comprising two electrodes, separated by a certain distance. One is a reference electrode (RE)

generally taken as a thin platinum (Pt) rod, and the other is a copper (Cu) rod on which the working electrode (WE) is clipped, the film is formed on WE. To deposit the particles onto the substrate, the particles should be uniformly dispersed in the liquid. The common solvents used for dispersion are acetone, distilled water, ethanol, acetonitrile, chloroform, etc. Applied potential and depositing time are optimized to produce the desired films of particular thickness [5, 6]. Heat treatment is sometimes given to the films to enhance adhesion. **Fig. 2.3** shows a typical EPD setup in which the charged particles suspended in the liquid are deposited onto the substrate upon application of a DC power supply for an optimized period.

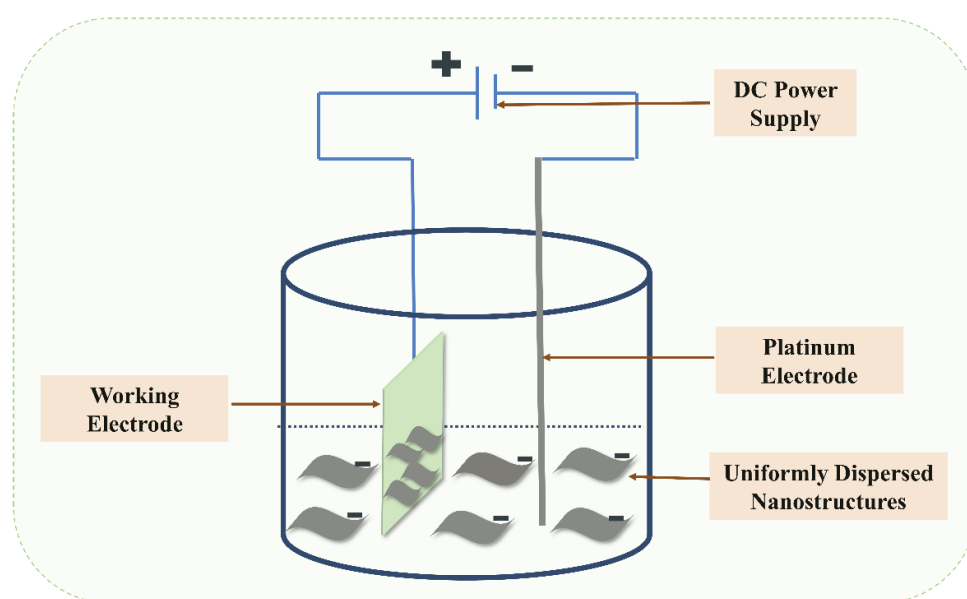


Fig. 2.3: An insight into EPD setup

2.3 Characterization techniques used for structural, morphological, topographical, and spectroscopic investigation of MoS₂ and modified nanostructures

The confirmation of the successful formation of MoS₂ nanostructures and subsequent modifications are examined using various characterization techniques. First of all, the structural study is done using X-ray diffraction (XRD), followed by morphological investigations using

scanning electron microscopy (SEM), field emission scanning electron microscopy (FESEM), and transmission electron microscopy (TEM). Then, the confirmation of layered structures is probed using Raman spectroscopy. The thermal analysis is done using thermogravimetric analysis (TGA) and the examination of attachment of desired functional groups is studied using Fourier transform infrared spectroscopy (FTIR). Elemental analysis is done using energy dispersive X-ray analysis (EDAX), energy dispersive X-ray fluorescence (EDXRF), and carbon, hydrogen, nitrogen, and sulfur (CHNS). Atomic force microscopy (AFM) is used for topographical investigations of the various steps of preparation of the biosensor. The working and principles of all these characterization techniques are discussed in brief in the following section.

2.3.1 X-ray diffraction (XRD) for structural investigations

XRD is one of the most fundamental and powerful tools used commonly to study and identify the structure of both bulk materials as well as nanostructures. This technique can be used to determine several parameters of a crystal structure like its phase orientation, geometry, and lattice constants. The technique can also be employed to examine the stress and strain in a material [7, 8]. Moreover, the analysis using XRD does not call for any sample preparation to obtain the data. XRD is based on the principle of diffraction, therefore, when the X-ray waves having wavelength $\sim 1\text{\AA}$ are incident on a crystal, they get diffracted by the crystal planes since the interplanar spacing is comparable to the wavelength of x-rays. The planes of crystal act analogous to mirrors and thus can give information about the crystal structure [9]. The diffraction pattern of every crystal is unique just like the fingerprint of a human being.

The diffraction of a crystal can be described by Bragg's **equation 2.1** and the schematic explaining the diffraction from a crystal is shown in **Fig. 2.4**.

$$2d_{hkl}\sin\theta_{hkl} = n\lambda \quad (2.1)$$

where,

λ stands for the wavelength of the incident light, d stands for the interplanar spacing, θ stands for the diffraction angle, h , k , and l are the miller indices for the planes of crystals, and n is the order of diffraction.

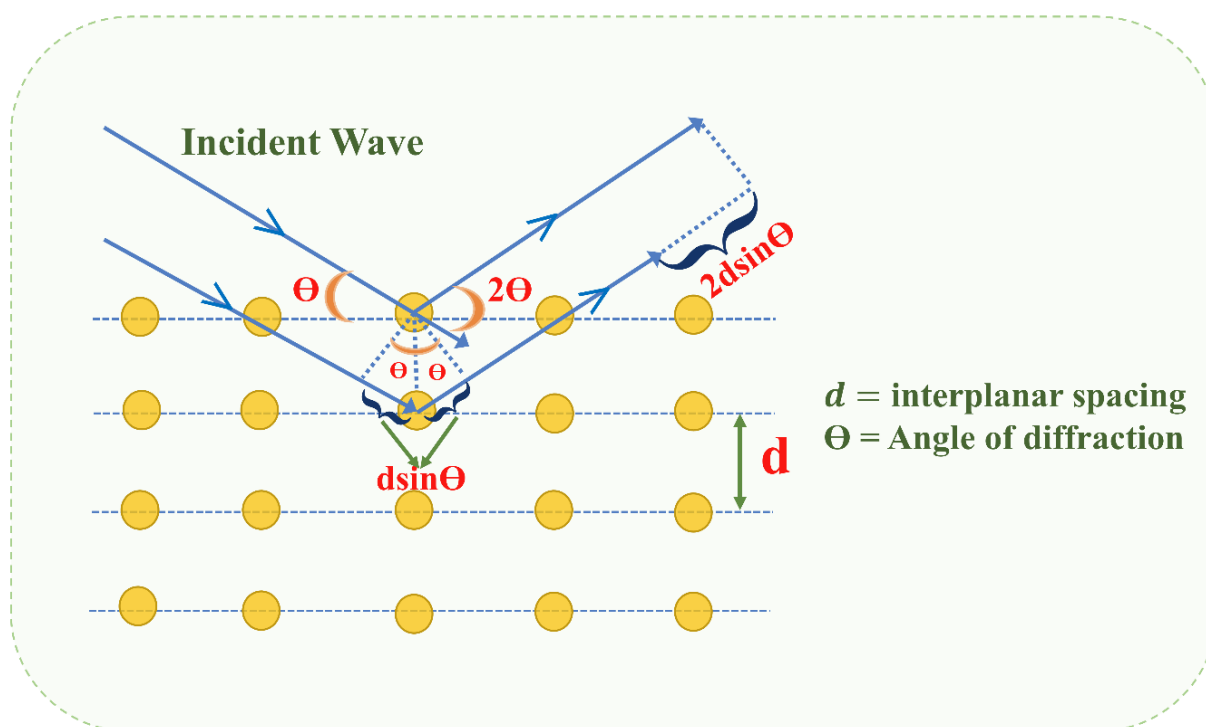


Fig. 2.4: Schematic diagram showing grating-like crystal structure and the diffraction of incident X-rays obeying Bragg's law

The XRD setup consists of a movable copper [Cu-(K_{α})] source for emission of X-ray spectrum of wavelength 1.54 \AA , a fixed sample holder assembly, and a high-speed energy-dispersive compound silicon detector with an automatic adjustable window that can measure patterns in the angular range of 0.150° to 90° . The source tube produces a highly collimated X-ray by hitting an anode metal target like Cu, Mo, iron (Fe), or chromium (Cr) through the high voltage electron beam in a vacuum environment. For single-crystal diffraction, Cu is the most

frequently used target material. The X-ray beam falls on the sample and while the sample and detector spin, the X-ray intensity is detected. The Bragg equation is satisfied when the incident X-ray geometry impinges on the sample, causing constructive interference, and then an intensity peak appears. This radiation is captured by a detector, which also processes it. The signal is then translated to a count rate and the output is taken through a printer or computer monitor.

By using Scherer's formula (**Equation 2.2**), the crystallite size 'D' of the materials can be determined from the peak width [10]

$$D = \frac{k\lambda}{\beta \cos\theta} \quad (2.2)$$

Where θ is the Bragg angle, β is the full width at half maxima (FWHM) of the peak and 'k' is the constant depending upon the geometry of the material.

The sample to be analyzed can be in the form of powder, pellet, or even a thin film, which consists of tiny crystals called crystallites [11].

2.3.2 Scanning electron microscopy (SEM) and field emission scanning electron microscopy (FESEM) for morphological investigations

SEM is a sophisticated kind of microscope that studies the three-dimensional structure of solid samples using electrons rather than light. SEM technique can be utilized to accumulate a lot of information about a sample like the solid sample's topography, composition, and morphology details. On a scale varying from nano to micro scale, it can be regarded as the most efficient approach for analyzing the morphology of organic and inorganic materials. With high magnification up to 30k x and even 1000k x in some contemporary models, SEM creates extremely exact pictures of a variety of materials. A scanning electron microscope uses electromagnetic "lenses" to concentrate an electron beam onto a specimen (which can be a

metal, metal oxide, ceramic, or biological sample). Thus, an image is formed by documenting how the electron beam interacts with the specimen surface. When the electron beam interacts with the specimen, various types of electrons are deflected.

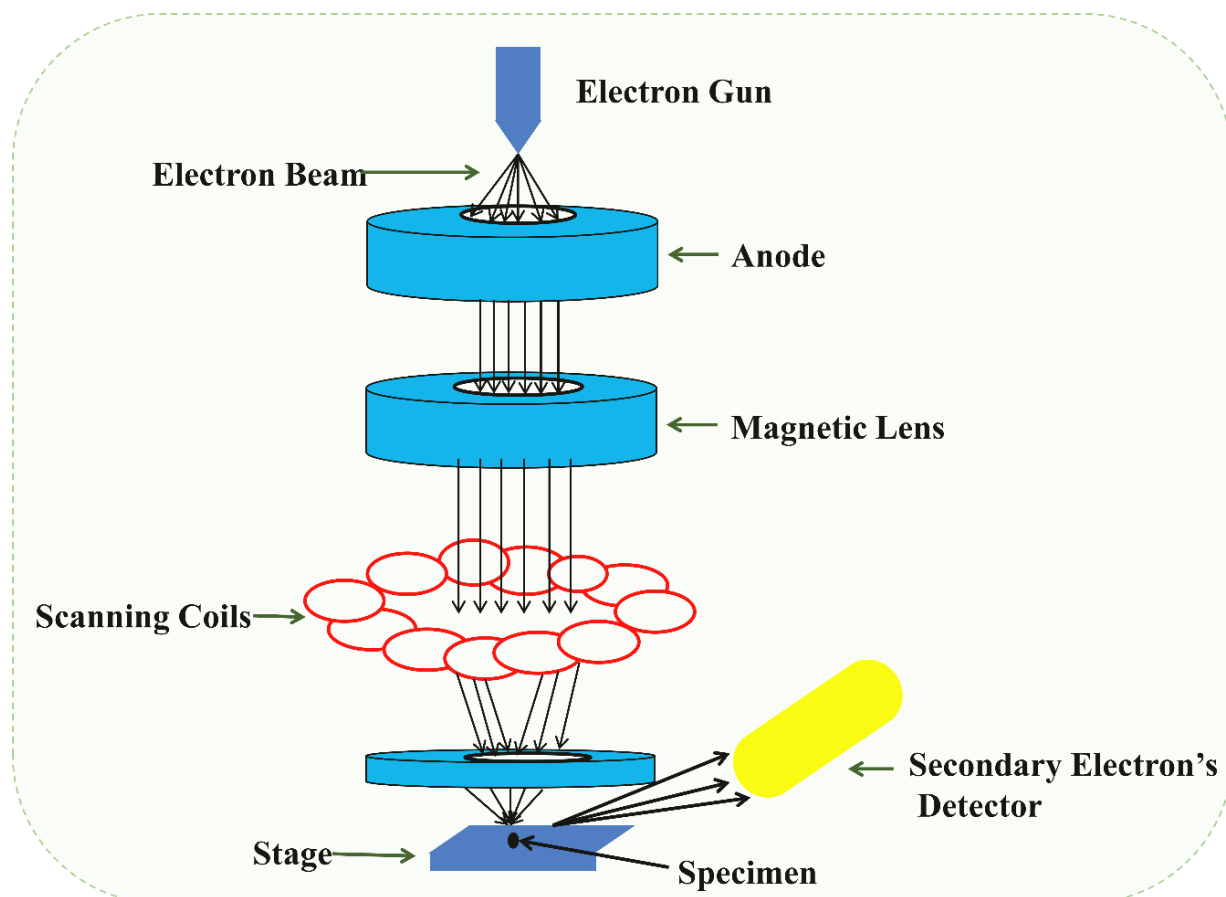


Fig. 2.5: Schematic representation of basic SEM components

A sample for SEM analysis is prepared by distributing powder samples or placing a thin film or a pellet over the conducting carbon tape and coating them with conducting metals like gold (Au) or platinum (Pt) [12]. The sample is coated with conducting metals to avoid the accumulation of incident electrons at a particular spot in the sample. The electron beam is thus swapped across the sample resulting in their interaction with the specimen. The interaction of electrons takes place in the form of their scattering from the surface thereby producing secondary electrons along with backscattered electrons (BSE) and these are used to visually

inspect the sample's surface. Secondary electrons are generated in the entire volume of interaction, but they escape only from a few surface layers and they have energy < 50 eV, they give morphological information about the sample. BSE are elastically scattered from the surface and penetrate more deeply as compared to the secondary electron as their energy is > 50 eV [13]. High atomic number elements generate more BSE than the low atomic number elements and thus appear as bright spots in SEM images. Hence, the different chemical compositions of elements on the surface can be visualized using contrast in images formed by BSE. The bright and dark contrasting image of the surface corresponds to the concentration of BSE while the intensity of the signal is proportional to the concentration of secondary electrons [14]. **Fig. 2.5** shows a schematic representation of basic SEM components.

FESEM is the microscopy technique that uses a field emission source that scans the specimen in a zig-zag pattern. The electron emitters of the field emission gun have an emission capacity up to 1000 times greater than that of a tungsten filament used in ordinary SEM [15]. Like in SEM, here also secondary electrons are collected by a scintillator detector which produces photons. In addition to this, FESEM needs higher vacuum levels and the sample is prepared by coating a very thin layer of Au or palladium (Pd). Using metal apertures and magnetic lenses, the electrons are then concentrated into a thin, monochromatic beam after leaving the electron gun. To create an image of the object, signals from detectors of each type of electron are collected. FESEM delivers information on topography and elements at very high magnifications and an almost limitless depth of field. It is three to six times more effective than ordinary SEM at producing crisper pictures with spatial resolution down to $1/2$ nanometers that are less electrostatically distorted [16]. FESEM is a very popular technique amongst physicists, chemists, biologists, material scientists, and electronic engineers since structures as small as nuclei of cells to microchips can be observed.

2.3.3 Transmission electron microscopy (TEM) for morphological and crystallographic investigations

TEM is a microscopic technique that uses an electron beam that transmits through an ultrathin specimen and interacts with it to give us various information about the specimen. As it passes through it gathers the specimen's morphological, and crystallographic information. In TEM an electron beam is used which is having a short wavelength, resulting in a much higher resolution of the specimen [17]. For a magnified image, imaging equipment like fluorescent screens, photographic film, or sensors like charge-coupled devices (CCD) are utilized. The system operates in two modes, namely diffraction mode and image mode.

TEM setup consists of an electron gun with a high-energy electron beam that passes through a microscope vacuum tube. Next are the condenser lenses, which are used to focus the electrons. Then is a motorized specimen stage, which is used for holding conducting copper grid coated with the sample. The objective lens and the specimen chamber represent the heart of the TEM, where an electron beam gets transmitted through the thin specimen and interacts with it [18]. For the excellent TEM image, the sample thickness is usually around 100 - 200 nm as electrons cannot readily perforate through thickness greater than 200 nm. An objective lens and other lenses form an imaging system that helps in producing high-resolution images and diffraction patterns. The intensity distribution of electrons after transmittance is imaged with a three-stage lens system onto a fluorescent screen [19]. Lastly, there is a charged coupled device (CCD) camera to convert the electric charge into pixels of the image. The operating modes of TEM are high-resolution TEM (HR-TEM), selected area electron diffraction (SAED), or simple TEM to study particle dimensions, morphology, lattice parameters, and expansion direction of the material. **Fig.2.6** shows the schematic diagram of TEM.

The complete setup of TEM is placed in a high vacuum chamber and is interfaced with a graphical user interface (GUI) data acquisition system. Electron beams from electron guns

interact with the sample, resulting in beam scattering. Two types of distribution take place, elastic and inelastic. Elastic scattering occurs due to the arrangement of atoms in the crystal of nanostructures. It yields spot patterns because of coherence in electron beam scattering. On the other hand, inelastic scattering gives rise to beam absorption or emission, which is specific to the compound or chemical structure of nanomaterials.

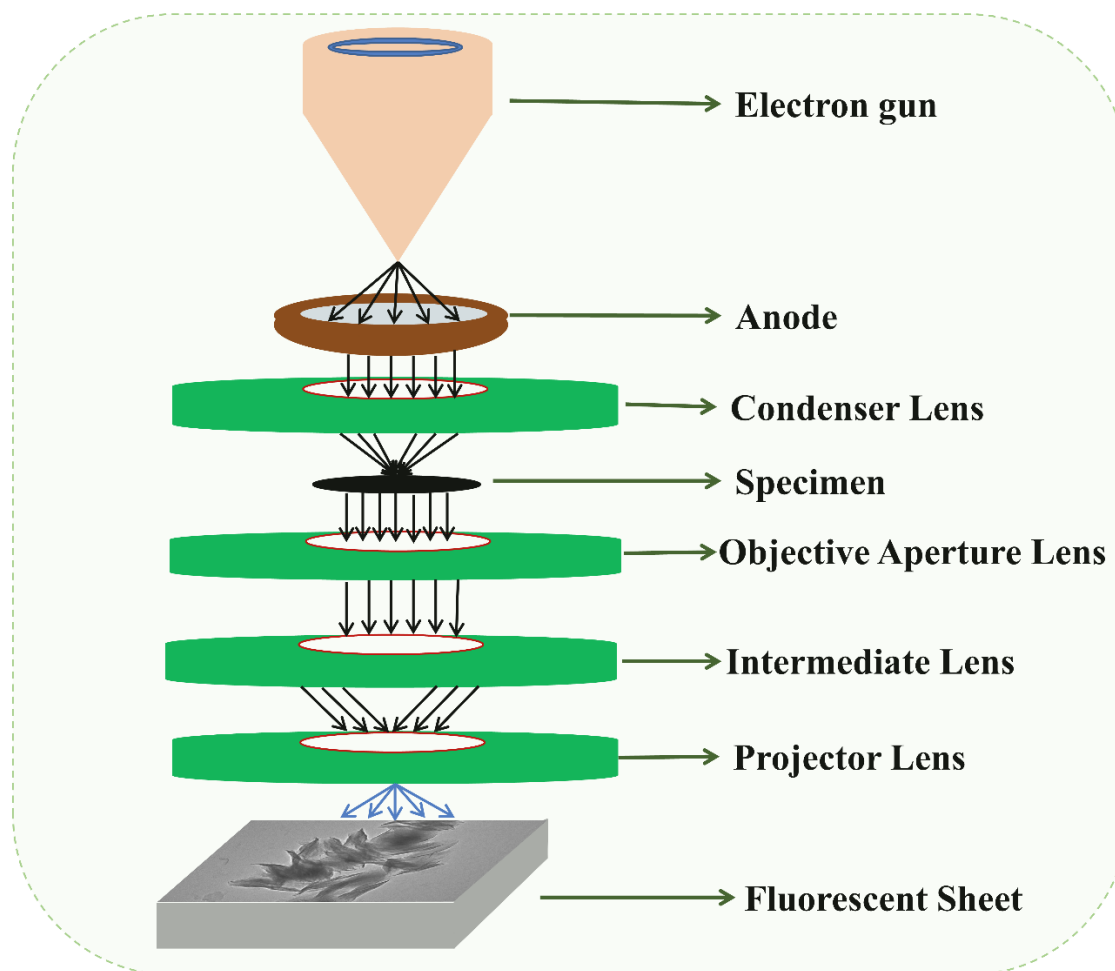


Fig. 2.6: Schematic diagram of TEM

The distinction of the image depends on the bright-field image and the dark-field image mechanism.

Bright-field image: It is formed by uniformly illuminating the entire specimen image in dark against a bright background and collecting the transmitting electrons and blocking the scattered ones.

Dark field image: Image formed on the objective lens's back focal plane by selecting the scattered electrons and blocking unscattered electrons using the objective aperture [20].

HRTEM: By increasing the accelerating voltage of the field emission gun up to 300 kV depending upon the sample compatibility, the wavelength of the electron decreases, and hence point resolution of the image can be enhanced.

The sample used in TEM must be electron transparent. The dimensions of nanostructures act as a diffraction grating for incoming electrons and electrons scattered at different angles depending on the crystal structure, satisfying Bragg's law. At the same time, transmitted electrons are allowed to pass through the sample, forming the monochromatic spots on dark backgrounds corresponding to the reciprocal lattice of crystal planes. This is called the SAED technique and is used to confirm the XRD results

2.3.4 Energy dispersive X-ray analysis (EDAX) for elemental investigation

An effective and simple method for detecting the chemical compounds and elements present in a sample is EDAX. The setup of EDAX is similar to that of SEM which primarily consists of a high electron emission source that releases high-energy electrons in an electron microscope, and then the distinctive X-rays that each element produces are detected [21]. Then, using a method known as X-ray mapping, the sample's elemental composition may be seen superimposed on top of the magnified image of the sample. EDAX is particularly valuable since the number of X-ray photons released by each component inside a sample directly correlates with the concentration of that element. Because of this, it is feasible to determine the amounts of the various compounds present in a sample by converting the X-ray observations into a final X-ray spectrum. As a consequence, material science is the field that has benefited the most from EDAX. It can be used for quality control screening, verification, and certification

as well as to identify and analyze products, including spotting impurities or figuring out unknown constituents.

The electron beam source, detector, processor, and analyzer make up the majority of an EDAX system. The charge that the incident X-ray releases within the crystal are measured by a field-effect transistor (FET) and transforms into a voltage output signal. A computer-assisted system, like the multichannel analyzer (MCA), is in charge of all unattended and automatic operations [22]. The X-ray coming out from the sample hits the detector and causes a charge pulse in the detector. The energy of the observed X-ray is subsequently reflected in the amplitude of the current, which is then transformed into a voltage pulse. The last step is to convert this pulse voltage to a digital signal and increment the relevant energy channel by one more count. Due to the cumulative counts, the final measurement yields a typical X-ray spectrum which can be used to map various elements present in the specimen [23].

2.3.5 Energy dispersive X-ray fluorescence (EDXRF) spectroscopy for elemental investigation

This spectroscopy method utilizes X-rays for identifying different elements in a given sample. The method is highly useful for a variety of different characterization requirements, as it can be used on samples in different states [24]. The sample which is to be analyzed can be solid, liquid, powdered, in the form of a thin film, in the form of slurry, or in the form of a paste [24]. The EDXRF spectroscopy method is very fast, and it can analyze different elements present in a sample in real-time. The method exploits the difference in the energy of electrons present in different shells of an atom to identify the elements and their amount present in the sample. The steps followed to perform EDXRF spectroscopy are quite simple. The X-rays from an X-ray source are first passed through a filter and then a collimator; the radiation is then made incident on the sample. When the X-rays are incident on an inner shell electron of an atom, the radiation

excites the electron, and it moves to an outer shell of the atom. An electron, already present in one of the outer shells of the atom swiftly replaces the electron which moved to the outer shell and emits radiation in the process. The radiation emitted is characteristic of the element and is hence measured to identify the elements present in the sample. This emitted radiation is then detected using an XRF detector. The measure of the energy of radiation is used along with Moseley's law for the qualitative analysis of the elements present in the sample. The count of the number of photons incident on the XRF detector is used for the quantitative analysis of the elements present in the sample. The XRF detector measures both these quantities and sends this data to a computer that analyses this data and produces a graph. The graph so obtained is essentially a plot of energies of radiation on the x-axis versus its respective Intensity on the y-axis. The graph may contain several peaks depending on the elements and their quantities present in the sample. The peaks of the graph are further studied in contrast to the pre-available data of energy peaks for the respective elements. This helps to identify different elements and their amount present in a given sample.

2.3.6 CHNS for elemental analysis

CHNS analysis, also known as elemental microanalysis (or organic elemental analysis), is used to determine the amount of carbon, hydrogen, nitrogen, and sulfur in a sample. It applies to an extensive range of samples including powder, liquid, viscous and volatile samples. In the CHNS analysis, the sample is frozen, dried, and powdered fine, before it is mixed with an oxidizer like vanadium pentoxide (V_2O_5) [25]. Thereafter the sample is heated in a tin vial at 1000 °C. Due to the high temperatures, the sample and the capsule melt releasing many gaseous oxides like CO_2 , SO_2 , and NO_2 [26]. These gases are carried by a current of helium that runs through a column of glass which is filled with an oxidizing agent, like tungsten trioxide (WO_3) and a reducer made of Cu, at a temperature of 1000 °C [27]. Cu is used for the removal of

unconsumed oxygen and reduction of NO₂ to elemental nitrogen. The gasses are then separated and analyzed at 290 °C. The measured values are computed against pre-analyzed data of samples and chromatic responses are reported as per weight percentages. This gives us the crystallographic signature of the sample which helps us identify its organic nature. The composition understood from this technique is also used to check the purity of the sample. The C/N ratios are used to single out the origin of the organic matter. The oxidizing agents and the catalysts used in the classical CHN have also been found applicable in automated analyzers [26].

2.3.7 Surface profilometer for thickness measurement of films

With the increasing demand for machine-made surfaces, the need for precision has brought surface profilometers in trend [28]. Their job is to measure the roughness of the surface with the help of a stylus tip. The conventional surface profilometers had a stylus tip made of diamond and were widely used for research purposes and industrial fields. Despite the mass shift to optically enhanced profilometers, the stylus tip profilometers are still in use because of their self-reliance with the surface and compatibility with the data collected in the past [28].

The stylus tip profilometer uses a probe to stay in constant contact with the surface and takes the measurements in the x, y, and z directions. The motion of the stylus is monitored mechanically using a feedback loop that works on the bases of the reaction force that the probe feels from the surface. A feedback system is used to keep the probe arm with the required amount of torque on it to maintain proper contact. Since the probe is continually touching the surface, it might cause damage. The phenomenon of profile distortion occurs due to the stylus tip's shape and size. **Fig. 2.7** shows a simple schematic of the stylus tip surface profilometer.

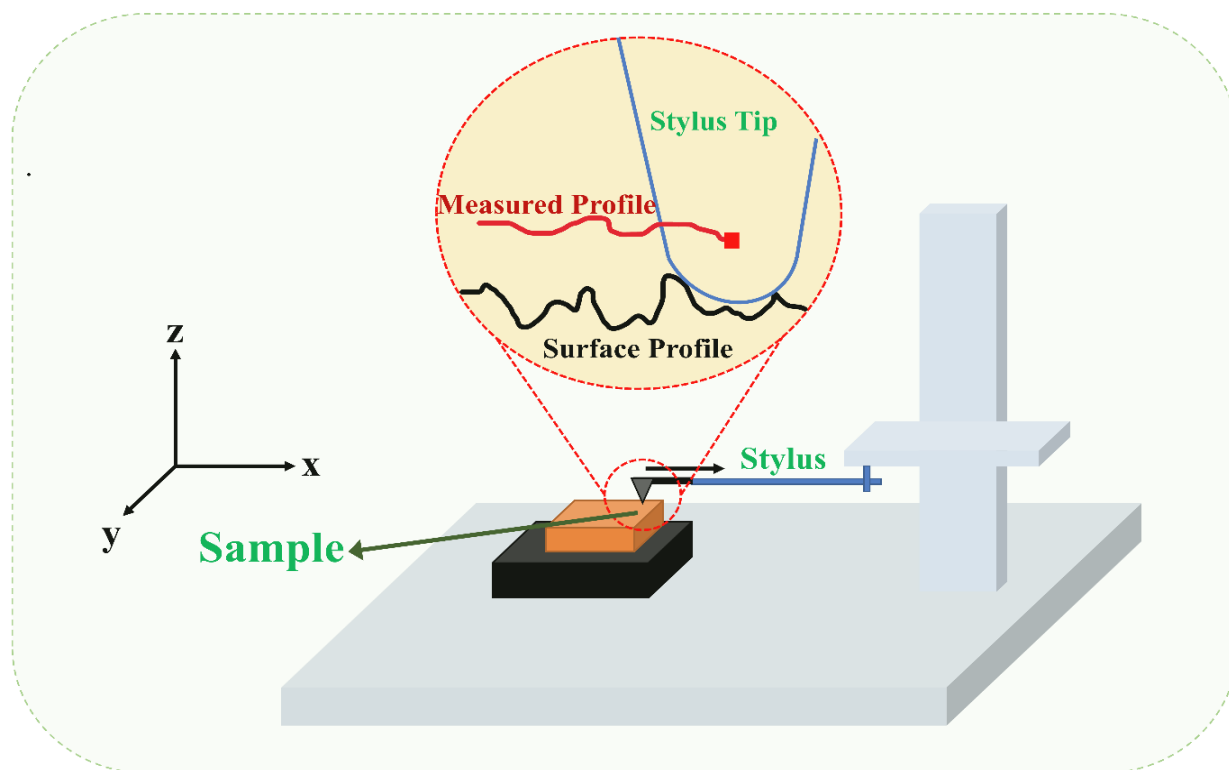


Fig. 2.7: Profile data acquisition by stylus type surface profilometer

2.3.8 Fourier transform infrared spectroscopy (FTIR) for the identification of functional groups

FTIR spectroscopy uses infrared radiation which covers a wide spectrum including a range from 400 cm^{-1} to 4000 cm^{-1} mainly used in research laboratories to identify different compounds present in a given sample. FTIR spectroscopy is a simple yet extremely important characterization technique having numerous applications. One of the uses of this technique includes the analysis of thin films and coatings for determining the functional groups. The FTIR spectroscopy method has several advantages which include its fast-scanning speeds as compared to other dispersive methods and the ability of the method to be used for solids, liquids as well as gases.

The method is dependent on the molecular bonds of the compounds present in the sample. The nature of the molecular bonds of different molecules is dependent on the atoms

present in the molecule. When these substances in a sample are illuminated with IR radiation, the molecules of the substance, upon its absorption, attain a higher energy state. When these molecules return to their original (de-excited) state, they emit radiation which has energy equal to the difference between the energies of the de-excited and the excited state of the molecules. Each substance absorbs a unique wavelength of IR light from the many available wavelengths present in the incident light [29]. The FTIR measures these absorbed wavelengths and hence can determine the nature of the substance and its bonds. The resulting graph can include “transmittance” or “absorption” of the IR radiation plotted on the y-axis against the wavenumber on the x-axis. There can be several peaks present in the graph depending upon the nature of the molecule. These peaks are then studied and analyzed against the known standard IR peaks for different materials and bonds to identify the functional groups present in the sample.

Michelson interferometer is commonly used for FTIR spectroscopy. The block diagram presented in **Fig. 2.8** can be referred, to understand the steps followed for the FTIR spectroscopy. The light from the IR radiation source in the interferometer setup reaches the beam splitter through a collimator; the beam splitter splits the incident beam into two. Both the beams then travel to the two mirrors of the interferometer, one of which is in constant motion. This introduces a path difference between the two beams and modulates every wavelength present in the incident beam at a distinct frequency. When the beams combine after being reflected from the mirrors, they form a complex interferogram. This interferogram so obtained is then made incident on the sample, which as described earlier, will absorb light of specific wavelengths out of the several available wavelengths in the light incident on it. The detector measures the intensity of the respective wavelengths in the transmitted light. The signal obtained is then processed and converted into meaningful data using the “Fourier transform”

method. The final graph obtained after using the Fourier transform method helps to identify different functional groups present in the sample of interest.

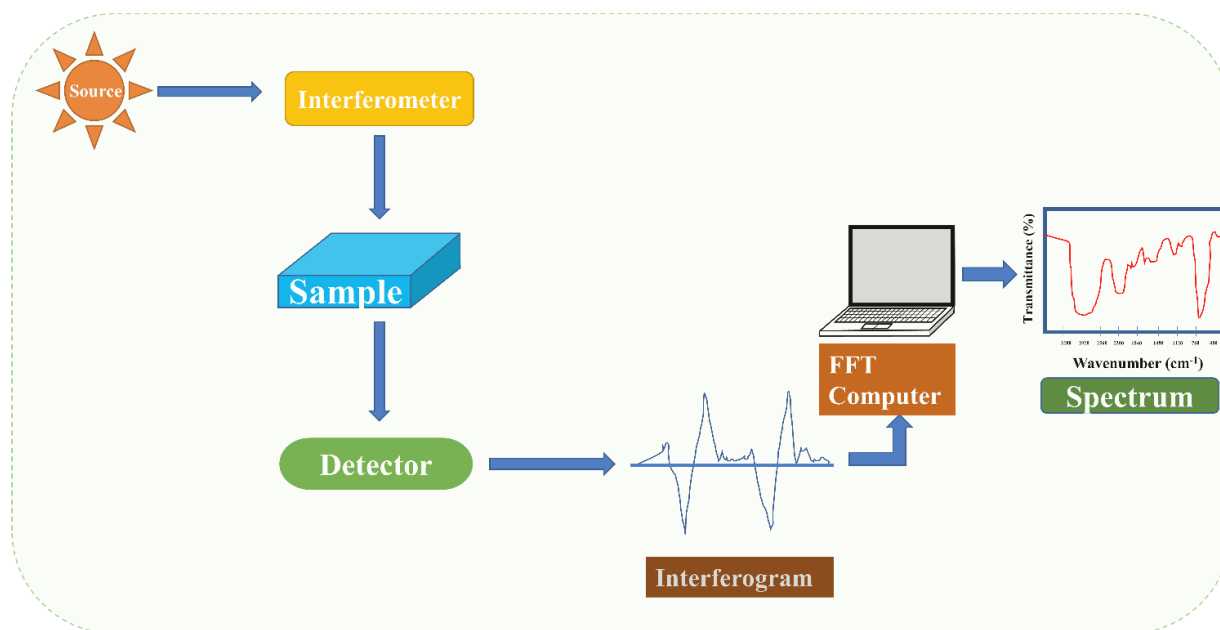


Fig. 2.8: Block diagram of FTIR spectroscopy

2.3.9 Raman spectroscopy

The specimen's rotational, vibrational, and other frequency modes are observed using the Raman spectroscopy method. It tells about the bonding and structure of the molecules. As a result, this method provides a fingerprint that can be used to identify molecules. This spectroscopy is based on the inelastic scattering of light (**Raman Effect**) [30]. Monochromatic radiation interacts with the sample differently as it incident on it and either gets scattered, reflected, or absorbed. Molecular structure information is obtained by scattered radiation. The coherent source is a general laser used for specimen analysis in Raman spectroscopy [31]. The majority of incoming radiation disperses elastically, producing Rayleigh scatter light. Only a tiny fraction, around 1 in 10^6 , is inelastically scattered and primarily consists of Stokes and anti-Stokes lines, and of this small fraction, Stoke's lines are used to collect the information about the specimen. In Rayleigh Raman scattering, incident and scattered light

frequency are the same. The frequency of the scattered light is higher than the frequency of the incident light in anti-Stokes Raman scattering, and the frequency of the scattered beam light in Stokes Raman scattering is lower than that of the incident beam light [32].

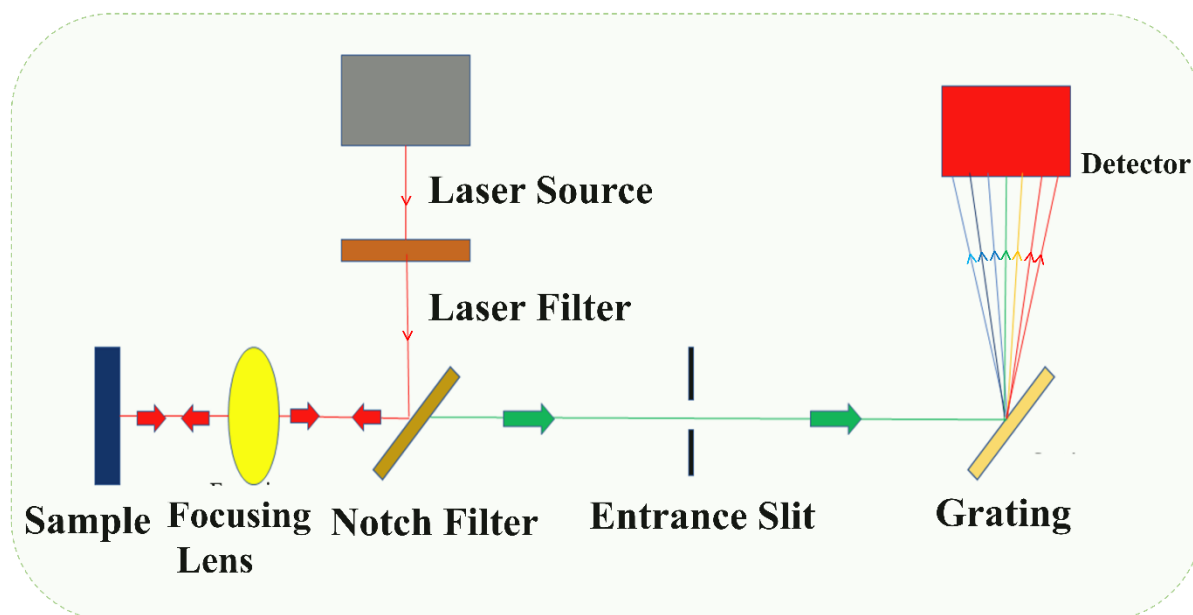


Fig. 2.9: Simplified block diagram of Raman spectrometer

Raman spectrum is plotted between the intensity of scattered light and energy difference termed as Raman shift. With the photon's interaction with the molecule, a dipole moment 'P' is induced by electric field 'E' given as

$$P = \alpha \cdot E \quad (2.3)$$

where α is the proportionality constant that tells us about the distortion of electron cloud around a molecule [33]. And these molecular bonds carrying specific energy transitions corresponding to changes in polarizability give rise to Raman active modes. Three main parts make up a modern Raman spectrometer: a laser source, a mechanism for illuminating the sample, and an appropriate spectrometer. Due to their monochromaticity and high-intensity beam, lasers are the most common sources utilized to study Raman spectra with good signal-to-noise (S/N) ratios. Raman spectrometers are either based on CCD or FTIR equipped with cooled germanium (Ge). Raman spectroscopy is frequently superior to IR spectroscopy because it may

be utilized to study inorganic systems in an aqueous solution. It has been widely applied to study biological systems. Analysis using Raman spectroscopy requires a small sample quantity, further liquid and film samples can also be analyzed. It can detect molecular impurities and additives. For quantitative and qualitative analysis in many settings, Raman spectroscopy has emerged as a non-corrosive technique. **Fig. 2.9** shows a simplified block diagram of the Raman spectrometer.

2.3.10 Atomic force microscopy (AFM) for topographical analysis

AFM was developed in 1986 by the great scientist G. Binnig, C Quate, C. F. Quate, and Herber at Stanford University by gluing a tiny shard of diamond onto one end of a tiny strip of gold foil. AFM can be used to study topography and surfaces (both even and uneven) of materials for several applications. The only basis for AFM's operation is the interaction force between the sample's surface and the tip (as shown in **Fig. 2.10**), which is composed of elastic cantilevers with a sharp end with a diameter of ~10 nm. The distance between the tip of the probe and the sample is controlled by forces perceived between them. There are two main kinds of forces acting between the tip and the sample surface i.e. attractive (non-contact) and repulsive (contact) forces. By observing the cantilever's bending and deflection, it is possible to determine the force acting between the tip and surface [34]. Therefore, three types of methods could be used for AFM.

- 1. Contact mode** - The contact mode is studied as quasi-static, and it acts in the Van der Waals curve's repulsive regime. In the contact method of measurement, the tip makes direct contact with the surface of the sample, and the deflected cantilever, which generates the elastic force, balances the force between the tip and sample. Researchers should use a cantilever with low rigidity in this mode.

2. **Non-contact mode** - The non-contact mode is known as an oscillatory mode. High sensitivity and stability of the feedback are necessary for non-contact mode. This is used as a semi-contact mode, to determine changes in the phase and amplitude of cantilever oscillations as the tip interacts through attractive Van der Waals forces with the specimen without touching it.

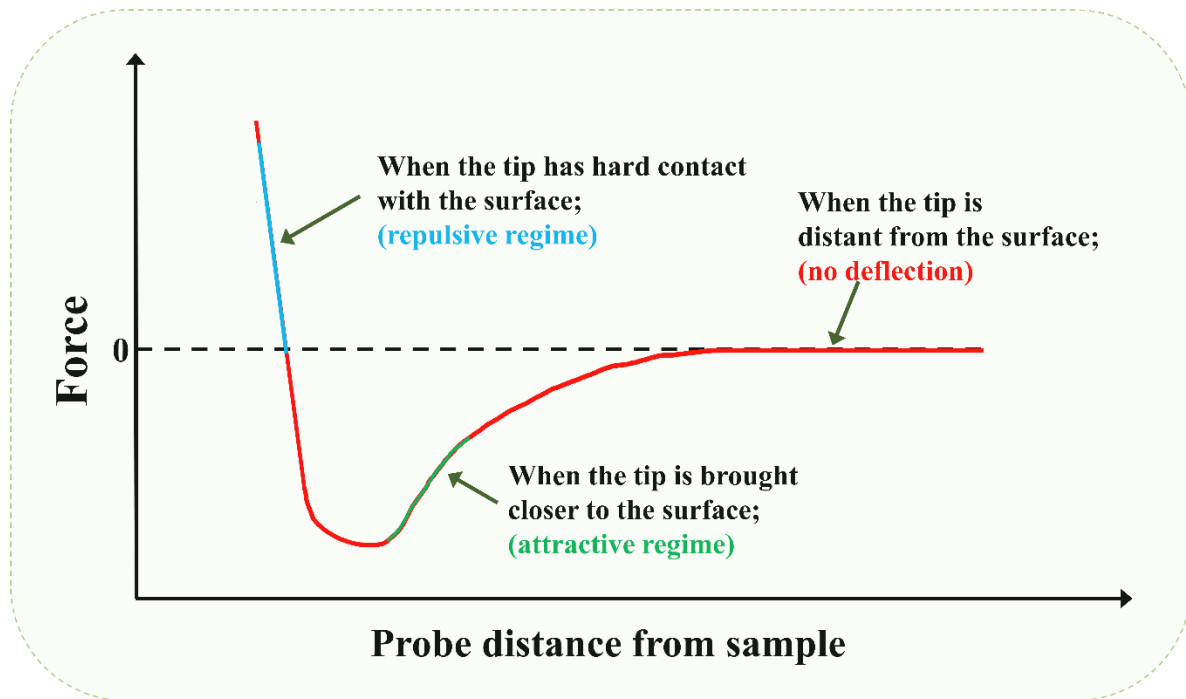


Fig. 2.10: Typical AFM force vs distance curve

3. **Tapping mode** - For this mode, we often use a cantilever with a high resonant frequency. As a result of the interaction of elastic and Van der Waals forces between the tip and the specimen high amplitude deflections are produced during scanning. Practically this mode is the same as the non-contact mode, but high amplitude deflection provides better control over the feedback loop for topography analysis.

In AFM, a technique known as beam bounce is frequently employed to detect the slight cantilever deflection. The exponential function - Lennard-Jones potential can be used to approximate the van der Waals potential energy of two atoms that are separated by distance 'r' [35]. The schematic diagram of the basic working principle of AFM is shown in **Fig. 2.11**.

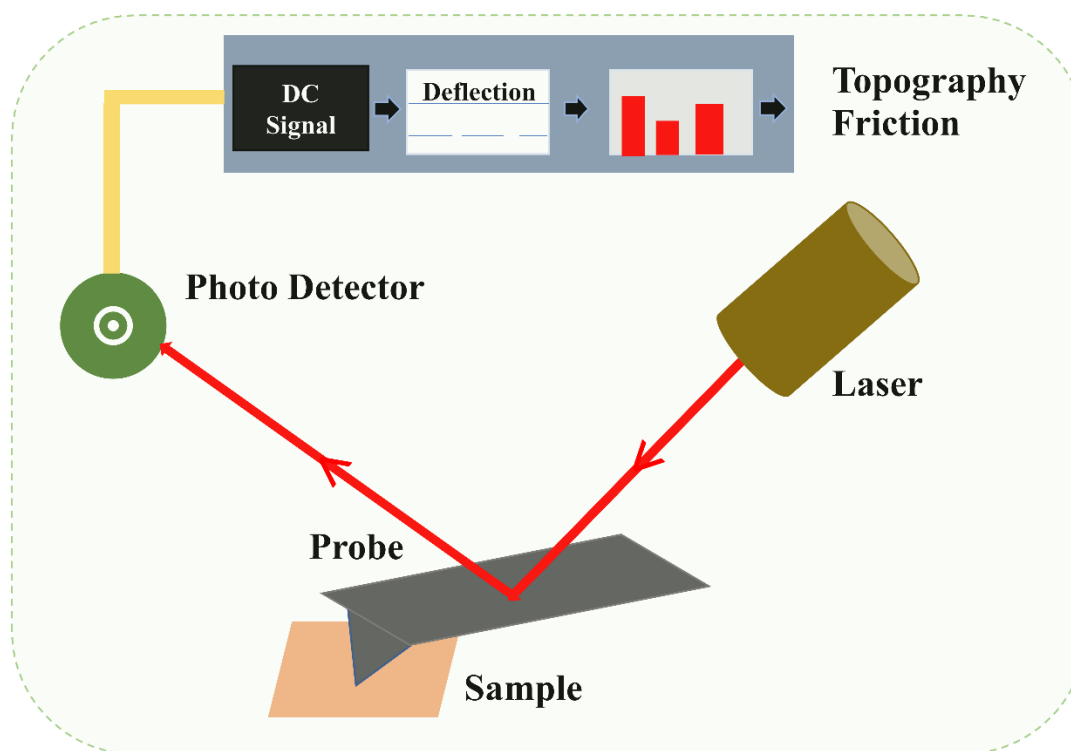


Fig. 2.11: Schematic diagram of basic working principle of AFM

2.3.11 Thermogravimetric Analysis (TGA) for thermal studies

Heat causes many chemical and physical changes in the material. Phase transitions, such as crystallization, vaporization, melting, switching between crystal forms, and modifications in mechanical behavior are examples of physical changes. Whereas chemical changes include oxidation, corrosion, breakdown, and dehydration. These changes occur in a wide range of temperatures. Thus thermal analysis of materials and the study of their behavior throughout a range of temperatures is very crucial. Once the temperature range is defined it is easy for a researcher to use the material for a specific application and predict safe operating conditions for products. This information can be obtained from TGA. **Fig. 2.12** shows the block diagram of TGA.

TGA involves heating a sample at a controlled rate in a given environment [nitrogen (N_2), carbon dioxide (CO_2), helium (He), argon (Ar), air, etc.]. A substance's weight fluctuates

in response to temperature or time. The temperature at which the sample begins to lose weight indicates that decomposition begins at this temperature.

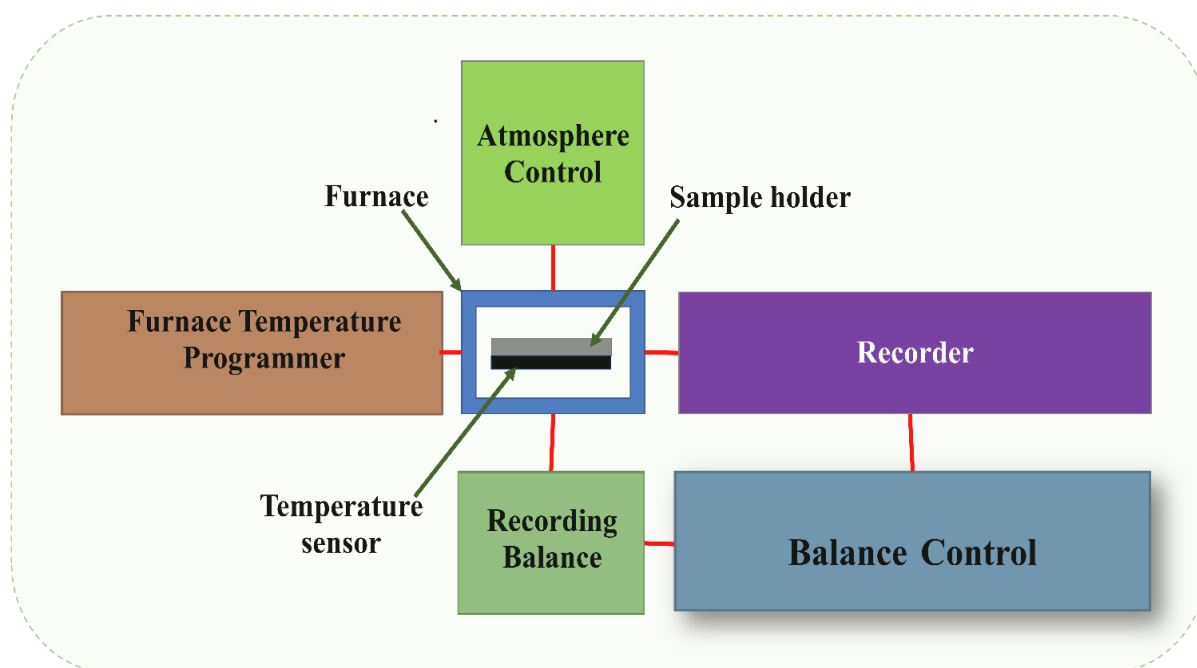


Fig. 2.12: Block diagram of TGA

The sample holder encircled by the furnace is a sensitive microbalance for continuously measuring sample weight. A purge gas system is provided for a reactive or inert atmosphere. In most cases, data (weight vs. sample temperature) is gathered and processed by the computer, which controls the furnace. It is advised to choose a sample weight of 10 – 20 mg because doing so removes the possibility of a temperature gradient in the sample. Particles should be uniform and small in size. Using wide-ranging particles or crystals may result in visible, quick weight loss during heating. The furnace heating rate and its atmosphere are two instrumental factors that influence the thermogravimetric (TG) curve. The speed used to capture either a rapid or slow reaction's TG curve significantly impacts the curve's form. It is recommended to carry out the scan at a slow rate, for a slow decomposition reaction and to prevent the flattening of the curve and obscure the acute decomposition temperature. Typically, a heating rate of 3.5

°C per minute is advised for accurate and repeatable TGA. Thus, complex mixture composition and decomposition can be obtained from TGA [20, 36].

2.4 Electrochemical Techniques

Electrochemistry is the interplay between chemistry and electricity, that is as a result of some chemical reactions, a change in parameters like capacitance, voltage, charge, current, resistance, etc takes place. The serenity of electrochemistry lies in the fact that the energy of electrons in the electrode can be modulated by an external power source like a potentiostat. For the electrochemical measurements, a three-electrode setup comprising a RE, counter electrode (CE), and a WE is used. To maintain a constant potential, the potential of WE is measured against the RE, while the current flow is seen through the CE. In our work, we have used three extremely sensitive and substantially popular techniques namely Electrochemical Impedance Spectroscopy (EIS), cyclic voltammetry (CV), and differential pulse voltammetry (DPV), for studying the electrochemical properties of MoS₂ and modified nanostructures.

2.4.1 Electrochemical impedance spectroscopy (EIS)

EIS is a potent technique that has gained momentum in the last few years since it is a non-corrosive technique that can be used to examine the interfacial kinetics prevailing between the electrode and the electrolyte. Further, EIS enables the separation of various components like double-layer capacitance, electron transfer resistance (R_{ct}), etc. In EIS, a small amplitude sinusoidal potential is applied, which is a function of frequency. The applied perturbation (potential) leads to a sinusoidal current and the ratio of applied potential to resultant current gives the impedance (Z), which comprises a real and imaginary part. Z is an imaginary quantity comprised of real (Z_r , ohmic resistance) and imaginary parts (Z_i , capacitive resistance) [37].

For our analysis, we draw the Nyquist plot (as shown in **Fig. 2.13**). The plot shows a semicircular region at higher frequencies which are obtained as a result of the electron transfer limited process. At lower frequencies, a straight line at an angle of 45° to the x-axis is observed which is ascribed to the diffusion-controlled process of electron transfer [38]. Since the impedance measurement is done by varying a vast spectrum of frequencies, as a consequence, this technique is termed electrochemical impedance spectroscopy.

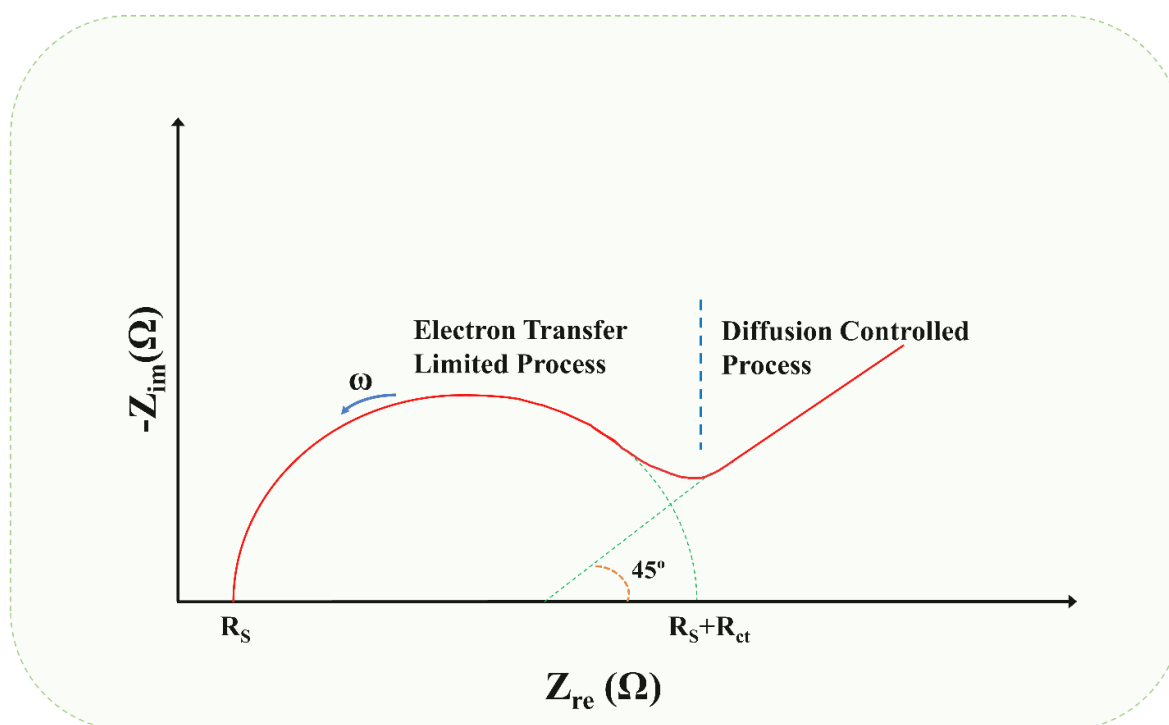


Fig. 2.13: Nyquist plot obtained by EIS technique

The resultant impedance is dependent on both applied potential as well as frequency (ω). For EIS measurements a small amplitude potential (generally 10 mV) is applied which proffers several advantages like

- (i) Impedance can be strictly defined only in the case when the current and voltage have a linear relationship.

(ii) In the cases where the biological element is not covalently bonded with the immobilization matrix, there the applied voltage may disturb the attachment by charging the biological element

(iii) Also, the energy of binding between the target analyte and immobilized biological element may be smaller than the applied potential, which may hamper the interaction between the two

Therefore, EIS is advantageous over amperometry or voltammetry where high amplitude potentials are applied which may damage the probe layer [39].

2.4.2 Cyclic Voltammetry (CV)

CV is the most popularly used technique used to acquire information governing the electrochemical processes undergoing at the interface of electrode and electrolyte. **Fig. 2.14** shows a typical CV curve in which the x-axis shows the potential applied as a function of time, while the y-axis shows the resultant current. Since the applied potential is ramped with time, a crucial parameter defined as scan rate (given in mV s^{-1}) is often mentioned in CV, which indicates the speed at which potential changes with time [40]. At higher scan rates, a high peak value of current is observed because the size of the diffusion layer decreases when applied potential changes faster. When the potential is applied to the WE the current increases until the oxidation potential of the analyte is reached (denoted by E_{pa}), and the corresponding current is called peak anodic current (denoted by i_{pa}). After this, a diffusion layer is formed and the region near the WE is devoid of ions that can be oxidized any further. Therefore the current starts decreasing and potential is applied in the opposite polarity. With the reverse polarity, the current starts increasing in the opposite direction until the reduction potential (denoted by E_{pc}) of the analyte is reached. The corresponding current is called peak anodic current. If the

oxidation and reduction peaks are near replicas of each other, then the process is termed electrochemically reversible [41, 42].

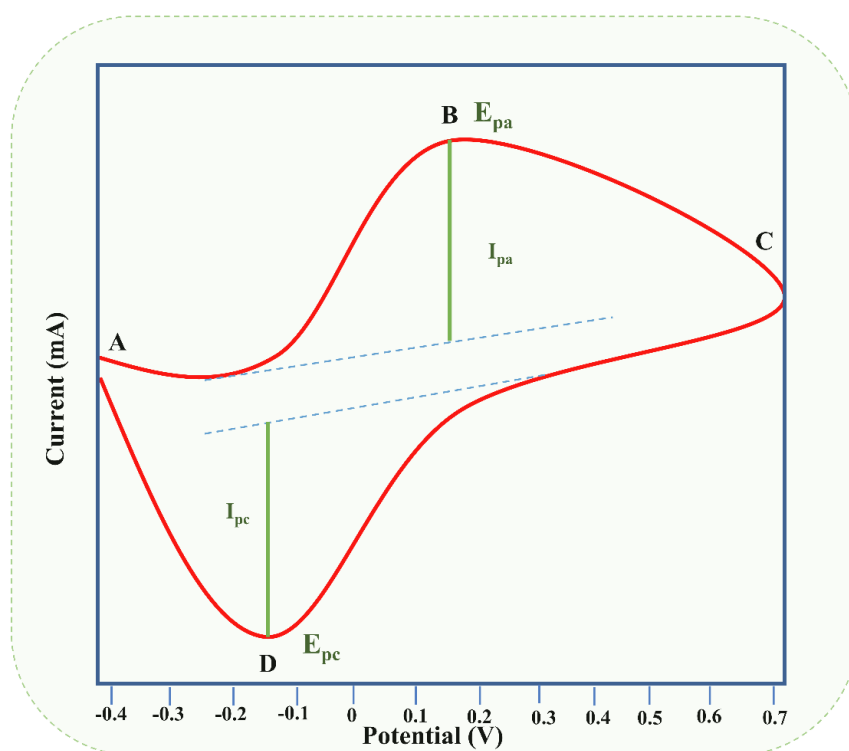


Fig. 2.14: A typical cyclic voltammogram curve.

In our case, we have used CV to determine various electrochemical parameters like electroactive surface area (A_e), heterogeneous rate transfer constant (HET), etc by scan rate dependent study. Also, the optimization studies for the fabrication of biosensors and modification of electrodes at various steps of fabrication are done using CV.

2.4.3 Differential Pulse Voltammetry (DPV)

Like in CV, in DPV also, a potential is applied across the electrode and the resultant current flowing between the WE and CE is measured. However, here in DPV, a staircase voltage is applied to have a series of pulses having a fixed magnitude such that the baseline voltage is continuously increasing. In a single pulse, the current is sampled twice, once at the beginning of the pulse (point 1 in **Fig. 2.15 (a)**) and then at the end of the pulse (point 2 in **Fig. 2.15 (a)**).

The difference between the two sampled currents is measured instrumentally and plotted against applied voltage which results in a voltammogram. This results in a gaussian curve as shown in **Fig. 2.15 (b)** and the peak current value is directly proportional to the concentration of the target analyte in the case of biosensors.

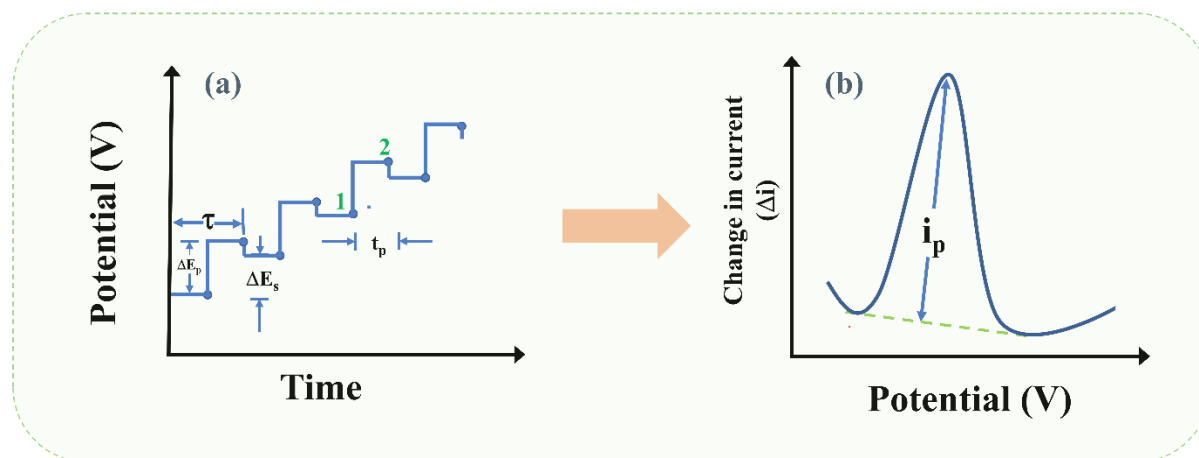


Fig. 2.15 (a): Input signal in DPV **(b)** Output voltammogram in DPV

DPV is advantageous over other voltammetry techniques because it is more sensitive since the background charging current is minimized due to the differential measurement. Since the sensitivity and resolution are improved due to its differential nature, therefore DPV is vastly employed for the analysis of mixtures.

References

- [1] Zhang, Hua, Hui-Ming Cheng, and Peide Ye. "2D nanomaterials: beyond graphene and transition metal dichalcogenides." *Chemical Society Reviews* 47, no. 16 (2018): 6009-6012.
- [2] Li, Jianlin, Qingliu Wu, and Ji Wu. "Synthesis of nanoparticles via solvothermal and hydrothermal methods." In *Handbook of nanoparticles*, pp. 295-328. Springer, Cham, 2016.
- [3] Hummers Jr, William S., and Richard E. Offeman. "Preparation of graphitic oxide." *Journal of the american chemical society* 80, no. 6 (1958): 1339-1339.
- [4] Marzouki, Riadh, Mahmoud A. Sayed, Mohsen Graia, and Mohamed Faouzi Zid. "Cobalt phosphates and applications." In *Cobalt Compounds and Applications*. IntechOpen, 2019.
- [5] Arora, Kamal, and Nitin K. Puri. "Electrophoretically deposited nanostructured PdO thin film for room temperature amperometric H_2 sensing." *Vacuum* 154 (2018): 302-308.
- [6] Khatri, Ritika, and Nitin K. Puri. "Electrochemical biosensor utilizing dual-mode output for detection of lung cancer biomarker based on reduced graphene oxide-modified reduced-

molybdenum disulfide multi-layered nanosheets." *Journal of Materials Research* 37, no. 8 (2022): 1451-1463.

[7] Warren, Bertram Eugene. *X-ray Diffraction*. Courier Corporation, 1990.

[8] Whittig, L. D., and W. R. Allardice. "X-ray diffraction techniques." *Methods of Soil Analysis: Part 1 Physical and Mineralogical Methods* 5 (1986): 331-362.

[9] Cullity, Bernard Dennis. *Elements of X-ray Diffraction*. Addison-Wesley Publishing, 1956.

[10] Hanawalt, J. D., H. W. Rinn, and L. K. Frevel. "Chemical analysis by X-ray diffraction." *Industrial & Engineering Chemistry Analytical Edition* 10, no. 9 (1938): 457-512.

[11] Warren, B. E. "X-ray diffraction methods." *Journal of applied physics* 12, no. 5 (1941): 375-384.

[12] Mohammed, Azad, and Avin Abdullah. "Scanning electron microscopy (SEM): A review." In *Proceedings of the 2018 International Conference on Hydraulics and Pneumatics—HERVEX, Băile Govora, Romania*, pp. 7-9. 2018.

[13] Zhou, Weilie, Robert Apkarian, Zhong Lin Wang, and David Joy. "Fundamentals of scanning electron microscopy (SEM)." In *Scanning microscopy for nanotechnology*, pp. 1-40. Springer, New York, NY, 2006.

[14] Inkson, Beverley J. "Scanning electron microscopy (SEM) and transmission electron microscopy (TEM) for materials characterization." In *Materials characterization using nondestructive evaluation (NDE) methods*, pp. 17-43. Woodhead Publishing, 2016.

[15] Sutton, Michael A., N. Li, D. C. Joy, Anthony P. Reynolds, and Xiaodong Li. "Scanning electron microscopy for quantitative small and large deformation measurements part I: SEM imaging at magnifications from 200 to 10,000." *Experimental mechanics* 47, no. 6 (2007): 775-787.

[16] Ul-Hamid, Anwar. *A beginners' guide to scanning electron microscopy*. Vol. 1. Cham, Switzerland: Springer International Publishing, 2018.

[17] Schwartz, Lyle H., and Jerome B. Cohen. "The nature of diffraction." In *Diffraction from Materials*, pp. 46-76. Springer, Berlin, Heidelberg, 1987.

[18] Lin, Feng. "Preparation and characterization of polymer TiO₂ nanocomposites via in-situ polymerization." Master's thesis, University of Waterloo, 2006.

[19] Bendersky, Leonid A., and Frank W. Gayle. "Electron diffraction using transmission electron microscopy." *Journal of research of the National Institute of Standards and Technology* 106, no. 6 (2001): 997.

[20] Willard, Hobart Hurd, Lynne L. Merritt Jr, John Aurie Dean, and Frank A. Settle Jr. "Instrumental methods of analysis." (1988).

[21] Jenkins, Ron. "X-ray techniques: overview." *Encyclopedia of analytical chemistry* (2000): 1-20.

[22] Friedbacher, Gernot, and Henning Bubert, eds. *Surface and thin film analysis: a compendium of principles, instrumentation, and applications*. John Wiley & Sons, 2011.

[23] Newbury, Dale E., and Nicholas WM Ritchie. "Performing elemental microanalysis with high accuracy and high precision by scanning electron microscopy/silicon drift detector energy-dispersive X-ray spectrometry (SEM/SDD-EDS)." *Journal of materials science* 50, no. 2 (2015): 493-518.

[24] Yao, Min, Dongyue Wang, and Min Zhao. "Element analysis based on energy-dispersive X-ray fluorescence." *Advances in Materials Science and Engineering 2015* (2015) (290593).

[25] Bligh, E. Graham, and W. Justin Dyer. "A rapid method of total lipid extraction and purification." *Canadian journal of biochemistry and physiology* 37, no. 8 (1959): 911-917.

[26] Fadeeva, V. P., V. D. Tikhova, and O. N. Nikulicheva. "Elemental analysis of organic compounds with the use of automated CHNS analyzers." *Journal of analytical chemistry* 63, no. 11 (2008): 1094-1106.

- [27] Mohd Salleh, M. A., H. K. Nsamba, H. M. Yusuf, A. Idris, and WA Wan Ab Karim Ghani. "Effect of equivalence ratio and particle size on EFB char gasification." *Energy Sources, Part A: Recovery, Utilization, and Environmental Effects* 37, no. 15 (2015): 1647-1662.
- [28] Lee, Dong-Hyeok. "3-Dimensional profile distortion measured by stylus type surface profilometer." *Measurement* 46, no. 1 (2013): 803-814.
- [29] Titus, Deena, E. James Jebaseelan Samuel, and Selvaraj Mohana Roopan. "Nanoparticle characterization techniques." In *Green synthesis, characterization and applications of nanoparticles*, pp. 303-319. Elsevier, 2019.
- [30] Pelletier, Michael J. "Quantitative analysis using Raman spectrometry." *Applied spectroscopy* 57, no. 1 (2003): 20A-42A.
- [31] Lewis, Ian R., and Howell Edwards. *Handbook of Raman spectroscopy: from the research laboratory to the process line*. CRC press, 2001.
- [32] Graves, P. R. G. D. J., and D. Gardiner. "Practical raman spectroscopy." *Springer* 10 (1989): 978-3.
- [33] Ferraro, John R. *Introductory raman spectroscopy*. Elsevier, 2003.
- [34] Giessibl, Franz J. "Advances in atomic force microscopy." *Reviews of modern physics* 75, no. 3 (2003): 949.
- [35] Anwar, Bhuiyan Muhammad Mukdashif. *Characterization of Heat-Treated and Laser-Treated Nano-Crystalline Soft Magnetic Alloys*. The University of Toledo, 2019.
- [36] Rotich, M. K., B. D. Glass, and M. E. Brown. "Thermal studies on some substituted aminobenzoic acids." *Journal of thermal analysis and calorimetry* 64, no. 2 (2001): 681-688.
- [37] Bahadır, Elif Burcu, and Mustafa Kemal Sezgintürk. "A review on impedimetric biosensors." *Artificial cells, nanomedicine, and biotechnology* 44, no. 1 (2016): 248-262.
- [38] Sri, Smriti, Deepika Chauhan, G. B. V. S. Lakshmi, Alok Thakar, and Pratima R. Solanki. "MoS₂ nanoflower based electrochemical biosensor for TNF alpha detection in cancer patients." *Electrochimica Acta* 405 (2022): 139736.
- [39] Daniels, Jonathan S., and Nader Pourmand. "Label-free impedance biosensors: Opportunities and challenges." *Electroanalysis: An International Journal Devoted to Fundamental and Practical Aspects of Electroanalysis* 19, no. 12 (2007): 1239-1257.
- [40] Elgrishi, Noémie, Kelley J. Rountree, Brian D. McCarthy, Eric S. Rountree, Thomas T. Eisenhart, and Jillian L. Dempsey. "A practical beginner's guide to cyclic voltammetry." *Journal of chemical education* 95, no. 2 (2018): 197-206.
- [41] Kissinger, Peter T., and William R. Heineman. "Cyclic voltammetry." *Journal of chemical education* 60, no. 9 (1983): 702.
- [42] Heinze, Jürgen. "Cyclic voltammetry—“electrochemical spectroscopy”. *New analytical methods* (25)." *Angewandte Chemie International Edition in English* 23, no. 11 (1984): 831-847.

Chapter 3

Electrochemical Study of Hydrothermally Synthesised MoS₂ Layered Nanosheets

This work is centered around a one-step, facile and cost-effective synthesis of 2-dimensional (2D) MoS₂ nanostructures via hydrothermal method using two reducing agents and their electrochemical study. The detection of the hexagonal phase is done using X-ray diffraction (XRD). Scanning electron microscopy (SEM) and Transmission electron microscopy (TEM) confirm the formation of nanosheet-like structures. MoS₂ reduced using hydrazine hydrate (HH) is found to have better electrochemical properties with heterogenous rate transfer constant equal to $0.69 \times 10^{-3} \text{ cm s}^{-1}$ and electroactive surface area calculated as 51.38 mm^2 . Raman spectra and TEM images explain the better electrochemical performance of MoS₂ synthesized using HH. Also, it is observed that out of electrochemical impedance spectroscopy (EIS), cyclic voltammetry (CV), and differential pulse voltammetry (DPV), EIS turns out to be the best technique for studying the electrochemical properties of layered materials. The promising electrochemical performance of MoS₂ synthesized using HH enabled us to further modify it for its suitability for biosensing applications.

This work is published as: **Ritika Khatri and Nitin K. Puri.** *"Electrochemical study of hydrothermally synthesised reduced MoS₂ layered nanosheets."* **Vacuum (Elsevier) 175 (2020): 109250.**

3.1 Introduction

2D materials like graphene, transition metal chalcogenides, hexagonal boron nitride, Mxenes, etc are gaining huge popularity in the inter-disciplinary fields of nanoscience and materials science which include physics, chemistry as well as biology. 2D nanomaterials include benefits like low cost and high chemical stability. Amongst, these 2D nanomaterials MoS₂ has gained wide popularity pertaining to its layered structure, abundance in nature as molybdenite, good rate of electron transfer, dependency of band gap on no. of layers, the possibility of extraction in the considerable amount [1], and its plentiful applications like supercapacitors [2], Na/Li-ion batteries [3-5], Hydrogen Evolution Reaction (HER) [6], sensing [7], electronic devices [8, 9], etc. It also possesses fine mechanical strength, even better than steel [10]. MoS₂ in its bulk form is a semiconductor with a bandgap of 1.2 eV, which widens up to 1.8 eV for monolayer MoS₂. Bulk MoS₂ however has a low transfer of ions/electrons because it is a stacking of a large number of layers, which limits its conductivity [11]. Thus, an effective pathway to this is going to the nanoscale, thus increasing the surface area and decreasing the total number of layers to decrease the pathway for the diffusion of electrons. MoS₂ has characteristics similar to graphene-like covalently bonded S-Mo-S sheets which have weak Vander Waal forces amongst them and therefore have the tendency to be extracted in form of nanosheets like structures [12]. MoS₂ can be synthesised using various methods, among which hydrothermal method is one of the methods which gives large yield, is simple to perform, has low cost and gives an option of controlling the morphology of synthesized structures. Also, water is used as a reaction solvent making this method environmentally friendly as well [13, 14].

The electrochemical activity of MoS₂ determines its use in various applications, but different properties of MoS₂ and different types of parameters are seen for different applications. For instance, more no. of active sites will give a better HER and a low overpotential and Tafel plot will determine if a material is good for HER or not [15], while

pseudocapacitive behavior, charge-discharge rates, cycle stability will be seen for supercapacitor [2]. Charge-discharge capacity, cycling stability, and specific capacity are seen for Na/Li-ion batteries and the potential for Na/Li ions intercalation among layers of MoS₂ will determine the performance of batteries [3-5]. But for sensing, more surface area should be exposed with minimized interlayer spacing so that electron transfer is favored with a high value of heterogeneous electron transfer (HET) rate constant [16].

MoS₂ nanostructures are heterogenous on their surface containing mono-/bi-/multi-layered structures of different shapes and sizes. These shapes and sizes depend on different preparation methods and conditions. For instance, flower-like MoS₂ nanostructures are shown to exhibit a better performance as an anode material for Li-ion batteries in comparison to the sphere MoS₂ nanostructures because flower-like MoS₂ nanostructures can have better structure change during the conversion process while the dense structures of spheres impede charge transfer. Ultrathin nanosheets in flower-like MoS₂ shorten the diffusion pathway for electrons and Li⁺ ions, which enhances its electrochemical performance [17]. In another work, Ramadoss et al [18] synthesized mesoporous structures of MoS₂ for supercapacitor applications where capacity is found to increase due to porous morphology and large surface area of nanostructures which reduces the pathway for ion diffusion which in turn enables fast electron transfer between the working electrode and electrolyte. Chen et al [19] synthesized MoS₂ nanosheets and nanosheets based on hollow porous flat boxes and nanotubes for electrochemical hydrogen evolution. MoS₂ flat boxes and nanotubes are found to exhibit better electrochemical performance than MoS₂ nanosheets because of a greater number of S²⁻ units, and stable arrangement of nanosheets which exposes a greater number of active sites rendering them low overpotentials to reach 10 mA cm⁻². Kumar et al [20] reported the synthesis of MoS₂ nanoclusters for electrochemical detection of 4 aminophenol (AP). The large surface area of MoS₂ nanoclusters exhibits high electrocatalytic activity towards 4-AP. MoS₂ nanoflakes (size

$\geq 1 \mu\text{m}$) for the fabrication of screen-printed electrochemical sensor for the detection of bovine serum has been developed by Kukkar et al [21]. A simple sensor with a detection limit of 6 pg mL^{-1} is made by utilizing the cyclic voltammetry (CV) technique. Wang et al [22] synthesized three different morphologies of MoS_2 namely nanospheres, nanoribbons, and nanoparticles, and studied their electrochemical performance for Li-ion Batteries. MoS_2 nanospheres are found to exhibit the best electrochemical performance amongst all morphologies owing to the large surface area which provides a large number of reaction sites, reduced diffusion length for electrons and ions, and can accommodate structural changes. This gives a clear indication that the morphology of synthesized MoS_2 nanostructures has a direct role to play in the electrochemical performance for any application.

Therefore, for proceeding in our work, we synthesized MoS_2 using hydrazine hydrate (HH) and citric acid (CA) as reducing agents to mediate the growth of MoS_2 nanostructure by aiding the reduction of the oxidation state of Mo (VI) to Mo (IV). Due to excess ammonia released during the hydrothermal synthesis of MoS_2 , NH_3 intercalated MoS_2 nanosheets are formed leading to an increase in inter-layer spacing constituting the nanosheets [23, 24]. Without the use of reducing agents, samples obtained are not having a pure crystalline phase of MoS_2 . It has also been reported that intercalated MoS_2 is not in the pure crystalline phase [13, 24] which renders it low stability. Also, intercalated MoS_2 nanosheets increase the overall distance between layers which will decrease the sensing response. We have also shown in our study that the MoS_2 sample synthesized using CA as a reducing agent shows low electrochemical performance because of an increase in the stacking height of layers. Therefore, the reduction of ammonia intercalated MoS_2 becomes very important such that the original nanosheet-like structure is also retained. Min Li et al [13] and Mohsin Ali Raza Anjum et al [24] have given an additional treatment in H_2 reducing atmosphere to hydrothermally synthesized intercalated MoS_2 nanostructures, whereas we have reduced ammonia intercalated

MoS₂ nanostructures chemically during the hydrothermal process only. However, HH and CA lead to the growth of these nanosheets in different ways which directly affects the electrochemical properties of these nanostructures and their performance for various applications.

3.2 Experimental Details

3.2.1 Materials and Solutions

Ammonium Molybdate Tetrahydrate [(NH₄)₆Mo₇O₂₄·4H₂O, AMT] with 99.98% purity is purchased from Sigma Aldrich. Thiourea is purchased from SRL Pvt Ltd. HH, potassium bromide, sodium chloride, and potassium chloride are purchased from Thermo Fisher Scientific. Concentrated hydrochloric acid is purchased from RFCL limited. All other chemicals including acetonitrile, potassium hexacyanoferrate (III)/potassium ferricyanide [K₃Fe(CN)₆], potassium hexacyanoferrate(II) trihydrate/ potassium ferrocyanide [K₄Fe(CN)₆·3H₂O], sodium dihydrogen phosphate dihydrate (NaH₂PO₄·2H₂O, M.W. – 156.01 g mol⁻¹), di sodium hydrogen diphosphate dihydrate (Na₂HPO₄·2H₂O) and ethanol are purchased from Merck. All solutions in the experiments are prepared with ultrapure water (Milli-Q water) from a Millipore Milli-Q system (Bedford, MA, USA). All the materials are of analytical grade and are used directly without further purification.

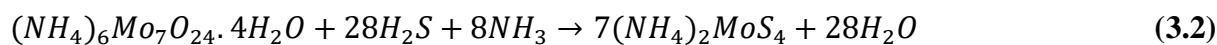
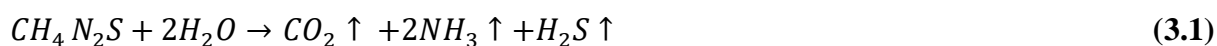
3.2.2 Preparation of MoS₂ Nanostructures

3.2.2.1 Preparation of MoS₂ without using reducing agents

0.08 M of AMT and 1.13 M of thiourea are dissolved in de-ionized (DI) water under continuous stirring for 30 minutes. The resulting solution is then put in a 50 mL Teflon-lined stainless-steel autoclave at a temperature of 230 °C for 24 hours. Then it is allowed to cool down to room temperature. The finally obtained product is collected by centrifugation and washed several

times using water and ethanol. The precipitates are then vacuum dried at 140 °C for 8 hours.

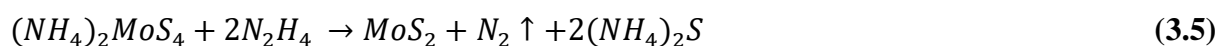
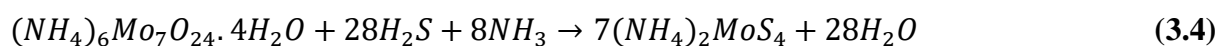
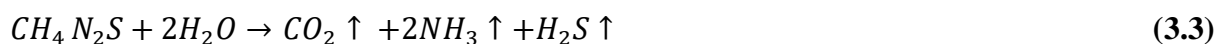
The reactions which occur during the above procedure are written as follows:



This Sample is labeled as-prepared MoS₂ sample.

3.2.2.2 Preparation using HH as a reducing agent (MoS₂HH)

0.08 M of AMT and 1.13 M of thiourea are dissolved in dI water under continuous stirring for 30 minutes. 2 mL HH is added to the above-prepared solution while stirring only. An acidic pH of 5 is maintained using dilute HCL. The resulting solution is then put in a 50 mL Teflon-lined stainless-steel autoclave at a temperature of 230 °C for 24 hours. Then it is allowed to cool down to room temperature. The finally obtained product is collected by centrifugation and washed several times using water and ethanol. The precipitates are then vacuum dried at 140 °C for 8 hours. The reactions which occur during the above procedure are written as follows:

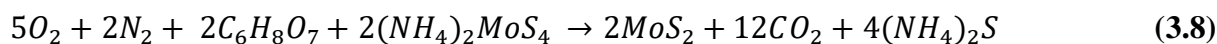
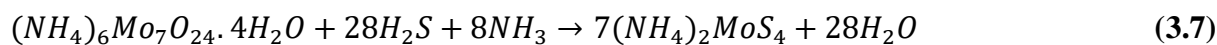
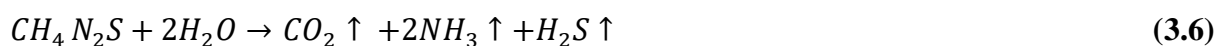


The sample is labeled as MoS₂HH.

3.2.2.3 Preparation using CA as a reducing agent (MoS₂CA)

0.08 M of AMT and 1.13 M of thiourea are dissolved in DI water under continuous stirring for 30 minutes. 0.44 M of CA is added to the above solution while stirring only. The resulting solution is then put in a 50 mL Teflon-lined stainless-steel autoclave at a temperature of 230 °C for 24 hours. Then it is allowed to cool down to room temperature. The finally obtained product is collected by centrifugation and washed several times using water and ethanol. The

precipitates are then vacuum dried at 140 °C for 8 hours. The reactions which occur during the above procedure are written as follows:



This sample is labeled as MoS₂CA.

Equation (3.1), (3.3), and (3.6) shows the sulfurated reaction, **equation (3.2), (3.4), and (3.7)** shows the formation of an intermediate product (NH₄)₂MoS₄ while **equation (3.5) and (3.8)** shows the final reduction step of (NH₄)₂MoS₄ which leads to the formation of MoS₂. Both these steps that are sulfurization and reduction are important for the formation of single-phase MoS₂ nanostructures without any presence of MoO₂ or MoO₃ intermediate phases [25] and to remove intercalated NH₃ ions between MoS₂ layers due to the production of excess ammonia in **equations (3.5) and (3.8)**, respectively [24]. The final reduction step does not take place in the case of the as-prepared sample as no reducing agent is present to reduce (NH₄)₂MoS₄ due to which pure MoS₂ phase cannot be obtained as shown XRD pattern in **Fig. 3.2**. G Nagaraju et al [25] have reported the formation of MoS₂ nano bundles using CA as a reducing agent using a different sulfur source. However, temperature and time play a huge role in controlling the morphology in the hydrothermal synthesis of MoS₂ nanostructures.

3.2.3 Preparation of MoS₂-based electrode for electrochemical Studies

MoS₂ is known to have an excess of surface negative charge [26, 27], therefore stable films of it can be made by applying an electric field to its stable colloidal suspension in between two electrodes. The electrophoretic method of film deposition offers many advantages like

smoothness, homogeneity, uniformity, and economic viability, therefore has been chosen for film formation [28, 29].

MoS₂HH and MoS₂CA are separately dispersed in DI water, acetone, ethanol, and acetonitrile with a concentration of 1 mg mL⁻¹ and sonicated in an ultrasonic bath for 30 minutes at room temperature. The dispersion of solutions for both the samples is shown in **Fig. 3.1**. It is observed that in DI water and ethanol, particles of samples are not uniformly and homogeneously spread throughout the solution but rather get settled at the bottom. Films using electrophoretic deposition (EPD) are made using dispersions in acetone and acetonitrile. However, films for samples dispersed in acetone could not be uniformly formed, whereas films could be easily formed for samples dispersed in acetonitrile, hence conditions are optimized for dispersion of samples in acetonitrile.

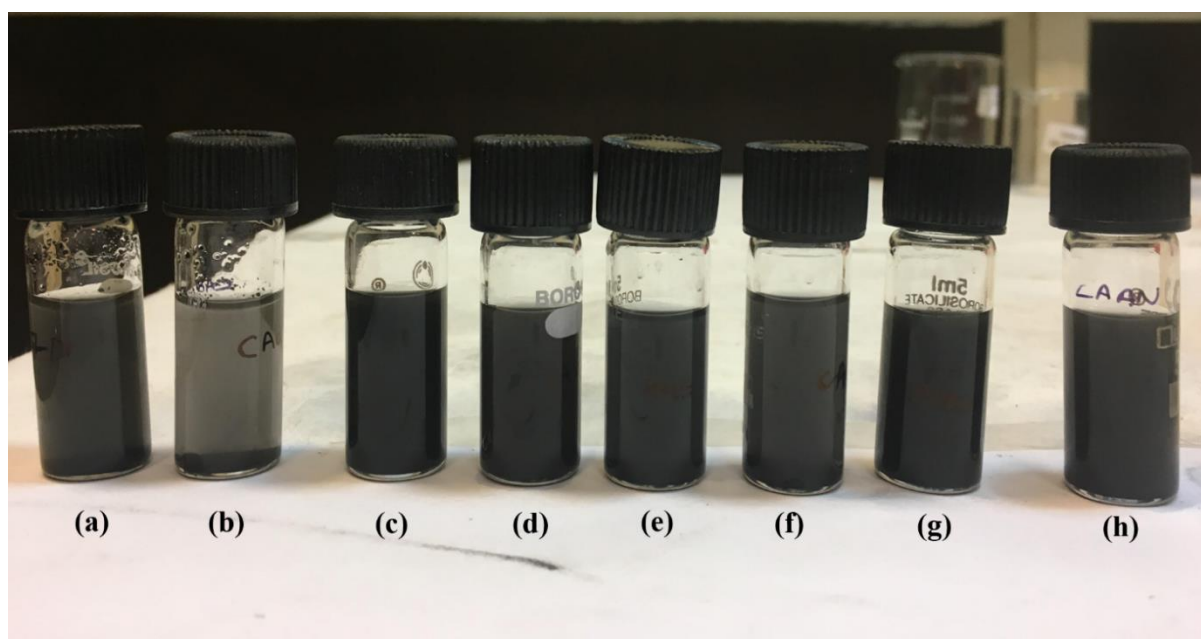


Fig. 3.1: Dispersion solution of (a) MoS₂HH in DI water (b) MoS₂CA in DI water (c) MoS₂HH in acetone (d) MoS₂CA in acetone (e) MoS₂HH in ethanol (f) MoS₂CA in ethanol (g) MoS₂HH in acetonitrile (h) MoS₂CA in acetonitrile

Hence, MoS₂HH and MoS₂CA are separately dispersed in Acetonitrile with a concentration of 1 mg mL⁻¹ and sonicated in an ultrasonic bath for 30 minutes at room

temperature. This solution is then poured into a 2-electrode cell comprising a copper (Cu) rod at which the working electrode (WE) is clipped and a platinum (Pt) rod as the counter electrode (CE). Indium tin oxide (ITO) coated glass slide of dimension 2.5 cm × 1 cm is used as a conducting substrate for depositing films of MoS₂. ITO is attached to WE and put in the solution. Positive polarity is applied to WE and negative polarity is applied to CE. Under a potential of 40 V, negatively charged MoS₂ particles move towards ITO, and films are formed by the deposition of MoS₂ particles at the electrode-suspension interface. Films are deposited in an area of 1 cm × 1 cm by EPD.

3.3 Results and Discussion

This section discusses the results of the characterization studies performed to confirm the formation of MoS₂ nanostructures and the subsequent electrochemical properties that have been investigated.

3.3.1 Characterization of samples and instrumentation

Various techniques have been utilized to characterize synthesized samples. X-ray diffraction (XRD) patterns have been recorded using a Bruker D8 Advance facility with Cu K_α radiation of wavelength 1.514 Å. Field emission scanning electron microscopy (FESEM) is done using the TESCAN model LYRA 3 XMU and is used to examine the morphology of samples. Raman spectra are measured using a WITec Raman spectrometer with an excitation wavelength of 532 nm. JEOL transmission electron microscope (TEM) is used to record morphological images. Elemental analysis of synthesized samples is carried out using energy dispersive X-ray fluorescence (EDXRF) technique, using Epsilon 5, PANalytical, and CHNS elemental analysis using Vario Micro Cube Elementar Analysensysteme Germany. The electrochemical measurements are done at room temperature by a Metrohm Autolab Potentiostat/Galvanostat using Nova software. The conventional three-electrode electrochemical cell is used for

electrochemical measurements using MoS₂/ITO as the WE, platinum (Pt) wire as the CE, and silver/silver chloride (Ag/AgCl) electrode (in 3 M KCL) as the reference electrode. PBS solution (pH 7.0) containing 5 mM of [Fe (CN)₆]^{3-/4-} and 0.9% NaCl is used as a supporting electrolyte.

3.3.2 Structural study of MoS₂ nanostructures using XRD

Fig. 3.2 shows XRD patterns of samples prepared without using any reducing agent (as-prepared sample) and with reducing agents which are (MoS₂HH) and (MoS₂CA). Identified peaks for MoS₂HH and MoS₂CA can be indexed to hexagonal MoS₂ (2H MoS₂) with JCPDS card no. 37-1492. A low intensity broadened (002) peak around 11° corresponds to low crystallinity of the as-prepared sample and the Peaks (100) and (103) are also not distinguishably visible. Also, the (110) peak is shifted slightly left in comparison to MoS₂ samples prepared using reducing agents. From here it can be concluded that this sample prepared without using any reducing agents is not having a pure crystalline phase of MoS₂ and hence further studies are not carried out on this sample. For the other two samples which are prepared using reducing agents, the peaks are found to be broadened and have a weak intensity which is due to a decrease in size as compared to bulk MoS₂. 002 peak which corresponds to periodicity along the c direction is observed to be of less intensity and is broadened which shows that the sample is in the nano range, however, its presence in both the samples (MoS₂HH and MoS₂CA) indicates that MoS₂ formed is not monolayer, rather stacking of large no. of layers [25, 30]. Also, the (002) peak which appears at 14.4° in the case of bulk MoS₂ is shifted slightly towards the low angle side (13.57°) indicating an expansion towards the (001) direction [31]. (002) peak arises because of interlayer Mo–Mo scattering and it can be seen that sample MoS₂HH has a relatively strong and sharp (002) peak in comparison to MoS₂CA, indicating a formation of well crystalline MoS₂HH with ordered stacking along the c-axis [32].

XRD data were analyzed using X Powder software for structure determination. The best matching of peaks for both the samples was observed for hexagonal structure. Lattice parameters a, b and c are found using X Powder software and their values are given as shown in **Table 3.1**, concerning the JCPDS value. Crystallite size is calculated for both the samples using the Debye-Scherrer formula given by **equation 3.9** [33]

$$t = \frac{0.9\lambda}{\beta \cos\theta} \quad (3.9)$$

Where t is the crystallite size (average crystallite diameter), λ is the X-ray wavelength i.e. 1.54064 Å, K is the shape factor (0.9), β is the line broadening at half the maximum intensity (FWHM), $\Theta=2\theta/2$, i.e. the Bragg Angle (in radian). The average crystallite size is found to be 2.69 nm and 2.73 nm for MoS₂HH and MoS₂CA samples respectively.

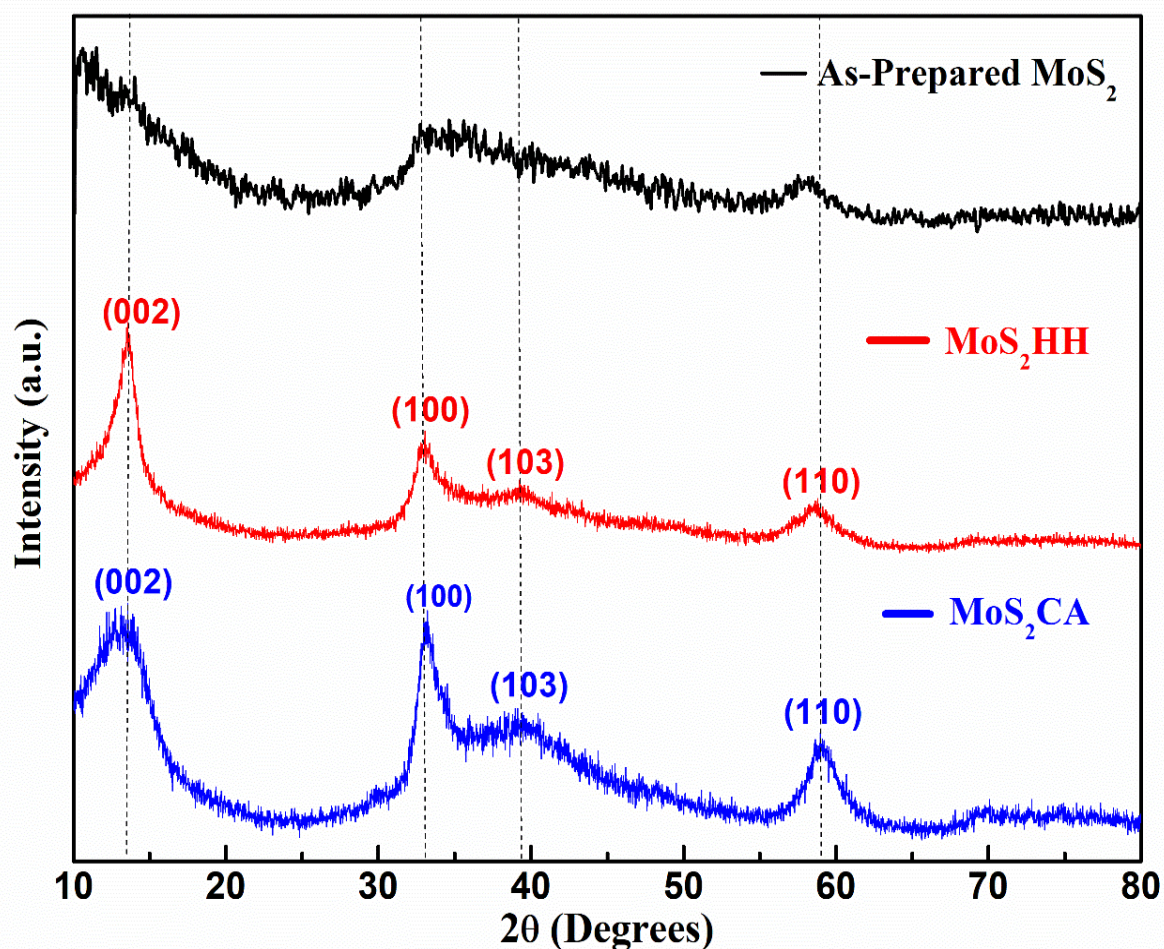


Fig. 3.2: XRD patterns of as-prepared MoS₂, MoS₂HH, and MoS₂CA

Table 3.1: Lattice parameters of two samples calculated using X-Powder software

Lattice Parameters	JCPDS (37-1492)	MoS ₂ HH	MoS ₂ CA
a	3.1612 Å	3.135 Å	3.111 Å
b	3.1612 Å	3.135 Å	3.111 Å
c	12.2985 Å	12.998 Å	13.654 Å
Volume of unit cell	106.43 Å ³	110.63 Å ³	114.44 Å ³

3.3.3 Morphological investigations using FESEM

The morphology of MoS₂ nanostructures formed using two different reducing agents HH and CA is shown in **Fig. 3.3 a, b, and c** and **Fig. 3.3 d, e, and f** respectively.

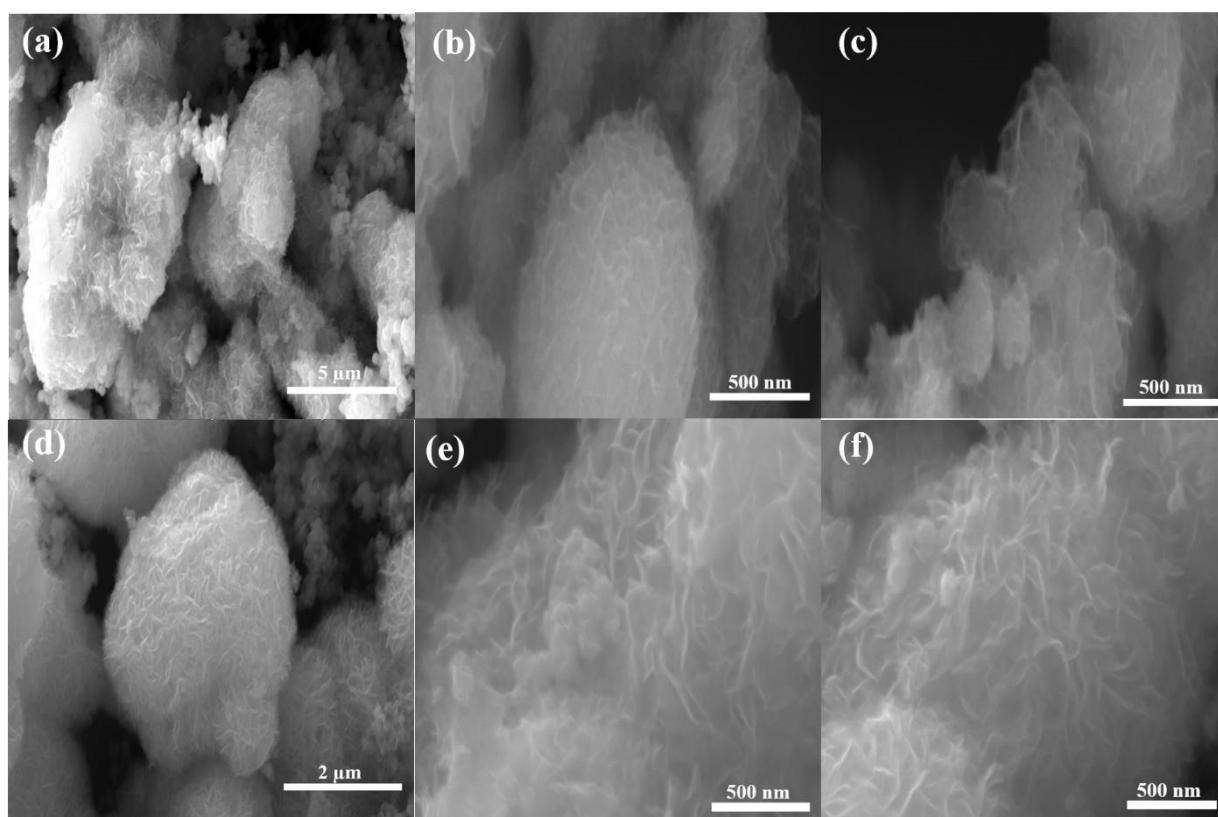


Fig. 3.3: FESEM Image of MoS₂ nanostructures (a, b, c) MoS₂HH (d, e, f) MoS₂CA

At lower magnification [**Fig. 3.3 (a) and 3.3 (d)**] flowers constituting a huge no. of nanopetals/nanosheets which are curled and stacked up together can be seen for both the

samples. At higher magnifications [Fig. 3.3 (b), 3.3 (c), 3.3 (e) and 3.3 (f)], these nanosheets are seen to be growing in all directions rendering an uneven surface morphology.

3.3.4 Qualitative analysis of the layered structure using Raman spectroscopy

Fig. 3.4 shows Raman spectra of MoS₂HH and MoS₂CA excited by a laser source having a wavelength of 532 nm. The Raman Spectrum of MoS₂ has two main peaks: an in-plane (E^{1}_{2g}) mode located around 383 cm⁻¹ and an out-of-plane mode (A_{1g}) located around 407 cm⁻¹ corresponding to 2H-phase.

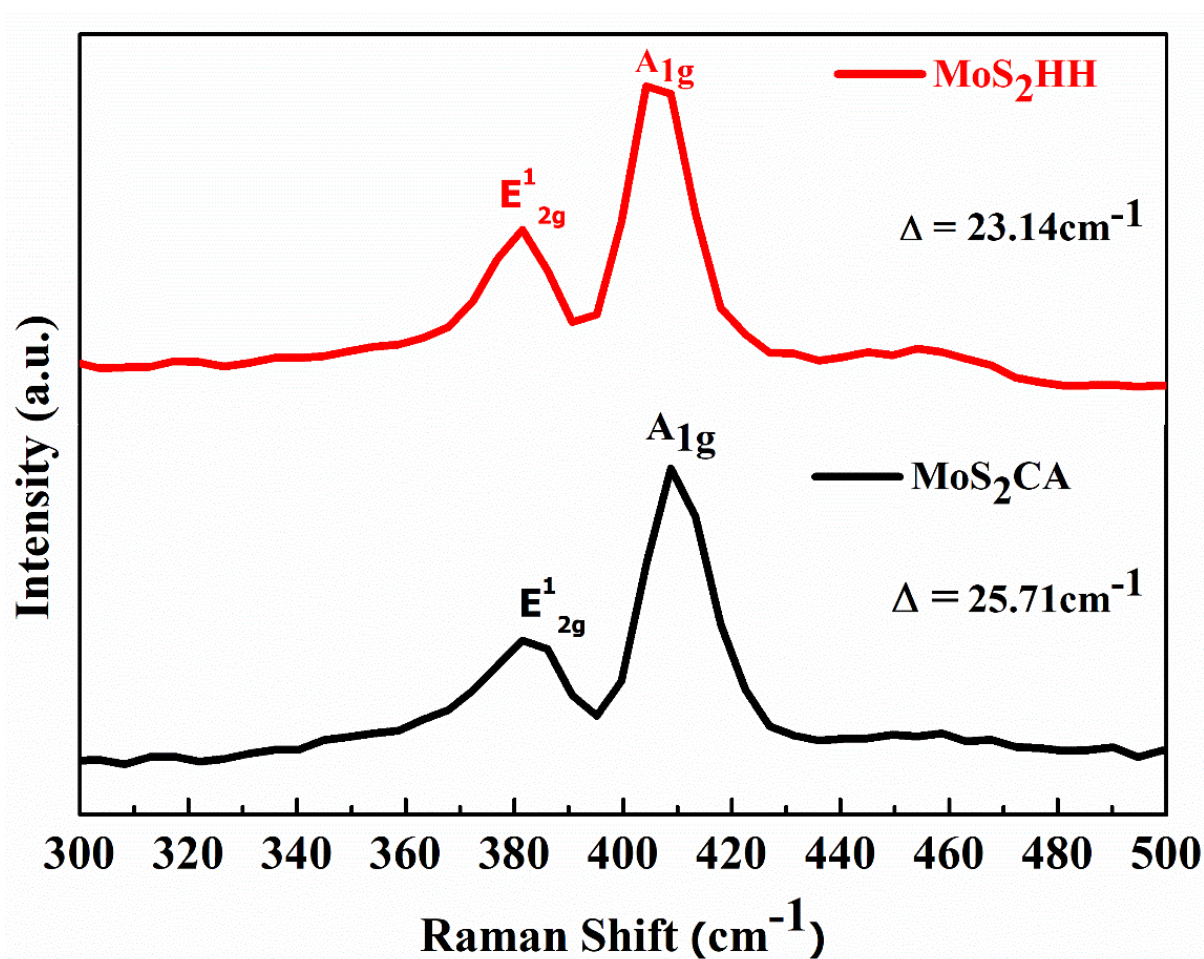


Fig. 3.4: Raman Spectra of MoS₂HH and MoS₂CA

The difference (Δ) between (E^{1}_{2g}) and (A_{1g}) modes can be used to estimate the layer number of MoS₂ nanosheets [34, 35]. This value Δ is around 18 cm⁻¹ for monolayer and

approximately equal to 25 cm^{-1} for multilayer MoS_2 [36, 37]. For MoS_2HH , (E_{2g}^1) mode lies at 382.68 cm^{-1} , and (A_{1g}) mode lies at 405.82 cm^{-1} leading to wavenumber Separation (Δ) of 23.14 cm^{-1} , while for MoS_2CA (E_{2g}^1) mode lies at 385.25 cm^{-1} and (A_{1g}) mode lies at 410.96 cm^{-1} leading to wavenumber Separation (Δ) of 25.71 cm^{-1} . Also, the Raman frequencies (E_{2g}^1) and (A_{1g}) peaks vary repeatedly with the number of layers of MoS_2 nanosheets, whereas intensities and widths of the peaks vary arbitrarily. Although the calculated Δ value shows the non-existence of one layer (1L), two layers (2L), three layers (3L) or four layers (4L) but the presence of stacked structures constituting more than four layers [38, 39]. With the increase in the number of layers, atomic vibrations are suppressed by Van der Waals forces leading to a higher force constant and blue shift of (A_{1g}) mode [23]. Here, a blue shift in (A_{1g}) mode of MoS_2CA confirms higher stacking height in comparison to MoS_2HH which is evident from TEM (Fig. 3.5) images as well.

3.3.5 Morphological investigations using TEM

TEM analysis is carried out by sonicating dispersions of both samples in ethanol and loading a single drop on the TEM copper grid. From the TEM images (Fig. 3.5) it can be observed that layered nanosheets can be observed for both samples. However, for MoS_2HH these sheets are in tight contact with each other making the nanosheet film more stable, while for MoS_2CA the nanosheets are not tightly packed together. An increase in stacking height of MoS_2CA is also evident from the blue shift of A_{1g} mode in the Raman spectrum. Both HH and CA act as a reducing agents to reduce the oxidation state of Mo (VI) to Mo (IV), but besides this CA also acts as a surfactant to grow nanosheets in a particular way. Such a kind of morphological direction to nanostructures by CA has also been reported for MoO_2 nano discs [40]. In another work, the effect of CA on the growth of ferric oxide was studied, where the size of nanoparticles decreases with an increase in the concentration of CA [41]. This happens because the

adsorption of surfactant molecules hinders the growth of Fe_2O_3 nanoparticles. The same thing is perhaps happening in our case where, CA molecules are attached to the layers of MoS_2 nanostructures not allowing them to form tightly packed structures, as seen in TEM images. Therefore, sheets obtained here for MoS_2CA are of small lateral length, growing randomly and increasing the overall stacking height of layers.

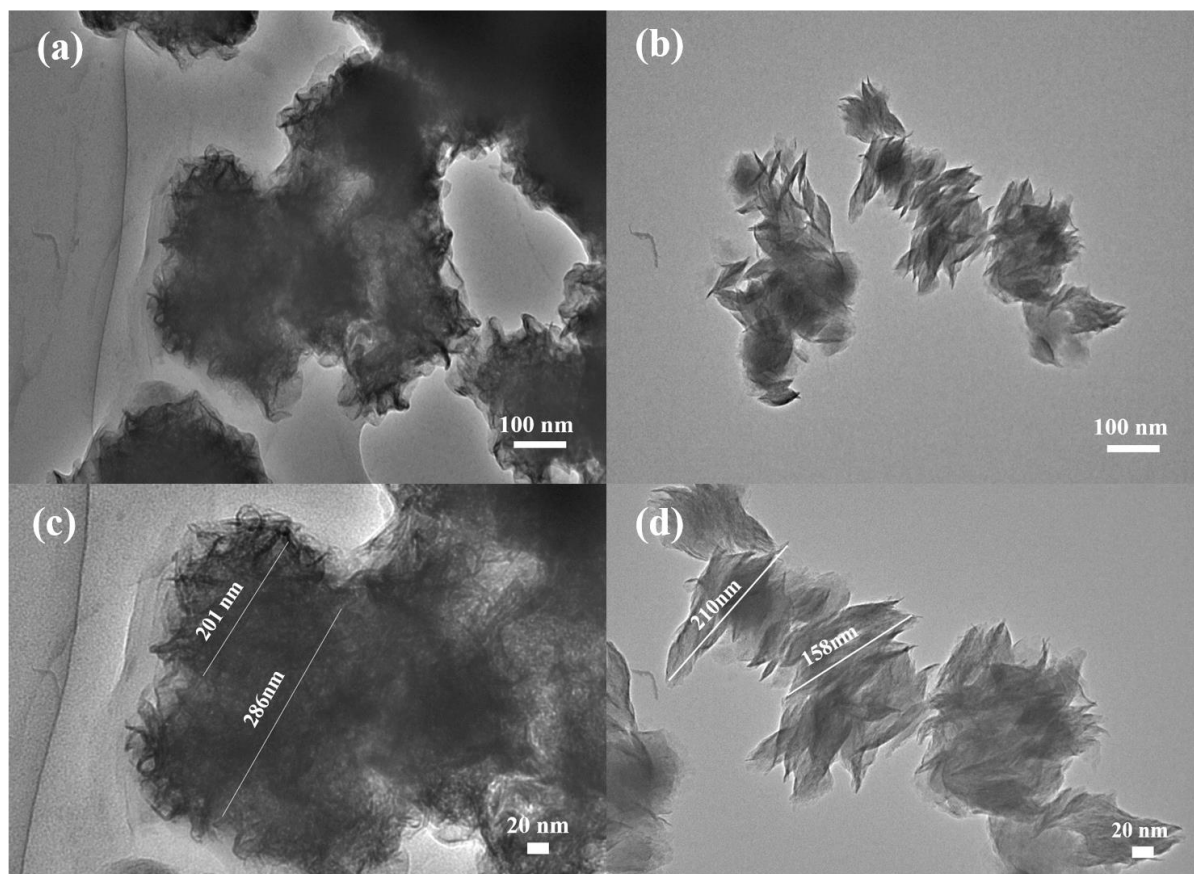


Fig. 3.5: TEM image (a) MoS_2HH at 100 nm (b) MoS_2CA at 100 nm (c) MoS_2HH at 20 nm (d) MoS_2CA at 20 nm

3.3.6 EDXRF

The purpose of this technique is to determine the Molybdenum (Mo) elemental composition of samples. MoS_2HH and MoS_2CA samples are mixed with boric acid to form a pellet by applying

a pressure of 5 tons for 10 seconds. The elemental composition of Mo is listed in **Table 3.2** for MoS₂HH and MoS₂CA.

3.3.7 CHNS

To identify the sulfur (S) content present in synthesized MoS₂ samples and the presence of other impurity elements like carbon (C), hydrogen (H), and nitrogen (N), a CHNS analysis is done. The elemental percentage for the above-stated elements is given in **Table 3.2**. It can be seen that elemental N impurity in MoS₂HH is more in comparison to MoS₂CA, while elemental C impurity in MoS₂CA is more than in MoS₂HH, which indicates that HH is a source of more N impurity in MoS₂HH, while CA is the source of C impurity in MoS₂CA. Total C, H, and N contamination is 7.59% and 5.06% in MoS₂HH and MoS₂CA respectively.

Table 3.2: Elemental composition of MoS₂HH and MoS₂CA determined using EDXRF and CHNS elemental analysis

Elemental Percentage	Mo (from EDXRF)	S (from CHNS)	C (from CHNS)	H (from CHNS)	N (from CHNS)
MoS₂HH	64.41%	28.01%	1.35%	1.86%	4.38%
MoS₂CA	61.30%	33.64%	3.14%	0.95%	0.97%

3.3.8 Electrochemical Studies

To examine the electrochemical properties of MoS₂ samples prepared using two different reducing agents, EIS, CV, and differential pulse voltammetry (DPV) are conducted. Electrodes are made by deposition of prepared samples on ITO and are labeled as MoS₂HH_ITO and MoS₂CA_ITO. For these studies mentioned above three-electrode cell is taken in which prepared electrodes are employed as WE and their electrochemical studies are recorded. The

electroactive surface area and the HET rate constant are the main factors that determine the electrochemical performance and hence are found using these analytical techniques.

3.3.8.1 Electrochemical analysis using EIS and determination of HET rate constant

EIS is done in a frequency range of 10^5 Hz to 0.1 Hz at a set potential of 0.01 V. Semi-circular diameter in the case of MoS₂HH is smaller in comparison to that of MoS₂CA giving an R_{ct} value of 150 Ω and 456 Ω respectively (**Fig. 3.6**). Larger resistance is offered to electrons in the case of MoS₂CA which may be due to the larger height and irregular orientation of nanosheet arrays as observed in TEM images (**Fig. 3.5**) and confirmed from Raman spectra as well. Whereas, MoS₂HH has stacked nanosheets, therefore, decreasing the overall distance that electron has to travel to reach conducting ITO substrate. HET constant (K_o) can be calculated using the **equation 3.10** [16]

$$K_o = \frac{RT}{n^2 F^2 A_e R_{ct} C} \quad (3.10)$$

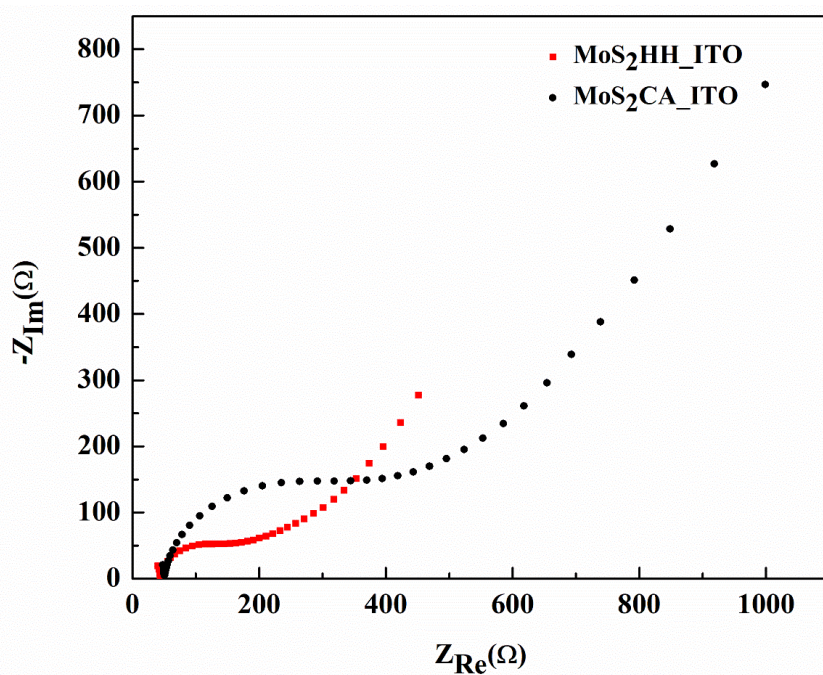


Fig. 3.6: Nyquist plot of MoS₂HH_ITO and MoS₂CA_ITO using EIS technique

Where, R is the universal gas constant, T is room temperature ($25\text{ }^\circ\text{C}$), n is the no. of electrons transferred in the redox event, F is Faraday's constant, and A_e is electroactive surface area (in cm^2), C is the bulk concentration of the analyte. From here we can calculate the value of K_0 for MoS_2HH as $0.69 \times 10^{-3} \text{ cm s}^{-1}$ for A_e (51.38 mm^2 , as calculated using CV) and K_0 for MoS_2CA as $0.38 \times 10^{-3} \text{ cm s}^{-1}$ for A_e (30.70 mm^2 , as calculated using CV).

3.3.8.2 Electrochemical analysis using CV and determination of the electroactive surface area

CV studies are done in a potential window of -0.6 V to 1.5 V at a scan rate of 50 mV s^{-1} (**Fig. 3.7**). For MoS_2HH value of peak current in the positive direction of voltage scan is found to be $546.17 \text{ } \mu\text{A}$ at a potential of 0.693 V while the peak current in the negative direction of voltage scan is $-545.53 \text{ } \mu\text{A}$ at a potential of -0.176 V . While for MoS_2CA same peak currents in two directions of the potential scan are found to be a little lesser with a value of $504.15 \text{ } \mu\text{A}$ at a potential value 0.544 V and $-523.5 \text{ } \mu\text{A}$ at a potential of -0.119 V . Scan rate study for both the samples is done using CV by varying the scan rate from 10 mV s^{-1} to 150 mV s^{-1} (**Fig. 3.8**). **Fig. 3.9** shows the variation of peak anodic current (i_{pa}) and peak cathodic current (i_{pc}) with the square root of scan rate which is a straight line showing that the process is diffusion-controlled [42, 43]. By diffusion controlled we mean that the electron transfer takes place between electrode and electrolyte solution and not by adsorption of analyte on the electrode surface. For both the samples, the electron transfer process is found to be diffusion controlled and can be fitted by the equations given as

$$I_{pa}(\text{MoS}_2\text{HH}) = 0.14137\text{mA} + \left[\left(0.05639\text{mA} \times \sqrt{\frac{\text{s}}{\text{mV}}} \right) \times \left(\sqrt{\text{Scan Rate} \frac{\text{mV}}{\text{s}}} \right) \right] \quad (3.11)$$

$$R^2 = 0.99$$

$$I_{pc}(\text{MoS}_2\text{HH}) = -0.08271\text{mA} + \left[\left(-0.07165\text{mA} \times \sqrt{\frac{\text{s}}{\text{mV}}} \right) \times \left(\sqrt{\text{Scan Rate} \frac{\text{mV}}{\text{s}}} \right) \right] \quad (3.12)$$

$$R^2 = 0.99$$

$$I_{pa}(MoS_2CA) = 0.14366mA + \left[\left(0.03369mA \times \sqrt{\frac{s}{mV}} \right) \times \left(\sqrt{Scan Rate \frac{mV}{s}} \right) \right] \quad (3.13)$$

$$R^2 = 0.99$$

$$I_{pc}(MoS_2CA) = -0.07235mA + \left[\left(-0.07525mA \times \sqrt{\frac{s}{mV}} \right) \times \left(\sqrt{Scan Rate \frac{mV}{s}} \right) \right] \quad (3.14)$$

$$R^2 = 0.99$$

Here, R is correlation coefficient

The peak current for a reversible couple is given by the Randles-Sevcik equation (3.15) [44]

$$i_p = 0.446nFA_eC\sqrt{\left(\frac{nFvD_o}{RT}\right)} \quad (3.15)$$

Where,

n is the no. of electrons transferred in the redox event, F is Faraday's constant, A_e is electroactive surface area (in cm^2), v is scan rate (in $V s^{-1}$), D_o is diffusion coefficient of oxidized analyte (in $cm^2 s^{-1}$), C is the bulk concentration of analyte, R is the universal gas constant, T is room temperature (25 °C). By substituting the value of Faraday's constant as 96485 C/mol, the value of T as 25 °C and R as 8.314 J K⁻¹ mol⁻¹ equation (15) is reduced to

$$i_p = 2.69 \times 10^5 n^{3/2} A_e C \sqrt{D_o v} \quad (3.16)$$

Now, by substituting the values of $\left(\frac{i_p}{\sqrt{v}}\right)$ from the slope of **equations 3.11** and **3.13**, the number of electrons transferred (n=1 for Ferro/Ferri), D_o ($0.667 \times 10^{-5} cm^2 s^{-1}$ for ferrocyanide [45], which is an oxidized analyte for our system), C ($5 \times 10^{-6} mol cm^{-3}$), the A_e of MoS₂HH electrode can be calculated as 51.38 mm², while for MoS₂CA it is 30.70 mm². The value of $i_{pa}/i_{pc}=1.001$, for MoS₂HH, which is very close to unity shows that the redox system is nearly reversible, however, its value for MoS₂CA is 0.96 which shows that system is semi-reversible.

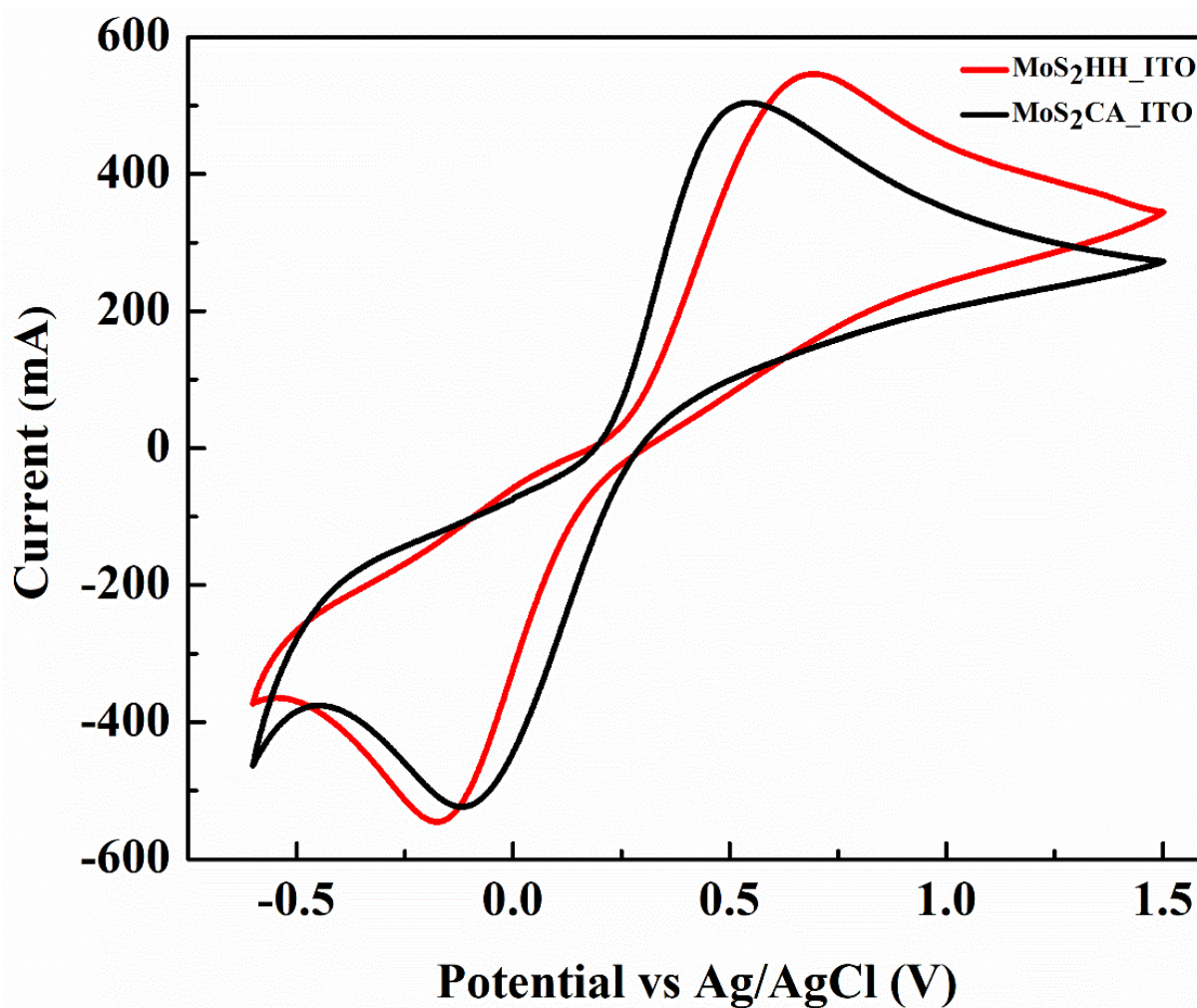


Fig. 3.7: Cyclic Voltammogram of MoS₂HH_ITO and MoS₂CA_ITO

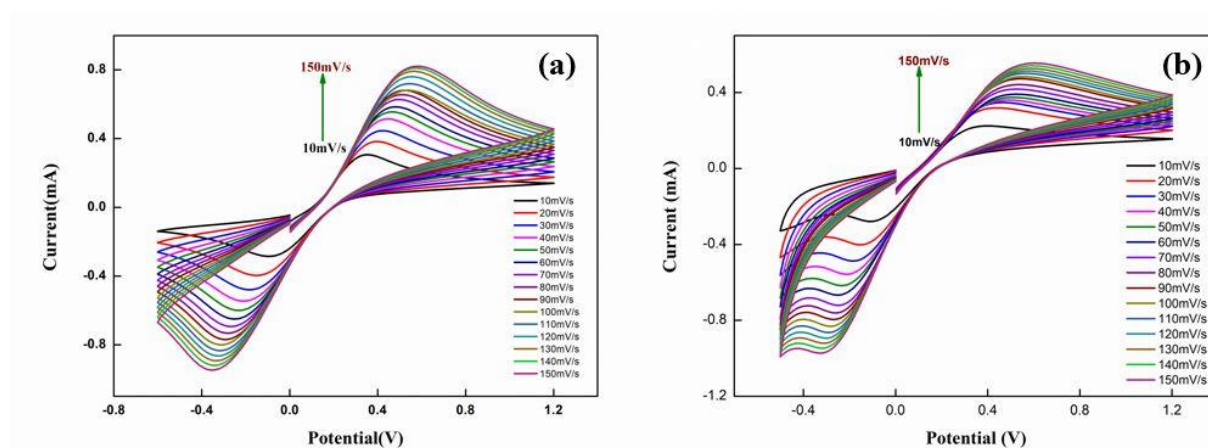


Fig. 3.8: Scan rate study of (a) MoS₂HH_ITO and (b) MoS₂CA_ITO at scan rate varying from 10 mV s⁻¹ – 150 mV s⁻¹

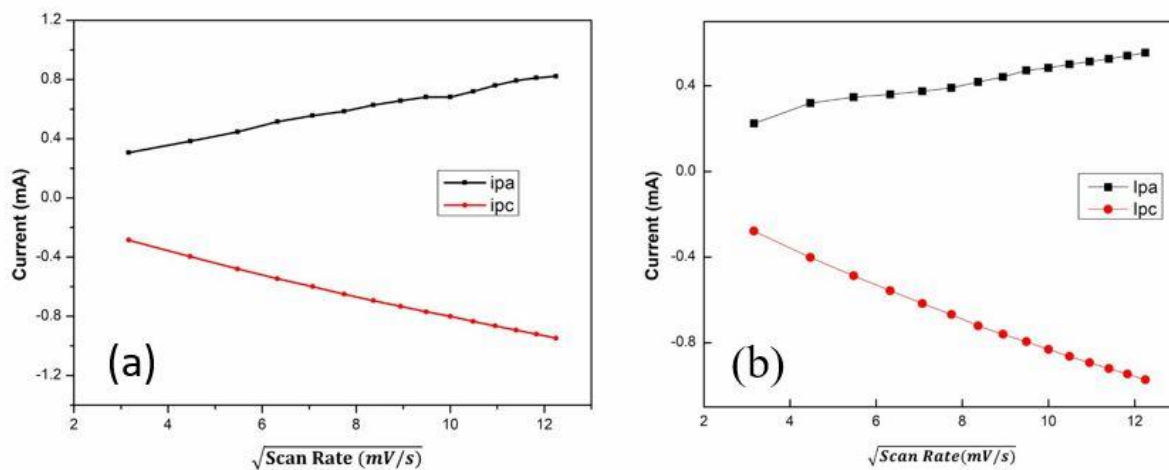


Fig. 3.9: Variation of i_{pa} and i_{pc} with under root of scan rate (a) MoS₂HH_ITO (b) MoS₂CA_ITO

3.3.8.3 Electrochemical analysis using DPV

DPV studies are conducted in the same electrochemical cell with the same redox probes as used in CV with a step potential of 0.005 V in a potential window of 0 V to 0.6 V with a scan rate of 10 mV s⁻¹ (Fig. 3.10).

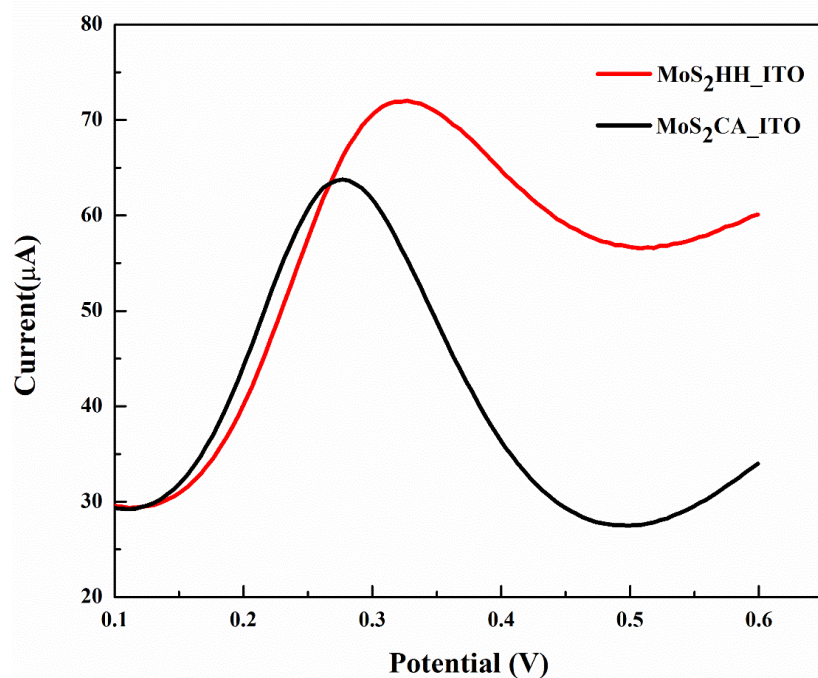


Fig. 3.10: Differential pulse voltammograms of MoS₂HH_ITO and MoS₂CA_ITO

For MoS₂HH peak current value is 72.02 μ A which is reached at a potential of 0.33 V, while MoS₂CA shows peak current at 63.78 μ A reaching at a potential of 0.28 V. The results are similar to that of CV, but in this case, it can be seen that the difference is more amplified, the reason being in DPV we take a differential pulse which results in an enhanced response.

A higher current value (in CV and DPV) and lower resistance (EIS) for MoS₂HH is caused by increased effective surface area for HET, due to its highly dense, closely packed nanosheet structure. The stacking height of layers is more in the case of MoS₂CA as seen in TEM images (**Fig. 3.5**) whose confirmation is given by the Raman spectrum as well. More stacking height of layers increases the diffusion distance of electrons which in turn increases the resistance value and decreases the current response as observed in EIS, DPV, and CV respectively.

It can also be observed that the difference between signals for two samples is maximum observable in EIS (67%) in comparison to DPV (13%) and CV (8.33%) (shown in **Table 3.3**). This can be attributed to the layered structure of MoS₂ and excess negative charge on the surface of MoS₂ which repels the negative redox probe and hinders the electron transport between the redox couple and electrode surface [23, 32]. **Table 3.4** shows the values of various electrochemical parameters obtained using EIS and CV.

Table 3.3: Percentage change between results of different electrochemical techniques

	R_{ct} (EIS)	i_p (CV)	i_p (DPV)
MoS₂HH_ITO	150 Ω	546.17 μ A	72.02 μ A
MoS₂CA_ITO	456 Ω	504.15 μ A	63.78 μ A
Percentage Change	67%	8.33%	13%

Table 3.4: Comparison of parameters calculated using, various electrochemical techniques

	HET constant (K_0)	Electroactive surface area (A_e)	Diffusion controlled process	Electrochemical reversibility
MoS₂HH_ITO	$0.69 \times 10^{-3} \text{ cm s}^{-1}$	51.38 mm ²	Yes	$i_{pa}/i_{pc} = 1.001$ ~Reversible
MoS₂CA_ITO	$0.38 \times 10^{-3} \text{ cm s}^{-1}$	30.70 mm ²	Yes	$i_{pa}/i_{pc} = 0.96$ Semi reversible

3.4 Conclusion

MoS₂ nanostructures are synthesized using a simple, one-step hydrothermal method by reducing MoS₂ using HH and CA. Sample reduced using HH is found to exhibit a higher electroactive surface area (51.38 mm²) and HET constant ($0.69 \times 10^{-3} \text{ cm s}^{-1}$) thus imparting better electrochemical properties which can be utilized for electrochemical sensing applications where an increase or decrease in current or resistance value can confirm the attachment of gas or biomolecules. Overall, diffusion distance is increased in the case of MoS₂ sample reduced using CA which is due to stacking of layers confirmed by, the blue shift in A_{1g} peak in Raman spectra and visible morphology from TEM images which renders it a low electroactive surface area (30.70 mm²) and low heterogeneous electron transfer constant ($0.38 \times 10^{-3} \text{ cm s}^{-1}$). We believe that MoS₂ synthesized using HH can be further explored for its applications in sensing owing to its high electroactive surface area, good HET, and nanosheets-like structure increasing the total surface area for the loading of bio or gas molecules. It can also be concluded that EIS is a better technique for observing measurable differences in layered materials.

References:

- [1] C. Anichini, W. Czepa, D. Pakulski, A. Aliprandi, A. Ciesielski, P. Samorì, Chemical sensing with 2D materials, *Chemical Society Reviews* 47(13) (2018) 4860-4908.
- [2] L. Wang, Y. Ma, M. Yang, Y. Qi, Hierarchical hollow MoS₂ nanospheres with enhanced electrochemical properties used as an electrode in supercapacitor, *Electrochimica Acta* 186 (2015) 391-396.
- [3] J. Park, J.-S. Kim, J.-W. Park, T.-H. Nam, K.-W. Kim, J.-H. Ahn, G. Wang, H.-J. Ahn, Discharge mechanism of MoS₂ for sodium ion battery: Electrochemical measurements and characterization, *Electrochimica Acta* 92 (2013) 427-432.
- [4] W. Qin, T. Chen, L. Pan, L. Niu, B. Hu, D. Li, J. Li, Z. Sun, MoS₂-reduced graphene oxide composites via microwave assisted synthesis for sodium ion battery anode with improved capacity and cycling performance, *Electrochimica Acta* 153 (2015) 55-61.
- [5] V.H. Pham, K.-H. Kim, D.-w. Jung, K. Singh, E.-S. Oh, J.S. Chung, Liquid phase co-exfoliated MoS₂-graphene composites as anode materials for lithium ion batteries, *Journal of Power Sources* 244 (2013) 280-286.
- [6] Z. Li, J. Ma, Y. Zhou, Z. Yin, Y. Tang, Y. Ma, D. Wang, Synthesis of sulfur-rich MoS₂ nanoflowers for enhanced hydrogen evolution reaction performance, *Electrochimica Acta* 283 (2018) 306-312.
- [7] M. Pumera, A.H. Loo, Layered transition-metal dichalcogenides (MoS₂ and WS₂) for sensing and biosensing, *TrAC Trends in Analytical Chemistry* 61 (2014) 49-53.
- [8] F. Urban, M. Passacantando, F. Giubileo, L. Iemmo, A. Di Bartolomeo, Transport and field emission properties of MoS₂ bilayers, *Nanomaterials* 8(3) (2018) 151.
- [9] A. Di Bartolomeo, A. Grillo, F. Urban, L. Iemmo, F. Giubileo, G. Luongo, G. Amato, L. Croin, L. Sun, S.J. Liang, Asymmetric schottky contacts in bilayer MoS₂ field effect transistors, *Advanced Functional Materials* 28(28) (2018) 1800657.
- [10] S. Bertolazzi, J. Brivio, A. Kis, Stretching and breaking of ultrathin MoS₂, *ACS nano* 5(12) (2011) 9703-9709.
- [11] L. Zhang, W. Fan, W.W. Tjiu, T. Liu, 3D porous hybrids of defect-rich MoS₂/graphene nanosheets with excellent electrochemical performance as anode materials for lithium ion batteries, *RSC Advances* 5(44) (2015) 34777-34787.
- [12] A.B. Yousaf, M. Imran, M. Farooq, P. Kasak, Synergistic effect of Co-Ni co-bridging with MoS₂ nanosheets for enhanced electrocatalytic hydrogen evolution reactions, *RSC advances* 8(7) (2018) 3374-3380.
- [13] M. Li, D. Wang, J. Li, Z. Pan, H. Ma, Y. Jiang, Z. Tian, Facile hydrothermal synthesis of MoS₂ nano-sheets with controllable structures and enhanced catalytic performance for anthracene hydrogenation, *RSC Advances* 6(75) (2016) 71534-71542.
- [14] S. Vattikuti, C. Byon, Synthesis and characterization of molybdenum disulfide nanoflowers and nanosheets: nanotribology, *Journal of Nanomaterials* 2015 (2015) 9.
- [15] Q. Zhang, X. Li, C. Qian, L. Dou, F. Cui, X. Chen, Label-free electrochemical immunoassay for neuron specific enolase based on 3D macroporous reduced graphene oxide/polyaniline film, *Analytical biochemistry* 540 (2018) 1-8.
- [16] D. Sandil, S. Srivastava, B. Malhotra, S. Sharma, N.K. Puri, Biofunctionalized tungsten trioxide-reduced graphene oxide nanocomposites for sensitive electrochemical immunosensing of cardiac biomarker, *Journal of Alloys and Compounds* 763 (2018) 102-110.
- [17] P. Sun, W. Zhang, X. Hu, L. Yuan, Y. Huang, Synthesis of hierarchical MoS₂ and its electrochemical performance as an anode material for lithium-ion batteries, *Journal of Materials Chemistry A* 2(10) (2014) 3498-3504.

- [18] A. Ramadoss, T. Kim, G.-S. Kim, S.J. Kim, Enhanced activity of a hydrothermally synthesized mesoporous MoS₂ nanostructure for high performance supercapacitor applications, *New Journal of Chemistry* 38(6) (2014) 2379-2385.
- [19] L. Chen, H. Zhu, Molybdenum Sulfide Nanosheet-Based Hollow Porous Flat Boxes and Nanotubes for Efficient Electrochemical Hydrogen Evolution, *ChemCatChem* 10(2) (2018) 459-464.
- [20] J.V. Kumar, R. Karthik, S.-M. Chen, K. Saravanakumar, M. Govindasamy, V. Muthuraj, Novel hydrothermal synthesis of MoS₂ nanocluster structure for sensitive electrochemical detection of human and environmental hazardous pollutant 4-aminophenol, *RSC Advances* 6(46) (2016) 40399-40407.
- [21] M. Kukkar, A. Sharma, P. Kumar, K.-H. Kim, A. Deep, Application of MoS₂ modified screen-printed electrodes for highly sensitive detection of bovine serum albumin, *Analytica chimica acta* 939 (2016) 101-107.
- [22] X. Wang, Z. Zhang, Y. Chen, Y. Qu, Y. Lai, J. Li, Morphology-controlled synthesis of MoS₂ nanostructures with different lithium storage properties, *Journal of Alloys and Compounds* 600 (2014) 84-90.
- [23] F. Wang, M. Zheng, B. Zhang, C. Zhu, Q. Li, L. Ma, W. Shen, Ammonia intercalated flower-like MoS₂ nanosheet film as electrocatalyst for high efficient and stable hydrogen evolution, *Scientific reports* 6 (2016) 31092.
- [24] M.A.R. Anjum, H.Y. Jeong, M.H. Lee, H.S. Shin, J.S. Lee, Efficient Hydrogen Evolution Reaction Catalysis in Alkaline Media by All-in-One MoS₂ with Multifunctional Active Sites, *Advanced Materials* 30(20) (2018) 1707105.
- [25] G. Nagaraju, C. Tharamani, G. Chandrappa, J. Livage, Hydrothermal synthesis of amorphous MoS₂ nanofiber bundles via acidification of ammonium heptamolybdate tetrahydrate, *Nanoscale research letters* 2(9) (2007) 461.
- [26] T.N. Narayanan, C.S. Vusa, S. Alwarappan, Selective and efficient electrochemical biosensing of ultrathin molybdenum disulfide sheets, *Nanotechnology* 25(33) (2014) 335702.
- [27] S. Su, W. Cao, W. Liu, Z. Lu, D. Zhu, J. Chao, L. Weng, L. Wang, C. Fan, L. Wang, Dual-mode electrochemical analysis of microRNA-21 using gold nanoparticle-decorated MoS₂ nanosheet, *Biosensors and Bioelectronics* 94 (2017) 552-559.
- [28] K. Arora, N.K. Puri, Electrophoretically deposited nanostructured PdO thin film for room temperature amperometric H₂ sensing, *Vacuum* 154 (2018) 302-308.
- [29] K. Zhang, H. Zhang, P. Liu, C. Zhang, W. Li, X. Chen, F. Ma, Electrophoretic deposition of graphene oxide on NiTi alloy for corrosion prevention, *Vacuum* 161 (2019) 276-282.
- [30] K.-K. Liu, W. Zhang, Y.-H. Lee, Y.-C. Lin, M.-T. Chang, C.-Y. Su, C.-S. Chang, H. Li, Y. Shi, H. Zhang, Growth of large-area and highly crystalline MoS₂ thin layers on insulating substrates, *Nano letters* 12(3) (2012) 1538-1544.
- [31] S. Muralikrishna, K. Manjunath, D. Samrat, V. Reddy, T. Ramakrishnappa, D.H. Nagaraju, Hydrothermal synthesis of 2D MoS₂ nanosheets for electrocatalytic hydrogen evolution reaction, *RSC Advances* 5(109) (2015) 89389-89396.
- [32] K.M. Kwok, S.W.D. Ong, L. Chen, H.C. Zeng, Constrained growth of MoS₂ nanosheets within a mesoporous silica shell and its effects on defect sites and catalyst stability for H₂S decomposition, *ACS Catalysis* 8(1) (2017) 714-724.
- [33] L. Alexander, H.P. Klug, Determination of crystallite size with the X-Ray spectrometer, *Journal of Applied Physics* 21(2) (1950) 137-142.
- [34] B. Sirota, N. Glavin, A.A. Voevodin, Room temperature magnetron sputtering and laser annealing of ultrathin MoS₂ for flexible transistors, *Vacuum* 160 (2019) 133-138.
- [35] M. Barzegar, A. Tiwari, On the performance of vertical MoS₂ nanoflakes as a gas sensor, *Vacuum* 167 (2019) 90-97.

- [36] H. Li, Q. Zhang, C.C.R. Yap, B.K. Tay, T.H.T. Edwin, A. Olivier, D. Baillargeat, From bulk to monolayer MoS₂: evolution of Raman scattering, *Advanced Functional Materials* 22(7) (2012) 1385-1390.
- [37] X. Li, H. Zhu, Two-dimensional MoS₂: Properties, preparation, and applications, *Journal of Materiomics* 1(1) (2015) 33-44.
- [38] Y. Wang, Y. Du, J. Deng, Z. Wang, Friction reduction of water based lubricant with highly dispersed functional MoS₂ nanosheets, *Colloids and Surfaces A: Physicochemical and Engineering Aspects* 562 (2019) 321-328.
- [39] A.P. Gaur, S. Sahoo, M. Ahmadi, S.P. Dash, M.J.-F. Guinel, R.S. Katiyar, Surface energy engineering for tunable wettability through controlled synthesis of MoS₂, *Nano letters* 14(8) (2014) 4314-4321.
- [40] V. Ramakrishnan, C. Alex, A.N. Nair, N.S. John, Designing Metallic MoO₂ Nanostructures on Rigid Substrates for Electrochemical Water Activation, *Chemistry–A European Journal* 24(68) (2018) 18003-18011.
- [41] A. Bee, R. Massart, S. Neveu, Synthesis of very fine maghemite particles, *Journal of Magnetism and Magnetic Materials* 149(1-2) (1995) 6-9.
- [42] A. Vasudev, A. Kaushik, S. Bhansali, Electrochemical immunosensor for label free epidermal growth factor receptor (EGFR) detection, *Biosensors and Bioelectronics* 39(1) (2013) 300-305.
- [43] B.R. Wiston, M. Ashok, Electrochemical performance of hydrothermally synthesized flower-like α -nickel hydroxide, *Vacuum* 160 (2019) 12-17.
- [44] N. Elgrishi, K.J. Rountree, B.D. McCarthy, E.S. Rountree, T.T. Eisenhart, J.L. Dempsey, A practical beginner's guide to cyclic voltammetry, *Journal of Chemical Education* 95(2) (2017) 197-206.
- [45] S. Konopka, B. McDuffie, Diffusion coefficients of ferri- and ferrocyanide ions in aqueous media, using twin-electrode thin-layer electrochemistry, *Analytical Chemistry* 42(14) (1970) 1741-1746.

Chapter 4

Electrochemical Study of reduced graphene oxide (rGO) Modified MoS₂ Layered Nanosheets for Detection of Lung Cancer Biomarker

This work presents an electrochemical biosensor for sensitive, specific, and rapid detection of lung cancer biomarker, neuron-specific enolase (NSE) by utilization of rGO modified MoS₂ multi-layered nanosheets as a matrix. Layered structures along with the synergetic effect of MoS₂ and rGO allow easy grafting of two materials into one another. This empowers the sensor to have a heterogeneous rate transfer constant of $1.29 \times 10^{-3} \text{ cm s}^{-1}$ and an electroactive surface area of 27.83 mm^2 . Electrochemical impedance spectroscopy (EIS) and cyclic voltammetry (CV) are used as dual modes for the detection of NSE and the sensor exhibits a wide linear detection range. The sensor is found to be reproducible with a relative standard deviation (RSD) of less than 5% along with an invariant response towards other endogenous interfering species found in human serum. The investigations done in this study will further help us to fabricate a device for rapid and early detection of lung cancer.

This work is published as: **Ritika Khatri and Nitin K. Puri.** *"Electrochemical biosensor utilizing dual-mode output for detection of lung cancer biomarker based on reduced graphene oxide-modified reduced-molybdenum disulfide multi-layered nanosheets."* **Journal of Materials Research (Springer) 37 (8), (2022): 1451-1463.**

4.1 Introduction

Cancer poses a serious life threat to the human race [1]. Amongst, different types of cancers, lung cancer is found to be the major cause of cancer mortality in men, while it is the second major cause of cancer-related deaths in women with the first major cause being breast cancer [1]. Smoking, use of tobacco, and air pollution are found to be some of the major reasons for lung cancer and only 10% to 20% of people are found to survive after 5 years of diagnosis in most countries [1]. To ensure effective and timely treatment and thus alleviate the contribution of lung cancer towards a high rate of mortality across the world, early detection of this cancer is critically important. Conventional techniques that are being used for the detection of cancer *i.e.*, computed tomography (CT), chest radiography, biopsy, and magnetic resonance imaging (MRI) are accompanied by many disadvantages like limited availability, heavy machinery involved, the skill required for their operations, high cost, etc., which make it very challenging to use them in true essence for early and easy detection of lung cancer. Thus, alternative and non-cumbersome strategies are required for early detection, to suppress the elevation of cancerous cells in the body at the initial stage. Electrochemical immunosensors have steadily gained ground in the last decade, all thanks to a large number of advantages which they proffer like a fast response, real-time monitoring, the minimal requirement for pre-processing of the sample, high sensitivity, low sample requirement, and high specificity to name a few [2, 3]. Since the over-expression of cancer protein biomarkers can be closely related to the development or occurrence of cancer, therefore sensitive and specific detection of these biomarkers at an early stage can reduce the mortality rate.

Neuron-specific enolase (NSE) is found to be expressed in high concentrations in patients suffering from small cell lung cancer (SCLC), which makes it a highly specific and sensitive biomarker [4, 5]. A concentration value greater than 12 ng mL^{-1} is found in serum for the target biomarker (NSE) in the case of 69% of patients diagnosed with small cell lung

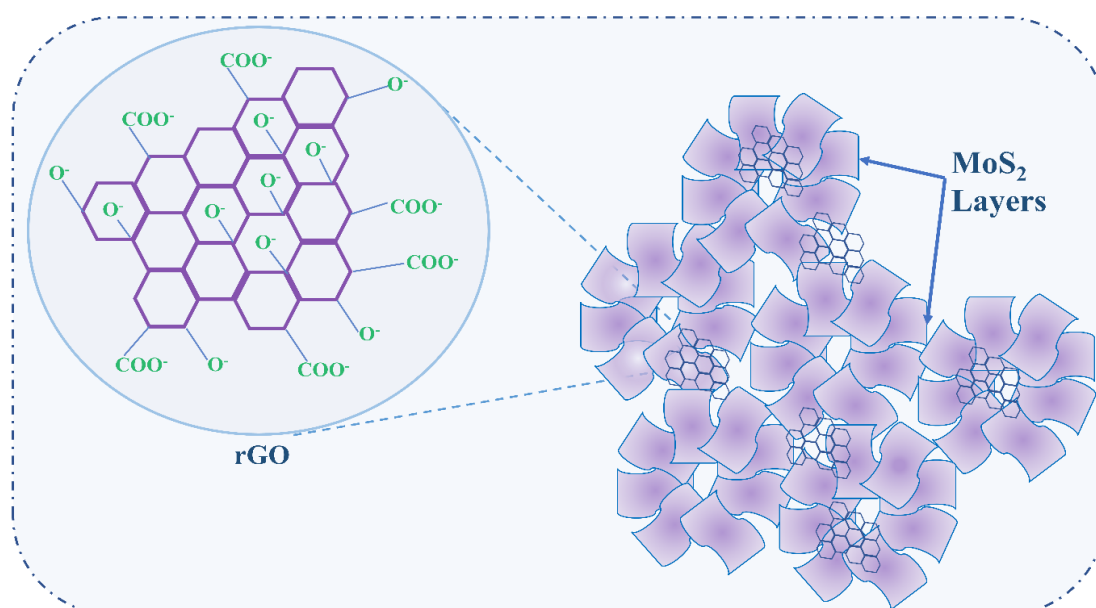
cancer (SCLC) [6]. SCLC has a poor prognosis in comparison to other types of lung cancer which necessitates its specific detection at an early stage [5]. Since NSE is overexpressed in serum in case of malignant proliferation of cells leading to SCLC [7] therefore, NSE can be used for diagnosis, prognosis, progression of the disease, and follow-up of SCLC (treatment efficacy) [8]. SCLC has two clinical stages namely limited-stage disease (LD) and another one is extensive-stage disease (ED) [7]. The serum NSE level is raised to 13.8 ng mL⁻¹ and 59 ng mL⁻¹ in LD and ED patients respectively [6]. Further, it can be used to check if a patient is responding to cancer treatment or not [6]. Several appreciable reports are available for the detection of NSE using electrochemical techniques. For instance, Han et al reported the use of gold (Au) nanoparticles functionalized graphene-based biosensor for detecting NSE in the range of 0.001 to 100 ng mL⁻¹ [4]. Yin et al utilized the synergistic effect of multi-walled carbon nanotubes (MWCNTs) with metal nanoparticles like Au and palladium (Pd) for realizing an electrochemical biosensor in the linear detection range of 0.001 to 100 ng mL⁻¹ for NSE [9]. Zhang and co-workers employed another carbon-based nanomaterial that is reduced graphene oxide (rGO) along with polyaniline (PANI) on a gold electrode for detection of NSE in a linear range of 0.5 pg mL⁻¹ to 100 ng mL⁻¹ with an Ag incubation time of 40 minutes [10]. Wang et al used polyresorcinol nanocomposite with Au and Platinum (Pt) for detecting NSE, with an optimized incubation time of 50 minutes [11]. Fu and co-workers synthesized catalysts based on Pt nanoflowers and obtained a pseudo-linear relationship between the log of NSE concentrations and cyclic voltammetry (CV) currents [12]. However, the commercial realization of these platforms is impeded by the high cost of metal nanoparticles like gold, palladium, platinum etc, or usage of gold electrode for fabrication of biosensor, beating the essence of making an electrochemical biosensor. This also shows that still, a considerable room is available for the development of new biosensors and exploration of different nanomaterials

and substrates to reduce the cost and simultaneously have great electrochemical parameters with enriched activity for early detection of NSE.

MoS₂ is a widely explored material for various applications including biomarker-based biosensing due to its layered structure, a high value of heterogeneous electron transfer (HET) constant along with large electroactive surface area [13, 14]. However, the non-availability of any pristine functional groups limits its capability to attach biomolecules onto it, therefore causing unspecific interaction with analytes. The absence of any dangling bonds promotes physisorption in place of chemisorption, which may be suited when fast response and recovery are required. However covalent linkages are more suitable when biomolecules are immobilized and tested in buffer saline solutions as discussed in chapter 1 [15, 16]. Thus, the use of MoS₂ in its pristine form is hindered in biosensors. However, an enriched surface-to-volume ratio and its synergistic effect with most of the materials including polymers, carbon nanomaterials, metal nanoparticles, metal oxides, etc provide leeway in its surface modification and chemical functionalization [14]. Hence, the incorporation of functional groups can provide reactive sites for covalent linkage on biomolecules in turn enhancing the sensitivity and specificity. Reduced graphene oxide (rGO) which has abundant functional groups like hydroxylate and carboxylate can provide sites for covalent linkages of biomolecules, providing an alternative for the functionalization of MoS₂ and harnessing the sensitivity and specificity of the device [17]. The utilization of bare rGO as an electrode material is prohibited by the fact that the layers tend to stick together and cause aggregation to reduce the free energy [18]. Both MoS₂ and rGO are 2D nanomaterials which impart them the capability to load more and more biomolecules onto them owing to their high surface-to-volume ratio. Thus, a new gateway is provided to the potential use of various nano-composites like MoS₂-rGO for the detection of various protein biomarkers. There are innumerable reports available on the utilization of rGO modified MoS₂ based matrix as a sensing platform for the detection of many potential biomarkers, various

organic as well as inorganic molecules [13, 19-21]. However, there is no such report available on the employment of rGO modified MoS₂ multi-layered nanosheets-based matrix utilizing dual modes for electrochemical detection of NSE.

Therefore, in this work, we explored for the first-time employment of rGO modified MoS₂ multi-layered nanosheets-based matrix for electrochemical detection of NSE, a potential lung cancer biomarker using dual modes. **Scheme 4.1** shows layers of MoS₂ bridged by rGO which provides immobilization sites to biomolecules and also acts as conducting channels. Dual-mode output is realized by electrochemical impedance spectroscopy (EIS) and CV electrochemical techniques, which are used to assess the performance of the bioelectrode. The rGO/MoS₂-based bioelectrode is found to demonstrate a good sensitivity, a wide linear range of detection, a low incubation time for attachment of NSE, colossal reproducibility, and stability as well as specificity against various other endogenous interferents found in human serum. Since both the cut-off values for LD and ED lie well within the linear detection range of the fabricated bioelectrode, therefore it can be useful for early detection as well as detection of SCLC at advanced stages.



Scheme 4.1: Pictorial representation of layers of MoS₂ bridged by rGO

4.2 Experimental Details

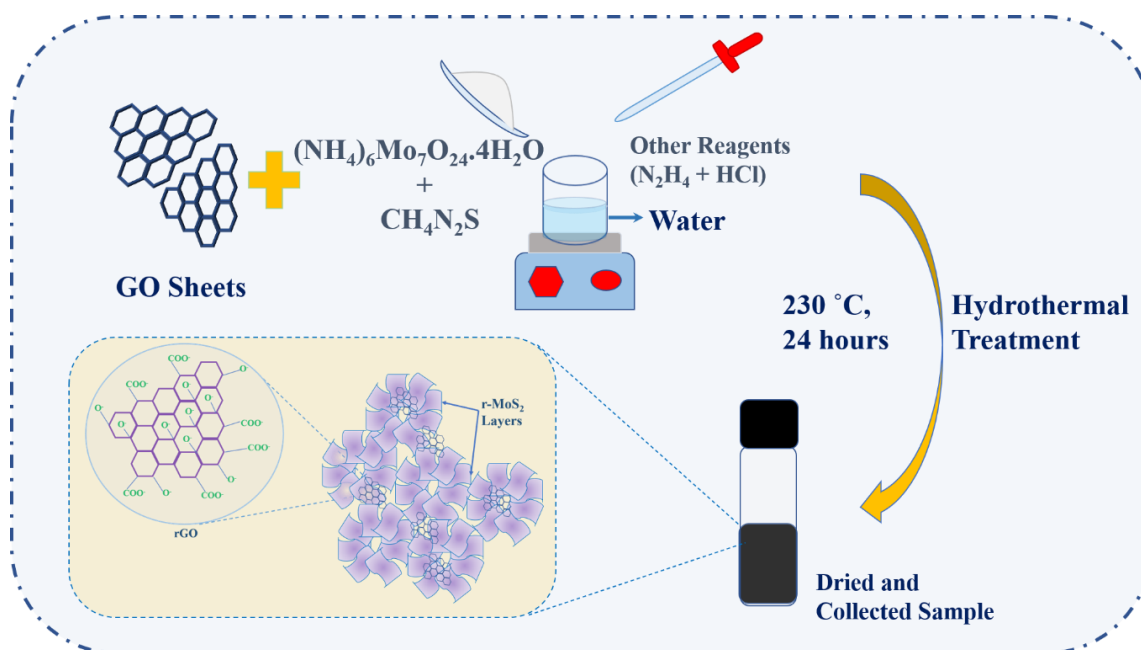
4.2.1 Materials and solutions

The monoclonal anti-NSE antibody, NSE, N-(3-Dimethylaminopropyl)-N'-ethyl carbodiimide hydrochloride (EDC), N-hydroxysuccinimide (NHS), bovine serum albumin (BSA), and ammonium molybdate tetrahydrate $[(\text{NH}_4)_6\text{Mo}_7\text{O}_{24}\cdot 4\text{H}_2\text{O}]$ are the products bought from Sigma-Aldrich. While thiourea ($\text{CH}_4\text{N}_2\text{S}$) is purchased from SRL. Some chemicals are procured from Thermo Fisher Scientific like hydrazine hydrate (HH), sodium chloride, and potassium Bromide. Concentrated hydrochloric acid is bought from RFCL limited. Other chemicals include acetonitrile, potassium hexacyanoferrate (II) trihydrate/ potassium ferrocyanide $[\text{K}_4\text{Fe}(\text{CN})_6\cdot 3\text{H}_2\text{O}]$, potassium hexacyanoferrate (III)/ potassium ferri cyanide $[\text{K}_3\text{Fe}(\text{CN})_6]$, di sodium hydrogen diphosphate dihydrate ($\text{Na}_2\text{HPO}_4\cdot 2\text{H}_2\text{O}$), and sodium dihydrogen phosphate dihydrate ($\text{NaH}_2\text{PO}_4\cdot 2\text{H}_2\text{O}$) are all purchased from Merck. A millipore milli-Q system (Bedford, MA, USA) is used to obtain milli-Q water for the preparation of the solutions which are used for various experiments. Potassium permanganate (KMnO_4) and orthophosphoric acid (H_3PO_4) are purchased from Fisher Scientific. Tris hydrochloride (Tris-HCl), magnesium sulfate (MgSO_4), and potassium chloride (KCl) which serves as a buffer for dilution of NSE are purchased from lobachemie and Thermo Fisher Scientific. The prepared buffers are kept at 4 °C after preparation and brought to room temperature (RT) before usage.

4.2.2 In-situ preparation of rGO modified MoS_2 multi-layered nanosheets

Graphene oxide (GO) powder is prepared by improved Hummer's method [22]. In brief, a 9:1 combination of H_2SO_4 and H_3PO_4 is added to 1 g of graphitic flakes. After 15 minutes, 12 g of KMnO_4 is added to the reaction mixture in small steps, and these reaction products are stirred at 50 °C for 12 hours. After 12 hours the reaction is quenched, by adding ice and 2 mL of hydrogen peroxide (H_2O_2). The suspension mixture is then washed with de-ionized (DI) water

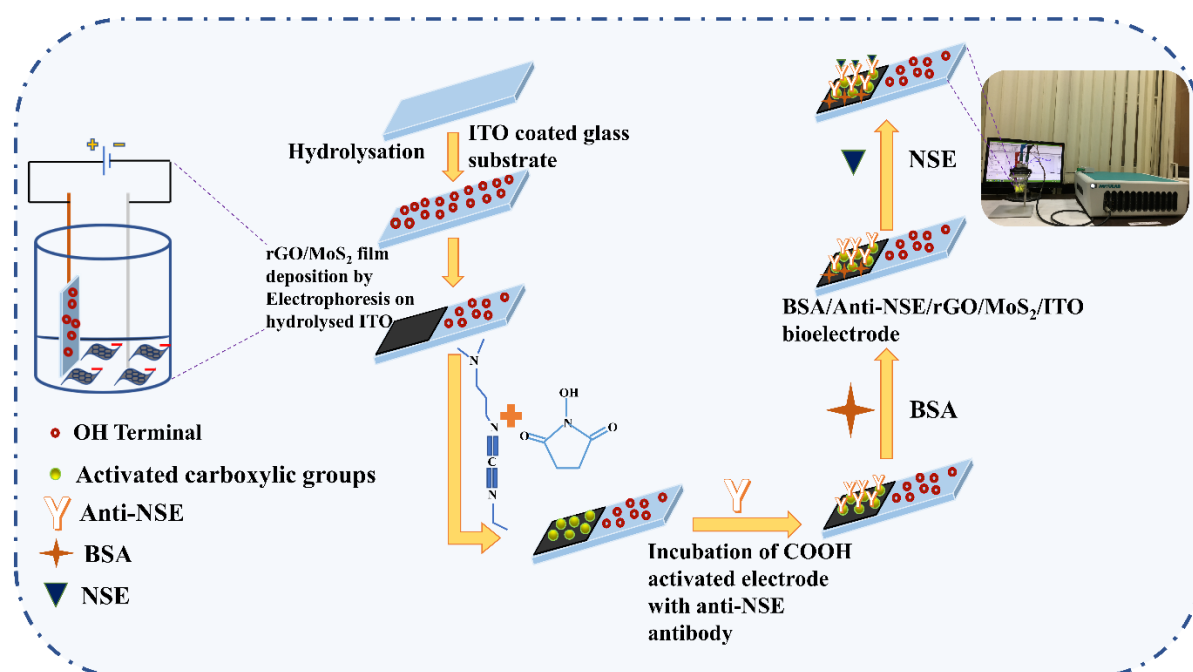
until its pH becomes 7. The obtained solid precipitate is filtered out and kept for drying in an oven at 90 °C, overnight. Then, 40 mg of as-obtained dried powder of GO is dispersed in 20 mL of DI water and kept for ultrasonication for 1 hour. After 1 hour this dispersion is added to the process of synthesis of MoS₂, reported elsewhere [23]. Briefly, appropriate amounts of ammonium molybdate tetrahydrate and thiourea are dissolved in DI water and 2 mL of HH is added to this reaction mixture. A pH value of 5 is maintained using dilute HCl and then dispersion of GO is added and this reaction mixture is left for stirring for 30 minutes. Then, the reaction mixture is put in a hydrothermal autoclave and maintained at 230 °C for 24 hours. Obtained black precipitates are washed using DI water and ethanol and are dried subsequently in a vacuum oven. The reduction of GO to rGO occurs during reaction [24] due to the release of H₂S gas by thiourea and henceforth, rGO is introduced into the MoS₂ matrix in an in-situ way. Also, the addition of HH aids the reduction of GO to rGO, along with the reduction of (NH₄)₂MoS₄ [25]. **Scheme 4.2** shows the preparation steps of rGO modified MoS₂ (rGO/MoS₂) multi-layered nanosheets in a pictorial way.



Scheme 4.2: Pictorial representation of the hydrothermal synthesis of rGO modified MoS₂ multi-layered nanosheets

4.2.3 Preparation of electrochemical immuno-sensing platform for detection of lung cancer biomarker

The electrochemical immuno-sensing platform is prepared by depositing rGO/MoS₂ on pre-hydrolyzed indium tin oxide (ITO) coated glass substrates by electrophoretic deposition (EPD) technique. Before deposition, a uniform dispersion (1 mg mL⁻¹) of rGO/MoS₂ is prepared in acetonitrile by ultrasonication. An assembly constituting platinum (Pt) as a counter electrode (CE) and copper (Cu) as a connector to attach the working electrode (WE) is taken. ITO is attached at Cu as our WE and these 2 electrodes are placed 1 cm apart in a glass cell. Prepared dispersion is poured into the glass cell and films are formed on a geometrical area of 1 × 1 cm² by applying an optimized potential of 40 V for 120 seconds. The prepared films are left for air-drying overnight.



Scheme 4.3: Step-by-step preparation of BSA/anti-NSE/rGO/MoS₂/ITO bioelectrode and detection of NSE

The as-prepared rGO/MoS₂/ITO electrode is loaded with an optimized concentration (25 µg mL⁻¹) of anti-NSE antibodies. Before immobilization of antibodies, freshly prepared

0.4 M EDC (coupling agent) and 0.1 M NHS (intermediate stabilizer) are aliquoted, which are used for activating COOH groups on the rGO/MoS₂ matrix. Thereafter, 20 μL of antibodies of NSE are uniformly spread onto rGO/MoS₂/ITO electrode, which is then incubated in a humid chamber for 5 hours. Following this period, the anti-NSE/rGO/MoS₂/ITO electrode is washed with plain PBS buffer (pH 7.4) to remove unbound anti-NSE antibodies. After this step, 10 μL of BSA is attached for 1 hour, to prepare the final bioelectrode by masking any remaining active sites. Prepared BSA/anti-NSE/rGO/MoS₂/ITO bioelectrode is kept at 4 °C for future use.

Scheme 4.3 shows the step-by-step preparation of the bioelectrode. The covalent bonding occurs by activation of the carboxyl group (-COOH) present on the matrix of rGO/MoS₂ by EDC and NHS and the formation of a strong carbamide (CO-NH) bond with the amino (NH₂) group of anti-NSE antibody.

4.3 Results and Discussion

4.3.1 Characterization of Samples and Instrumentation

Various characterization tools are used to confirm the formation of samples as well as to conduct biosensing studies. A Bruker D8 advance facility is used to record the X-ray diffraction (XRD) pattern of samples. A WITec Raman spectrometer producing a wavelength of 532 nm is used to record Raman spectra. Scanning electron microscopy (SEM) and elemental analysis is done using Jeol Japan mode and Zeiss EVO 18. The Fourier transform infrared (FTIR) spectroscopy measurements are done using Perkin Elmer spectrum two to identify the functional groups present in samples. A Perkin Elmer 4000 thermogravimetric analyzer is used to study the thermal stability of prepared samples. WITec alpha 300 RA is used for atomic force microscopy (AFM) to study various steps of fabrication of bioelectrode. A Metrohm potentiostat/galvanostat (Multi Autolab M204) along with NOVA software is used for recording all the electrochemical measurements.

4.3.2 Results of characterization studies of the samples

4.3.2.1 Structural study of synthesized nanostructures using XRD

Fig. 4.1 shows the XRD pattern of synthesized graphene oxide (GO) and rGO/MoS₂. XRD pattern of GO shows a diffraction peak centered at 12.73° which confirms the successful formation of GO by improved Hummer's method [26]. The peak at 12.73° corresponds to a spacing of 0.69 nm in between the layers, which is large in comparison to graphite and has an interlayer spacing of 0.34 nm ($2\theta = 26.57^\circ$). An increase in interlayer spacing in GO indicates the presence of oxygen-containing functional groups like ketonic and enolic groups [27, 28]. Using, the interlayer spacing and the crystallite size obtained from XRD data, the estimated number of layers in GO is found to be ~7. The disappearance of the peak around 12.73° in rGO/MoS₂ indicates the reduction of GO to rGO [29].

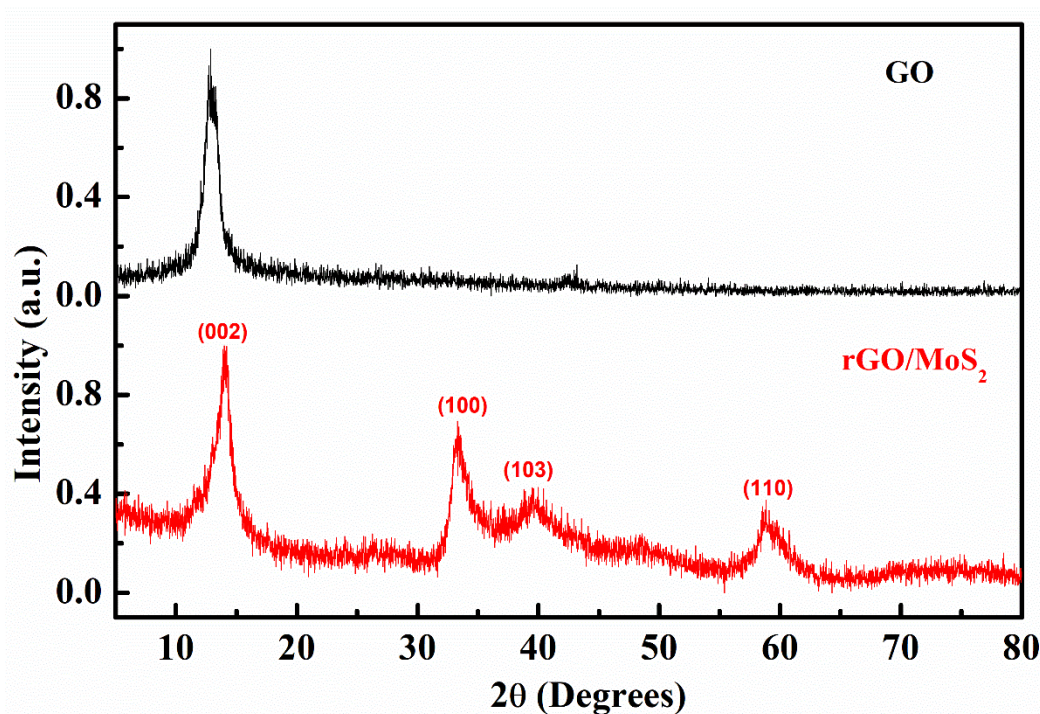


Fig. 4.1: XRD pattern of GO and rGO modified MoS₂

Peaks observed in the XRD pattern of rGO/MoS₂ at 13.91°, 33.27°, 39.62°, and 58.57° are found to be matching with JCPDS card no. 37-1492 of MoS₂. The absence of any additional peaks indicates the incorporation of only rGO into MoS₂, without any impurities being formed.

A peak around 26.6° corresponding to rGO could not be observed, which indicates that rGO is uniformly dispersed into layers of MoS₂ [30, 31] without altering the crystal structure of MoS₂ [26].

4.3.2.2 Confirmation of layered structure using Raman spectroscopy

The Raman spectra of GO and rGO modified MoS₂ are shown in Fig. 4.2. Raman spectrum of GO shows the D band at 1343.69 cm^{-1} and the G band at 1583.12 cm^{-1} . The I_D/I_G value, which corresponds to the ratio of the intensity of the D and G peaks, is calculated to be 0.99. The D peak corresponds to the defect peak which arises due to intervalley scattering, or disorder, while the G peaks arise from in-plane stretching of the C-C bonds present in graphitic structure [30, 32]. Besides, the D and G bands, two overtones are also observed corresponding to 2D and D+G peaks at 2697.25 cm^{-1} and 2895.71 cm^{-1} respectively.

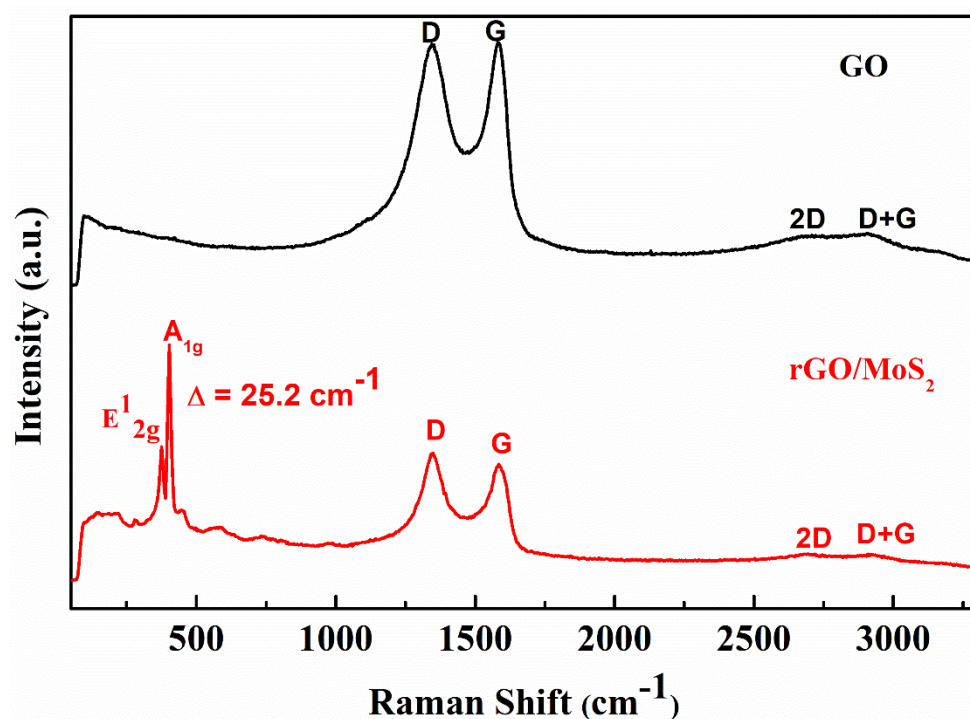


Fig. 4.2: Raman spectra of GO and rGO/MoS₂

rGO/MoS₂ shows two peaks corresponding to E^1_{2g} and A^1_{1g} modes of MoS₂ at 380.77 cm^{-1} and 405.97 cm^{-1} respectively. The separation between E^1_{2g} and A^1_{1g} modes can be used to

identify the number of layers in MoS₂ [23]. A separation of 25.2 cm⁻¹ in our case pertains to multi-layers of MoS₂ in rGO/MoS₂. In addition to these peaks, the D and G bands corresponding to rGO were also observed at 1348.92 cm⁻¹ and 1584.16 cm⁻¹. Also, the I_D/I_G value is found to be ~1.03 in rGO/MoS₂. An increase in the value of I_D/I_G for rGO/MoS₂ in comparison to GO indicates the creation of new graphitic domains which are smaller in size in comparison to those present in GO before reduction [33]. Also, an increase in I_D/I_G value from 0.99 to 1.03 implies a successful reduction of GO in rGO/MoS₂ [34].

4.3.2.3 Identification of functional groups using FTIR

The FTIR spectra of GO and rGO modified MoS₂ are shown in Fig. 4.3. Absorption peaks which are seen in the case of GO are assigned to OH stretching (3436 cm⁻¹), C=O carbonyl (1705 cm⁻¹), aromatic C=C (1624 cm⁻¹), -C-O carbonyl (1366 cm⁻¹), epoxy -C-O (1262 cm⁻¹), -C-OH- (1235 cm⁻¹) and C-O alkoxy (1098 cm⁻¹) [35, 36].

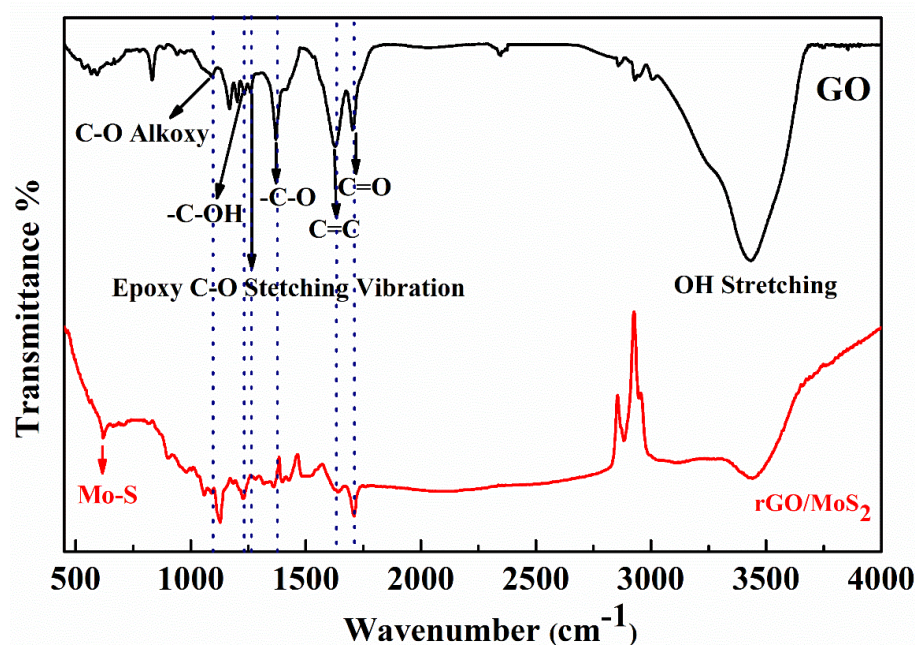


Fig. 4.3: FTIR spectra of GO and rGO/MoS₂

In the FTIR spectrum of rGO/MoS₂, a peak corresponding to Mo-S vibrations is observed at 619 cm⁻¹ [37]. A decrease in the peak intensity of all the oxygen-containing

functional groups as well as the disappearance of some groups like epoxy and alkoxy -C-O indicates a successful reduction of GO into rGO [38, 39] in rGO/MoS₂. Simultaneously the presence of all the other functional groups also shows successful grafting of rGO into multilayers of MoS₂ [40, 41].

4.3.2.4 Morphological study of modified nanostructures using SEM

Fig. 4.4 shows the morphology obtained for GO as well as rGO modified MoS₂.

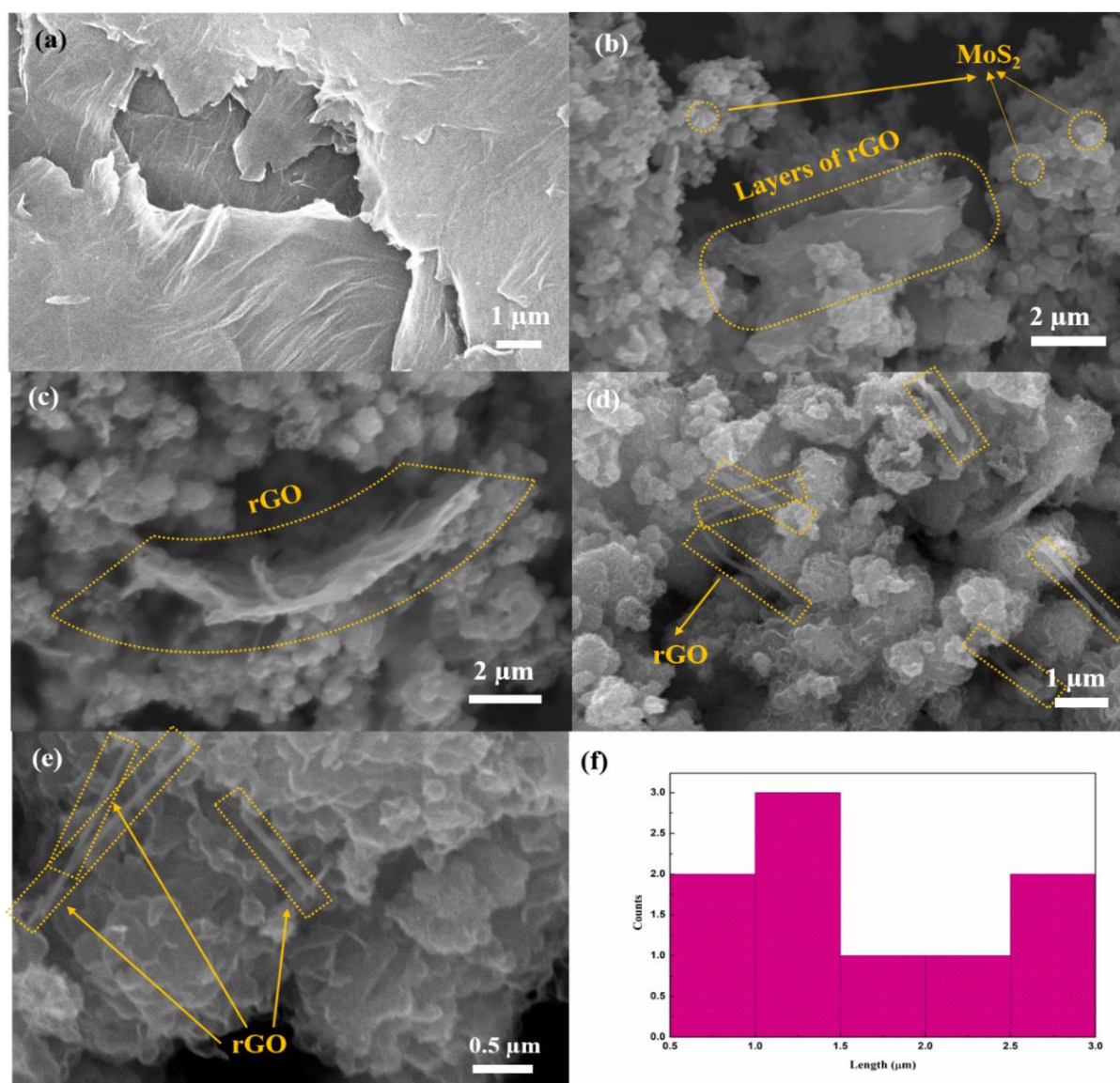


Fig. 4.4: (a) SEM image of GO and (b, c, d, e) SEM images of rGO modified MoS₂ multilayered nanosheets (f) Histogram of length distribution of rGO in rGO/MoS₂

Fig. 4.4(a) shows large, crinkled sheets pertaining to GO, with large lateral length and surface area. At low magnification (**Fig. 4.4(b) and 4.4(c)**), nano units comprising layers of rGO, as well as various irregularly shaped flowers of MoS₂, can be observed. Further, at higher magnifications (**Fig. 4.4(d) and Fig. 4.4(e)**) flowers of MoS₂ can be seen consisting of numerous layers and nano rod-like structures of rGO are visible. rGO layers have a natural tendency to scroll and curl up, because of the thermodynamic stability which accompanies bending [42, 43]. The average length for rGO nanorods is calculated to be 1.66 μm by plotting a histogram (**Fig. 4.4(f)**). This type of interconnected bridging network formed between rGO and MoS₂ can provide conduction pathways for rapid transportation of electrons and can be greatly beneficial for the formation of electrochemical sensors. The consonance of the multi-layered nature of both GO and MoS₂ as affirmed by XRD and Raman, probably lead to the unstinted grafting of rGO into the MoS₂ matrix. This also indicates the synergetic nature of both materials.

4.3.2.5 Elemental analysis using EDX

Elemental analysis of GO and rGO/MoS₂ is done using EDX on different areas of the sample. **Fig. 4.5(a), 4.5(b), and 4.5(c)** show some of the selected areas, and **Table 4.1** shows the atomic percentages of elements present in GO and rGO/MoS₂.

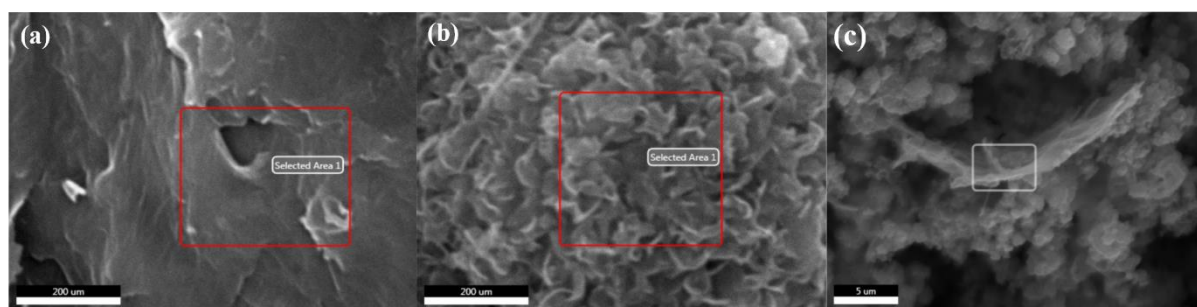


Fig. 4.5: Selected area of (a) GO and (b, c) rGO modified MoS₂ multi-layered nanosheets for elemental analysis using EDX

EDX data shows the presence of carbon (C) and oxygen (O) in both GO and rGO/MoS₂ along with molybdenum (Mo) and sulfur (S) content in rGO/MoS₂. The lower oxygen content (20.60%) in rGO/MoS₂ in comparison to GO (31.68%) indicates the reduction of GO to rGO [44].

Table 4.1: Atomic percentages for different elements present in GO and rGO modified MoS₂ multi-layered nanosheets

Element	GO (Atomic %)	rGO/MoS ₂ (Atomic %)
C	66.95	45.40
O	31.68	20.60
Mo	-	16.585
S	-	16.01

4.3.2.6 Thermal Analysis using TGA

Thermal stability of as-prepared samples is determined by TGA in presence of air with a heating rate of 10 °C in the temperature range from 10 °C to 900 °C (shown in **Fig. 4.6**). The thermal instability of GO is quite evident from **Fig. 4.6** which shows a huge weight loss at 200 °C. This high weight loss could be due to the thermal decomposition of oxygen-containing functional groups present in GO [33, 35]. On the other hand, it is observed that MoS₂ and rGO/MoS₂ are found to have better thermal stabilities in comparison to GO. The TGA of MoS₂ shows two steps of weight loss, (i) below 100 °C and (ii) between 300 °C to 550 °C, indicating a weight loss of 46%. rGO/MoS₂ is found to exhibit weight loss in the range of 320 °C to 400 °C, after which the sample is found to be stable (with a weight loss of only 17%). Due to the decrease in the number of oxygen-containing functional groups in rGO present in rGO/MoS₂, a sudden weight loss of around 200 °C is not observed; rather the modified matrix is rendered

the highest thermal stability among all three samples. All three samples undergo a weight loss below 100 °C due to the evaporation of adsorbed water molecules.

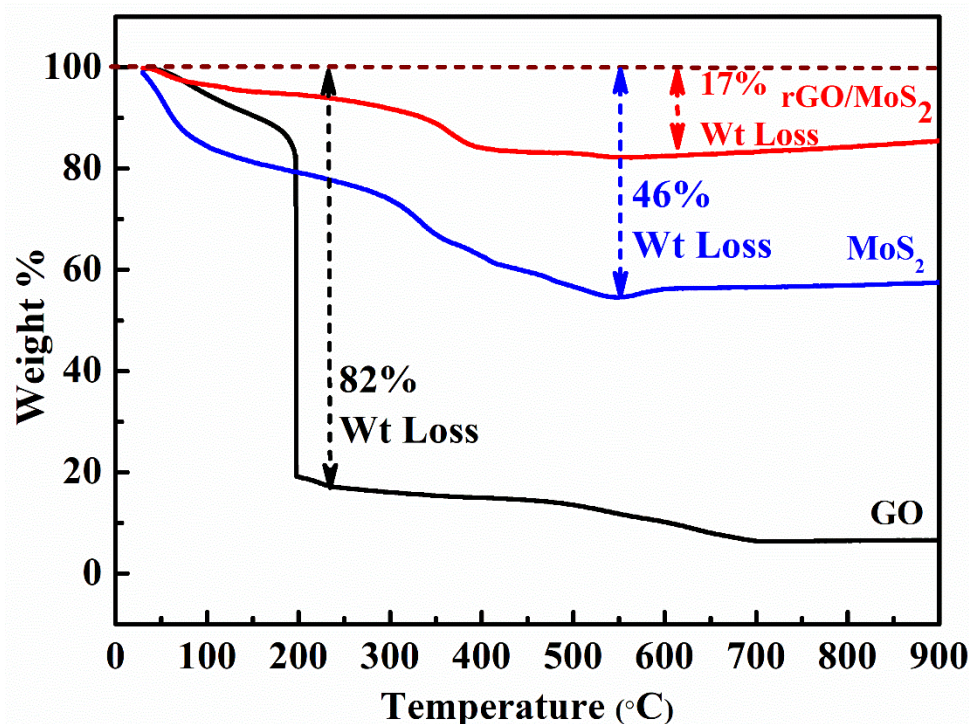


Fig. 4.6: TGA curves of GO, MoS₂, and rGO/MoS₂

4.3.2.7 Analysis of various steps of preparation of bioelectrode using AFM

To assess the topography of the final bioelectrode, AFM images are recorded for various stages of preparation of the bioelectrode. **Fig. 4.7** shows the topographical image of (a) rGO/MoS₂/ITO (b) anti-NSE/rGO/MoS₂/ITO and (c) BSA/anti-NSE/rGO/MoS₂/ITO. The topography varies from large clusters in **Fig. 4.7(a)** to small globules in **Fig. 4.7(b)** to larger globules as observed in **Fig. 4.7(c)**. The anti-NSE/rGO/MoS₂/ITO electrode is found to have a root mean square (RMS) roughness value of 0.80 nm, due to the smooth distribution of globular antibodies onto rGO/MoS₂/ITO, which itself has an RMS roughness value of 1.01 nm. The BSA/anti-NSE/rGO/MoS₂/ITO is found to have an RMS roughness value of 0.87 nm. An increase in the value of RMS roughness of the bioelectrode in comparison to anti-NSE/

rGO/MoS₂/ITO could be ascribed to the attachment of BSA to block the non-specific binding sites. The observable change in topography along with the RMS value of surface roughness confirms the modification at each step of the preparation of the bioelectrode.

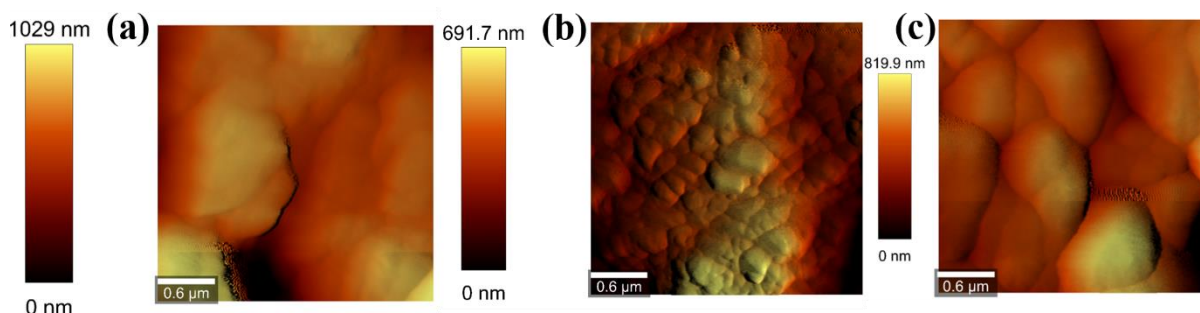


Fig. 4.7: Topographical images taken using AFM of (a) rGO/MoS₂/ITO (b) anti-NSE/rGO/MoS₂/ITO (c) BSA/anti-NSE/rGO/MoS₂/ITO electrodes

4.3.3 Electrochemical studies

Investigation of the electrochemical performance of the as-prepared biosensor is done using various electrochemical studies. All the EIS experiments are performed at a biasing potential of 0.01 V and in the frequency range of 0.1 Hz to 100 kHz. The optimization of antibody concentration, antigen incubation time, stability, and sensitivity study of bioelectrode is done by CV in a potential bracket of -0.4 V to 1.2 V at a 50 mV s⁻¹ scan rate. The EIS and CV studies are done in 0.1 M phosphate buffer saline (PBS, pH 7.4) solution containing a 5 mM redox probe [Fe(CN)₆]^{3-/4-}.

4.3.3.1 Optimization of biosensing parameters

The concentration of antibodies to be attached to the rGO/MoS₂ matrix is optimized by varying concentrations of anti-NSE antibodies from 10 to 100 μg mL⁻¹. CV studies [Fig. 4.8(a)] are carried out and the peak current is found to decrease with the increase in concentration up to

25 $\mu\text{g mL}^{-1}$. After 25 $\mu\text{g mL}^{-1}$ a small increase in the value of current is observed for concentrations 50 and 100 $\mu\text{g mL}^{-1}$. The minimum value of current for a concentration of 25 $\mu\text{g mL}^{-1}$ implies maximum attachment of antibodies, while for higher concentrations (50 and 100 $\mu\text{g mL}^{-1}$) an increase in current could be due to overcrowding of antibodies resulting in lesser attachment to the surface. Thus, 25 $\mu\text{g mL}^{-1}$ is finalized for attachment of anti-NSE onto the rGO/MoS₂/ITO electrode. To optimize the time of incubation of NSE, 5 ng mL⁻¹ of NSE is attached to the bioelectrode (BSA/Anti-NSE/rGO/MoS₂/ITO). The incubation time of NSE is varied from 5 minutes to 30 minutes. The CV study is conducted and the peak current varies with the variation of incubation time plotted in [Fig. 4.8(b)]. It can be seen that, with the increase in time from 5 to 15 minutes, the current is found to be decreasing. However, after 15 minutes the current becomes nearly constant indicating that the maximum attachment of NSE onto the BSA/Anti-NSE/rGO/MoS₂/ITO has occurred. Henceforth, 15 minutes is finalized as the time for incubation of NSE on the bioelectrode.

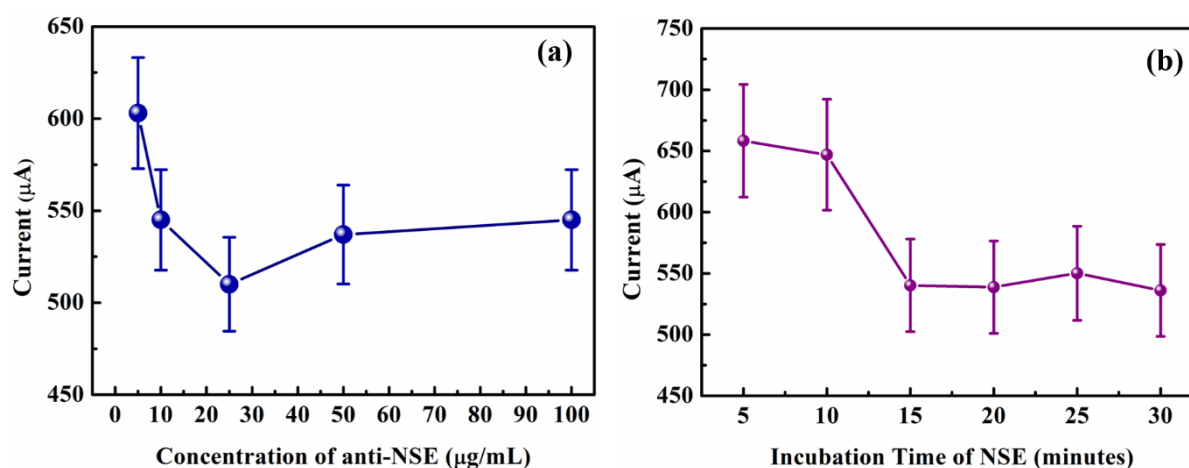


Fig. 4.8: (a) Variation of CV peak current with the concentration of antibody attached on rGO/MoS₂/ITO electrode (b) Variation of peak current with the incubation time of antigen NSE over BSA/Anti-NSE/rGO/MoS₂/ITO.

4.3.3.2 Electrochemical characterization and stability study of the modified electrode

EIS technique gives the Nyquist plot between the imaginary part versus the real part of the impedance and the diameter of the semicircle thus obtained gives the value of charge transfer resistance (R_{ct}). To confirm the modification at various steps of preparation of the bioelectrode, EIS measurements are done at each step and the attachment is readily probed by varying Nyquist plots. **Fig. 4.9(a)** shows EIS curves of rGO/MoS₂/ITO, anti-NSE/rGO/MoS₂/ITO and BSA/Anti-NSE/rGO/MoS₂/ITO electrodes. The corresponding R_{ct} values are found to be 211.69 Ω , 125.38 Ω , and 147.75 Ω for rGO/MoS₂/ITO, anti-NSE/rGO/MoS₂/ITO, and BSA/anti-NSE/rGO/MoS₂/ITO electrodes respectively. The variation in values of R_{ct} at different steps of modification confirms the attachment of moieties at the electrode surface.

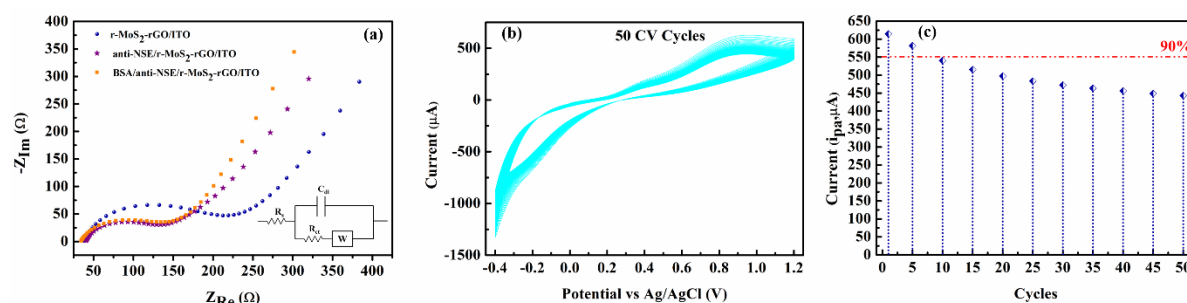


Fig. 4.9: (a) Electrochemical response of rGO/MoS₂/ITO, anti-NSE/rGO/MoS₂/ITO and BSA/Anti-NSE/rGO/MoS₂/ITO electrodes, (b) Stability study of BSA/anti-NSE/rGO/MoS₂/ITO bioelectrode with 50 continuous CV cycles at scan rate 50 mV s⁻¹ (c) Plot of anodic peak current (i_{pa}) with respect to CV cycles.

The R_{ct} value is found to be lowest for the anti-NSE/rGO/MoS₂/ITO electrode, which may be due to the orientation of antibodies on the electrodes in such a way that the transfer of electrons between the redox probe $[\text{Fe}(\text{CN})_6]^{3-/4-}$ and the electrode is facilitated [45]. The value of R_{ct} for the BSA/anti-NSE/rGO/MoS₂/ITO electrode increases when compared to that of the anti-NSE/rGO/MoS₂/ITO electrode because of the insulating nature of the BSA protein molecule [46]. However the impedance offered to the flow of electrons is still balanced by the

formation of an iron-binding complex between BSA and Fe present in the redox probe, which leads to the formation of iron chelates facilitating the easy flow of electrons [47]. rGO/MoS₂/ITO electrode is found to exhibit maximum resistance to the flow of electrons which might be due to the presence of negatively charged carboxyl groups (COO⁻), on the rGO/MoS₂ matrix which repels the flow of electrons from the electrolyte to the electrode.

Demonstration of stability of the bioelectrode is done by scanning the BSA/anti-NSE/rGO/MoS₂/ITO electrode for 50 continuous CV cycles (**Fig. 4.9(b)**). 94% and 88% of the initial current is still retained after the 5th and 10th cycle respectively (**Fig. 4.9(c)**). Thus, the bioelectrode demonstrates acceptable stability till the 10th cycle. This essentially unchanged behavior of CV indicates that antibodies are stably immobilized onto the bioelectrode for 10 cycles. To acquire a better understanding of the electrochemical performance of the bioelectrode, a scan rate-dependent study is conducted by varying the scan rate from 10 to 100 mV s⁻¹ (**Fig. 4.10**). The anodic peak current (*i*_{pa}) is found to be varying linearly with the under root scan rate, showing that the process is diffusion-controlled [48](**Fig. 4.10, inset**). The equation of the linearly fitted curve is given by **equation 4.1**

$$i_{pa(\text{BSA/anti-NSE/rGO/MoS}_2\text{/ITO})} = 195.29 \mu\text{A} + \left[30.55 \frac{\mu\text{A}}{\sqrt{\frac{\text{mV}}{\text{s}}}} \times \sqrt{\text{Scan rate} \frac{\text{mV}}{\text{s}}} \right] \quad (4.1)$$

$$R^2 = 0.997$$

Various electrochemical parameters are also calculated like electroactive surface area (*A*_e), and HET constant (*K*_o). The value of electroactive surface area (*A*_e) is calculated by using the slope of **equation 4.1** and Randles Sevcik equation (4.2) [23], [49]:

$$i_p = 2.69 \times 10^5 n^{3/2} A_e C \sqrt{D_o v} \quad (4.2)$$

here, *i*_p is the peak current, *n* denotes the number of transferred electrons (which is equal to 1 for Ferro/Ferri), *C* denotes the concentration of redox-active species (5 mM), *D*_o is the diffusion coefficient (0.667 × 10⁻⁵ cm²/s) [50] and *v* is the scan rate. Hence, the electroactive surface

area is determined to be 27.83 mm^2 . Correspondingly, the HET constant (K_o) is determined by the equation (4.3) mentioned below [23]

$$K_o = \frac{RT}{n^2 F^2 A_e R_{ct} C} \quad (4.3)$$

Where, F is Faraday's constant ($96,485 \text{ C/mol}$), R is the universal gas constant (8.314 J/K/mol) and all the other parameters are the same as equation (3). And thus, using equation (4), the value of K_o is determined to be $1.29 \times 10^{-3} \text{ cm s}^{-1}$ for BSA/anti-NSE/rGO/MoS₂/ITO bioelectrode.

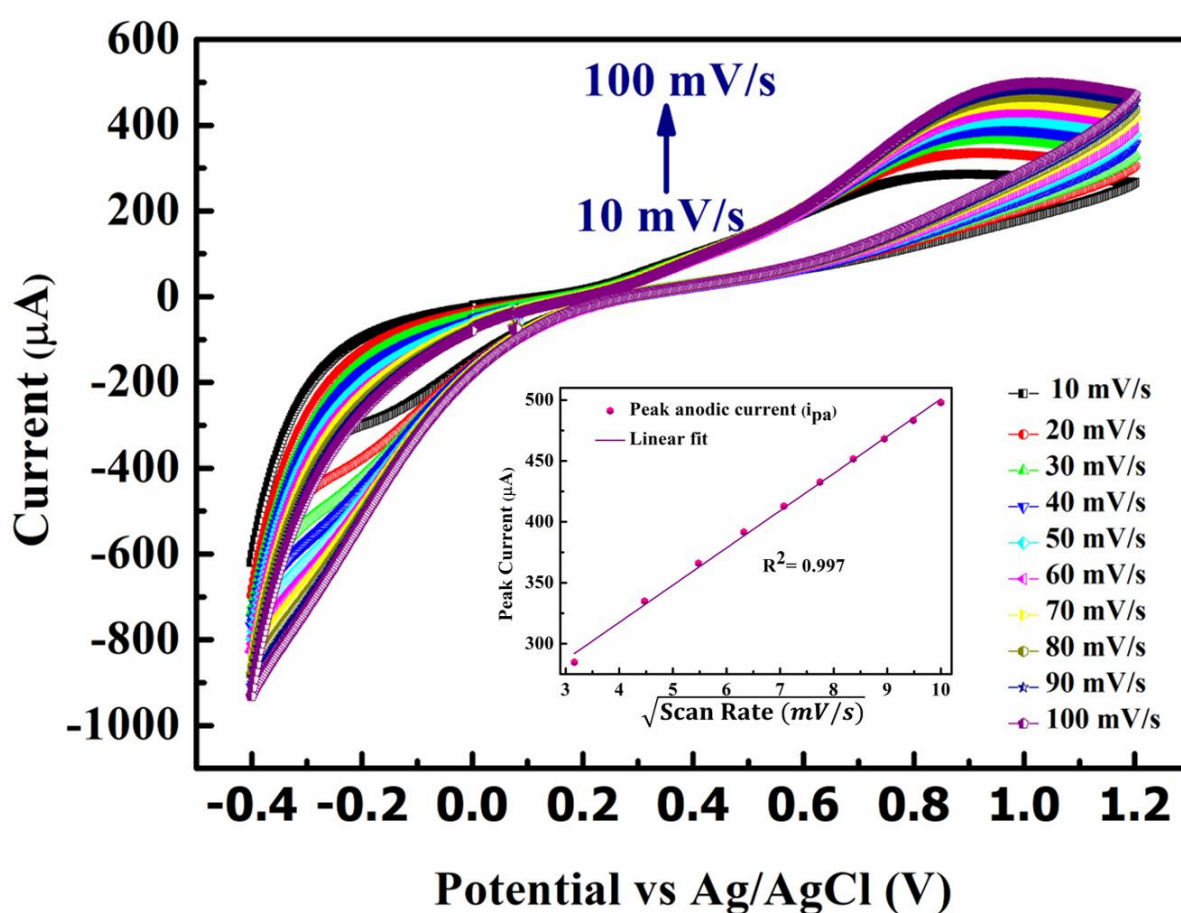


Fig. 4.10: Scan rate dependent plot of BSA/anti-NSE/rGO/MoS₂/ITO bioelectrode, inset shows the variation of i_{pa} of BSA/anti-NSE/rGO/MoS₂/ITO bioelectrode with under root of scan rate.

Interestingly, the BSA/anti-NSE/rGO/MoS₂/ITO bioelectrode is found to exhibit better electrochemical parameters in comparison to various other electrochemical biosensors which have been reported for detection of other biomarkers (**Table 4.2**). The superior behavior as shown by our platform may be attributed to the synergistic nature and interconnected network formed between MoS₂ and bridging rGO, which imparts more conduction pathways.

Table 4.2: Electrochemical parameters calculated for the prepared bioelectrode and its comparison to other electrochemical sensors, reported in the literature.

Platform	Biomarker Detected	Electroactive Surface Area (A_e, in mm²)	HET Constant (K₀, in cm s⁻¹)	Reference
EA/anti-cTnI/APTES/WO ₃ NRs/ITO	cTnI	-	4.47×10^{-5}	[51]
BSA/anti-VD/Fe ₃ O ₄ -PANnFs/ITO	Vitamin D ₃	3.8	1.55×10^{-6}	[52]
BSA/anti-CYFRA-21-1/APTES/nYZR/ITO	CYFRA-21-1	2.58	3.77×10^{-7}	[53]
BSA/anti-NSE/rGO/MoS₂/ITO	NSE	27.83	1.29×10^{-3}	Present Work

EA- ethanolamine, cTnI – cardiac troponin, APTES – (3-aminopropyl)triethoxysilane, WO₃-tungsten trioxide, NRs - nanorods, VD – Vitamin D, Fe₃O₄ – iron oxide, PANnFs- polyacrylonitrile nanofibers, nYZR – yttria-doped zirconia-reduced graphene oxide nanocomposite

4.3.3.3 Analytical performance of bioelectrode towards detection of NSE

The analytical performance of the prepared bioelectrode is recorded using EIS and CV techniques. The concentration of NSE antigen is varied from 0.01 ng mL⁻¹ to 200 ng mL⁻¹, as shown in **Fig. 4.11(a)**. Before the incubation of NSE, the bioelectrode is washed using plain PBS (pH 7.4), to remove any unbound BSA on the surface of the bioelectrode. This is followed by incubation of antigen onto the bioelectrode for an optimized time duration of 15 minutes. This gives sufficient time to antigen for interaction with antibodies. The impedance is found to be increasing with the increase in the concentration of the analyte. This occurs due to the immuno-reaction between antibody and antigen, leading to the formation of an immunocomplex. This leads to a decrease in the redox-active surface area and deaccelerates the transfer of electrons from the redox probe [Fe(CN)₆]^{3-/4-} to the electrode surface. The change in impedance can be directly correlated to the change in concentration of NSE.

Hence a calibration curve is plotted to determine the concentration of NSE antigen (shown in **Fig. 4.11(b)**). The calibration curve is linearly fitted using the following **equation 4.4** with the regression coefficient R² value equal to 0.96

$$R_{ct} = 187.58 \Omega + 3.80 \frac{\Omega \text{mL}}{\text{ng}} \times \left[\text{Concentration of NSE} \left(\frac{\text{ng}}{\text{mL}} \right) \right] \quad (4.4)$$

The sensor is found to exhibit a linear variation in the range of 1- 200 ng mL⁻¹. The sensitivity of the biosensor is determined using the slope of the calibration curve and it is found to be 3.80 Ω ng⁻¹ mL cm⁻². The lowest value which can be detected by using the EIS technique is 1 ng mL⁻¹.

Further, an illustration of the reliability of the as-prepared bioelectrode is done by studying its response to the variation of NSE concentration using the CV technique [**Fig. 4.11(c)**]. The bioelectrode displays a linear response in the range of 0.1 to 100 ng mL⁻¹, with a sensitivity of 2.32 μA ng⁻¹ mL cm⁻² with CV (**Fig. 4.11(d)**). The CV response calibration curve

is linearly fitted using the following **equation 4.5** with the regression coefficient R^2 value equal to 0.97

$$i (\mu A) = 636.67 \mu A + 2.32 \frac{\mu A mL}{ng} \times \left[\text{Concentration of NSE} \left(\frac{ng}{mL} \right) \right] \quad (4.5)$$

Oxygenated functional groups on rGO/MoS₂ assist the covalent immobilization of biological entities onto the matrix. A large surface area along with the availability of oxygenated functional groups empowers the bioelectrode to exhibit a wide detection range and manifest a good sensitivity.

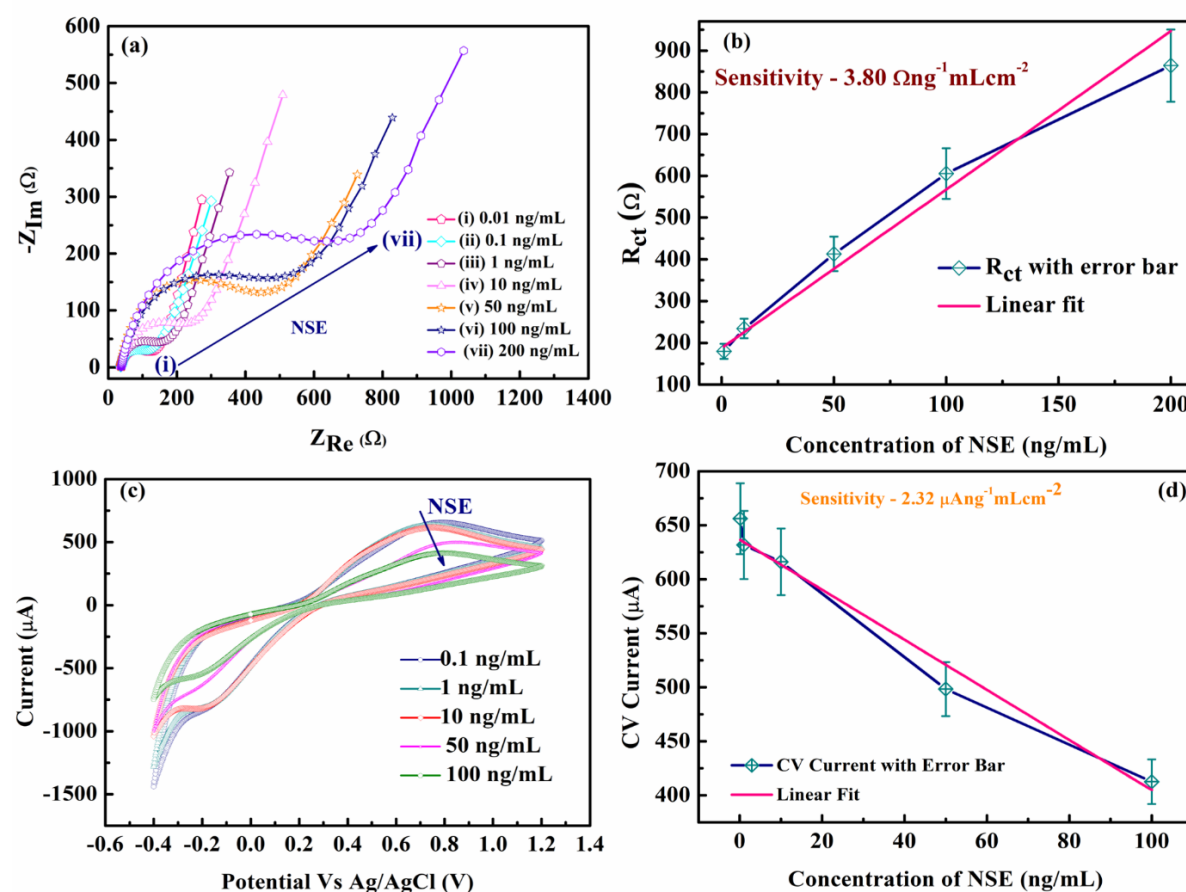


Fig. 4.11 Response of BSA/anti-NSE/rGO/MoS₂/ITO bioelectrode as a function of the concentration of NSE (a) using EIS (c) using CV; Calibration plot BSA/anti-NSE/rGO/MoS₂/ITO bioelectrode (b) using EIS (d) using CV

4.3.3.4 Reproducibility check of the bioelectrode

To check the reproducibility of the prepared BSA/anti-NSE/rGO/MoS₂/ITO bioelectrode, EIS and CV response is recorded for 4 electrodes prepared under similar conditions [Fig. 4.12]. All 4 bioelectrodes are tested for 10 ng mL⁻¹ of NSE antigen. The relative standard deviation (RSD) value is found to be below 5%, which is in an acceptable range, indicating that the sensor is reproducible. The covalent binding of biomolecules onto the bioelectrode attributes to the reproducibility of the sensor.

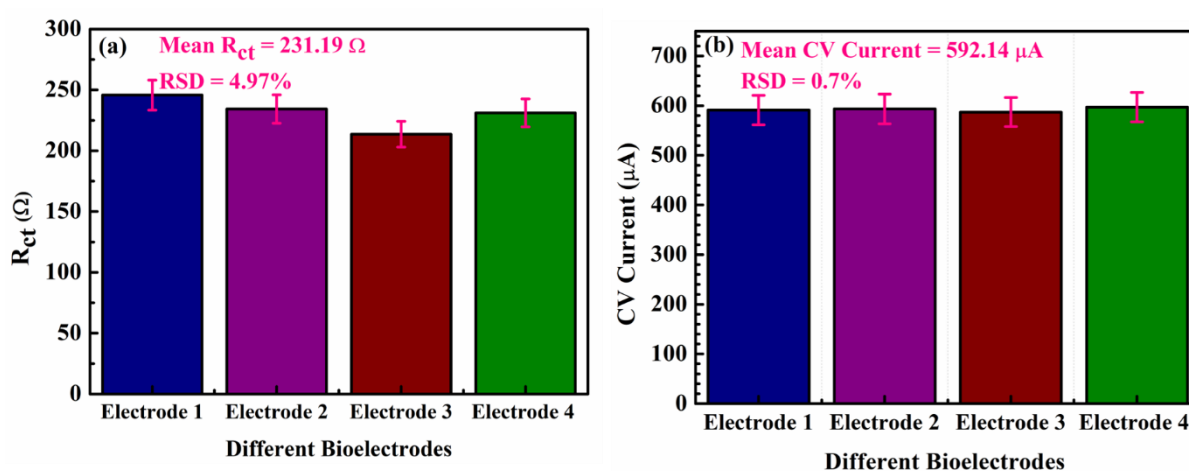


Fig. 4.12: Reproducibility check of BSA/anti-NSE/rGO/MoS₂/ITO bioelectrode by preparing 4 different bioelectrodes under similar conditions using dual modes (a) EIS (b) CV

4.3.3.5 Specificity study of the bioelectrode

The specificity of the prepared bioelectrode, BSA/anti-NSE/rGO/MoS₂/ITO is investigated against different interferents which are also present in human serum, for instance (cTnI, 0.1 ng mL⁻¹), Myoglobin (mB, 85 ng mL⁻¹), C-reactive protein (CRP, 10 μ g mL⁻¹), Urea (0.1 mg mL⁻¹), Sodium Chloride (NaCl, 6.2 mg mL⁻¹) etc. The concentrations are taken in physiological ranges of these interferents in the serum of a human being. The bar graph in Fig. 4.13 shows the R_{ct} and CV current values of BSA/anti-NSE/rGO/MoS₂/ITO when incubated with different interferents for 15 minutes. The negligible change in R_{ct} and CV current of the bioelectrode

with the interferents shows insignificant cross-linking between BSA/anti-NSE/rGO/MoS₂/ITO bioelectrode and interferents. Correspondingly, a huge difference in R_{ct} (**Fig. 4.13(a)**) and CV current (**Fig. 4.13(b)**) value for NSE shows the interaction between NSE and anti-NSE antibodies, which shows the specificity of the bioelectrode towards NSE.

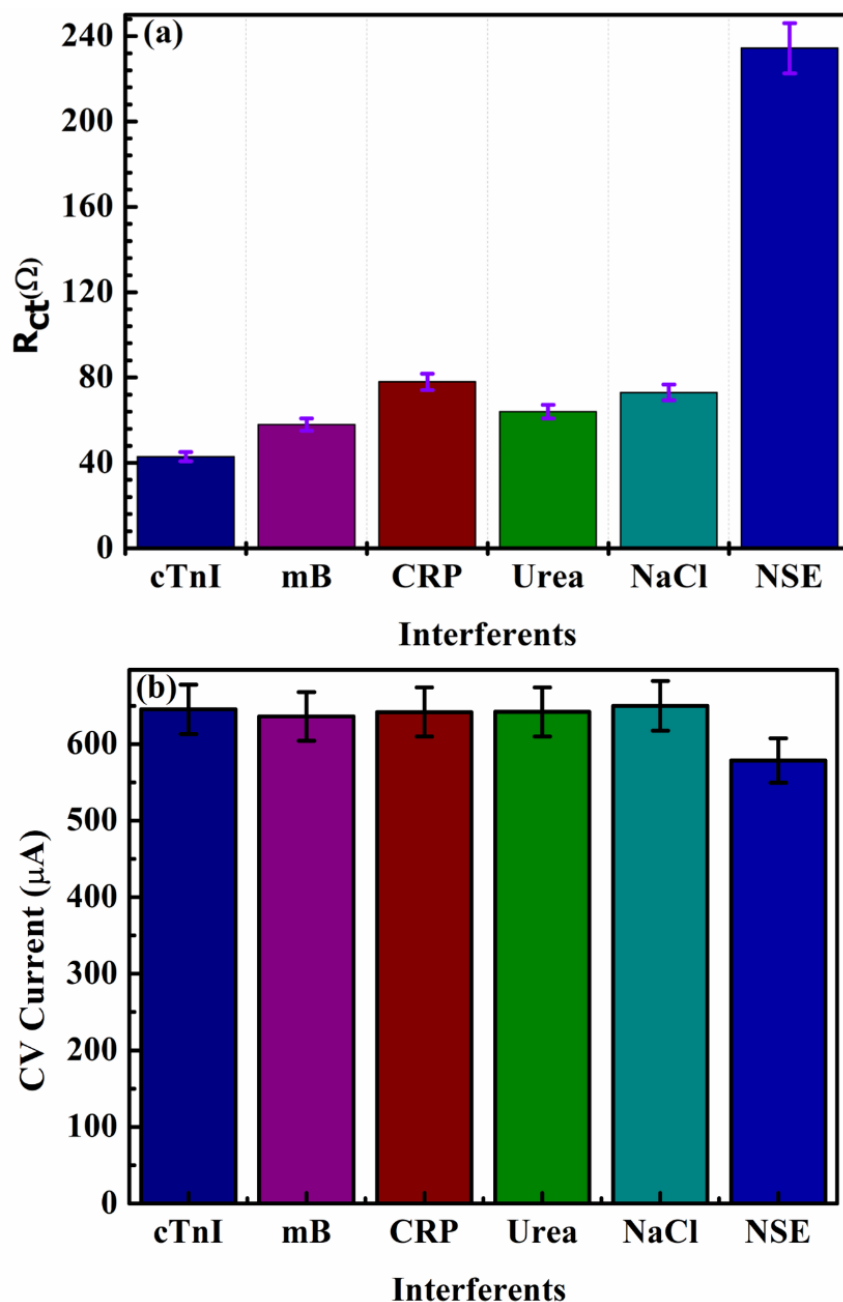


Fig. 4.13: Specificity Study of BSA/Anti-NSE/rGO/MoS₂/ITO bioelectrode against other interferents present in human serum using dual modes (a) EIS (b) CV.

Some previous reports along with the biosensing parameters are reported in **Table 4.3**. We found that our bioelectrode detected NSE using 2 electrochemical techniques and is found to exhibit less incubation time for attachment of NSE as well as a wide linear detection range in comparison to other bioelectrodes reported in the literature.

Table 4.3: Some previous works reported in the literature for the detection of NSE.

Platform	The technique used for detection	Time of Incubation of NSE on the as-prepared sensor	Range of linear detection	Sensitivity	Reference
anti-NSE/Au–Gra/NiHCFNPs/AuNCs/GCE	CV	30 minutes	0.001 to 100 ng/mL	-	[4]
BSA/anti-NSE/AuPd-MWCNT/CS-Fc/GCE	Square wave voltammetry (SWV)	50 minutes	0.001 to 100 ng/mL	7.22 μA $(\log_{10} C_{\text{NSE}})^{-1}$	[9]
BSA/NSE-Ab/3DM rGO/PANI/Au	Differential pulse voltammetry (DPV)	40 minutes	0.5 pg/mL to 100 ng/mL	91.40 μA $\text{pg}^{-1}\text{cm}^{-2}$	[10]
BSA/anti-NSE/polyresor	SWV	50 minutes	0.01-100 ng/mL	14.37 μA $(\log C_{\text{NSE}})^{-1}$	[11]

cinol- Au/Pt/GCE					
PtNF- pAb/NSE/mAb -CD-GCE	CV	-	0.05-150 ng/mL	-	[12]
BSA/anti- NSE/rGO/Mo S₂/ITO	EIS and CV	15 minutes	1 to 200 ng mL⁻¹ (EIS), 0.1 to 100 ng/mL (CV)	3.80 Ω ng⁻¹ mL cm⁻² (EIS), 2.32 μA ng⁻¹ mL cm⁻² (CV)	Present work

Au- Gold, Gra- graphene, NiHCFNPs- nickel hexacyanoferrate nanoparticles, NCs – nanocrystals, GCE – glassy carbon electrode, Pd – palladium, MWCNT – multiwalled carbon nanotube, CS- Chitosan, Fc- Ferrocene, 3DM- three dimensionally microporous, rGO – reduced graphene oxide, PANI – polyaniline, Pt – platinum, NF- nanoflowers, pAb- polyclonal rabbit anti-NSE human antibody, mAb- monoclonal anti-human NSE antibody, CD- cyclodextrin.

4.4 Conclusions

A sensitive, specific, fast, and economical biosensor is prepared by utilizing the synergistic effect of MoS₂ and rGO for the detection of a potential lung cancer biomarker. Layered structures of these 2D nanomaterials allow easy grafting of rGO into MoS₂. Electrochemical parameters like HET constant and electroactive surface area are determined to be 1.29×10^{-3} cm s⁻¹ and 27.83 mm² respectively. The superior performance of the prepared bioelectrode is

owed to the bridged interconnected network between MoS₂ and rGO, which provides more conduction pathways. A large surface area empowers the bioelectrode to exhibit a wide detection range and demonstrate a good sensitivity. It is found that the availability of oxygenated functional groups onto rGO/MoS₂ assists covalent immobilization of biological moieties onto the matrix which makes it specific as well as reproducible. This study also proposes the use of an rGO/MoS₂-based matrix for the preparation of biosensors for the detection of other biomarkers too by using their respective antibodies.

References

- [1] F. Bray, J. Ferlay, I. Soerjomataram, R.L. Siegel, L.A. Torre, A. Jemal, Global cancer statistics 2018: GLOBOCAN estimates of incidence and mortality worldwide for 36 cancers in 185 countries, CA: a cancer journal for clinicians 68(6) (2018) 394-424.
- [2] Singh, Harish, Jillian Bernabe, Justin Chern, and Manashi Nath. "Copper selenide as multifunctional non-enzymatic glucose and dopamine sensor." Journal of Materials Research 36, no. 7 (2021): 1413-1424.
- [3] Wang, Haoran, Shining Wu, Tongtong Cao, Bo Zhao, Jianjun Ruan, Jiakai Cao, Zhiwei Tong, and Xiaobo Zhang. "Self-assembly behavior of layered titanium niobate and methylene blue cation and electrochemical detection of dopamine." Journal of Materials Research 36, no. 7 (2021): 1437-1446.
- [4] J. Han, Y. Zhuo, Y.-Q. Chai, Y.-L. Yuan, R. Yuan, Novel electrochemical catalysis as signal amplified strategy for label-free detection of neuron-specific enolase, Biosensors and Bioelectronics 31(1) (2012) 399-405.
- [5] G. Yang, Z. Xiao, C. Tang, Y. Deng, H. Huang, Z. He, Recent advances in biosensor for detection of lung cancer biomarkers, Biosensors and Bioelectronics 141 (2019) 111416.
- [6] Carney, DesmondN, DanielC Ihde, MartinH Cohen, PaulJ Marangos, PaulA Bunn JR, JohnD Minna, and AdiF Gazdar. "Serum neuron-specific enolase: a marker for disease extent and response to therapy of small-cell lung cancer." The Lancet 319, no. 8272 (1982): 583-585.
- [7] Xu, Cai-Ming, Ya-Lan Luo, Shuai Li, Zhao-Xia Li, Liu Jiang, Gui-Xin Zhang, Lawrence Owusu, and Hai-Long Chen. "Multifunctional neuron-specific enolase: its role in lung diseases." Bioscience reports 39, no. 11 (2019).
- [8] Kalkal, Ashish, Sachin Kadian, Sumit Kumar, Gaurav Manik, Prosenjit Sen, Saurabh Kumar, and Gopinath Packirisamy. "Ti₃C₂-MXene decorated with nanostructured silver as a dual-energy acceptor for the fluorometric neuron specific enolase detection." Biosensors and Bioelectronics 195 (2022): 113620.
- [9] S. Yin, L. Zhao, Z. Ma, Label-free electrochemical immunosensor for ultrasensitive detection of neuron-specific enolase based on enzyme-free catalytic amplification, Analytical and bioanalytical chemistry 410(4) (2018) 1279-1286.
- [10] Q. Zhang, X. Li, C. Qian, L. Dou, F. Cui, X. Chen, Label-free electrochemical immunoassay for neuron specific enolase based on 3D macroporous reduced graphene oxide/polyaniline film, Analytical biochemistry 540 (2018) 1-8.
- [11] H. Wang, Z. Ma, Amperometric immunoassay for the tumor marker neuron-specific enolase using a glassy carbon electrode modified with a nanocomposite consisting of

- polyresorcinol and of gold and platinum nanoparticles, *Microchimica Acta* 184(9) (2017) 3247-3253.
- [12] X. Fu, R. Huang, J. Wang, X. Feng, Platinum nanoflower-based catalysts for an enzyme-free electrochemical immunoassay of neuron-specific enolase, *Analytical Methods* 5(16) (2013) 3803-3806.
- [13] A. Mohammadi, E. Heydari-Bafrooei, M.M. Foroughi, M. Mohammadi, Electrochemical aptasensor for ultrasensitive detection of PCB77 using thionine-functionalized MoS₂-rGO nanohybrid, *Microchemical Journal* 155 (2020) 104747.
- [14] A. Sinha, B. Tan, Y. Huang, H. Zhao, X. Dang, J. Chen, R. Jain, MoS₂ nanostructures for electrochemical sensing of multidisciplinary targets: a review, *TrAC Trends in Analytical Chemistry* 102 (2018) 75-90.
- [15] C. Anichini, W. Czepa, D. Pakulski, A. Aliprandi, A. Ciesielski, P. Samorì, Chemical sensing with 2D materials, *Chemical Society Reviews* 47(13) (2018) 4860-4908.
- [16] K. Kalantar-zadeh, J.Z. Ou, Biosensors based on two-dimensional MoS₂, *Acs Sensors* 1(1) (2016) 5-16.
- [17] V. Georgakilas, J.N. Tiwari, K.C. Kemp, J.A. Perman, A.B. Bourlinos, K.S. Kim, R. Zboril, Noncovalent functionalization of graphene and graphene oxide for energy materials, biosensing, catalytic, and biomedical applications, *Chemical reviews* 116(9) (2016) 5464-5519.
- [18] H.-H. Huang, K.K.H. De Silva, G. Kumara, M. Yoshimura, Structural evolution of hydrothermally derived reduced graphene oxide, *Scientific reports* 8(1) (2018) 1-9.
- [19] H. Yang, J. Zhou, J. Bao, Y. Ma, J. Zhou, C. Shen, H. Luo, M. Yang, C. Hou, D. Huo, A simple hydrothermal one-step synthesis of 3D-MoS₂/rGO for the construction of sensitive enzyme-free hydrogen peroxide sensor, *Microchemical Journal* 162 (2021) 105746.
- [20] S. Gao, Y. Zhang, Z. Yang, T. Fei, S. Liu, T.J.J.o.A. Zhang, Compounds, Electrochemical chloramphenicol sensors-based on trace MoS₂ modified carbon nanomaterials: Insight into carbon supports, 872 (2021) 159687.
- [21] Jalil, Owais, Chandra Mouli Pandey, and Devendra Kumar. "Highly sensitive electrochemical detection of cancer biomarker based on anti-EpCAM conjugated molybdenum disulfide grafted reduced graphene oxide nanohybrid." *Bioelectrochemistry* 138 (2021): 107733.
- [22] D.C. Marcano, D.V. Kosynkin, J.M. Berlin, A. Sinitskii, Z. Sun, A. Slesarev, L.B. Alemany, W. Lu, J.M. Tour, Improved synthesis of graphene oxide, *ACS nano* 4(8) (2010) 4806-4814.
- [23] R. Khatri, N.K. Puri, Electrochemical study of hydrothermally synthesised reduced MoS₂ layered nanosheets, *Vacuum* 175 (2020) 109250.
- [24] M. Saraf, K. Natarajan, A.K. Saini, S.M. Mobin, Small biomolecule sensors based on an innovative MoS₂-rGO heterostructure modified electrode platform: a binder-free approach, *Dalton Transactions* 46(45) (2017) 15848-15858.
- [25] Y. Li, H. Wang, L. Xie, Y. Liang, G. Hong, H. Dai, MoS₂ nanoparticles grown on graphene: an advanced catalyst for the hydrogen evolution reaction, *Journal of the American Chemical Society* 133(19) (2011) 7296-7299.
- [26] X. Bai, Y. Du, X. Hu, Y. He, C. He, E. Liu, J. Fan, Synergy removal of Cr (VI) and organic pollutants over RP-MoS₂/rGO photocatalyst, *Applied Catalysis B: Environmental* 239 (2018) 204-213.
- [27] W.-K. Jo, S. Kumar, M.A. Isaacs, A.F. Lee, S. Karthikeyan, Cobalt promoted TiO₂/GO for the photocatalytic degradation of oxytetracycline and Congo Red, *Applied Catalysis B: Environmental* 201 (2017) 159-168.

- [28] H. Sun, S. Liu, G. Zhou, H.M. Ang, M.O. Tadé, S. Wang, Reduced graphene oxide for catalytic oxidation of aqueous organic pollutants, *ACS applied materials & interfaces* 4(10) (2012) 5466-5471.
- [29] L. Chen, D. Ding, C. Liu, H. Cai, Y. Qu, S. Yang, Y. Gao, T. Cai, Degradation of norfloxacin by CoFe_2O_4 -GO composite coupled with peroxymonosulfate: a comparative study and mechanistic consideration, *Chemical Engineering Journal* 334 (2018) 273-284.
- [30] J. Zhou, H. Xiao, B. Zhou, F. Huang, S. Zhou, W. Xiao, D. Wang, Hierarchical MoS_2 -rGO nanosheets with high MoS_2 loading with enhanced electro-catalytic performance, *Applied Surface Science* 358 (2015) 152-158.
- [31] S. Yang, X. Feng, S. Ivanovici, K. Müllen, Fabrication of graphene-encapsulated oxide nanoparticles: towards high-performance anode materials for lithium storage, *Angewandte Chemie International Edition* 49(45) (2010) 8408-8411.
- [32] H. Wang, J.T. Robinson, X. Li, H. Dai, Solvothermal reduction of chemically exfoliated graphene sheets, *Journal of the American Chemical Society* 131(29) (2009) 9910-9911.
- [33] S. Stankovich, D.A. Dikin, R.D. Piner, K.A. Kohlhaas, A. Kleinhammes, Y. Jia, Y. Wu, S.T. Nguyen, R.S. Ruoff, Synthesis of graphene-based nanosheets via chemical reduction of exfoliated graphite oxide, *carbon* 45(7) (2007) 1558-1565.
- [34] J. Zhang, L. Zhao, A. Liu, X. Li, H. Wu, C. Lu, Three-dimensional MoS_2 /rGO hydrogel with extremely high double-layer capacitance as active catalyst for hydrogen evolution reaction, *Electrochimica Acta* 182 (2015) 652-658.
- [35] L. Lin, S. Zhang, Effective solvothermal deoxidization of graphene oxide using solid sulphur as a reducing agent, *Journal of Materials chemistry* 22(29) (2012) 14385-14393.
- [36] T. Yang, L.-h. Liu, J.-w. Liu, M.-L. Chen, J.-H. Wang, Cyanobacterium metallothionein decorated graphene oxide nanosheets for highly selective adsorption of ultra-trace cadmium, *Journal of Materials Chemistry* 22(41) (2012) 21909-21916.
- [37] R. Vinoth, I.M. Patil, A. Pandikumar, B.A. Kakade, N.M. Huang, D.D. Dionysios, B. Neppolian, Synergistically enhanced electrocatalytic performance of an N-doped graphene quantum dot-decorated 3D MoS_2 -graphene nanohybrid for oxygen reduction reaction, *Acs Omega* 1(5) (2016) 971-980.
- [38] G. Sun, X. Zhang, R. Lin, J. Yang, H. Zhang, P. Chen, Hybrid fibers made of molybdenum disulfide, reduced graphene oxide, and multi-walled carbon nanotubes for solid-state, flexible, asymmetric supercapacitors, *Angewandte Chemie* 127(15) (2015) 4734-4739.
- [39] S. Kumar, V. Sharma, K. Bhattacharyya, V. Krishnan, Synergetic effect of MoS_2 -RGO doping to enhance the photocatalytic performance of ZnO nanoparticles, *New Journal of Chemistry* 40(6) (2016) 5185-5197.
- [40] N. Kumar, S. Kumar, R. Gusain, N. Manyala, S. Eslava, S.S. Ray, Polypyrrole-Promoted rGO- MoS_2 Nanocomposites for Enhanced Photocatalytic Conversion of CO_2 and H_2O to CO, CH_4 , and H_2 Products, *ACS Applied Energy Materials* 3(10) (2020) 9897-9909.
- [41] E.G. da Silveira Firmiano, A.C. Rabelo, C.J. Dalmaschio, A.N. Pinheiro, E.C. Pereira, W.H. Schreiner, E.R. Leite, Supercapacitor electrodes obtained by directly bonding 2D MoS_2 on reduced graphene oxide, *Advanced Energy Materials* 4(6) (2014) 1301380.
- [42] Chen, Yan-Li, Zhong-Ai Hu, Yan-Qin Chang, Huan-Wen Wang, Zi-Yu Zhang, Yu-Ying Yang, and Hong-Ying Wu. "Zinc oxide/reduced graphene oxide composites and electrochemical capacitance enhanced by homogeneous incorporation of reduced graphene oxide sheets in zinc oxide matrix." *The Journal of Physical Chemistry C* 115, no. 5 (2011): 2563-2571.
- [43] Wang, Guoxiu, Xiaoping Shen, Jane Yao, and Jinsoo Park. "Graphene nanosheets for enhanced lithium storage in lithium ion batteries." *Carbon* 47, no. 8 (2009): 2049-2053.

- [44] L. Zhang, W. Fan, W.W. Tjiu, T. Liu, 3D porous hybrids of defect-rich MoS₂/graphene nanosheets with excellent electrochemical performance as anode materials for lithium ion batteries, *RSC Advances* 5(44) (2015) 34777-34787.
- [45] V.K. Singh, S. Kumar, S.K. Pandey, S. Srivastava, M. Mishra, G. Gupta, B. Malhotra, R. Tiwari, A. Srivastava, Fabrication of sensitive bioelectrode based on atomically thin CVD grown graphene for cancer biomarker detection, *Biosensors and Bioelectronics* 105 (2018) 173-181.
- [46] S. Kumar, S. Kumar, S. Tiwari, S. Srivastava, M. Srivastava, B.K. Yadav, S. Kumar, T.T. Tran, A.K. Dewan, A. Mulchandani, Biofunctionalized nanostructured zirconia for biomedical application: a smart approach for oral cancer detection, *Advanced Science* 2(8) (2015) 1500048.
- [47] M. Kukkar, A. Sharma, P. Kumar, K.-H. Kim, A. Deep, Application of MoS₂ modified screen-printed electrodes for highly sensitive detection of bovine serum albumin, *Analytica chimica acta* 939 (2016) 101-107.
- [48] Farrokhnia, Mohammadreza, Ghassem Amoabediny, Mohammad Ebrahimi, Mohammadreza Ganjali, and Mohammad Arjmand. "Ultrasensitive early detection of insulin antibody employing novel electrochemical nano-biosensor based on controllable electro-fabrication process." *Talanta* 238 (2022): 122947.
- [49] Jalil, Owais, Chandra Mouli Pandey, and Devendra Kumar. "Electrochemical biosensor for the epithelial cancer biomarker EpCAM based on reduced graphene oxide modified with nanostructured titanium dioxide." *Microchimica Acta* 187, no. 5 (2020): 1-9.
- [50] Xi, Xin, Dongqing Wu, Wei Ji, Shinan Zhang, Wei Tang, Yuezeng Su, Xiaojun Guo, and Ruili Liu. "Manipulating the Sensitivity and Selectivity of OECT-Based Biosensors via the Surface Engineering of Carbon Cloth Gate Electrodes." *Advanced Functional Materials* 30, no. 4 (2020): 1905361.
- [51] D. Sandil, S.C. Sharma, N.K. Puri, Protein-functionalized WO₃ nanorods-based impedimetric platform for sensitive and label-free detection of a cardiac biomarker, *Journal of Materials Research* 34(8) (2019) 1331-1340.
- [52] D. Chauhan, P.K. Gupta, P.R. Solanki, Electrochemical immunosensor based on magnetite nanoparticles incorporated electrospun polyacrylonitrile nanofibers for Vitamin-D3 detection, *Materials Science and Engineering: C* 93 (2018) 145-156.
- [53] S. Kumar, N. Gupta, B.D. Malhotra, Ultrasensitive biosensing platform based on yttria doped zirconia-reduced graphene oxide nanocomposite for detection of sali vary oral cancer biomarker, *Bioelectrochemistry* 140 (2021) 107799.

Chapter 5

Electrochemical Study of Chitosan (CS) Modified MoS₂ Layered Nanosheets for Detection of Lung Cancer Biomarker

This chapter discusses chitosan (CS) bio-functionalized MoS₂ which is prepared to serve as a biosensing matrix, to address the issue of lack of stable immobilization of antibodies on the biosensing matrix for repeated cycles of measurement. Electrochemical performance of CS/MoS₂ matrix towards detection of neuron-specific enolase (NSE), a lung cancer biomarker is also investigated. Unlike other complex matrices involving various steps of modification, the matrix studied herein involves only 2 steps of modification without the use of any label, amplifying its appeal for biosensing applications. The fabricated bioelectrode is found to exhibit remarkable cyclic stability, with a sensitivity of 3.5 $\mu\text{A ng}^{-1} \text{mL cm}^{-2}$ and a wide linear detection range of 0.1 to 100 ng mL^{-1} . Also, the sensor is found to be fast, specific, reproducible, regenerable for up to 4 cycles, and has a shelf life of 6 weeks. The stability study of fabricated bioelectrode revealed that the cumulative effect of CS and MoS₂ ensures stable immobilization of biomolecules on the bioelectrode for 50 cyclic voltammetry (CV) cycles. The results of this study suggest that as proposed matrix will be promising in the fabrication of devices for early monitoring of protein biomarkers.

This work is published as: **Ritika Khatri and Nitin K. Puri.** "*Electrochemical studies of biofunctionalized MoS₂ matrix for highly stable immobilization of antibodies and detection of lung cancer protein biomarker.*" **New Journal of Chemistry (Royal Society of Chemistry) 46 (16) (2022): 7477-7489.**

5.1 Introduction

Electrochemical biosensors have gained momentum in the development of point-of-care devices owing to the ease of miniaturization, requirement of small sample volumes, rapid response, and low requirement for power [1, 2]. They use electron mediators to translate the events of analyte binding into a detectable electrical signal. The preparation of an electrochemical biosensor requires the fabrication of a suitable immobilization matrix that can hold the bio-recognition elements efficiently and effectively [3]. Nanostructured materials have been proven a good choice to fabricate the platform for loading biological molecules to detect even very low levels of analytes [4]. However, the chosen material should be able to escalate the charge transfer process without passivating the electrode surface to maintain its performance along with increasing its effective surface area. For the fabrication of an electrochemical biosensor, it is inevitably important to ensure that the bioactivity of the immobilized biomolecule is not lost on the continuous application of potential on it and with repeated interaction with redox media.

In recent times, molybdenum disulfide (MoS_2) has gained great attention in electrochemical applications (i.e., supercapacitors, lithium (Li)/sodium (Na) ion batteries, hydrogen evolution reaction (HER), sensors, etc. [5]) as it possesses many intriguing properties like layered structure, various routes for synthesis, ease of tailoring the morphology, large surface to volume ratio, ease of dispersibility in aqueous solution, fast rate of heterogeneous electron transfer (HET), the feasibility of surface functionalization and modification and exceptional cyclic stability [5-9]. Owing to its hydrophobicity, MoS_2 can be utilized to fabricate the immobilization platform because it provides a strong affinity for the adsorption of protein on its surface [6]. Because of its layered structure and high surface/volume ratio, it enhances the total surface area for the immobilization of biomolecules. Owing to all these fascinating

properties of MoS₂, it is used to fabricate the matrix for electrochemical biosensing. As discussed in chapter 1, covalent binding is the most preferred method of immobilization of biological elements on the immobilization matrix. Therefore, to anchor functional groups on MoS₂ and impart biocompatibility to the matrix, Chitosan (CS) is used. CS is a non-toxic biocompatible polymer, which is present in abundance, and has excellent film-forming and stabilizing properties along with polycationic nature [10, 11]. It is rich in functional groups like amino and hydroxyl, on its polysaccharide chain [12]. Thus, CS is blended with MoS₂ in the presence of ionic liquid (IL) because of its high polarity [13]. Due to its polar nature, IL provides a reaction atmosphere for MoS₂ and CS to interact with each other. The benefit of compositing different materials is governed by the fact that both materials contribute to the properties of the final blend [1].

In this chapter, the sensing behavior of bio-functionalized MoS₂ is examined by choosing the protein biomarker neuron-specific enolase (NSE) as the target analyte. NSE is considered to be a specific protein biomarker for the diagnosis of small cell lung cancer (SCLC) and is found to be $> 12 \text{ ng mL}^{-1}$ in the case of 69% of patients diagnosed with SCLC [14]. Quite a few reports are available on the detection of NSE, using different matrices with outstanding performances [15-18]. However, achieving a high signal response along with maintaining the signal stability and the bioactivity of the platform, is still a significant challenge [15]. For instance, Tang et al [16] developed PPy-PEDOT-Au-GCE as a substrate material for stable immobilization of immune molecules along with the maintenance of their bioactivity for detection of NSE. They found that their platform could provide a stable environment for sensing till 30 CV cycles. Yu and co-workers designed an electrochemical immunosensor for the detection of NSE based on graphene supported by hollow carbon balls [17]. A stable trend for this immobilization matrix was found for 30 cycles of CV. Mo et al fabricated an immunosensor for simultaneous detection of NSE and CYFRA21-1 and found the stability of

the immunosensor for 15 CV cycles [18]. Thus, it has been observed that after a few cycles of measurements the signal response tends to degrade. In this investigation, we explored the CS/MoS₂ matrix for stable immobilization of anti-NSE antibodies and the detection of NSE for the first time, to the best of our knowledge. The CS/MoS₂-based matrix proved to be a stable matrix, with nearly 94% of the initial signal response still retained after continuous scanning for 50 CV cycles. The composite ensures the bioactivity of immobilized antibodies is retained along with a stable cyclic current response.

The method of synthesis and fabrication of bioelectrode discussed in this work is appealing because of its large yield, scalability, and simplicity without involving various steps of modifications which ensures remarkable electrochemical performance and stability. There are three major novel features of this work. First, a highly stable matrix is formed favorable for immobilization of biomolecules during repeated cycles of measurement. Second, the platform is functionalized for the attachment of biomolecules without any harsh chemical treatment. Third, the large electroactive surface [55% of the geometric area ($1 \times 1 \text{ cm}^2$)], makes it a remarkable platform for electrochemical sensors. The sensor is found to be very fast, reproducible, specific, stable, and regenerable, with a wide linear detection range and remarkable shelf life. Considering the concentration of NSE found in the serum of SCLC patients, the sensitivity and lowest limit which could be detected by our sensor, are expected to meet the requirement of detection of NSE in clinical samples too.

5.2 Experimental Details

5.2.1 Chemicals and reagents used for synthesis, cleaning, and biosensing

The monoclonal anti-NSE antibody, NSE antigen, N-(3-Dimethylaminopropyl)-N'-ethyl carbodiimide hydrochloride (EDC), N-Hydroxysuccinimide (NHS), bovine serum albumin (BSA), ammonium molybdate tetrahydrate $(\text{NH}_4)_6\text{Mo}_7\text{O}_{24} \cdot 4\text{H}_2\text{O}$, and acetic acid (CH_3COOH)

are purchased from Sigma-Aldrich. Thiourea ($\text{CH}_4\text{N}_2\text{S}$) is bought from SRL. Liquor ammonia (NH_4OH) and N, N-dimethylformamide (DMF) are bought from Fisher Scientific. CS is purchased from HIMEDIA. 1-butyl-3-methylimidazolium hexafluorophosphate ($[\text{C}_4\text{mim}][\text{PF}_6]$) is procured from GLR innovations. Other Chemicals like hydrazine hydrate (N_2H_4), Sodium chloride (NaCl), and potassium bromide (KBr) are procured from Thermo Fisher Scientific. Hydrogen peroxide (H_2O_2) is purchased from Qualigens. Concentrated hydrochloric acid (HCl) is bought from RFCL limited. Chemicals including acetonitrile, potassium hexacyanoferrate(II) trihydrate/ potassium ferrocyanide [$\text{K}_4\text{Fe}(\text{CN})_6 \cdot 3\text{H}_2\text{O}$], potassium hexacyanoferrate (III)/potassium ferricyanide [$\text{K}_3\text{Fe}(\text{CN})_6$], disodium hydrogen diphosphate dihydrate ($\text{Na}_2\text{HPO}_4 \cdot 2\text{H}_2\text{O}$), Sodium dihydrogen phosphate dihydrate ($\text{NaH}_2\text{PO}_4 \cdot 2\text{H}_2\text{O}$), isopropyl alcohol (IPA) and ethanol are procured from Merck. A Millipore Milli-Q system (Bedford, MA, USA) is used to obtain milli-Q water for the preparation of the solutions which are used for various experiments. Tris hydrochloride (Tris-HCl), magnesium sulfate (MgSO_4), and potassium chloride (KCl) which serve as a buffer for dilution of NSE are purchased from lobachemie (Tris- HCl) and Thermo Fisher Scientific (MgSO_4 and KCl).

Before usage and storing the buffer solutions, all the glassware is autoclaved and cleaned using 70% isopropyl alcohol (IPA). All the aqueous solutions are prepared in autoclaved de-ionized (DI) water.

5.2.2 Synthesis of CS/MoS₂ nanostructures

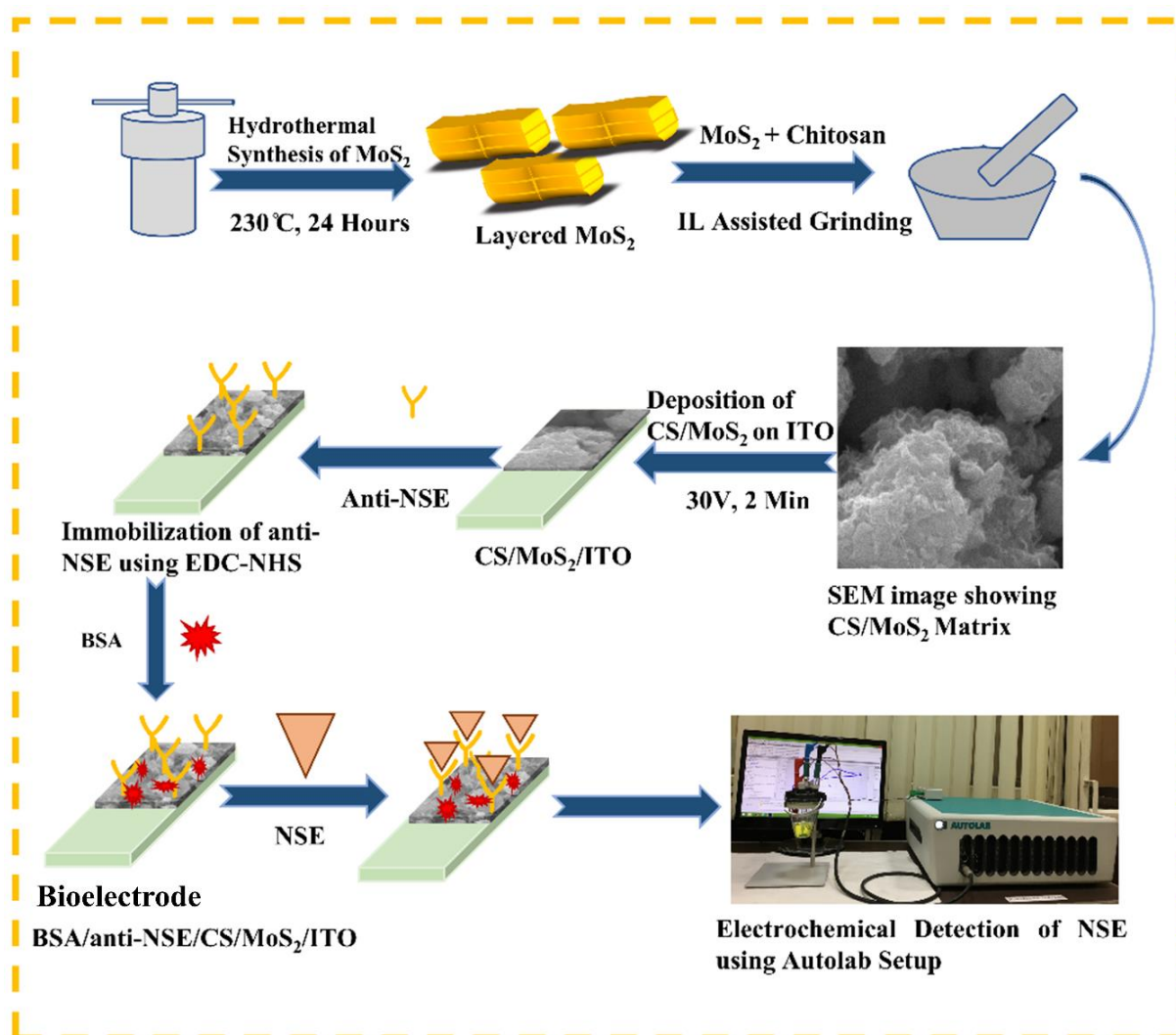
MoS₂ nanostructures constituting a large number of layers are synthesized using our previously reported work using hydrazine hydrate as a reducing agent [19], as discussed in chapter 3. To synthesize CS/MoS₂, an ionic liquid (IL) assisted mechanical grinding method is used. The synthesis of CS/MoS₂ is done according to the method adopted by Zhang et al [20] with slight modifications for scaling up the quantity of the finally obtained product. For this, 500 mg of

the above synthesized MoS₂ powder is mixed with 200 mg of CS. The mixture is ground in an agate mortar pestle for 20 minutes. Next, a gel is formed by dropping 1 mL of IL (1-butyl-3-methyldiazolium hexafluorophosphate, [C₄mim][PF₆]) in the mortar pestle. This mixture of MoS₂, CS, and IL is further grounded for 60 minutes. Then the obtained product is washed using acetone, acetic acid, and DMF to remove excess CS and IL. Then the obtained residue is put in an oven at 100 °C for 24 hours for desolvation. Thus, dried powder of CS/MoS₂ is collected in an Eppendorf for further use.

5.2.3 Fabrication of bioelectrode

To fabricate the bioelectrode BSA/anti-NSE/CS/MoS₂/ITO, a series of steps are followed. First of all, ITO cut in a dimension of 3 × 1 cm² are hydrolyzed using NH₃:H₂O₂:H₂O in the ratio of 1:1:5 at 80 °C for 1 hour. The hydrolyzed ITO is cleaned using water and IPA. Next, films of CS/MoS₂ are deposited on hydrolyzed ITO using electrophoretic deposition (EPD). For this CS/MoS₂ is well dispersed in acetonitrile at a concentration of 1 mg mL⁻¹. This solution is taken in an EPD cell containing a copper (Cu) wire and platinum (Pt) counter electrode (CE). Hydrolyzed ITO is clipped at Cu as a working electrode (WE) and a potential of 30 V is applied for 120 seconds. CS/MoS₂ film is formed on a geometric area of 1 × 1 cm². The film is left for overnight air drying at room temperature. The thickness is measured at various points of the CS/MoS₂/ITO electrode and it is found to be varying in the range of 1.1 to 3 μm indicating a non-uniform surface. For the immobilization of anti-NSE on CS/MoS₂/ITO, 0.4 M EDC (used as a coupling agent), 0.1 M NHS (used as an intermediate stabilizer), and 25 μg mL⁻¹ anti-NSE are aliquoted together in a ratio of 1:1:2. Then, 20 μL of this aliquoted solution is spread uniformly on CS/MoS₂/ITO electrode. The anti-NSE/CS/MoS₂/ITO electrode is kept in a humid chamber for 5 hours for proper attachment of anti-NSE on CS/MoS₂/ITO. Then, the anti-NSE/CS/MoS₂/ITO is washed in PBS 7.4 to remove unbound antibodies from the

electrode surface. To mask the non-specific binding sites on anti-NSE/CS/MoS₂/ITO, 10 μL of 0.1 mg mL⁻¹ of BSA is dropped cast to make the final bioelectrode BSA/anti-NSE/CS/MoS₂/ITO. After 1 hour the bioelectrode is washed in PBS 7.4 to remove excess BSA from the surface of the bioelectrode. The BSA/anti-NSE/CS/MoS₂/ITO bioelectrode is finally prepared and kept at 4 °C when not in use. The illustration of the synthesis of the CS/MoS₂ matrix and fabrication of BSA/anti-NSE/CS/MoS₂/ITO bioelectrode for detection of NSE is shown in **Scheme 5.1**.



Scheme 5.1: Schematic diagram illustrating the synthesis of CS/MoS₂ matrix and fabrication of BSA/anti-NSE/CS/MoS₂/ITO bioelectrode for detection of NSE.

5.3 Results and Discussion

5.3.1 Characterization Equipment and Facilities

To record the X-ray diffraction (XRD) pattern of samples, a Bruker D8 Advance facility is used. Raman spectrum for the samples is recorded at a wavelength of 532 nm using a WITec Raman spectrometer. Scanning electron microscopy (SEM) is done using Jeol Japan mode. The Fourier Transform Infrared (FTIR) spectroscopy measurements are done using Perkin Elmer spectrum two. The thermal stability of samples is recorded using a Perkin Elmer 4000 thermogravimetric analyzer. To carry out the thickness measurement an Ambios XP-200 stylus profiler is used. A Metrohm Potentiostat/Galvanostat Autolab along with NOVA software is used for recording all the electrochemical measurements.

5.3.2 Characterization studies of synthesized nanostructures

5.3.2.1 Crystallographic study of CS/MoS₂ matrix using XRD

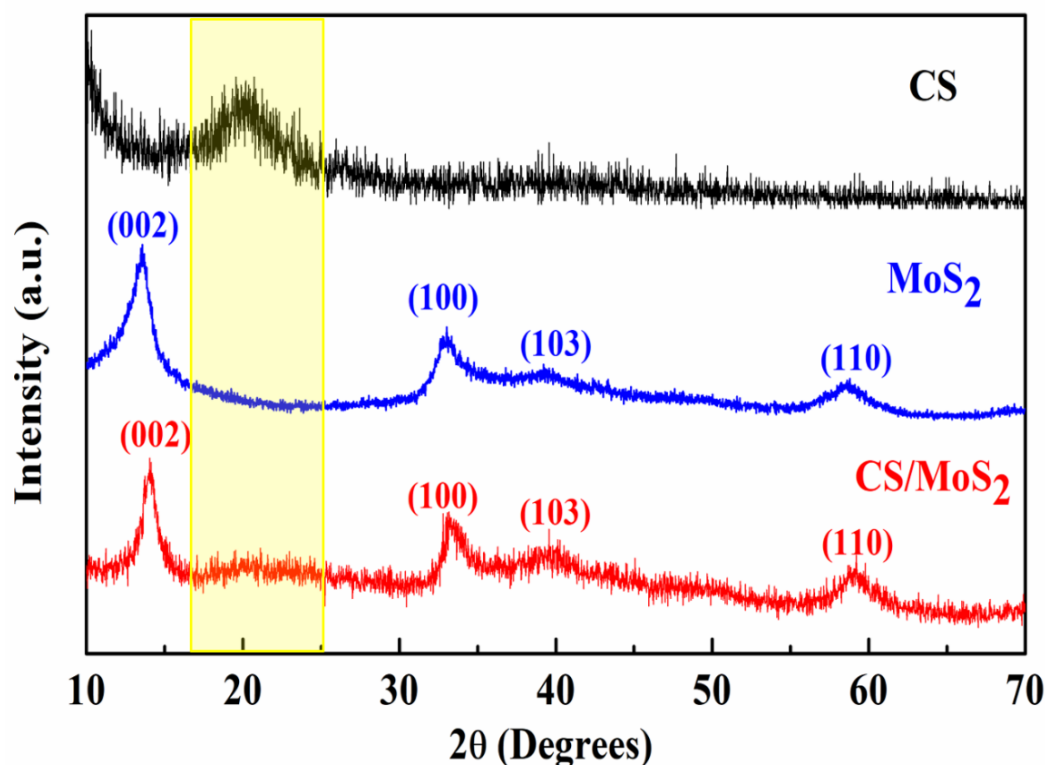


Fig. 5.1: XRD pattern of CS, MoS₂, and, CS/MoS₂

The primary confirmation of the formation of the CS/MoS₂ matrix and the study of its crystallographic structure is done using XRD (**Fig. 5.1**). The XRD pattern obtained for commercially purchased CS shows a broad diffraction peak around 20°, without the presence of any additional impurity peaks. For comparison, the XRD of MoS₂ is also shown and both MoS₂ and CS/MoS₂, XRD patterns show the peaks corresponding to the planes (002), (100), (103), (110) of 2H-MoS₂ (JCPDS card no. – 37-1492) [19]. Besides these peaks, a halo around 20° in the pattern of CS/MoS₂ confirms the formation of the composite of CS and MoS₂.

5.3.2.2 Study of vibrational modes and qualitative information about layered structure and functionalization using Raman spectroscopy

Fig. 5.2(a) shows the Raman spectra obtained for CS as well as CS/MoS₂ in the range of 250 cm⁻¹ to 3700 cm⁻¹. The appearance of the A_{1g} and E¹_{2g} vibrational modes of MoS₂ in the Raman spectrum of CS/MoS₂, (**shown in Fig. 5.2(a) and 5.2(b)**) confirm the retention of the structure of MoS₂ after the addition of CS. The A_{1g} vibrational mode corresponding to monolayer MoS₂ is found to be at 402.72 cm⁻¹ (**Fig. 5.2(b)**) [21]. However, the E¹_{2g} mode is found to be red-shifted to 375.39 cm⁻¹ leading to a wavenumber separation between two modes to 27.3 cm⁻¹ [**Fig. 5.2(b)**]. An increase in wavenumber separation in comparison to the MoS₂HH sample (23.24 cm⁻¹) as discussed in chapter 3, may be attributed to the stacking of layers of MoS₂ due to the incorporation of CS in the structure of MoS₂. Further, the characteristic peaks of CS are observed at 893.14 cm⁻¹, 1096 cm⁻¹, 1372.67 cm⁻¹, and 2885.37 cm⁻¹ corresponding to the C-H bond of polysaccharide in CS, with OH peak at 3311.37 cm⁻¹ and 3376.83 cm⁻¹ [**Fig. 5.2(a)**] [22]. The confirmation of functionalization of MoS₂ by CS can be drawn from the Raman spectrum of CS/MoS₂ [**Fig. 5.2(a)**], which shows a peak at 1368.61 cm⁻¹ corresponding to the δCH of the polysaccharide chain of CS. Further, a halo is observed in the range 2500 - 3260

cm^{-1} , which could be due to the νCH_2 peak of CS. This study confirms the successful incorporation of CS in between the layers of MoS_2 .

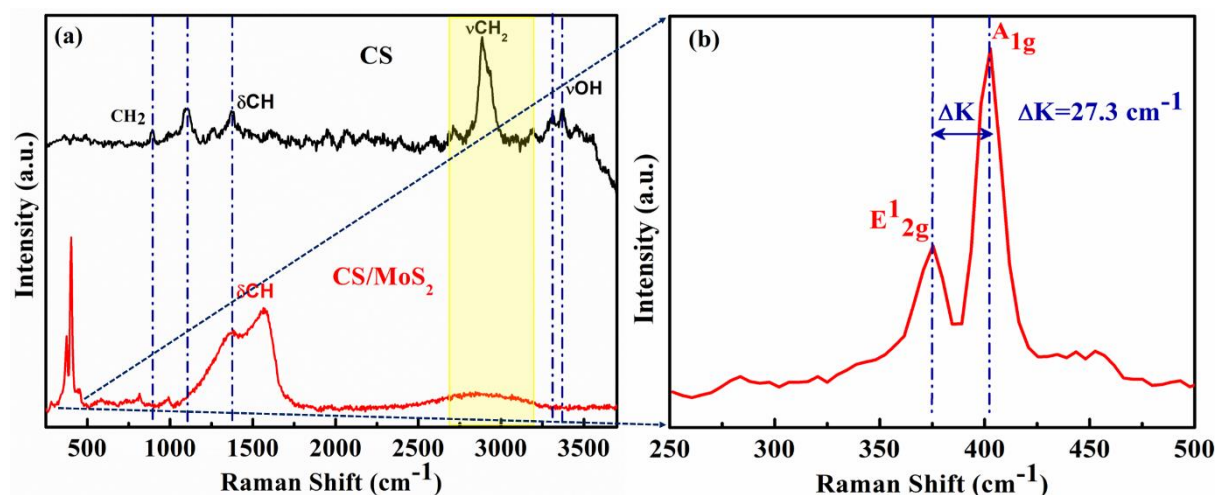


Fig. 5.2: (a) Raman spectra of CS and CS/ MoS_2 (b) Raman spectrum of CS/ MoS_2 in the range 250 to 500 cm^{-1} showing A_{1g} and E^1_{2g} modes of MoS_2 in CS/ MoS_2

5.3.2.3 Thermogravimetric analysis using TGA of CS/ MoS_2 matrix

Fig. 5.3 shows the thermal behavior of CS, MoS_2 , and CS/ MoS_2 from 30 °C to 850 °C. An initial weight loss at around 100 °C in all the samples could be attributed to moisture loss. The weight loss for CS starts at 280 °C while CS/ MoS_2 starts losing some weight around 220 °C, which could be due to some leftovers from the process of synthesis of MoS_2 [23]. The weight loss in the case of CS and CS/ MoS_2 is more in the range of 280 °C to 500 °C, which can be ascribed to the decomposition of carbon skeleton at such high temperatures [24]. After 500 °C, 57% and 32% weight of MoS_2 and CS/ MoS_2 are retained respectively, while CS is completely lost. Thus, the matrix CS/ MoS_2 is found to have more thermal stability in comparison to CS. This study also implies that the incorporation of functional groups in MoS_2 reduces its thermal stability at high temperatures. But, as long as application to biosensors is concerned, this is not worrisome because biological testings are always done at room temperatures or even lower

temperatures. Further, the successful incorporation of CS in MoS₂ could be derived from TGA.

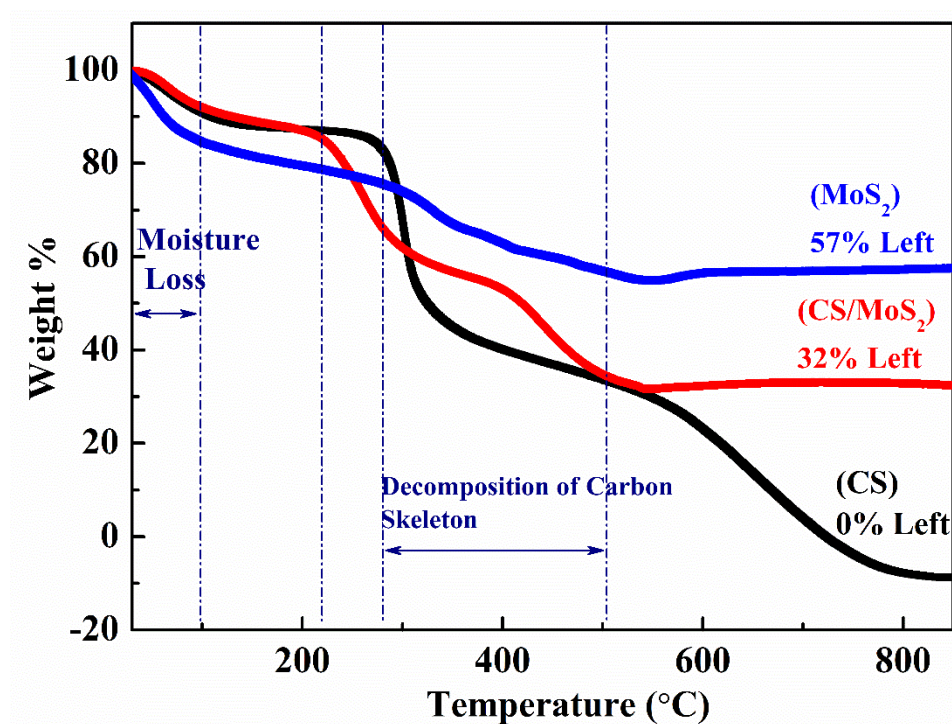


Fig. 5.3: TGA curves of CS, MoS₂, and CS/MoS₂

5.3.2.4 Study of functional groups attached on CS/MoS₂ matrix using FTIR

The confirmation of successful functionalization of MoS₂ using CS is done using FTIR (Fig. 5.4).

Peaks observed in CS [Fig. 5.4(a)] at 1416 cm⁻¹, 1303 cm⁻¹, and 1089 cm⁻¹ correspond to CH₂ bending, -NH stretching and C-O stretch of CS respectively [25]. The peak observed at 1561 cm⁻¹ in CS is due to the bending vibration of -NH [23]. These peaks corresponding to -NH stretching (1303 cm⁻¹) and -NH bending (1561 cm⁻¹) are missing in CS/MoS₂ [Fig. 5.4(b)]. The disappearance of these -NH peaks in the FTIR spectrum of CS/MoS₂ could be attributed to the polycationic nature of CS which leads to the protonation of the amine group during grinding in IL, which leads to electrostatic interaction between MoS₂ layers and CS [24]. Peaks observed in CS at 1262 cm⁻¹ and 1162 cm⁻¹ correspond to C-N and C-O-C bonds in CS [26].

The peak observed in the range 3440-3480 cm^{-1} in both CS and CS/MoS₂ corresponds to the hydroxyl group (OH) [24]. The peak observed in both CS and CS/MoS₂ at 1371 cm^{-1} corresponds to wagging CH₃ [27]. Further, a peak corresponding to NH₂ is observed in both CS and CS/MoS₂ at 895 cm^{-1} [28] and 1625 cm^{-1} [29], indicating functionalization of CS/MoS₂ with the amino group. The peak observed at 618 cm^{-1} corresponds to Mo-S vibration [30].

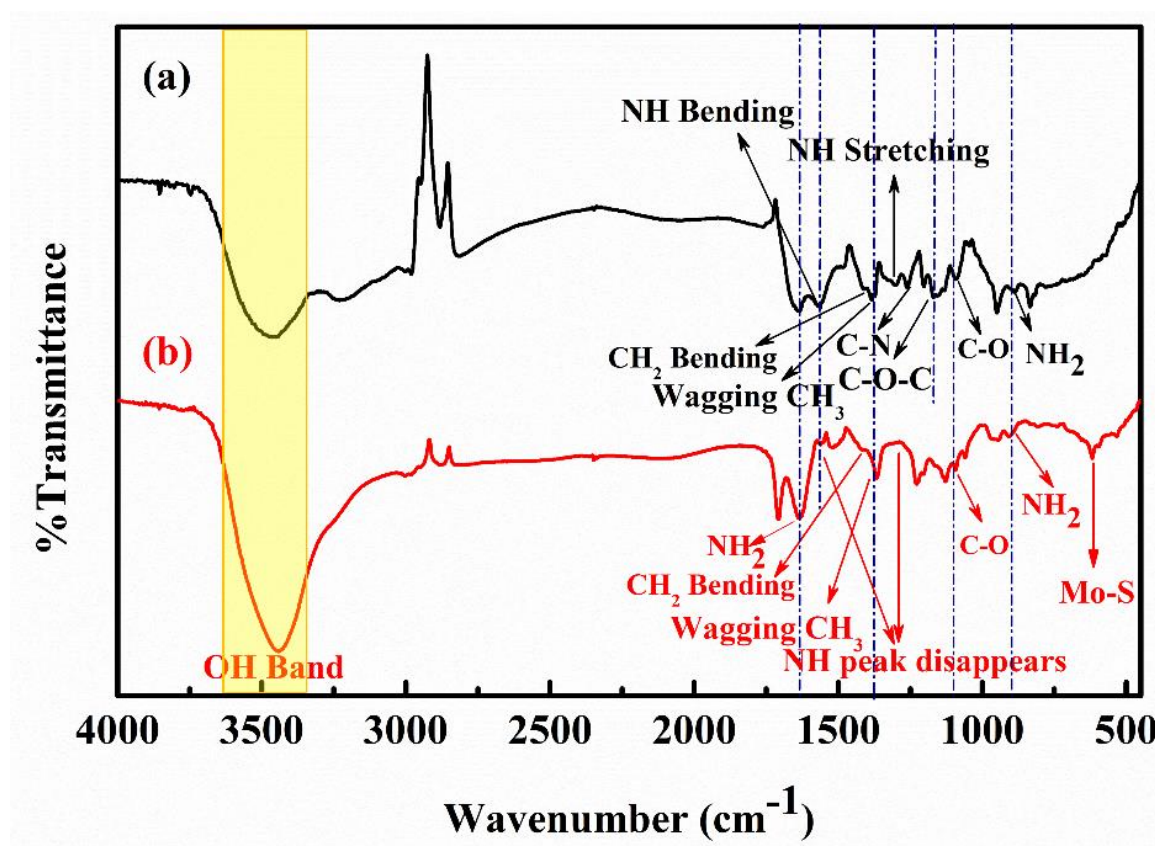


Fig. 5.4: FTIR curves of (a) CS and (b) CS/MoS₂

5.3.2.5 Study of surface morphology of CS/MoS₂ matrix using SEM

Fig. 5.5(a) shows nanostructures of MoS₂ of varying sizes. A larger magnification of these nanostructures can be seen constituting a large number of layers of MoS₂ in Fig. 5.5(b). Fig. 5.5(c) shows a large continuous membrane of CS. The evidence of surface modification of MoS₂ nanostructures by CS is given in Fig. 5.5(d), which shows that layers of MoS₂ are stacked

together and encapsulated by CS membrane rendering a rough and uneven surface to the composite.

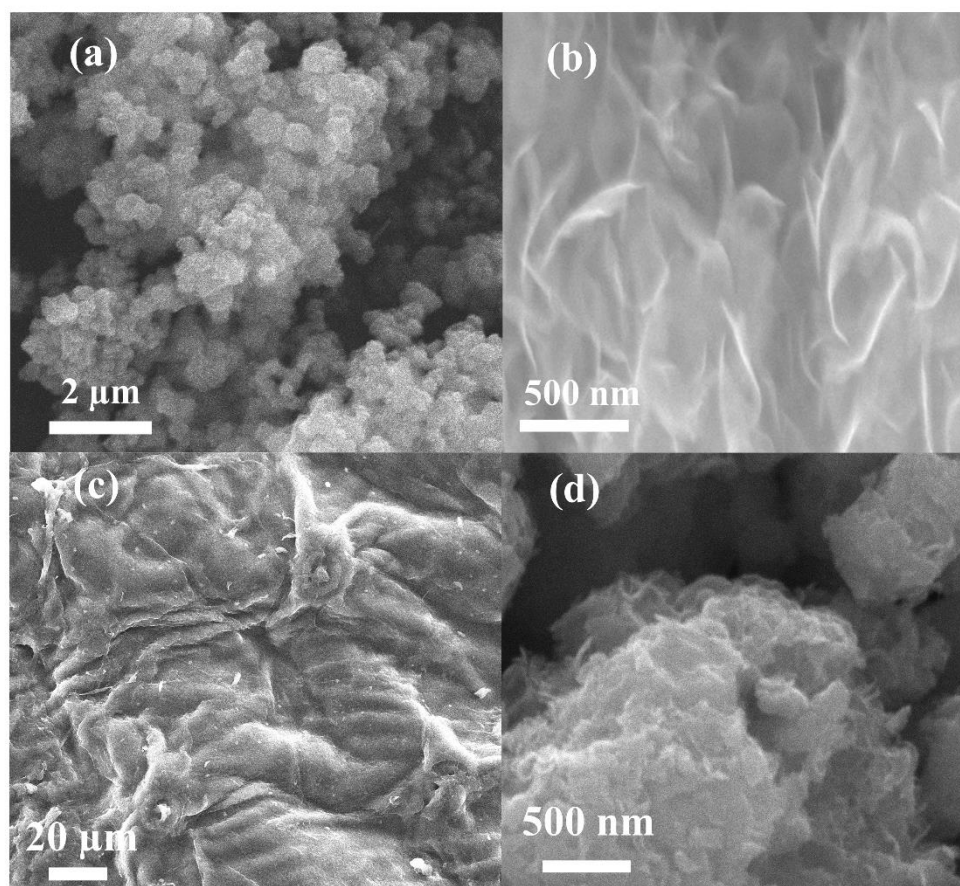


Fig. 5.5: SEM micrographs of (a, b) MoS₂ (c) CS (d) CS/MoS₂

5.3.3 Electrochemical performance of bioelectrode prepared using CS/MoS₂ matrix

5.3.3.1 Optimization of biosensing parameters

The concentration of anti-NSE to be attached to the CS/MoS₂/ITO electrode is optimized by attaching varying concentrations of anti-NSE using EDC-NHS chemistry. **Fig. 5.6 (a)** shows the response of current along with the varying concentration of anti-NSE (5 μg mL⁻¹, 10 μg mL⁻¹, 25 μg mL⁻¹, 50 μg mL⁻¹, 100 μg mL⁻¹). The response is found to be decreasing initially till 25 μg mL⁻¹ of anti-NSE's concentration, after which it becomes constant.

Thus, $25 \mu\text{g mL}^{-1}$ is finalized as the concentration for attachment of anti-NSE throughout the studies.

The maximum time required for immunoreaction to take place between NSE and anti-NSE is found by incubation of BSA/anti-NSE/CS/MoS₂/ITO bioelectrode with NSE for varying times [Fig. 5.6(b)]. $20 \mu\text{L}$ of 5 ng mL^{-1} of NSE is incubated on bioelectrode and the CV response is recorded by varying incubation times from 0, 5, 10, 15, 20, and 25 minutes. Initially, the current decreases till 15 minutes of incubation time, after which the current becomes nearly constant. Thus, the time required for immunoreaction to take place is found to be 15 minutes and is used for all further studies.

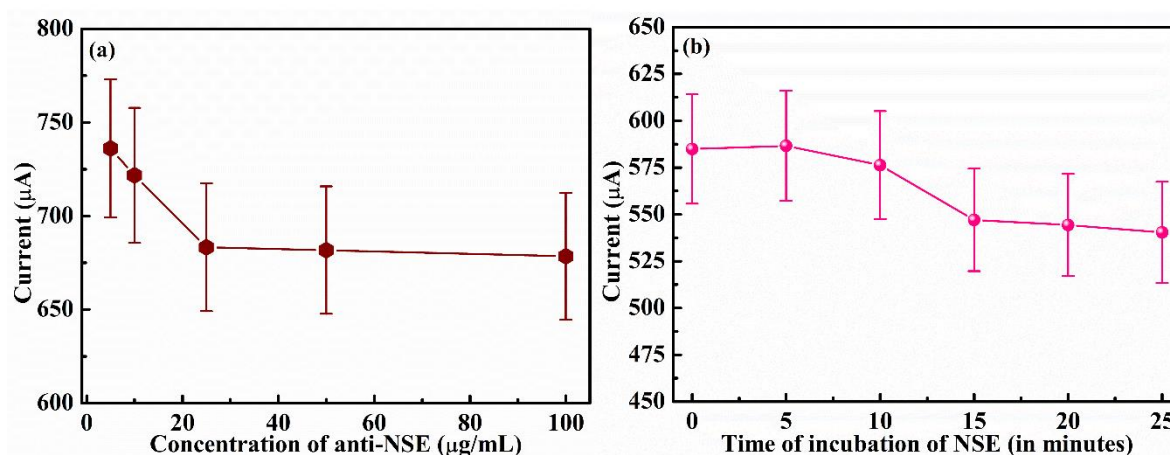


Fig. 5.6: (a) Current response with varying concentration of anti-NSE (b) Current response with variation in incubation time of NSE on BSA/anti-NSE/CS/MoS₂/ITO bioelectrode

5.3.3.2 Electrochemical study of the various steps of fabrication of bioelectrode

Various steps of modification of the bioelectrode are evaluated by recording the CV profiles at each step, in PBS 7.4 at a scan rate of 50 mV s^{-1} [Fig. 5.7(a)]. A distinct anodic and cathodic current peak (i_{pa} and i_{pc} respectively) is observed in each step. The maximum value of i_{pa} and i_{pc} is recorded to be $640.26 \mu\text{A}$ and $-810.55 \mu\text{A}$ for anti-NSE/CS/MoS₂/ITO electrode followed by BSA/anti-NSE/CS/MoS₂/ITO bioelectrode having the values as $579.35 \mu\text{A}$ and $-762.63 \mu\text{A}$.

Further, the minimum current values of i_{pa} and i_{pc} are found to be $436.71 \mu\text{A}$ and $-579.53 \mu\text{A}$ for CS/MoS₂/ITO. The variation in peak current values at each step confirms the modification of the electrode. The sequential modification at each step of fabrication of bioelectrode is also confirmed by electrochemical impedance spectroscopy (EIS). EIS studies are done at a biasing potential of 0.01 V in the frequency range of 0.1 Hz to 100 kHz. **Fig. 5.7(b)** shows the Nyquist plots for (i) CS/MoS₂/ITO, (ii) anti-NSE/CS/MoS₂/ITO and (iii) BSA/anti-NSE/CS/MoS₂/ITO. The results are found to complement CV results with a minimum value of charge transfer resistance (R_{ct}) observed as 161.78Ω for anti-NSE/CS/MoS₂/ITO. This is followed by an increase in R_{ct} value to 245.40Ω for BSA/anti-NSE/CS/MoS₂/ITO and the maximum value of R_{ct} is found to be 313.38Ω for CS/MoS₂/ITO.

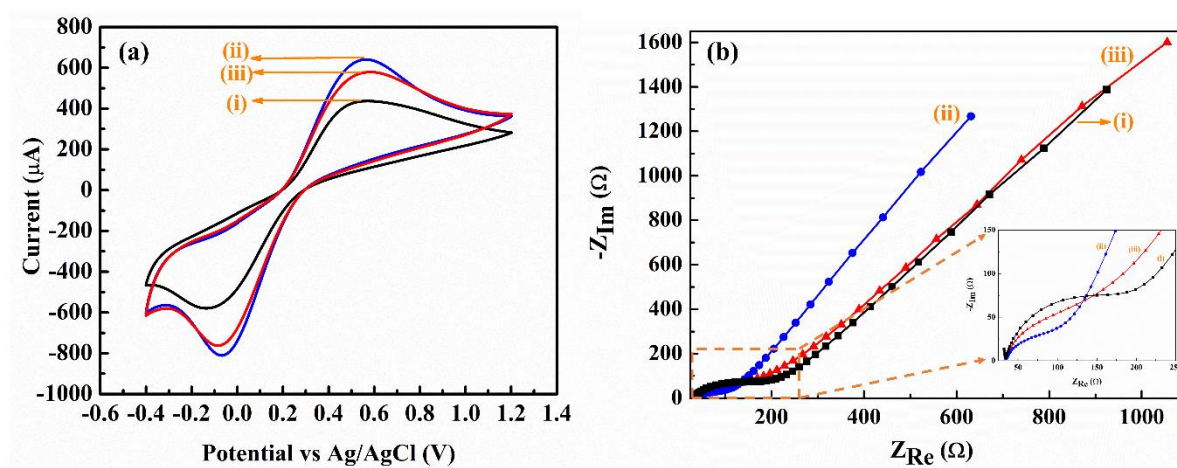


Fig. 5.7: (a) CV curves of (i) CS/MoS₂/ITO (ii) anti-NSE/CS/MoS₂/ITO (iii) BSA/anti-NSE/CS/MoS₂/ITO (b) EIS curves of (i) CS/MoS₂/ITO (ii) anti-NSE/CS/MoS₂/ITO (iii) BSA/anti-NSE/CS/MoS₂/ITO. The inset shows the magnified Nyquist plots (in the range of 25 to 250 Ω)

An increase in the value of i_{pa} and a decrease in the value of R_{ct} is observed when anti-NSE is immobilized on CS/MoS₂/ITO. This happens because of the interaction between anti-NSE and CS/MoS₂ and the spatial orientation of antibodies which provides conduction pathways to the charge carriers on the interface [31, 32]. Further, a decrease in current and

increase in R_{ct} is found after attachment of BSA onto anti-NSE/CS/MoS₂/ITO, due to masking of non-specific sites for attachment, by this blocking agent.

Fig. 5.8(a) displays the CV response of the prepared bioelectrode BSA/anti-NSE/CS/MoS₂/ITO with varying scan rates. The CV profile is recorded in PBS solution of pH 7.4 having 50 mM of [Fe(CN)₆]^{3-/4-}. An increase in i_{pa} and i_{pc} currents is observed for increasing scan rates. Further, a linear variation of i_{pa} and i_{pc} with $\sqrt{\text{Scan Rate}}$ (**Fig. 5.8(b)**) shows that the process of reduction and oxidation of [Fe(CN)₆]^{3-/4-} at the bioelectrode is diffusion-controlled [33, 34], which indicates that adsorbents when gets conjugated on the electrode will inhibit the diffusion of [Fe(CN)₆]^{3-/4-}. The linearly fitted plots as shown in **Fig. 5.8(b)** are given by the following equations 5.1 and 5.2:

$$i_{pa} = \left[(60.21 \mu\text{A} \times \sqrt{\frac{s}{mV}}) \times \sqrt{\text{Scan Rate} \left(\frac{mV}{s} \right)} + 119.61 (\mu\text{A}) \right] \quad (5.1)$$

$$R^2 = 99.92$$

$$i_{pc} = \left[(-91.84 \mu\text{A} \times \sqrt{\frac{s}{mV}}) \times \sqrt{\text{Scan Rate} \left(\frac{mV}{s} \right)} - 81.91 (\mu\text{A}) \right] \quad (5.2)$$

$$R^2 = 98.83$$

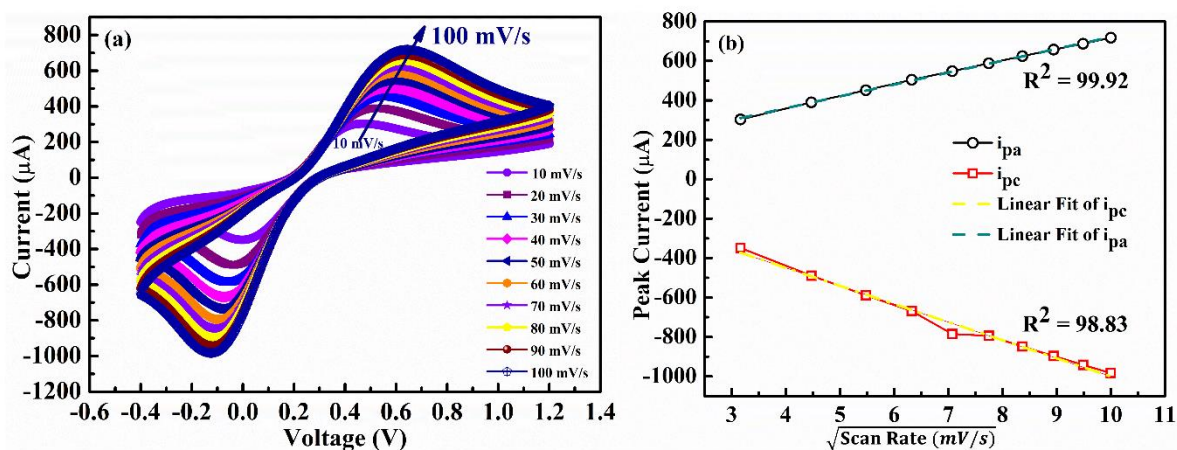


Fig. 5.8: (a) Scan Rate Study of bioelectrode BSA/anti-NSE/CS/MoS₂/ITO by varying scan rate from 10 to 100 mV s⁻¹ and recording CV profiles (b) Variation of peak anodic current (i_{pa}) and peak cathodic current (i_{pc}) with under root of scan rate

The evaluation of electrochemical kinetics parameters of BSA/anti-NSE/CS/MoS₂/ITO like electroactive surface area (A_e), HET rate transfer constant (K_o) is done as follows. The electroactive surface area (A_e) is determined using the Randles Sevcik equation [19, 35]

$$i_p = 2.69 \times 10^5 n^{3/2} A_e C \sqrt{D_o v} \quad (5.3)$$

Where i_p is peak anodic current as obtained in CV profile of the electrode (in A), n is the number of electrons transferred during redox reaction ($n=1$, for ferro/ferri), A_e is electroactive surface area, C is the concentration of redox probe ($C = 5 \text{ mM} = 5 \text{ mol cm}^{-3}$), D_o is the diffusion coefficient ($D_o = 0.667 \times 10^{-5} \text{ cm}^2 \text{ s}^{-1}$ [19, 35]), v is scan rate. The unit of the constant 2.69×10^5 is $\frac{C}{\text{mol}\sqrt{V}}$ [36]. From the plot between i_{pa} and $v^{1/2}$ [Fig. 5.8(b)] the value of the slope is obtained as $60.21 \mu\text{A} \sqrt{\frac{s}{mV}}$ (from equation 5.1). By substituting all the above values in equation 5.3 the electroactive surface area is determined to be 0.55 cm^2 for BSA/anti-NSE/CS/MoS₂/ITO. A high value of electroactive surface area allows the sensor to accommodate large concentrations of analyte, in turn increasing the linear detection range of the device.

The value of electron transfer constant (k_o) is determined using Nicholson's Equation [35], which is given as

$$\Psi = k_o \left(\frac{D_o}{D_R} \right)^{\frac{\alpha}{2}} \left(\frac{RT}{\pi n F D_o v} \right)^{\frac{1}{2}} \quad (5.4)$$

Where,

D_o and D_R are the diffusion coefficient of oxidized and reduced electroactive species, which is approximately equal to 1 for symmetrical redox reaction, α is the transfer coefficient, R is the universal gas constant ($8.314 \text{ JK}^{-1} \text{ mol}^{-1}$), F is the Faraday constant (96485 C mol^{-1}), v is scan rate (50 mV s^{-1}), remaining parameters are same as equation 5.3 and Ψ is a dimensionless kinetic parameter which can be calculated using ΔE_p [35] as follows

$$\Psi = \frac{-0.6288 + 0.0021X\Delta E_p}{1 - 0.017X\Delta E_p} \quad (5.5)$$

Using, **equations 5.4** and **5.5**, the value of k_o is calculated to be $-4.05 \times 10^{-3} \text{ cm s}^{-1}$ for BSA/anti-NSE/CS/MoS₂/ITO.

5.3.3.3 Stability study of prepared bioelectrode

The prepared bioelectrode BSA/anti-NSE/CS/MoS₂/ITO is checked for the stability of immobilized antibodies on the continuous application of potential and repeated interaction with redox media ($[\text{Fe}(\text{CN})_6]^{3-/4-}$) by carrying out CV for 50 consecutive cycles. The scans are done at a scan rate of 50 mV s^{-1} in the potential window of -0.4 V to 1.2 V in $[\text{Fe}(\text{CN})_6]^{3-/4-}$. An essentially unchanged value of anodic and cathodic peak current is observed as shown in **Fig. 5.9(a)**. 95% and 93.66% of initial i_{pa} are retained, after 15 and 50 CV cycles respectively while 99.45% of initial i_{pc} is retained after 50 CV cycles as shown in **Fig. 5.9(b)**. Retention of a high percentage of initial current even after 50 CV cycles demonstrate that the prepared bioelectrode has high stability. CS in CS/MoS₂ imparts biocompatibility to the matrix, which helps the biomolecules to remain stably immobilized, after interaction with the redox media in continuous cycles of CV.

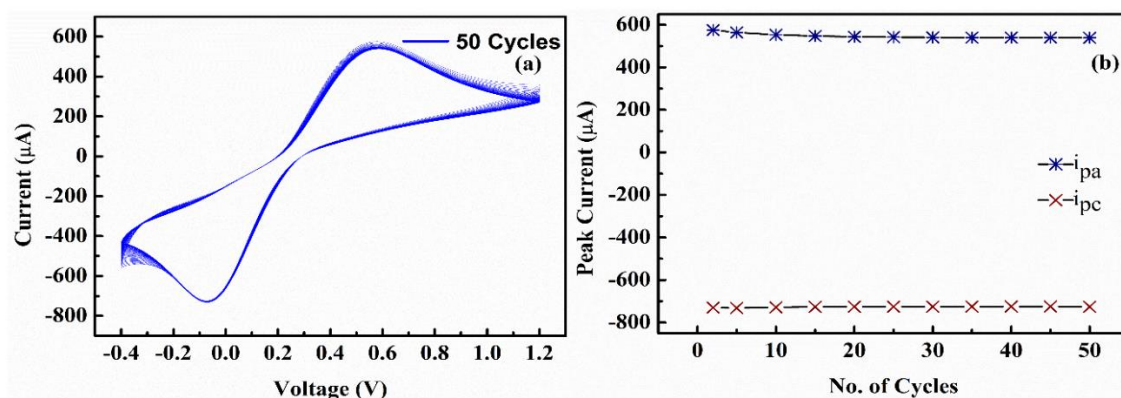


Fig. 5.9 (a) Consecutive scans of bioelectrode (BSA/anti-NSE/CS/MoS₂/ITO) for 50 CV cycles **(b)** Variation of peak anodic (i_{pa}) and peak cathodic current (i_{pc}) with no. of CV cycles.

5.3.3.4 Electrochemical performance of bioelectrode (BSA/anti-NSE/CS/MoS₂/ITO) and control electrode (CS/MoS₂/ITO) towards detection of NSE

Electrochemical detection of NSE is done by incubating the BSA/anti-NSE/CS/MoS₂/ITO bioelectrode by varying concentrations of NSE from 0.1 ng mL⁻¹ to 200 ng mL⁻¹. The response is recorded using CV at a scan rate of 50 mV s⁻¹. The current response is found to be inversely proportional to the concentration of NSE, which is a result of specific binding between NSE and anti-NSE. This specific binding results in the formation of an immunocomplex that impedes the diffusion of [Fe(CN)₆]^{3-/4-}. **Fig. 5.10(a)** shows the variation in CV response of BSA/anti-NSE/CS/MoS₂/ITO bioelectrode when incubated with varying concentrations of NSE from 0.1 ng mL⁻¹ to 200 ng mL⁻¹. **Fig. 5.10(b)** shows the variation of i_{pa} with the concentration of NSE from 0.1 ng mL⁻¹ to 100 ng mL⁻¹. The variation is found to be linearly decreasing and can be fitted using the following equation (5.6) with R² equal to 0.94.

$$y = -1.84 \frac{\mu A}{\frac{ng}{mL}} \times \left[\text{Concentration of NSE} \left(\frac{ng}{mL} \right) \right] + 675.37 \mu A \quad (5.6)$$

The sensitivity of the bioelectrode can be calculated from here to be 3.35 $\mu A \text{ ng}^{-1} \text{ mL cm}^{-2}$ by dividing the slope of the calibration curve by the electroactive surface area calculated for BSA/anti-NSE/CS/MoS₂/ITO [37]. The lowest concentration which could be detected for NSE from the prepared bioelectrode is 0.1 ng mL⁻¹.

Fig. 5.10(c) shows the response of the control electrode (CS/MoS₂/ITO) towards varying concentrations of NSE from 0.1 ng mL⁻¹ to 100 ng mL⁻¹. The response is recorded similarly as done for BSA/anti-NSE/CS/MoS₂/ITO. An invariant response towards NSE by the control electrode shows that response of the bioelectrode (BSA/anti-NSE/CS/MoS₂/ITO) is due to specific interaction between NSE and anti-NSE. This interaction leads to the formation of immunocomplex leading to a decrease in the peak current of bioelectrode with increasing concentration of NSE. Thus, this study concludes that CS/MoS₂/ITO cannot interact with NSE

on its own without the conjugation of anti-NSE, (the biological element as discussed in chapter 1) onto its surface.

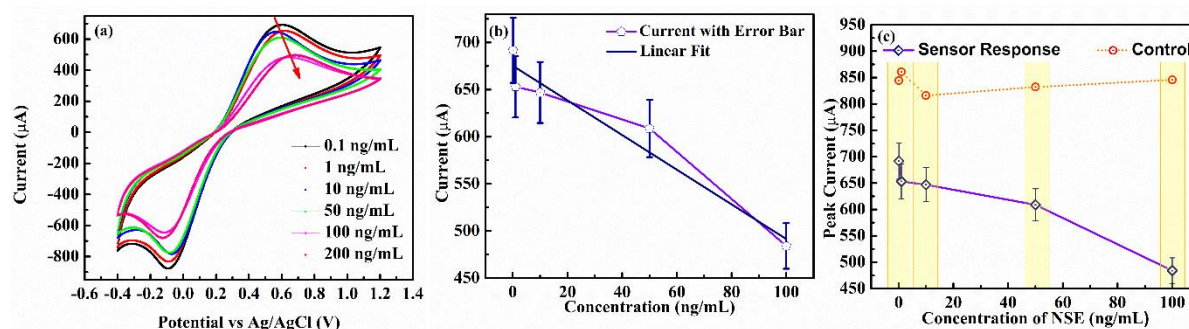


Fig. 5.10: (a) Electrochemical detection of NSE studied using CV with variation in concentration of NSE from 0.1 ng mL^{-1} to 200 ng mL^{-1} in PBS 7.4 containing $50 \text{ mM } [\text{Fe}(\text{CN})_6]^{3-/4-}$ (b) Calibration plot between CV peak current and concentration of NSE (c) Response of control electrode (CS/MoS₂/ITO) towards varying concentrations of NSE from 0.1 to 100 ng mL^{-1}

5.3.3.5 Investigation of reproducibility and specificity of prepared bioelectrode towards NSE

To assess the reproducibility of prepared bioelectrode BSA/anti-NSE/CS/MoS₂/ITO, 5 different bioelectrodes are prepared under the same conditions and following a similar protocol. The response of these bioelectrodes is checked for 10 ng mL^{-1} of NSE. The bioelectrodes exhibit an acceptable relative standard deviation (RSD) of 3.10% [Fig. 5.11(a)], indicating the protocol mentioned in section 5.2.3 gives reproducible bioelectrodes.

To examine the specificity of the prepared bioelectrode BSA/anti-NSE/CS/MoS₂/ITO towards NSE, various other commonly present interferents in human serum, like C-reactive protein (CRP, $10 \text{ } \mu\text{g mL}^{-1}$), Myoglobin (mB, 85 ng mL^{-1}), Cardiac Troponin I (cTnI, 0.1 ng mL^{-1}), Urea (0.1 mg mL^{-1}), Sodium Chloride (NaCl, 6.2 mg mL^{-1}), are taken. For recording the CV

response, 20 μL of each of these interferents are incubated onto the bioelectrode for 15 minutes. The bioelectrode shows an RSD value in the range of 0.27% to 0.94% for other interferents whereas a relatively higher value of RSD equal to 7.8% is found for NSE, showing the specificity of bioelectrode towards NSE. **Fig. 5.11(b)** displays the bar graph depicting the response of prepared bioelectrode towards various other interferents in human serum including NSE (10 ng mL^{-1}). Further, to examine the performance of bioelectrode towards the detection of NSE, when all the other common interferents are also present simultaneously, a simple control experiment is performed using the CV technique. **Fig. 5.11(c)** shows the performance of bioelectrode when all the other interferents like CRP ($10 \mu\text{g mL}^{-1}$), mB (85 ng mL^{-1}), cTnI (0.1 ng mL^{-1}), Urea (0.1 mg mL^{-1}), NaCl (6.2 mg mL^{-1}) are present in their physiological concentrations at the same time without NSE (0 ng mL^{-1} , control) and along with NSE (10 ng mL^{-1}). It is observed that the bioelectrode displays an RSD value of 0.33% in the case of control measurement which increases to 6.06% when NSE is also present along with all the other interferents. The results indicate excellent specificity of BSA/anti-NSE/CS/MoS₂/ITO towards NSE. The immobilization of anti-NSE antibodies onto the bioelectrode confers it to the requisite specificity.

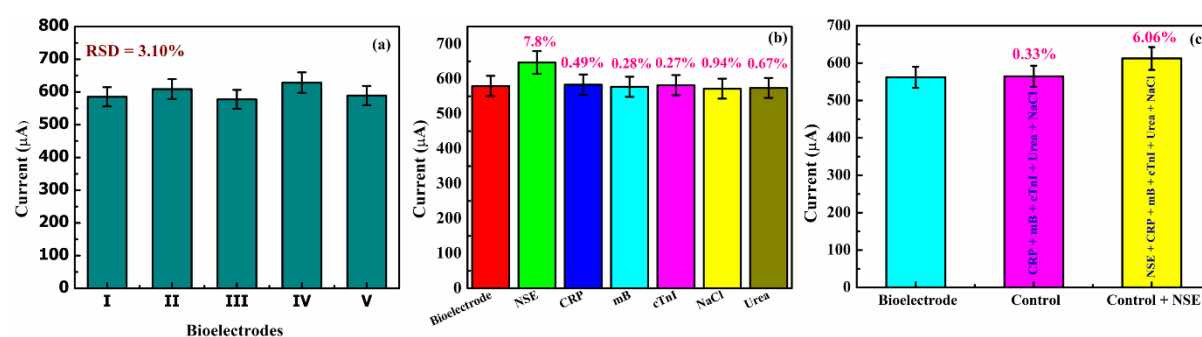


Fig. 5.11: (a) Reproducibility study of 5 different bioelectrodes prepared under similar conditions (b) Specificity study of bioelectrode towards various interferents commonly present in human serum (c) Specificity study of bioelectrode towards NSE in the simultaneous presence of various other interferents.

5.3.3.6 Shelf life and regeneration study of prepared bioelectrode

The shelf life of BSA/anti-NSE/CS/MoS₂/ITO bioelectrode is done by incubating it with 10 ng mL⁻¹ of NSE for 15 minutes at a regular interval of 7 days. The bioelectrode is found to retain more than 80% of its initial response till the 6th week [Fig. 5.12(a)]. While the response reduces to 70% in the 7th week. Thus, the bioelectrode displays a shelf life of up to 6 weeks.

To check the regeneration ability of the bioelectrode, 0.1M of glycine HCl buffer of pH 2.5 is prepared. The bioelectrode is first tested for 10 ng mL⁻¹ of NSE and the CV response is recorded. Then the bioelectrode is washed in glycine HCl buffer solution followed by washing in PBS 7.4 buffer solution and then, it is tested for 10 ng mL⁻¹ of NSE. The bioelectrode is tested for 4 cycles and is found to retain more than 90% of its initial response till the 4th cycle [Fig. 5.12(b)].

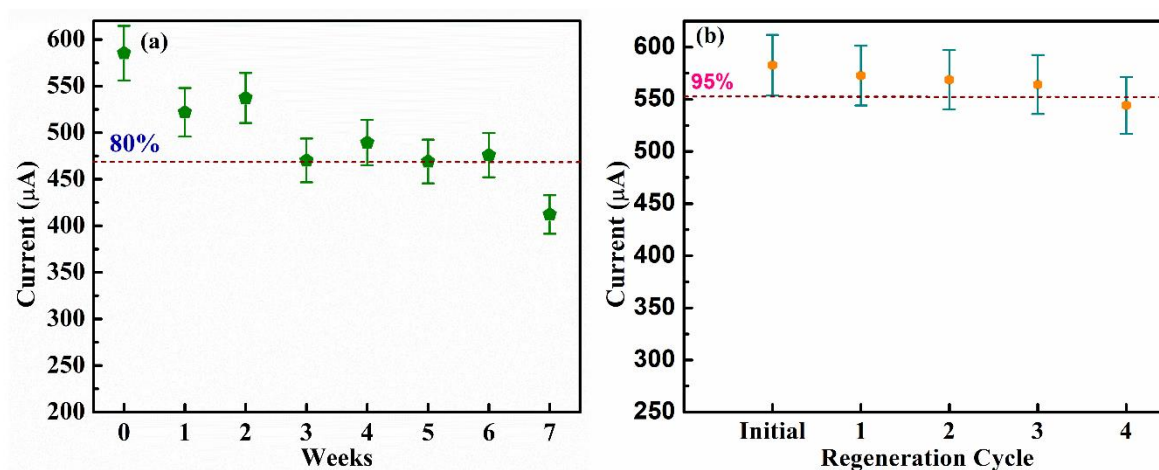


Fig. 5.12: (a) Shelf-life study of fabricated bioelectrode (b) Regeneration study of prepared bioelectrode

Table 5.1 represents the comparison of the platform proposed in this work with other platforms reported for the detection of NSE. The proposed bioelectrode is found to exhibit better performance in comparison to other bioelectrodes, especially in terms of the response time of

the bioelectrode (incubation time of NSE). Other parameters like linear detection range, shelf life, and regenerability are also found to be appreciably good.

Table 5.1: Comparison of the analytical performance of bioelectrode proposed in this study with other bioelectrodes reported earlier for detection of NSE.

Platform	Linear Detection Range	Shelf Life (in days)	Incubation Time of NSE (in minutes)	Regenerable	Reference
Au/PANI/3D-rGO/Ab	0.5 pg mL ⁻¹ to 10 ng mL ⁻¹	30	40	Yes (5 cycles)	[3]
PPD-GR-AuNPs/Ab/SPE	1 to 1000 ng mL ⁻¹	30	60	-	[38]
GCE/Ab/Ag/AuNPs-rGO/AP-anti-IgG	0.1 to 2000 ng mL ⁻¹	-	40	-	[39]
BSA/anti-NSE/Polyresorcinol-Au/Pt/GCE	10 pg mL ⁻¹ to 100 ng mL ⁻¹	30	50	-	[40]
Au-MoS ₂ /MOF	1 pg mL ⁻¹ to 100 ng mL ⁻¹	30	40	-	[41]
Fc-g-Au@Pd-P(BBY) and rGO/Thi/AuPt NAs	0.0001 to 50 ng mL ⁻¹	15	-	-	[42]

BSA/anti-NSE/CS/MoS₂/ITO	0.1 to 100 ng mL⁻¹	42	15	Yes (4 Cycles)	This work
--	--------------------------------------	-----------	-----------	-----------------------	------------------

PANI- Polyaniline, rGO- reduced graphene oxide, SPE: Screen printed electrode, PPD: poly pphenylenediamine, GR- Graphene, Au – Gold, NP- nanoparticle, Ab- antibody, GCE-Glassy carbon electrode, AP-alkaline phosphatase, Ag- antigen, Fc-g – ferrocene grafted, Au- gold, BBY- Bismarck Brown Y, Thi- Thionine, Pt- Platinum, NAs – Nanoassemblies

5.4 Conclusions

In this chapter, we have discussed CS bio-functionalized MoS₂, a simple matrix based on 2 step modification process, and tested its electrochemical performance towards the detection of NSE. Compositing MoS₂ with CS provides a strategic approach to prepare a highly stable matrix favorable for immobilization of biomolecules with retention of their bioactivity along with maintenance of signal response. Also, CS provides functional groups to MoS₂ to anchor sites for the attachment of biomolecules on the matrix. Further, the bioelectrode fabricated using CS/MoS₂ matrix exhibits a sensitivity of 3.35 $\mu\text{A ng}^{-1} \text{ mL cm}^{-2}$ and a wide linear detection range of 0.1 to 100 ng mL⁻¹. The bioelectrode is found to be specific, reproducible, regenerable for up to 4 cycles, and has a shelf life of 6 weeks. The sensor has an electroactive surface area of 0.55 cm² and the HET rate has a magnitude of $4.05 \times 10^{-3} \text{ cm s}^{-1}$. Excellent electrochemical performance toward detection of NSE can be attributed to:

- 1) the cumulative effect of MoS₂ and CS imparts stability and biocompatibility to the matrix,
- 2) the introduction of functional groups which lead to the covalent attachment between antibodies and the matrix without the use of any harsh chemicals and,

3) the electroactive surface area is 55% of the geometric area.

The proposed platform can further be explored for the analytical detection of various other protein biomarkers using various electrochemical techniques.

References

- [1] E.C. Welch, J.M. Powell, T.B. Clevinger, A.E. Fairman, A.J.A.F.M. Shukla, *Advances in Biosensors and Diagnostic Technologies Using Nanostructures and Nanomaterials, Advanced Functional Materials*, 31(44) (2021) 2104126.
- [2] T.Ö. Varol, O. Hakli, U.J.N.J.o.C. Anik, Graphene oxide–porphyrin composite nanostructure included electrochemical sensor for catechol detection, *New Journal of Chemistry*, 45(3) (2021) 1734-1742.
- [3] Q. Zhang, X. Li, C. Qian, L. Dou, F. Cui, X.J.A.b. Chen, Label-free electrochemical immunoassay for neuron specific enolase based on 3D macroporous reduced graphene oxide/polyaniline film, *Analytical biochemistry*, 540 (2018) 1-8.
- [4] M. Farrokhnia, G. Amoabediny, M. Ebrahimi, M. Ganjali, M.J.T. Arjmand, Ultrasensitive early detection of insulin antibody employing novel electrochemical nano-biosensor based on controllable electro-fabrication process, *Talanta*, 238 (2022) 122947.
- [5] I.T. Bello, A.O. Oladipo, O. Adedokun, S.M.J.M.T.C. Dhlamini, Recent advances on the preparation and electrochemical analysis of MoS₂-based materials for supercapacitor applications: A mini-review, *Materials Today Communications*, (2020) 101664.
- [6] X. Weng, S.J.I.s.j. Neethirajan, Immunosensor based on antibody-functionalized MoS₂ for rapid detection of avian coronavirus on cotton thread, *IEEE Sensors Journal*, 18(11) (2018) 4358-4363.
- [7] R.-M. Kong, L. Ding, Z. Wang, J. You, F.J.A. Qu, b. chemistry, A novel aptamer-functionalized MoS₂ nanosheet fluorescent biosensor for sensitive detection of prostate specific antigen, *Analytical and bioanalytical chemistry*, 407(2) (2015) 369-377.
- [8] A. Sinha, B. Tan, Y. Huang, H. Zhao, X. Dang, J. Chen, R.J.T.T.i.A.C. Jain, MoS₂ nanostructures for electrochemical sensing of multidisciplinary targets: A review, *TrAC Trends in Analytical Chemistry*, 102 (2018) 75-90.
- [9] N. Kaur, R.A. Mir, O.J.J.o.A. Pandey, Compounds, Electrochemical and optical studies of facile synthesized molybdenum disulphide (MoS₂) nano structures, *Journal of Alloys and Compounds*, 782 (2019) 119-131.
- [10] D.B. Altuntaş, F.J.M.S. Kuralay, E. B, MoS₂/Chitosan/GOx-Gelatin modified graphite surface: Preparation, characterization and its use for glucose determination, *Materials Science and Engineering: B*, 270 (2021) 115215.
- [11] M. Chen, H. Li, X. Su, R. Wu, H. Feng, X. Shi, J. Liang, J. Chen, G.J.N.J.o.C. Li, Label-free electrochemical aptasensor based on reduced graphene oxide–hemin–chitosan nanocomposite for the determination of glypican-3, *New Journal of Chemistry*, 45(19) (2021) 8608-8618.
- [12] Y. Wang, B. Zhang, Y. Tang, F. Zhao, B.J.M.J. Zeng, Fabrication and application of a rutin electrochemical sensor based on rose-like AuNPs-MoS₂-GN composite and molecularly imprinted chitosan, *Microchemical Journal*, 168 (2021) 106505.

- [13] M. Sabbaghan, A.S. Shahvelayati, K.J.S.A.P.A.M. Madankar, B. Spectroscopy, CuO nanostructures: optical properties and morphology control by pyridinium-based ionic liquids, *Spectrochimica Acta Part A: Molecular and Biomolecular Spectroscopy*, 135 (2015) 662-668.
- [14] Carney, DesmondN, DanielC Ihde, MartinH Cohen, PaulJ Marangos, PaulA Bunn JR, JohnD Minna, and AdiF Gazdar. "Serum neuron-specific enolase: a marker for disease extent and response to therapy of small-cell lung cancer." *The Lancet* 319, no. 8272 (1982): 583-585.
- [15] R.A. Soomro, N.H. Kalwar, A. Avci, E. Pehlivan, K.R. Hallam, M.J.B. Willander, Bioelectronics, In-situ growth of NiWO₄ saw-blade-like nanostructures and their application in photo-electrochemical (PEC) immunosensor system designed for the detection of neuron-specific enolase, *Biosensors and Bioelectronics*, 141 (2019) 111331.
- [16] C. Tang, P. Wang, K. Zhou, J. Ren, S. Wang, F. Tang, Y. Li, Q. Liu, L.J.B. Xue, Bioelectronics, Electrochemical immunosensor based on hollow porous Pt skin AgPt alloy/NGR as a dual signal amplification strategy for sensitive detection of Neuron-specific enolase, *Biosensors and Bioelectronics*, 197 (2022) 113779.
- [17] X. Yu, Y. Li, Y. Li, S. Liu, Z. Wu, H. Dong, Z. Xu, X. Li, Q.J.T. Liu, An electrochemical amplification strategy based on the ferrocene functionalized cuprous oxide superparticles for the detection of NSE, *talanta*, 236 (2022) 122865.
- [18] G. Mo, X. He, D. Qin, X. Jiang, X. Zheng, B.J.A. Deng, A potential-resolved electrochemiluminescence resonance energy transfer strategy for the simultaneous detection of neuron-specific enolase and the cytokeratin 19 fragment, *Analyst*, 146(4) (2021) 1334-1339.
- [19] R. Khatri, N.K.J.V. Puri, Electrochemical study of hydrothermally synthesised reduced MoS₂ layered nanosheets, *vacuum*, 175 (2020) 109250.
- [20] W. Zhang, Y. Wang, D. Zhang, S. Yu, W. Zhu, J. Wang, F. Zheng, S. Wang, J.J.N. Wang, A one-step approach to the large-scale synthesis of functionalized MoS₂ nanosheets by ionic liquid assisted grinding, *Nanoscale*, 7(22) (2015) 10210-10217.
- [21] H. Li, Q. Zhang, C.C.R. Yap, B.K. Tay, T.H.T. Edwin, A. Olivier, D.J.A.F.M. Baillargeat, From bulk to monolayer MoS₂: evolution of Raman scattering, *Advanced Functional Materials* 22(7) (2012) 1385-1390.
- [22] A. Zając, J. Hanuza, M. Wandas, L.J.S.A.P.A.M. Dymińska, B. Spectroscopy, Determination of N-acetylation degree in chitosan using Raman spectroscopy, *Spectrochimica Acta Part A: Molecular and Biomolecular Spectroscopy*, 134 (2015) 114-120.
- [23] K. Kasinathan, B. Murugesan, N. Pandian, S. Mahalingam, B. Selvaraj, K.J.I.j.o.b.m. Marimuthu, Synthesis of biogenic chitosan-functionalized 2D layered MoS₂ hybrid nanocomposite and its performance in pharmaceutical applications: in-vitro antibacterial and anticancer activity, *International Journal of Biological Macromolecules*, 149 (2020) 1019-1033.
- [24] J. Wang, W. Zhang, Y. Wang, W. Zhu, D. Zhang, Z. Li, J.J.P. Wang, P.S. Characterization, Enhanced exfoliation effect of solid auxiliary agent on the synthesis of biofunctionalized MoS₂ using grindstone chemistry, 33(11) (2016) 825-832.
- [25] H. Wang, P. Cheng, J. Shi, D. Wang, H. Wang, J. Pezoldt, M. Stich, R. Chen, P.A. van Aken, W.J.G.C. Huang, Efficient fabrication of MoS₂ nanocomposites by water-assisted exfoliation for nonvolatile memories, *Green Chemistry*, 23(10) (2021) 3642-3648.
- [26] M. Zhao, Z. Huang, S. Wang, L.J.C.E.J. Zhang, Ultrahigh efficient and selective adsorption of Au (III) from water by novel Chitosan-coated MoS₂ biosorbents: Performance and mechanisms, *Chemical Engineering Journal*, 401 (2020) 126006.
- [27] Z. Feng, X. Liu, L. Tan, Z. Cui, X. Yang, Z. Li, Y. Zheng, K.W.K. Yeung, S.J.S. Wu, Electrophoretic deposited stable chitosan@MoS₂ coating with rapid in situ bacteria-killing ability under dual-light irradiation, *Small*, 14(21) (2018) 1704347.

- [28] O. Akakuru, H. Louis, P. Amos, O. Akakuru, E. Nosike, E.J.B.P. Ogulewe, The chemistry of chitin and chitosan justifying their nanomedical utilities, *Biochemistry and Pharmacology* (Los Angel), 7(241) (2018) 2167-0501.1000241.
- [29] D. Sandil, S. Srivastava, B. Malhotra, S. Sharma, N.K.J.J.o.A. Puri, Compounds, Biofunctionalized tungsten trioxide-reduced graphene oxide nanocomposites for sensitive electrochemical immunosensing of cardiac biomarker, *Journal of Alloys and Compounds* 763 (2018) 102-110.
- [30] R. Vinoth, I.M. Patil, A. Pandikumar, B.A. Kakade, N.M. Huang, D.D. Dionysios, B.J.A.O. Neppolian, Synergistically enhanced electrocatalytic performance of an N-doped graphene quantum dot-decorated 3D MoS₂-graphene nanohybrid for oxygen reduction reaction, *Acs Omega*, 1(5) (2016) 971-980.
- [31] A.K. Singh, T.K. Dhiman, G. Lakshmi, P.R.J.B. Solanki, Dimanganese trioxide (Mn₂O₃) based label-free electrochemical biosensor for detection of Aflatoxin-B1, *Bioelectrochemistry*, 137 (2021) 107684.
- [32] V.K. Singh, S. Kumar, S.K. Pandey, S. Srivastava, M. Mishra, G. Gupta, B. Malhotra, R. Tiwari, A.J.B. Srivastava, Bioelectronics, Fabrication of sensitive bioelectrode based on atomically thin CVD grown graphene for cancer biomarker detection, *Biosensors and Bioelectronics*, 105 (2018) 173-181.
- [33] Y. Guo, Y. Shu, A. Li, B. Li, J. Pi, J. Cai, H.-h. Cai, Q.J.J.o.M.C.B. Gao, Efficient electrochemical detection of cancer cells on in situ surface-functionalized MoS₂ nanosheets, *Journal of Materials Chemistry B*, 5(28) (2017) 5532-5538.
- [34] Rezki, Muhammad, Ni Luh Wulan Septiani, Muhammad Iqbal, Suksmandhira Harimurti, Poetro Sambegoro, Damar Rastri Adhika, and Brian Yulianto. "Amine-functionalized Cu-MOF nanospheres towards label-free hepatitis B surface antigen electrochemical immunosensors." *Journal of Materials Chemistry B* 9, no. 28 (2021): 5711-5721.
- [35] X. Xi, D. Wu, W. Ji, S. Zhang, W. Tang, Y. Su, X. Guo, R.J.A.F.M. Liu, Manipulating the Sensitivity and Selectivity of OECT-Based Biosensors via the Surface Engineering of Carbon Cloth Gate Electrodes, *Advanced Functional Materials*, 30(4) (2020) 1905361.
- [36] A.A. Aljabali, J.E. Barclay, J.N. Butt, G.P. Lomonosoff, D.J.J.D.t. Evans, Redox-active ferrocene-modified Cowpea mosaic virus nanoparticles, *Dalton transactions*, 39(32) (2010) 7569-7574.
- [37] A. Kaur, S. Rana, A. Bharti, G.R. Chaudhary, N.J.M.A. Prabhakar, Voltammetric detection of vitamin D employing Au-MoS₂ hybrid as immunosensing platform, *Microchimica Acta*, 188(7) (2021) 1-14.
- [38] J. Amani, M. Maleki, A. Khoshroo, A. Sobhani-Nasab, M.J.A.b. Rahimi-Nasrabadi, An electrochemical immunosensor based on poly p-phenylenediamine and graphene nanocomposite for detection of neuron-specific enolase via electrochemically amplified detection, *Analytical biochemistry*, 548 (2018) 53-59.
- [39] Z. Wei, J. Zhang, A. Zhang, Y. Wang, X.J.M. Cai, Electrochemical detecting lung cancer-associated antigen based on graphene-gold nanocomposite, *Molecules*, 22(3) (2017) 392.
- [40] H. Wang, Z.J.M.A. Ma, Amperometric immunoassay for the tumor marker neuron-specific enolase using a glassy carbon electrode modified with a nanocomposite consisting of polyresorcinol and of gold and platinum nanoparticles, *Microchimica Acta*, 184(9) (2017) 3247-3253.
- [41] H. Dong, S. Liu, Q. Liu, Y. Li, Y. Li, Z.J.B. Zhao, Bioelectronics, A dual-signal output electrochemical immunosensor based on Au-MoS₂/MOF catalytic cycle amplification strategy for neuron-specific enolase ultrasensitive detection, *Biosensors and Bioelectronics*, 195 (2022) 113648.

[42] Y. Chen, X.-Y. Ge, S.-Y. Cen, A.-J. Wang, X. Luo, J.-J.J.S. Feng, A.B. Chemical, Ultrasensitive dual-signal ratiometric electrochemical aptasensor for neuron-specific enolase based on Au nanoparticles@ Pd nanoclusters-poly (bismarck brown Y) and dendritic AuPt nanoassemblies, *Sensors and Actuators B: Chemical*, 311 (2020) 127931.

Chapter 6

Summary, Conclusions, and Future Scope of Work

This chapter summarizes the outcomes of the research work carried out to fulfil the objectives of the thesis. It highlights, in brief, the dependency of electrochemical performance on the morphology of MoS₂ nanostructures followed by their modification for their utility in biosensors. Then, the chapter gives a brief overview of the electrochemical performance of fabricated biosensors toward a lung cancer biomarker, neuron-specific enolase (NSE), by modifying MoS₂ nanostructures using reduced graphene oxide (rGO) and chitosan (CS). The chapter also gives a comparison of the electrochemical performance of our bioelectrode with some other platforms. It is found that our bioelectrodes outperform the other bioelectrodes in terms of electroactive surface area and heterogeneous electron transfer rate constant. It also emphasizes the importance of the orientation direction of antibodies on the immobilization matrix and thus explains a superior electrochemical performance of CS/MoS₂ than the rGO/MoS₂-based matrix for the detection of NSE. The chapter concludes by illuminating some prospects of this research work.

6.1 Summary of research work

The main objective of our thesis work was to synthesize and modify 2D nanomaterials for sensing applications. For this purpose, MoS₂ is chosen as one of the 2D nanomaterials owing to its plentiful intriguing properties and its extraordinary performance in various electrochemical applications. Further, MoS₂ nanostructures are modified using reduced graphene oxide (rGO) and chitosan (CS) to anchor functional groups on them for the fabrication of biosensors. The performance of the biosensors is testified for the detection of a lung cancer biomarker. Both the developed platforms exhibited a wide linear detection range, good sensitivity, reproducibility as well as specificity. Our work indicates that surface chemistry plays a crucial role in determining the performance of the biosensor in terms of all the parameters. This unequivocally foretells that tailoring the surface chemistry can be investigated to enhance the sensor performance. The scientific motivation, methodologies adopted and the research work carried out to achieve the objectives of the thesis have been discussed in detail in chapters 1 to 5 and are briefly recapitulated as follows:

➤ **Chapter 1** presents unequalled properties possessed by 2D nanomaterials followed by the versatility of MoS₂ due to which it is chosen for our work. This is followed by a discussion about biosensors, their important components, and their various types. Out of the three main components of biosensors, the antibody is fixed as a biological element, and electrochemical is fixed as the transducing mechanism leaving our main focus on the fabrication of a highly efficient immobilization matrix. An extensive literature is done on the utilization of MoS₂ nanostructures for their utility in various biosensors to circumstantiate their suitability for the fabrication of immobilization matrix. The chapter culminates with a brief discussion about a lung cancer biomarker as the target analyte for examining the performance of fabricated biosensors along with the motivation to pursue this research work.

➤ **Chapter 2** unravels the methods used for synthesis and modifications of MoS₂ nanostructures, along with the EPD technique used for film fabrication. Further, various characterization techniques used to study structural (XRD) and morphological (SEM, FESEM, TEM) characteristics, functional groups, and layered structure (FTIR and Raman spectroscopy) are presented with their working principle and construction. Techniques used for elemental analysis (EDAX, EDXRF, and CHNS) are also talked about. TGA used for thermal analysis is also described with working principle and block diagram. AFM used for topographical analysis, and the surface profilometer used for thickness measurement of films are also elucidated. EIS, CV, and DPV techniques used for testing the electrochemical performance of MoS₂ and modified nanostructures are explained with the basics.

➤ **Chapter 3** encapsulates the extensive use of MoS₂ nanostructures for various electrochemical applications like supercapacitors, Li-ion batteries, hydrogen evolution reactions, sensors, etc. Based on literature it is found that the morphology of these nanostructures plays a huge role in determining the performance of the electrode. Therefore, two varied morphologies of MoS₂ nanostructures are synthesized using a facile and eco-friendly hydrothermal method using two different reducing agents (HH and CA) and characterized using a vast multitude of techniques like XRD, FESEM, TEM, and Raman spectroscopy, EDXRF, and CHNS. Further, they are characterized by their electrochemical performance. The MoS₂ sample synthesized using HH is found to exhibit better electrochemical performance than the sample synthesized using CA. The value of the electrochemical parameters like electroactive surface area (A_e) and heterogeneous electron transfer (HET) rate constant are found to be 51.38 mm² and 0.69×10^{-3} cm s⁻¹ for MoS₂HH and 30.70 mm² and 0.38×10^{-3} cm s⁻¹ for MoS₂CA respectively. Owing to a better

electrochemical performance of the MoS₂HH sample, it is utilized further for biosensing applications by required modification.

➤ **Chapter 4** discusses the modification of the synthesized MoS₂ nanostructures (MoS₂HH) using rGO to anchor carboxylate (-COOH) functional groups on the matrix and their electrochemical performance toward the detection of lung cancer biomarker NSE. rGO is chosen since it has abundant functional groups like carboxylate and hydroxylates, and also being a 2D layered material, it can synergistically graft into MoS₂ layers. The bioelectrode (BSA/anti-NSE/rGO/MoS₂/ITO) fabricated by rGO modified MoS₂ is found to have an electroactive surface area of 27.83 mm², a HET value equal to 1.29×10^{-3} cm s⁻¹. More conduction pathways are provided by a bridged interconnected network between rGO and MoS₂ layers which imparts the matrix a good electrochemical performance. Further, it displays a sensitivity of 2.32 μ A ng⁻¹ mL cm⁻², a linear detection range of 0.1 to 100 ng mL⁻¹, reproducibility with a relative standard deviation of less than 5% with an invariant response towards other endogenous interferents present in human serum. The bioelectrode is found to be stable for immobilization of antibodies till 10 CV cycles.

➤ **Chapter 5** describes the modification of synthesized MoS₂ nanostructures (MoS₂HH) using a biocompatible polymer CS, to enhance the biocompatibility of the matrix along with anchoring amino (-NH₂) functional groups on it. CS is chosen for modification since it has abundant amino groups, has excellent film forming and stabilizing characteristics. The as-fabricated bioelectrode (BSA/anti-NSE/CS/MoS₂/ITO) is tested for its electrochemical performance by again choosing NSE as the target analyte and it is found to have an electroactive surface area of 55 mm², with a HET value of 4.05×10^{-3} cm s⁻¹, a sensitivity of 3.35 μ A ng⁻¹ mL cm⁻², with a linear detection range of 0.1 to 200 ng mL⁻¹. Also, the

bioelectrode is found to be reproducible, specific, and regenerable (4 cycles) and has a shelf life of 6 weeks. It is also found that the bioelectrode can stably hold the antibodies without considerable loss in signal response for 50 CV cycles.

6.2 Conclusions and major takeaways from the research work

- The results of the conducted studies suggest that these matrices could further be explored for the fabrication of devices for early monitoring of various other diseases too using the same strategy.
- It is also observed that CS/MoS₂-based immobilization matrix manifests a better performance than the rGO/MoS₂-based matrix. The reason for an amplified performance shown by CS/MoS₂ matrix can be elucidated by understanding the attachment of antibodies to the immobilization matrix.

The orientation of immobilization of antibodies plays a direct role in determining the stability, along with other biosensing and electrochemical parameters of the matrix [1]. We could achieve covalent attachment of antibodies in both the matrices, however, the direction of attachment of Ab is different in both cases. In rGO/MoS₂, since the matrix has abundant COOH functional groups therefore the antibodies bind from their NH₂ side to form the amide bond. But, as seen in **Fig. 1.4** (chapter 1), the covalent attachment with the NH₂ group of Ab will also lead to partial blocking of antigen (Ag)-binding sites which in turn impacts the overall performance of the biosensor. Whereas in CS/MoS₂ the amino group is abundant, therefore the antibodies bind from the Fc region having the COOH group. Since the sites for attachment of target Ag are freely available in this case, therefore this orientation of attachment of Ab is favored.

Therefore, CS proffers three benefits: **1)** its excellent film forming and stabilizing characteristics ensure a stable matrix, **2)** attachment of amino group favors the orientation of

antibodies for maximum attachment of Ag, **3**) due to favorable attachment of Ab, shelf life and regeneration of the matrix could be possible. This points out that the merits possessed by CS/MoS₂ matrix deserve further exploration for the development of various other biosensors to detect different biomarkers.

➤ **Table 6.1** shows that both the bioelectrodes prepared in our work outperform some of the previously reported bioelectrodes in terms of electrochemical parameters like electroactive surface area and HET rate constant.

Table 6.1: Comparison table of electrochemical parameters of our bioelectrodes with previously reported electrochemical bioelectrodes.

Bioelectrode	Biomarker Detected	A _e (in mm ²)	K _o (cm s ⁻¹)	References
EA/anti-cTnI/APTES/WO ₃ NRs/ITO	cTnI	-	4.47 × 10 ⁻⁵	[2]
BSA/anti-VD/Fe ₃ O ₄ /PANnfs/ITO	Vitamin D	3.8	1.55 × 10 ⁻⁶	[3]
BSA/anti-CYFRA21-1/APTES/nYZR/ITO	CYFRA 21-1	2.58	3.77 × 10 ⁻⁷	[4]
Anti-EPCAM/MoS ₂ @rGO/ITO	EPCAM	-	2.135 × 10 ⁻⁷	[5]

BSA/anti-NSE/rGO/MoS₂/ITO	NSE	27.83	1.29×10^{-3}	Present work
BSA/anti-NSE/CS/MoS₂/ITO	NSE	55	4.04×10^{-3}	Present work

EA- ethanolamine, cTnI – cardiac troponin, APTES – (3-aminopropyl)triethoxysilane, WO₃-tungsten trioxide, NRs - nanorods, VD – Vitamin D, Fe₃O₄ – iron oxide, PANnFs- polyacrylonitrile nanofibers, nYZR – yttria-doped zirconia-reduced graphene oxide nanocomposite, TiO₂- titanium dioxide, EPCAM – epithelial cell adhesion molecules.

➤ Both the matrices are found to be specific because specificity is conferred by antibodies. While good reproducibility is observed in both cases because covalent attachment between the matrix and antibodies is occurring in both cases.

6.3 Prospects of this work

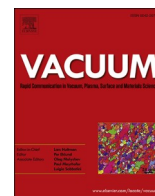
The work carried out in this thesis is an effort to explore the characteristic features of 2D nanomaterials for biosensing applications. Therefore, it opens up wide avenues for a foreseeable future like,

- Paper-based sensors can also be fabricated in the future since they are eco-friendly, disposable, flexible, wearable, and cost-effective [6, 7].
- Efforts can be made to have even better sensitivity and shelf-life of proposed platforms.
- Testing these platforms for various other biomarkers.
- Some other 2D nanomaterials can also be employed like Mxenes (Ti₂C₃), borophene, etc for the fabrication of the immobilization matrix.

- MoS₂ nanostructures can be modified in various other ways using polymers like polyaniline (PANI), and poly (3,4-ethylenedioxythiophene) and tested for their performance for biosensing applications.
- Disposable electrodes can be made for biomedical waste management.
- Advancements are still required to ensure the portability of the system to develop point-of-care devices which are possible by miniaturization of the potentiostat.
- It is well-known fact that monolayers of 2D nanomaterials can be prepared, and have properties different from the bulk. However true miniaturization and monolayers-based devices are possible only with a large-scale synthesis of monolayers. Therefore, a foreseeable future is possible only with a method for a high yield of monolayers.

References

- [1] Nassef, Hossam M., M. Carmen Bermudo Redondo, Paul J. Ciclitira, H. Julia Ellis, Alex Fragoso, and Ciara K. O'Sullivan. "Electrochemical immunosensor for detection of celiac disease toxic gliadin in foodstuff." *Analytical chemistry* 80, no. 23 (2008): 9265-9271.
- [2] Sandil, Deepika, Suresh C. Sharma, and Nitin K. Puri. "Protein-functionalized WO₃ nanorods-based impedimetric platform for sensitive and label-free detection of a cardiac biomarker." *Journal of Materials Research* 34, no. 8 (2019): 1331-1340.
- [3] Chauhan, Deepika, Pramod K. Gupta, and Pratima R. Solanki. "Electrochemical immunosensor based on magnetite nanoparticles incorporated electrospun polyacrylonitrile nanofibers for Vitamin-D3 detection." *Materials Science and Engineering: C* 93 (2018): 145-156.
- [4] Kumar, Suveen, Niharika Gupta, and Bansi D. Malhotra. "Ultrasensitive biosensing platform based on yttria doped zirconia-reduced graphene oxide nanocomposite for detection of salivary oral cancer biomarker." *Bioelectrochemistry* 140 (2021): 107799.
- [5] Jalil, Owais, Chandra Mouli Pandey, and Devendra Kumar. "Highly sensitive electrochemical detection of cancer biomarker based on anti-EpCAM conjugated molybdenum disulfide grafted reduced graphene oxide nanohybrid." *Bioelectrochemistry* 138 (2021): 107733.
- [6] Kumar, Saurabh, Anindita Sen, Suveen Kumar, Shine Augustine, Birendra K. Yadav, Sandeep Mishra, and Bansi D. Malhotra. "Polyaniline modified flexible conducting paper for cancer detection." *Applied Physics Letters* 108, no. 20 (2016): 203702.



Electrochemical study of hydrothermally synthesised reduced MoS₂ layered nanosheets

Ritika Khatri, Nitin K. Puri*

Nanomaterials Research Laboratory (NRL), Department of Applied Physics, Delhi Technological University, Delhi, 110042, India

ARTICLE INFO

Keywords:

rMoS₂
Reducing agents
Electrophoretic deposition
Electrochemical studies

ABSTRACT

In this work, we report one-step, facile and cost-effective synthesis of 2-dimensional (2D) reduced MoS₂ (r-MoS₂) nanostructures via hydrothermal method using two reducing agents. The detection of hexagonal phase, estimation of lattice parameters and crystallite size is done using X-ray diffraction and Williamson-Hall plots are drawn to estimate strain produced in the sample. Field emission scanning electron microscopy (FESEM) and transmission electron microscopy (TEM) confirms the formation of nanosheet like structures. MoS₂ reduced using hydrazine hydrate is found to have better electrochemical properties with heterogenous rate transfer constant equal to 5.03×10^{-4} cm/s and electroactive surface area calculated as 7.05×10^{-4} cm². Raman spectra, TEM images and W-H plots explains the better electrochemical performance of rMoS₂ synthesised using hydrazine hydrate. Also, it is observed that out of electrochemical impedance spectroscopy (EIS), cyclic voltammetry and differential pulse voltammetry, EIS turns out to be best technique for studying electrochemical properties of layered materials. This work provides theoretical guidance to use chemically synthesised rMoS₂ as a matrix for electrochemical sensing applications where an increase or decrease in current/resistance value gives confirmation of attachment of bio/gas molecules and determination of parameters like heterogenous rate transfer constant can indicate sensitivity towards a particular analyte.

1. Introduction

2D materials like graphene, transition metal chalcogenides, hexagonal boron nitride, Mxenes etc are gaining huge popularity in the interdisciplinary fields of nanoscience and material science which includes physics, chemistry as well as biology. 2D nanomaterials include benefits like low cost and high chemical stability. Amongst, these 2D nanomaterials MoS₂ has gained wide popularity pertaining to its layered structure, abundance in nature as molybdenite, good rate of electron transfer, dependency of band gap on no. of layers, possibility of extraction in considerable amount [1] and its plentiful applications like supercapacitors [2], Na/Li- ion batteries [3–5], Hydrogen Evolution Reaction (HER) [6], sensing [7], electronic devices [8,9] etc. It also possesses fine mechanical strength, even better than steel [10]. MoS₂ in its bulk form is a semiconductor with bandgap 1.2 eV, which widens up to 1.8 eV for monolayer MoS₂. Bulk MoS₂ however has low transfer of ions/electrons because it is stacking of large number of layers, which limits its conductivity [11]. Thus, an effective pathway to this is going to nanoscale, thus increasing the surface area and decreasing the total

number of layers to decrease the pathway for diffusion. MoS₂ has characteristics similar to graphene like covalently bonded S–Mo–S sheets which have weak Van Der Waals forces amongst them and therefore have the tendency to be extracted in form of nanosheets like structures [12]. MoS₂ can be synthesised using various methods, among which hydrothermal method is one of the methods which gives large yield, is simple to perform, has low cost and gives an option of controlling morphology of synthesised structures. Also, water is used as reaction solvent making this method environmentally friendly as well [13,14].

Electrochemical activity of MoS₂ determines its use in various applications, but different properties of MoS₂ and different types of parameters are seen for different applications, for instance more no. of active sites will give a better HER and a low overpotential and Tafel plot will determine if a material is good for HER or not [6], while pseudocapacitive behaviour, charge-discharge rates, cycle stability will be seen for supercapacitor [2]. Charge-discharge capacity, cycling stability and specific capacity is seen for Na/Li ion batteries and potential for Na/Li ions intercalation among layers of MoS₂ will determine performance of

* Corresponding author.

E-mail address: nitinkumarpuri@dtu.ac.in (N.K. Puri).

<https://doi.org/10.1016/j.vacuum.2020.109250>

Received 12 October 2019; Received in revised form 4 February 2020; Accepted 6 February 2020

Available online 8 February 2020

0042-207X/© 2020 Published by Elsevier Ltd.

batteries [3–5]. But for sensing, more surface area should be exposed with minimised interlayer spacing so that electron transfer is favoured with good value of heterogenous rate transfer constant [15].

MoS₂ nanostructures are heterogenous on their surface containing mono-/bi-/multi-layered structures of different shapes and sizes. These shapes and sizes depend upon different preparation methods and conditions. For instance, flower like MoS₂ nanostructures (mean diameter 500 nm) are shown to exhibit a better performance as an anode material for Li-ion batteries in comparison to sphere like MoS₂ nanostructures (5–10 μm) because, flower like MoS₂ nanostructures can have better structure change during the conversion process. In the electrochemical impedance spectroscopy (EIS) measurements flower like MoS₂ has a smaller value of charge transfer resistance R_{ct} than MoS₂ spheres, owing to the dense structures of spheres. Ultrathin nanosheets in flower like MoS₂ shortens the diffusion pathway for electrons and Li⁺ ions, which enhances its electrochemical performance [16]. In another work, Ramadoss et al. [17] have synthesised mesoporous structures of MoS₂ for supercapacitor applications where capacity is found to increase due to porous morphology and large surface area of nanostructures which reduces the pathway for ion diffusion which in turn enables fast electron transfer between working electrode and electrolyte. Chen et al. [18] have synthesised MoS₂ nanosheets and nanosheets based hollow porous flat boxes and nanotubes (outside diameter 200–500 nm and thickness 50–70 nm) for electrochemical hydrogen evolution. MoS₂ flat boxes and nanotubes are found to exhibit better electrochemical performance than MoS₂ nanosheets because of a greater number of S²⁻ units, stable arrangement of nanosheets which exposes a greater number of active sites rendering them low overpotentials to reach 10 mA cm⁻². Kumar et al. [19] have reported synthesis of MoS₂ nanoclusters for electrochemical detection of 4 aminophenol (AP). Large surface area of MoS₂ nanoclusters exhibits high electrocatalytic activity towards 4-AP. MoS₂ nanoflakes (size ≥ 1 μm) for fabrication of screen-printed electrochemical sensor for detection of bovine serum has been developed by Kukkar et al. [20]. A simple sensor with detection limit of 6 pg mL⁻¹ is made by utilising cyclic voltammetry technique. Wang et al. [21] synthesised three different morphologies of MoS₂ namely nanospheres (diameter 600–900 nm), nanoribbons (width 200–300 nm and length up to several micrometres) and nanoparticles (600 nm) and studied their electrochemical performance for Li-ion Batteries. MoS₂ nanospheres are found to exhibit best electrochemical performance amongst all morphologies owing to large surface area which provides large number of reaction sites, reduced diffusion length for electrons and ions and can accommodate structural changes.

In our work, Hydrazine hydrate and citric acid are used as reducing agents to mediate the growth of MoS₂ nanostructure by aiding the reduction of oxidation state of Mo (VI) to Mo (IV). Due to excess of ammonia released during the hydrothermal synthesis of MoS₂, NH₃ intercalated MoS₂ nanosheets are formed leading to an increase in interlayer spacing constituting the nanosheets [22,23]. When we don't use reducing agents, samples obtained are not having pure crystalline phase of MoS₂. It has also been reported that intercalated MoS₂ is not of pure crystalline phase [13,23] which renders it a low stability. Also, intercalated MoS₂ nanosheets increases overall distance between layers which will decrease the sensing response. We have also shown in our study that MoS₂ sample synthesised using citric acid as a reducing agent shows low electrochemical performance because of increase in stacking height of layers. Therefore, reduction of ammonia intercalated MoS₂ becomes very important such that the original nanosheet like structure is also retained. Min Li et al. [13] and Mohsin Ali Raza Anjum et al. [23] have given an additional treatment in H₂ reducing atmosphere to hydrothermally synthesised intercalated MoS₂ nano structures, whereas we have reduced ammonia intercalated MoS₂ nanostructures chemically during hydrothermal process only. However, hydrazine hydrate and citric acid leads to growth of these nanosheets in different ways which directly affects electrochemical properties of these nanostructures and their performance for various applications. Even though there are

numerous reports of hydrothermal synthesis of MoS₂ and its electrochemical activity [2–7], but very less emphasis has been given on synthesis of chemically reduced MoS₂ and electrochemical study of electro-phoretically grown films. Therefore, this work discusses electrochemical properties of reduced MoS₂ for its prospective application in the field of electrochemical sensing.

2. Experimental details

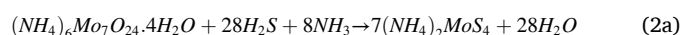
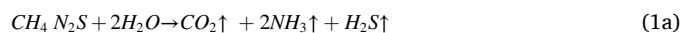
2.1. Materials and solutions

Ammonium Molybdate Tetrahydrate (NH₄)₆Mo₇O₂₄·4H₂O with 99.98% purity is purchased from Sigma Aldrich. Thiourea is purchased from SRL Pvt Ltd. Hydrazine hydrate, potassium bromide, sodium chloride and potassium chloride are purchased from Thermo Fisher Scientific. Concentrated hydro chloric acid is purchased from RFCL limited and acetone is purchased from Rankem. All other chemicals including acetonitrile, potassium hexacyanoferrate (III)/potassium ferricyanide (K₃Fe(CN)₆), potassium hexacyano ferrate(II) trihydrate/potassium ferrocyanide (K₄Fe(CN)₆·3H₂O), sodium di hydrogen phosphate dihydrate (NaH₂PO₄·2H₂O, MW – 156.01 g/mol), di sodium hydrogen diphosphate dihydrate (Na₂HPO₄·2H₂O) and ethanol are purchased from Merck. All the above-mentioned chemicals are used without further purification. All solutions in the experiments are prepared with ultrapure water (Milli-Q water, 18.2 MΩ cm) from a Millipore Milli-Q system (Bedford, MA, USA). All the materials are of analytical grade and are used directly without further purification.

2.2. Preparation of MoS₂ nanostructures

2.2.1. Preparation of MoS₂ without using reducing agents

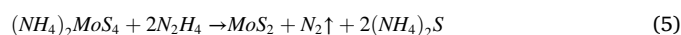
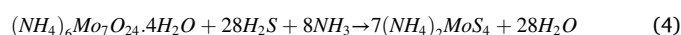
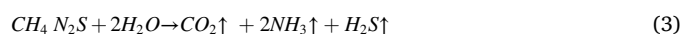
0.08 M of ammonium molybdate tetrahydrate and 1.13 M of thiourea are dissolved in de-ionised water under continuous stirring for 30 min. The resulting solution is then put in a 50 mL Teflon-lined stainless-steel autoclave at a temperature of 230 °C for 24 h. Then it is allowed to cool down to room temperature. The finally obtained product is collected by centrifugation and washed several times using water and ethanol. The precipitates are then vacuum dried at 140 °C for 8 h. The reactions which occur during above procedure are written as follows:



This Sample is labelled as-prepared sample.

2.2.2. Preparation using Hydrazine Hydrate as a reducing agent (MoS₂HH)

0.08 M of ammonium molybdate tetrahydrate and 1.13 M of thiourea are dissolved in de-ionised water under continuous stirring for 30 min 2 mL hydrazine hydrate is added into above prepared solution while stirring only. An acidic pH of 5 is maintained using dilute HCL. The resulting solution is then put in a 50 mL Teflon-lined stainless-steel autoclave at a temperature of 230 °C for 24 h. Then it is allowed to cool down to room temperature. The finally obtained product is collected by centrifugation and washed several times using water and ethanol. The precipitates are then vacuum dried at 140 °C for 8 h. The reactions which occur during above procedure are written as follows:

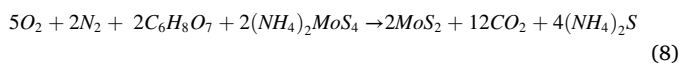
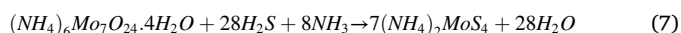
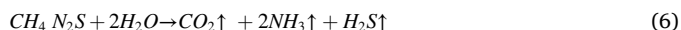


The sample is labelled as MoS₂HH.

2.2.3. Preparation using citric acid as a reducing agent (MoS₂CA)

0.08 M of ammonium molybdate tetrahydrate and 1.13 M of thiourea

are dissolved in de-ionised water under continuous stirring for 30 min. 0.44 M of citric acid is added into above solution while stirring only. The resulting solution is then put in a 50 mL Teflon-lined stainless-steel autoclave at a temperature of 230 °C for 24 h. Then it is allowed to cool down to room temperature. The finally obtained product is collected by centrifugation and washed several times using water and ethanol. The precipitates are then vacuum dried at 140 °C for 8 h. The reactions which occur during above procedure are written as follows:



This sample is labelled as MoS₂CA. Eqns 1a, 3, 6 shows the sulfured reaction, Eqns 2a, 4 and 7 shows the formation of an intermediate product (NH₄)₂MoS₄ while equations (5) and (8) shows the final reduction step of (NH₄)₂MoS₄ which leads to formation of MoS₂. Both these steps that is sulfurization and reduction are important for formation of single phase MoS₂ nanostructures without any presence of MoO₂ or MoO₃ intermediate phases [24] and to remove intercalated NH₃ ions between MoS₂ layers due to production of excess ammonia in equations (1) and (4), respectively [23]. Final reduction step does not take place in case of as-prepared sample as no reducing agent is present to reduce (NH₄)₂MoS₄ due to which pure MoS₂ phase cannot be obtained as shown in Fig. 2. G Nagaraju et al. [24] have reported the formation of MoS₂ Nano bundles citric acid as a reducing agent using a different sulphur source. However, temperature and time play a huge role in controlling the morphology in hydrothermal synthesis of MoS₂ nanostructures.

2.3. Preparation of MoS₂ based electrode for electrochemical studies

MoS₂ is known to have an excess of surface negative charge [25,26], therefore stable films of it can be made by applying an electric field to its stable colloidal suspension in between two electrodes. Electrophoretic method of film deposition offers many advantages like smoothness, homogeneity, uniformity and economic viability, therefore has been chosen for film formation [27,28].

MoS₂HH and MoS₂CA are separately dispersed in de-ionised (DI) water, acetone, ethanol and acetonitrile with a concentration of 1 mg/mL and sonicated in an ultrasonic bath for 30 min at room temperature. The dispersion solutions for both the samples are shown in Fig. 1. It is observed that in DI water and ethanol particles of samples are not

uniformly and homogeneously spread throughout the solution rather got settled at bottom. Films using electrophoretic deposition (EPD) are made using dispersions in acetone and acetonitrile. However, films for samples dispersed in acetone couldn't be uniformly formed, whereas films could be easily formed for samples dispersed in acetonitrile, hence conditions are optimised for dispersion of samples in acetonitrile.

Hence, MoS₂HH and MoS₂CA are separately dispersed in Acetonitrile with a concentration of 1 mg/mL and sonicated in an ultrasonic bath for 30 min at room temperature. This solution is then poured in a 2-electrode cell comprising of a Copper (Cu) working electrode (WE) and Platinum (Pt) as counter electrode (CE). Indium tin oxide (ITO) coated glass slide of dimension 2.5 cm x 1 cm is used as a conducting substrate for depositing film of MoS₂. ITO is attached to WE and put in the solution. Positive polarity is applied to WE and negative polarity is applied to CE. Under a potential of 40 V, negatively charged MoS₂ particles move towards ITO and films are formed by deposition of MoS₂ particles at the electrode-suspension interface. Films are deposited in an area of 1 cm x 1 cm by electrophoretic deposition.

3. Results and discussion

3.1. Characterisation

Various different techniques have been utilised to characterise as

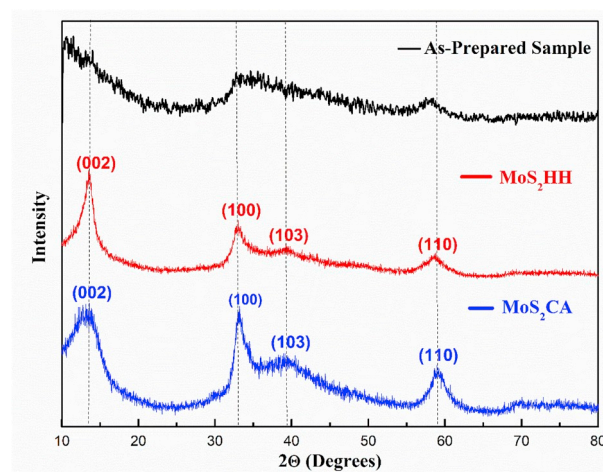


Fig. 2. XRD of as-prepared MoS₂, MoS₂HH and MoS₂CA.

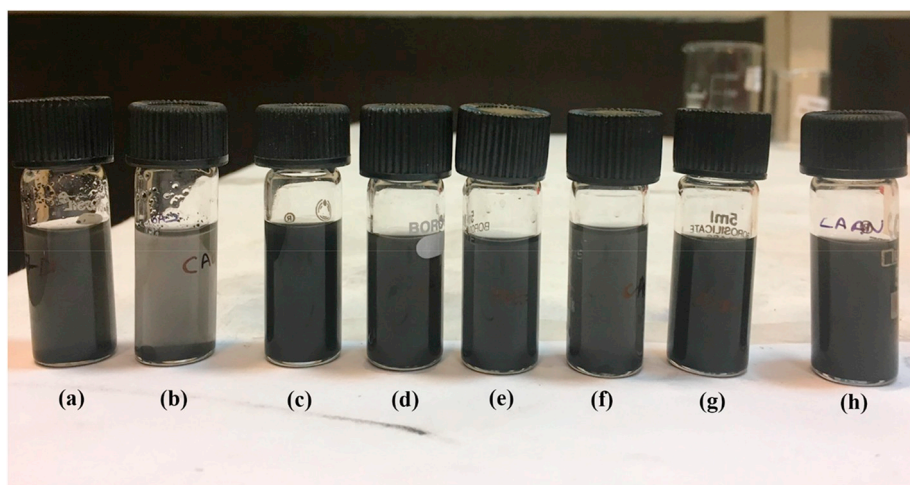


Fig. 1. Dispersion solution of (a) MoS₂HH in DI water (b) MoS₂CA in DI water (c) MoS₂HH in acetone (d) MoS₂CA in acetone (e) MoS₂HH in ethanol (f) MoS₂CA in ethanol (g) MoS₂HH in acetonitrile (h) MoS₂CA in acetonitrile.

synthesised samples. X – Ray diffraction spectra has been recorded using a Bruker D8 Advance facility with Cu K α radiation of wavelength 1.514 Å. Field emission scanning electron microscopy (FESEM) is done using TESCAN model LYRA 3 XMU and is used to examine the morphology of samples. Raman spectra is measured using WITec Raman spectrometer with an excitation wavelength of 532 nm. Fourier transform infrared spectroscopy (FT-IR) is performed using PerkinElmer FT-IR spectrometer. JEOL transmission electron microscope is used to record TEM images. Elemental analysis of synthesised samples is carried out using energy dispersive X-ray fluorescence (EDXRF) technique, using Epsilon 5, PANalytical and CHNS elemental analysis using Vario Micro Cube Elemental Analysensysteme Germany. The electrochemical measurements are done at room temperature by a Metrohm Autolab Potentiostat/Galvanostat using Nova software. The conventional three electrode electrochemical cell is used for electrochemical measurements using MoS₂/ITO as the working electrode, platinum (Pt) wire as the counter electrode, and silver/silver chloride (Ag/AgCl) electrode (in 3 M KCl) as the reference electrode. PBS solution (pH 7.0) containing 5 mM of [Fe(CN)₆]^{3-/4-} and 0.9% NaCl is used as a supporting electrolyte.

3.1.1. XRD

Fig. 2 shows XRD patterns of samples prepared without using reducing agents (as-prepared sample) and with reducing agents which are (MoS₂HH) and (MoS₂CA). Identified peaks for MoS₂HH and MoS₂CA can be indexed to hexagonal MoS₂ (2H MoS₂) with JCPDS card no. 37-1492. A low intensity broadened (002) peak around 11° corresponds to low crystallinity of as-prepared sample and the Peaks (100) and (103) are also not distinguishably visible. Also, the (110) peak is shifted slightly left in comparison to MoS₂ samples prepared using reducing agents. From here it can be concluded that this sample prepared without using any reducing agents is not having pure crystalline phase of MoS₂ and hence further studies are not carried out on this sample. For the other two samples which are prepared using reducing agents, the peaks are found to be broadened and have weak intensity which is due to decrease in size as compared to bulk MoS₂. (002) peak which corresponds to periodicity along c direction is observed to be of less intensity and is broadened which shows that sample is in nano range, however its presence in both the samples (MoS₂HH and MoS₂CA) indicates that MoS₂ formed is not monolayer, rather stacking of large no. of layers [24, 29]. Also, the (002) peak which appears at 14.4° in case of bulk MoS₂ is shifted slightly towards low angle side (13.57°) indicates an expansion towards (001) direction [30]. (002) peak arises because of interlayer Mo–Mo scattering and it can be seen that sample MoS₂HH has a relatively strong and sharp (002) peak in comparison to MoS₂CA, indicating a formation of well crystalline MoS₂HH with ordered stacking along the c-axis [31]. XRD data is analysed using X Powder software for structure determination. Best matching of peaks for both the samples is observed for hexagonal structure. Lattice parameters a, b and c are found using X Powder software and their values are given as shown in Table 1, with reference to JCPDS value. Crystallite size is calculated for both the samples using Debye-Scherrer formula [32].

$$t = 0.9\lambda / (\beta \cos\theta)$$

where t is the crystallite size (average crystallite diameter), λ is the X-ray wavelength i.e. 1.54064 Å, K is the shape factor (0.9), β is the line broadening at half the maximum intensity (FWHM), $\Theta = 2\theta/2$, i.e. the Bragg Angle (in radian). The average crystallite size and micro strain ϵ is

Table 1

Lattice parameters of two samples calculated using X-Powder software.

Lattice Parameters	JCPDS (37-1492)	MoS ₂ HH	MoS ₂ CA
a	3.1612 Å	3.135 Å	3.111 Å
b	3.1612 Å	3.135 Å	3.111 Å
c	12.2985 Å	12.998 Å	13.654 Å
Volume of unit cell	106.43 Å ³	110.63 Å ³	114.44 Å ³

also calculated using Williamson- Hall (W–H) plots using the relation [33].

$$\beta \cos\theta = 4\epsilon \sin\theta + \frac{k\lambda}{D}$$

Where, β is full width at the half maxima (in radian), k is the shape factor, λ is wavelength of the incident X-rays (CuK α , $\lambda = 1.54064$ Å). Fig. 3 shows linearly fitted W–H Plots and their values are given in Table 2. All the peaks (002), (100), (103) and (110) are considered for both the samples. Inverse of y-intercept gives the crystallite size and the slope is a measure of micro strain in the sample, whose values are given in Table 2. Average crystallite size using Debye Scherrer equation is calculated with an experimental error of ± 0.218 nm, while from W–H plots the crystallite size is calculated with an experimental error of ± 5.664 nm. Also, it can be seen that strain in sample MoS₂CA is greater than MoS₂HH which could be possibly due to more stacking of layers in MoS₂CA which is further confirmed from Raman spectra (Fig. 6) and TEM images (Fig. 7) as well.

3.1.2. FESEM

Fig. 4 shows the morphological structures of MoS₂ nanostructures formed using 2 different reducing agents. Fig. 4 a, b and c shows morphology obtained for MoS₂HH while Fig. 4 d, e and f shows the nanostructures obtained for MoS₂CA. At higher scales (Fig. 4a and d) flowers constituting a huge no. of nanopetals/nanosheets which are curled and stacked up together can be seen for both the samples. At small scales (Fig. 4b, 4c, 4e and 4f), these nanosheets are seen to be growing in all directions rendering an uneven surface morphology.

3.1.3. FTIR

Fig. 5 shows the FTIR spectra of MoS₂HH and MoS₂CA. The weak peak around 470 cm⁻¹ can be attributed to Mo–S vibrations [34]. The absorption band at 1633 cm⁻¹ and 1637 cm⁻¹ in case of MoS₂HH and MoS₂CA respectively corresponds to Mo–O vibrations. Strong absorption peak which is observed at 3450 cm⁻¹ can be attributed to stretching vibrations of O–H bonds [35]. Peak at 950 cm⁻¹ corresponds to the S–S bond. More intensity of transmittance peak in FTIR results for MoS₂CA clearly indicates more that more no. of O–H bonds is present than in MoS₂HH. These O–H bonds correspond to water molecules adsorbed on to the samples during synthesis process. Hydrazine hydrate is comparatively a stronger reducing agent than citric acid which removes more water molecules in comparison and decreases the total number of hydroxyl functional group (O–H) from the synthesised sample as evident from FTIR spectra. Another possible reason for more intensity of O–H peak could be O–H bonds itself present in citric acid (Chemical formula – C₆H₈O₇). In order to determine the hydroxide (OH) content present in both the samples, FTIR spectral study has been used. The Beer-Lambert law relates the attenuation of light to the properties of the material through which it is travelling. The Beer-Lambert law in terms of transmission intensities is given as follows [36]:

$$\epsilon cd = \lg \frac{T_0}{T_D} \quad (1b)$$

Where, ϵ is molar absorption coefficient in M⁻¹cm⁻¹, c is molar concentration in M, d is optical path length in cm, T₀ is the highest transmission intensity, while T_D is the transmission intensity of OH bond. To determine the OH content present in the samples, absorption coefficient α_{OH} is calculated [37] which is given by following expression

$$\alpha_{OH} = \frac{\lg \frac{T_0}{T_D}}{d} \quad (2b)$$

d is taken to be thickness of potassium bromide (KBr) pellet prepared of sample for FTIR, which is 1 mm for both MoS₂HH and MoS₂CA. Using Eqn 2b, the calculated value of OH content in MoS₂HH is 2.73 cm⁻¹ and for MoS₂CA it is 3.55 cm⁻¹. From the spectra also it is observed that

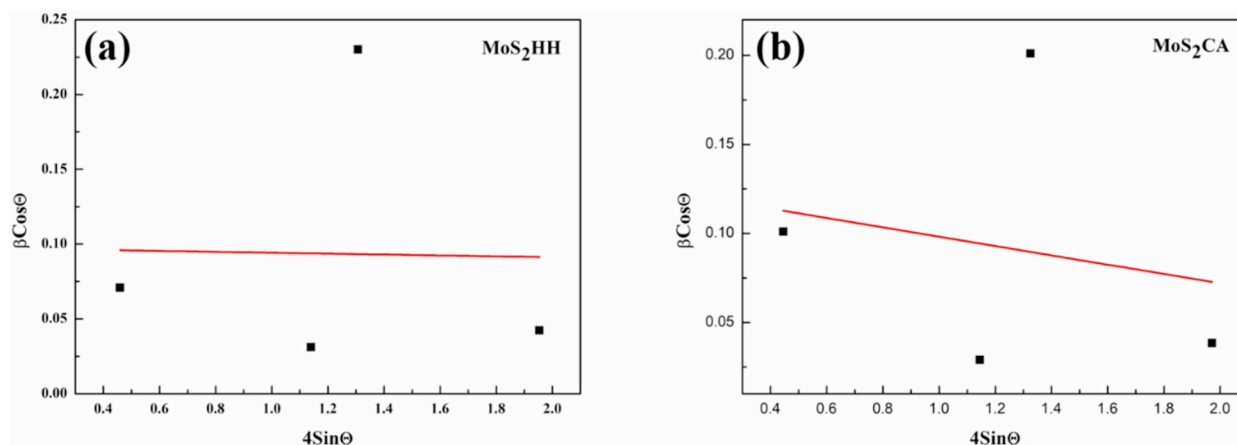


Fig. 3. W-H plots of (a) MoS₂HH and (b) MoS₂CA.

Table 2

Crystallite size calculated using Scherrer formula and W-H plots and strain estimation for two samples.

Sample	Average Crystallite size from Scherrer Formula	Crystallite size from W-H Plots	Strain from W-H Plots
MoS ₂ HH	2.69 nm	1.42 nm	-0.00301
MoS ₂ CA	2.73 nm	1.15 nm	-0.02618

MoS₂CA has more OH content which is shown by its value of absorption coefficient also.

3.1.4. Raman Spectra

Fig. 6 shows Raman spectra of MoS₂HH and MoS₂CA excited by a laser source having wavelength of 532 nm. The Raman Spectrum of MoS₂ has two main peaks: an in plane (E_{2g}^1) mode located around 383 cm⁻¹ and an out of plane mode (A_{1g}) located around 407 cm⁻¹ corresponding to 2H-phase. The in-plane mode corresponds to the sulphur atoms vibrating in one direction and the molybdenum atoms in other, while out of plane mode corresponds to the sulphur atoms vibrating out of plane. The difference (Δ) between (E_{2g}^1) and (A_{1g}) modes can be used to estimate the layer number of MoS₂ nanosheet [38,39]. This value Δ is

around 18 cm⁻¹ for monolayer and approximately equal to 25 cm⁻¹ for multilayer MoS₂ [40,41]. For MoS₂HH, (E_{2g}^1) mode lies at 382.68 cm⁻¹ and (A_{1g}) mode lies at 405.82 cm⁻¹ leading to wavenumber Separation (Δ) of 23.14 cm⁻¹, while for MoS₂CA (E_{2g}^1) mode lies at 385.25 cm⁻¹ and (A_{1g}) mode lies at 410.96 cm⁻¹ leading to wavenumber Separation (Δ) of 25.71 cm⁻¹. Also, the Raman frequencies (E_{2g}^1) and (A_{1g}) peaks vary repeatedly with the number of layers of MoS₂ nanosheets, whereas intensities and widths of the peaks vary arbitrarily. Although the calculated Δ value shows the non-existence of one layer (1L), two layers (2L), three layers (3L) or four layers (4L) but the presence of stacked structures constituting more than four layers [42,43]. With the increase in number of layers, atomic vibrations are suppressed by Vander Waals forces leading to a higher force constant and blue shift of (A_{1g}) mode [22]. Here, a blue shift in (A_{1g}) mode of MoS₂CA confirms higher stacking height in comparison to MoS₂HH which is evident from XRD pattern and TEM (Fig. 7) images as well.

3.1.5. TEM

TEM analysis is carried out by sonicating dispersions of both samples in ethanol and loading a single drop on TEM copper grid. From the TEM images (Fig. 7) it can be observed that layered nanosheets can be observed for both the samples. However, for MoS₂HH these sheets are in

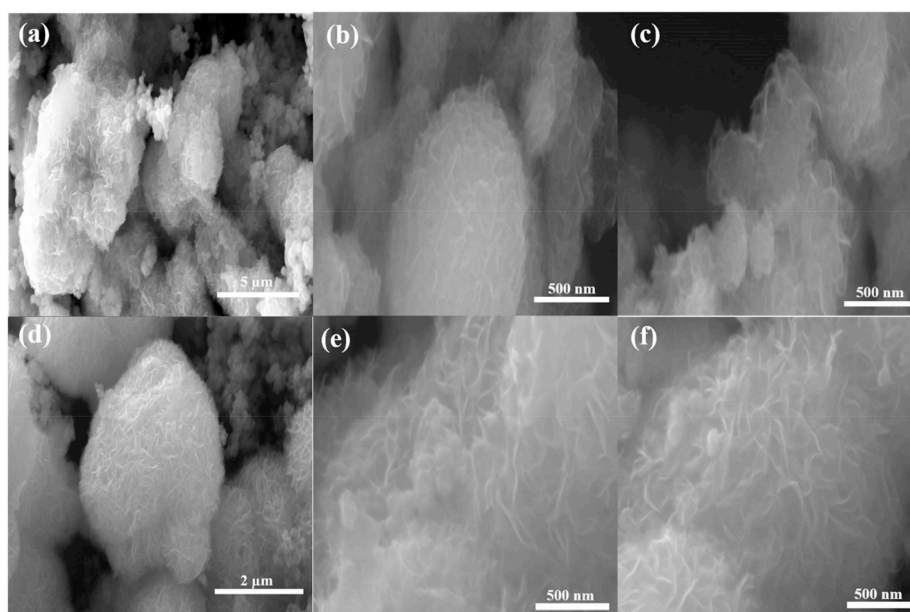
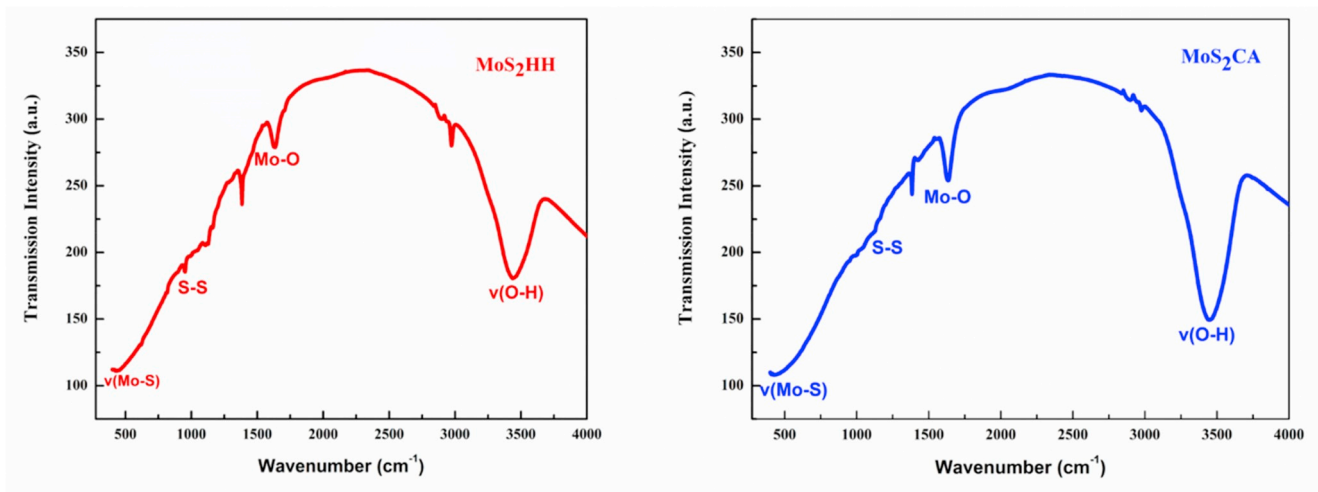
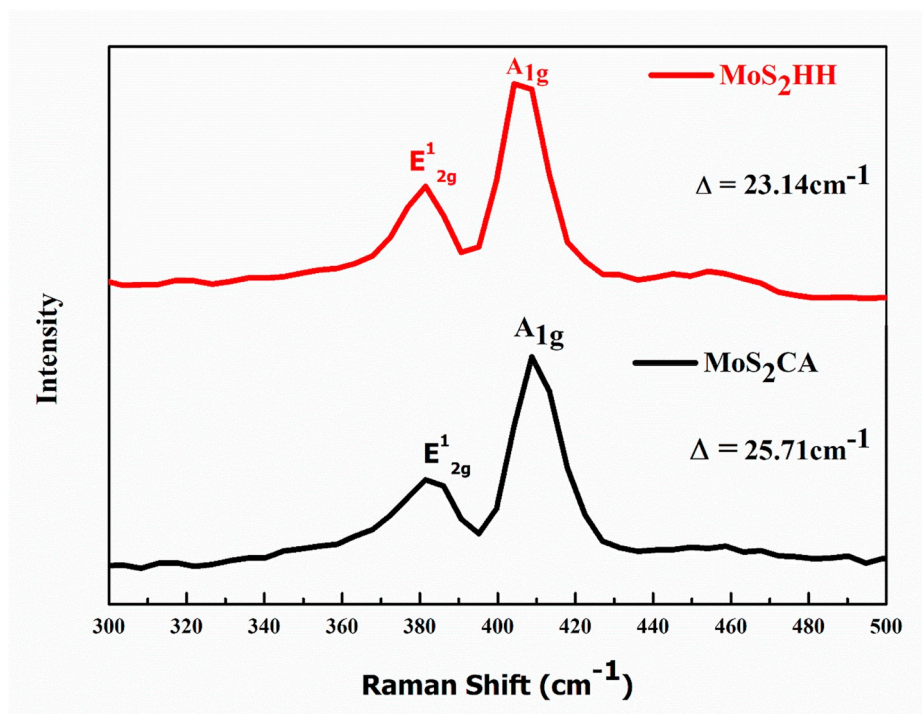


Fig. 4. FESEM Image of MoS₂ nanostructures (a, b, c) MoS₂HH (d, e, f) MoS₂CA.

Fig. 5. FTIR of MoS₂HH and MoS₂CA.Fig. 6. Raman spectra of MoS₂HH and MoS₂CA.

tight contact with each other making the nanosheet film more stable, while for MoS₂CA the nanosheets are not tightly packed together. Increase in stacking height of MoS₂CA is also evident from blue shift of A_{1g} mode in Raman spectra. Both hydrazine hydrate and citric acid acts as reducing agent to reduce the oxidation state of Mo (VI) to Mo (IV), but besides this citric acid also acts as a surfactant to grow nanosheets in a particular way. Such kind of morphological direction to nanostructures by citric acid has also been reported for MoO₂ nano discs [44]. In another work, the effect of citric acid on the growth of ferric oxide was studied, where the size of nanoparticles decreases with increase in concentration of citric acid [45]. This happens, because adsorption of surfactant molecules hinders the growth of Fe₂O₃ nanoparticles. Same thing is perhaps happening in our case where, citric acid molecules are attached on to the layers of MoS₂ nanostructures not allowing them to form tightly packed structures, as seen in TEM images. Therefore, sheets obtained here for MoS₂CA are of small lateral length, growing randomly

and increasing the overall stacking length of layers.

3.1.6. EDXRF

The purpose of this technique is to determine the Molybdenum (Mo) elemental composition of samples. MoS₂HH and MoS₂CA samples are mixed with boric acid to form a pellet by applying a pressure of 5 tons for 10 s. The elemental composition of Mo is listed in Table 3 for MoS₂HH and MoS₂CA.

3.1.7. CHNS

To identify the sulphur (S) content present in synthesised MoS₂ samples and presence of other impurity elements like carbon (C), hydrogen (H) and nitrogen (N), CHNS analysis is done. The elemental percentage for above stated elements is given in Table 3. It can be seen that elemental N impurity in MoS₂HH is more in comparison to MoS₂CA, while elemental C impurity in MoS₂CA is more than in MoS₂HH, which

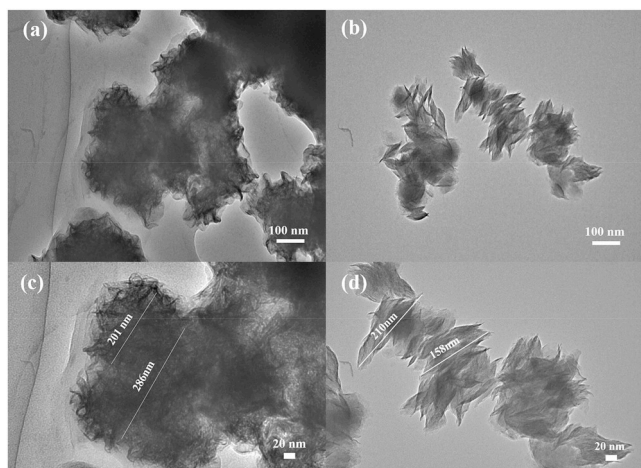


Fig. 7. TEM image (a) MoS₂HH at 100 nm (b) MoS₂CA at 100 nm (c) MoS₂HH at 20 nm (d) MoS₂CA at 20 nm.

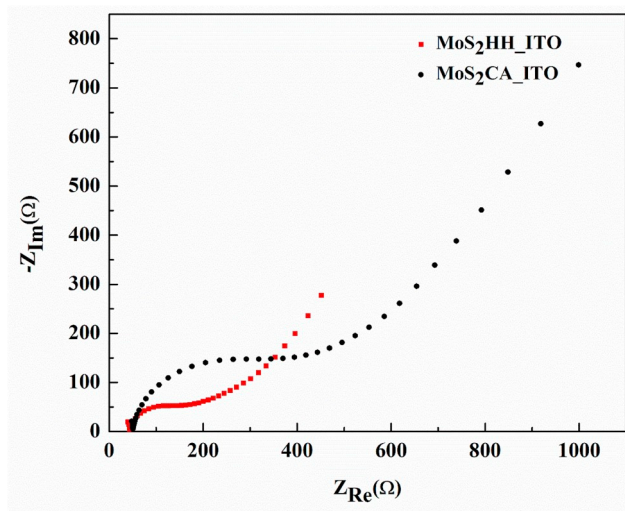


Fig. 8. Electron impedance spectroscopy of MoS₂HH_ITO and MoS₂CA_ITO.

clearly indicates that hydrazine hydrate is a source of more N impurity in MoS₂HH, while citric acid is source of C impurity in MoS₂CA. Total C, H, N contamination is 7.59% and 5.06% in MoS₂HH and MoS₂CA respectively.

3.2. Electrochemical studies

In order to see electrochemical properties of MoS₂ samples prepared using 2 different reducing agents, electrochemical impedance spectroscopy, cyclic voltammetry and differential pulse voltammetry are conducted. Electrodes are made by deposition of prepared samples on ITO and are labelled as MoS₂HH_ITO and MoS₂CA_ITO. For these studies mentioned above 3-electrode cell is taken in which prepared electrodes are employed as working electrode and their electrochemical studies are

Table 3

Elemental composition of MoS₂HH and MoS₂CA determined using EDXRF and CHNS elemental analysis.

Elemental Percentage	Mo	S	C	H	N
MoS ₂ HH	64.41%	28.01%	1.35%	1.86%	4.38%
MoS ₂ CA	61.30%	33.64%	3.14%	0.95%	0.97%

Table 4

Percentage change between results of different electrochemical techniques.

	R _{ct} (EIS)	i _p (CV)	i _p (DPV)
MoS ₂ HH_ITO	150 Ω	546.17 μA	72.02 μA
MoS ₂ CA_ITO	456 Ω	504.15 μA	63.78 μA
Percentage Change	67%	8.33%	13%

Table 5

Comparison of parameters calculated using, used electrochemical techniques.

	Heterogenous Rate Transfer Constant (K _o)	Electroactive Surface Area	Diffusion Controlled Process	Electrochemical Reversibility
MoS ₂ HH_ITO	5.03 × 10 ⁻⁴ cm/s	7.05 × 10 ⁻⁴ cm ⁻²	Yes	i _{pa} /i _{pc} = 1.001 ~Reversible
MoS ₂ CA_ITO	1.79 × 10 ⁻⁴ cm/s	6.51 × 10 ⁻⁴ cm ⁻²	Yes	i _{pa} /i _{pc} = 0.96 Semi reversible

recorded. The electroactive surface area and the heterogenous rate transfer constant are the main factors which determine the electrochemical performance and hence are found using these analytical techniques.

3.2.1. Electrochemical impedance spectroscopy (EIS)

Electrochemical impedance spectroscopy is done in a frequency range of 10⁵ Hz–0.1 Hz at a set potential of 0.01 V (Fig. 8). Semi-circular diameter in case of MoS₂HH is smaller in comparison to that of MoS₂CA giving a R_{ct} value of 150 Ω and 456 Ω respectively. Larger resistance is offered to electrons in case of MoS₂CA which may be due to the larger height and irregular orientation of nanosheet arrays as observed in TEM images (Fig. 7) and confirmed from Raman spectra and XRD pattern as well. Whereas, MoS₂HH has stacked nanosheets therefore decreasing the overall distance that electron has to travel to reach conducting ITO substrate. Software simulated fitting of obtained impedance spectra is done using Randles circuit as shown in Fig. 9 given by R_s (C_{dl}[R_{ct}W_z]) having Warburg impedance in series with charge transfer resistance with this total series component parallel to double layer capacitance (C_{dl}) which is in series with solution resistance R_s. It is observed that good fit for impedance spectra of both the samples can be obtained with χ² value given by 0.99908 and 0.99692 for MoS₂HH and MoS₂CA respectively. Heterogenous electron transfer constant (K_o) can be calculated using the following equation [15].

$$K_o = \frac{RT}{n^2 F^2 2A R_{ct} C}$$

Where, R is universal gas constant, T is room temperature (25 °C), n is the no. of electrons transferred in redox event, F is Faraday's constant, A is electroactive surface area (in cm²), C is bulk concentration of analyte. From here we can calculate value of K_o for MoS₂HH as 5.03 × 10⁻⁴ cm/s for electroactive area (7.05 × 10⁻⁴ cm⁻², as calculated using cyclic voltammetry) and K_o for MoS₂CA as 1.79 × 10⁻⁴ cm/s for electroactive area (6.51 × 10⁻⁴ cm⁻², as calculated using cyclic voltammetry).

3.2.2. Cyclic voltammetry (CV)

Cyclic voltammetry studies are done in a potential window of – 0.6 V to 1.5 V at a scan rate of 50 mV/s (Fig. 10). For MoS₂HH value of peak current in positive direction of voltage scan is found to be 546.17 μA at a potential of 0.693 V while the peak current in negative direction of voltage scan is –545.53 μA at a potential of –0.176 V. While for MoS₂CA same peak currents in two directions of potential scan are found to be a little lesser with a value of 504.15 μA at a potential value 0.544 V and

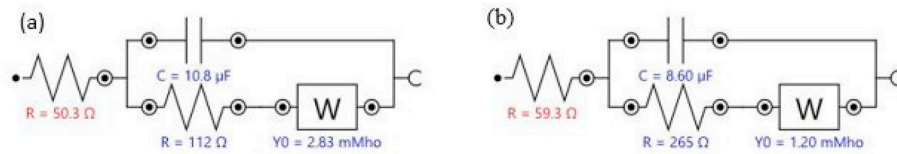


Fig. 9. Randle's circuit (a) MoS₂HH_ITO (b) MoS₂CA_ITO.

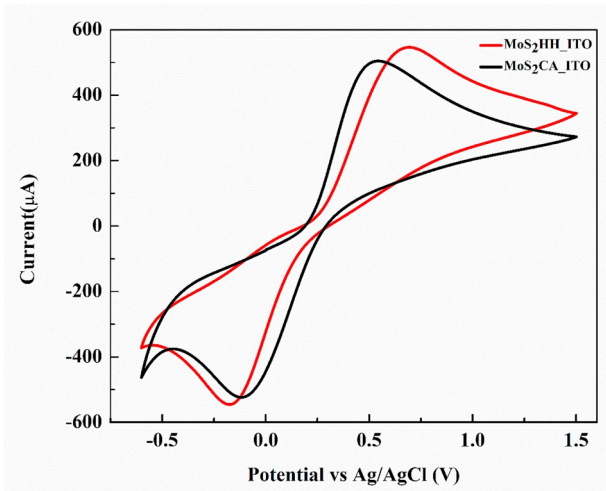


Fig. 10. Cyclic voltammetry of MoS₂HH_ITO and MoS₂CA_ITO.

−523.5 μA at a potential of −0.119 V. Scan rate study for both the samples is done using cyclic voltammetry in the potential window of −0.5 V to 1.2 V at a scan rate of 10 mV/s to 150 mV/s (Fig. 11). Fig. 12 shows the variation of peak anodic current (*i_{pa}*) and peak cathodic current (*i_{pc}*) with square root of scan rate which is a straight line showing that the process is diffusion-controlled [46,47]. By diffusion controlled we mean that the electron transfer takes place between electrode and electrolyte solution and not by adsorption of analyte on electrode surface. For both the samples, electron transfer process is found to be diffusion controlled and can be fitted by the equations (11, 12, 13 and 14);

$$I_{pa}(MoS_2HH) = 0.14137mA + \left[\left(0.05639mA \times \sqrt{\frac{s}{mV}} \right) \times \left(\sqrt{Scan Rate \frac{mV}{s}} \right) \right] \quad (11)$$

$$R^2 = 0.99$$

$$I_{pc}(MoS_2HH) = -0.08271mA + \left[\left(-0.07165mA \times \sqrt{\frac{s}{mV}} \right) \times \left(\sqrt{Scan Rate \frac{mV}{s}} \right) \right] \quad (12)$$

$$R^2 = 0.99$$

$$I_{pa}(MoS_2CA) = 0.14366mA + \left[\left(0.03369mA \times \sqrt{\frac{s}{mV}} \right) \times \left(\sqrt{Scan Rate \frac{mV}{s}} \right) \right] \quad (13)$$

$$R^2 = 0.99$$

$$I_{pc}(MoS_2CA) = -0.07235mA + \left[\left(-0.07525mA \times \sqrt{\frac{s}{mV}} \right) \times \left(\sqrt{Scan Rate \frac{mV}{s}} \right) \right] \quad (14)$$

$$R^2 = 0.99.$$

Here, R is correlation coefficient.

The peak current for a reversible couple is given by Randles-Sevcik equation [48].

$$i_p = 0.446nFAC \sqrt{\left(\frac{nFvD_0}{RT} \right)} \quad (15)$$

Where, n is the no. of electrons transferred in redox event is Faraday's constant, A is electrode surface area (in cm²), v is scan rate (in V/s), D₀ is diffusion coefficient of oxidised analyte (in cm²/s), C is bulk concentration of analyte, R is universal gas constant, T is room temperature (25 °C). By substituting the value of Faraday's constant as 96485 C/mol, value of T as 25 °C and R as 8.314 J/K/mol equation (15) is reduced to equation (16).

$$i_p = 2.69 \times 10^5 n^{3/2} AC \sqrt{D_0 v} \quad (16)$$

Now, by substituting the values of *i_p*, number of electrons transferred (n = 1 for ferro/ferri), D₀ (0.667 × 10^{−5} cm²/s for ferrocyanide [49],

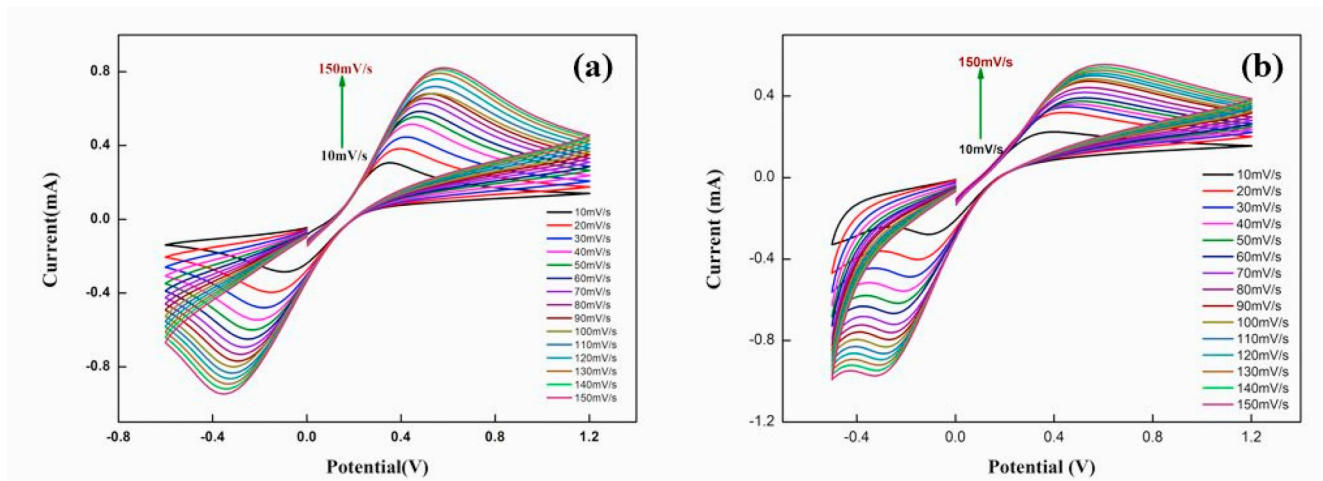


Fig. 11. Scan Rate study of (a) MoS₂HH_ITO and (b) MoS₂CA_ITO at scan rate varying from 10 mV/s - 150 mV/s.

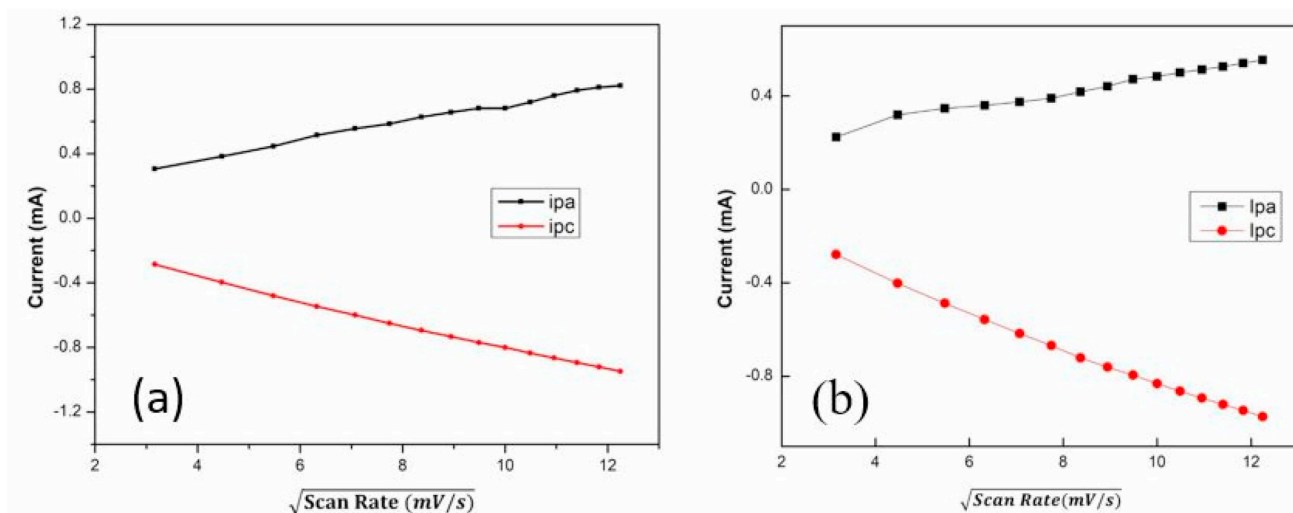


Fig. 12. Variation of i_{pa} and i_{pc} with under root of scan rate (a) MoS₂HH_ITO (b) MoS₂CA_ITO.

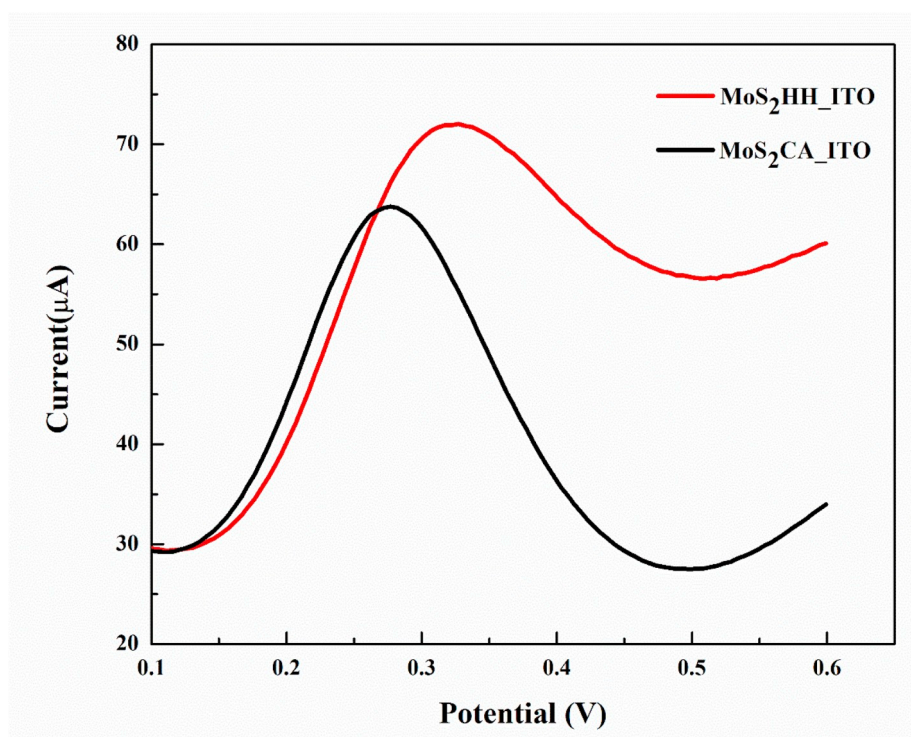


Fig. 13. Differential pulse voltammetry of MoS₂HH_ITO and MoS₂CA_ITO.

which is oxidised analyte for our system), C ($5 \times 10^{-3} \text{ mol cm}^{-2}$) and v (50 mV/s), the electroactive surface area of MoS₂HH electrode can be calculated as $7.05 \times 10^{-4} \text{ cm}^{-2}$, while for MoS₂CA it is $6.51 \times 10^{-4} \text{ cm}^{-2}$.

The value of $i_{pa}/i_{pc} = 1.001$, for MoS₂HH, which is very close to unity showing that the redox system is nearly reversible, however its value for MoS₂CA is 0.96 which shows that system is semi-reversible.

3.2.3. Differential pulse voltammetry (DPV)

DPV studies are conducted in same electrochemical cell with same redox probes as used in CV with a step potential of 0.005 V in a potential window of 0 V to 0.6 V with a scan rate of 10 mV/s (Fig. 13). For MoS₂HH peak current value is 72.02 µA which is reached at a potential of 0.33 V, while MoS₂CA shows peak current at 63.78 µA reaching at a

potential of 0.28 V.

The results are similar to that of cyclic voltammetry, but in this case, it can be seen that the difference is more amplified, reason being in DPV we take a differential pulse which results in an enhanced response.

Significant improvement in current value and resistance value for MoS₂HH is caused by increased effective surface area for heterogeneous electron transfer (HET), due to its high density, closely packed nano-sheet surface. More, stacking height of layers is seen in case of MoS₂CA in TEM images (Fig. 7) whose confirmation is given by Raman spectra and XRD pattern as well. More stacking height of layers increases the diffusion distance of electrons which in turn increases the resistance value and decreases the current response as observed in EIS, DPV and CV respectively.

It can also be clearly observed from Table 4 that the difference

between signals for two samples is maximum observable in EIS (67%) in comparison to DPV (13%) and CV (8.33%). This can be attributed to the layered structure of MoS₂ and excess negative charge on surface of MoS₂ which repels the negative redox probe which hinders the electron transport between redox couple and electrode surface [22,31]. Table 5 shows the comparison of various parameters calculated using different electrochemical techniques.

4. Conclusion

rMoS₂ nanostructures are synthesised using a simple, one-step hydrothermal method by reducing MoS₂ using hydrazine hydrate and citric acid. Sample reduced using hydrazine hydrate is found to exhibit a higher electroactive surface area ($7.05 \times 10^{-4} \text{ cm}^{-2}$) and heterogeneous electron transfer constant ($5.03 \times 10^{-4} \text{ cm/s}$) thus imparting it better electrochemical properties which can be utilised for electrochemical sensing applications where an increase or decrease in current or resistance value can confirm the attachment of gas or biomolecules. Overall, diffusion distance is increased in case of MoS₂ sample reduced using citric acid which is due to stacking of layers confirmed by increase in crystallite strain estimated using W-H plots from XRD data, Blue shift in A_{1g} peak in Raman spectra and visible morphology from TEM images which renders it a low electroactive surface area ($6.51 \times 10^{-4} \text{ cm}^{-2}$) and low heterogeneous electron transfer constant ($1.79 \times 10^{-4} \text{ cm/s}$). We believe that MoS₂ reduced using hydrazine hydrate can be further explored for its applications in sensing owing to its high surface area, good heterogeneous electron transfer constant and nanosheets like structure increasing the total surface area for loading of bio or gas molecules. It can also be concluded that EIS is a better technique for observing measurable difference for layered materials.

Acknowledgements

Authors are thankful to Prof. Yogesh Singh, Vice chancellor, Delhi Technological University, Delhi, India for arranging the research facilities. The financial support received from Science and Engineering Research Board (SERB), Department of Science and Technology (DST), Govt. of India (EMR/2016/007479) is gratefully acknowledged. One of the authors, Ritika is also thankful to Kamal Arora, Kanika Sharma for their support and motivation in writing the manuscript and Sandeep Sarpal and Saroj Kumar Jha for their support in analysis of characterisation techniques results.

References

- [1] C. Anichini, W. Czepa, D. Pakulski, A. Aliprandi, A. Ciesielski, P. Samorì, Chemical sensing with 2D materials, *Chem. Soc. Rev.* 47 (13) (2018) 4860–4908.
- [2] L. Wang, Y. Ma, M. Yang, Y. Qi, Hierarchical hollow MoS₂ nanospheres with enhanced electrochemical properties used as an electrode in supercapacitor, *Electrochim. Acta* 186 (2015) 391–396.
- [3] J. Park, J.-S. Kim, J.-W. Park, T.-H. Nam, K.-W. Kim, J.-H. Ahn, G. Wang, H.-J. Ahn, Discharge mechanism of MoS₂ for sodium ion battery: electrochemical measurements and characterization, *Electrochim. Acta* 92 (2013) 427–432.
- [4] W. Qin, T. Chen, L. Pan, L. Niu, B. Hu, D. Li, J. Li, Z. Sun, MoS₂-reduced graphene oxide composites via microwave assisted synthesis for sodium ion battery anode with improved capacity and cycling performance, *Electrochim. Acta* 153 (2015) 55–61.
- [5] V.H. Pham, K.-H. Kim, D.-w. Jung, K. Singh, E.-S. Oh, J.S. Chung, Liquid phase co-exfoliated MoS₂-graphene composites as anode materials for lithium ion batteries, *J. Power Sources* 244 (2013) 280–286.
- [6] Z. Li, J. Ma, Y. Zhou, Z. Yin, Y. Tang, Y. Ma, D. Wang, Synthesis of sulfur-rich MoS₂ nanoflowers for enhanced hydrogen evolution reaction performance, *Electrochim. Acta* 283 (2018) 306–312.
- [7] M. Pumera, A.H. Loo, Layered transition-metal dichalcogenides (MoS₂ and WS₂) for sensing and biosensing, *Trac. Trends Anal. Chem.* 61 (2014) 49–53.
- [8] F. Urban, M. Passacantando, F. Giubileo, L. Iemmo, A. Di Bartolomeo, Transport and field emission properties of MoS₂ bilayers, *Nanomaterials* 8 (3) (2018) 151.
- [9] A. Di Bartolomeo, A. Grillo, F. Urban, L. Iemmo, F. Giubileo, G. Luongo, G. Amato, L. Croin, L. Sun, S.J. Liang, Asymmetric Schottky contacts in bilayer MoS₂ field effect transistors, *Adv. Funct. Mater.* 28 (28) (2018) 1800657.
- [10] S. Bertolazzi, J. Brivio, A. Kis, Stretching and breaking of ultrathin MoS₂, *ACS Nano* 5 (12) (2011) 9703–9709.

- [11] L. Zhang, W. Fan, W.W. Tjui, T. Liu, 3D porous hybrids of defect-rich MoS₂/graphene nanosheets with excellent electrochemical performance as anode materials for lithium ion batteries, *RSC Adv.* 5 (44) (2015) 34777–34787.
- [12] A.B. Yousaf, M. Imran, M. Farooq, P. Kasak, Synergistic effect of Co-Ni co-bridging with MoS₂ nanosheets for enhanced electrocatalytic hydrogen evolution reactions, *RSC Adv.* 8 (7) (2018) 3374–3380.
- [13] M. Li, D. Wang, J. Li, Z. Pan, H. Ma, Y. Jiang, Z. Tian, Facile hydrothermal synthesis of MoS₂ nano-sheets with controllable structures and enhanced catalytic performance for anthracene hydrogenation, *RSC Adv.* 6 (75) (2016) 71534–71542.
- [14] S. Vattikuti, C. Byon, Synthesis and characterization of molybdenum disulfide nanoflowers and nanosheets: nanotribology, *J. Nanomater.* 2015 (2015) 9.
- [15] D. Sandil, S. Srivastava, B. Malhotra, S. Sharma, N.K. Puri, Biofunctionalized tungsten trioxide-reduced graphene oxide nanocomposites for sensitive electrochemical immunosensing of cardiac biomarker, *J. Alloys Compd.* 763 (2018) 102–110.
- [16] P. Sun, W. Zhang, X. Hu, L. Yuan, Y. Huang, Synthesis of hierarchical MoS₂ and its electrochemical performance as an anode material for lithium-ion batteries, *J. Mater. Chem.* 2 (10) (2014) 3498–3504.
- [17] A. Ramadoss, T. Kim, G.-S. Kim, S.J. Kim, Enhanced activity of a hydrothermally synthesized mesoporous MoS₂ nanostructure for high performance supercapacitor applications, *New J. Chem.* 38 (6) (2014) 2379–2385.
- [18] L. Chen, H. Zhu, Molybdenum sulfide nanosheet-based hollow porous flat boxes and nanotubes for efficient electrochemical hydrogen evolution, *ChemCatChem* 10 (2) (2018) 459–464.
- [19] J.V. Kumar, R. Karthik, S.-M. Chen, K. Saravanakumar, M. Govindasamy, V. Muthuraj, Novel hydrothermal synthesis of MoS₂ nanostructure for sensitive electrochemical detection of human and environmental hazardous pollutant 4-aminophenol, *RSC Adv.* 6 (46) (2016) 40399–40407.
- [20] M. Kukkar, A. Sharma, P. Kumar, K.-H. Kim, A. Deep, Application of MoS₂ modified screen-printed electrodes for highly sensitive detection of bovine serum albumin, *Anal. Chim. Acta* 939 (2016) 101–107.
- [21] X. Wang, Z. Zhang, Y. Chen, Y. Qu, Y. Lai, J. Li, Morphology-controlled synthesis of MoS₂ nanostructures with different lithium storage properties, *J. Alloys Compd.* 600 (2014) 84–90.
- [22] F. Wang, M. Zheng, B. Zhang, C. Zhu, Q. Li, L. Ma, W. Shen, Ammonia intercalated flower-like MoS₂ nanosheet film as electrocatalyst for high efficient and stable hydrogen evolution, *Sci. Rep.* 6 (2016) 31092.
- [23] M.A.R. Anjum, H.Y. Jeong, M.H. Lee, H.S. Shin, J.S. Lee, Efficient hydrogen evolution reaction catalysis in alkaline media by all-in-one MoS₂ with multifunctional active sites, *Adv. Mater.* 30 (20) (2018) 1707105.
- [24] G. Nagaraju, C. Tharamani, G. Chandrappa, J. Livage, Hydrothermal synthesis of amorphous MoS₂ nanofiber bundles via acidification of ammonium heptamolybdate tetrahydrate, *Nanoscale Res. Lett.* 2 (9) (2007) 461.
- [25] T.N. Narayanan, C.S. Vusa, S. Alwarappan, Selective and efficient electrochemical biosensing of ultrathin molybdenum disulfide sheets, *Nanotechnology* 25 (33) (2014) 335702.
- [26] S. Su, W. Cao, W. Liu, Z. Lu, D. Zhu, J. Chao, L. Weng, L. Wang, C. Fan, L. Wang, Dual-mode electrochemical analysis of microRNA-21 using gold nanoparticle-decorated MoS₂ nanosheet, *Biosens. Bioelectron.* 94 (2017) 552–559.
- [27] K. Arora, N.K. Puri, Electrophoretically deposited nanostructured PdO thin film for room temperature amperometric H₂ sensing, *Vacuum* 154 (2018) 302–308.
- [28] K. Zhang, H. Zhang, P. Liu, C. Zhang, W. Li, X. Chen, F. Ma, Electrophoretic deposition of graphene oxide on NiTi alloy for corrosion prevention, *Vacuum* 161 (2019) 276–282.
- [29] K.-K. Liu, W. Zhang, Y.-H. Lee, Y.-C. Lin, M.-T. Chang, C.-Y. Su, C.-S. Chang, H. Li, Y. Shi, H. Zhang, Growth of large-area and highly crystalline MoS₂ thin layers on insulating substrates, *Nano Lett.* 12 (3) (2012) 1538–1544.
- [30] S. Muralikrishna, K. Manjunath, D. Samrat, V. Reddy, T. Ramakrishna, D. H. Nagaraju, Hydrothermal synthesis of 2D MoS₂ nanosheets for electrocatalytic hydrogen evolution reaction, *RSC Adv.* 5 (109) (2015) 89389–89396.
- [31] K.M. Kwok, S.W.D. Ong, L. Chen, H.C. Zeng, Constrained growth of MoS₂ nanosheets within a mesoporous silica shell and its effects on defect sites and catalyst stability for H₂S decomposition, *ACS Catal.* 8 (1) (2017) 714–724.
- [32] L. Alexander, H.P. Klug, Determination of crystallite size with the X-Ray spectrometer, *J. Appl. Phys.* 21 (2) (1950) 137–142.
- [33] G. Williamson, W. Hall, X-ray line broadening from filed aluminium and wolfram, *Acta Metall.* 1 (1) (1953) 22–31.
- [34] S. Liu, X. Zhang, H. Shao, J. Xu, F. Chen, Y. Feng, Preparation of MoS₂ nanofibers by electrospinning, *Mater. Lett.* 73 (2012) 223–225.
- [35] K.-J. Huang, L. Wang, Y.-J. Liu, H.-B. Wang, Y.-M. Liu, L.-L. Wang, Synthesis of polyaniline/2-dimensional graphene analog MoS₂ composites for high-performance supercapacitor, *Electrochim. Acta* 109 (2013) 587–594.
- [36] D. Swinehart, The beer-lambert law, *J. Chem. Educ.* 39 (7) (1962) 333.
- [37] H. Eberndorf-Heidepriem, W. Seeber, D. Ehrh, Dehydration of phosphate glasses, *J. Non-Cryst. Solids* 163 (1) (1993) 74–80.
- [38] B. Sirota, N. Glavin, A.A. Voevodin, Room temperature magnetron sputtering and laser annealing of ultrathin MoS₂ for flexible transistors, *Vacuum* 160 (2019) 133–138.
- [39] M. Barzegar, A. Tiwari, On the performance of vertical MoS₂ nanoflakes as a gas sensor, *Vacuum* 167 (2019) 90–97.
- [40] H. Li, Q. Zhang, C.C.R. Yap, B.K. Tay, T.H.T. Edwin, A. Olivier, D. Baillargeat, From bulk to monolayer MoS₂: evolution of Raman scattering, *Adv. Funct. Mater.* 22 (7) (2012) 1385–1390.
- [41] X. Li, H. Zhu, Two-dimensional MoS₂: properties, preparation, and applications, *J. Materiomics* 1 (1) (2015) 33–44.

- [42] Y. Wang, Y. Du, J. Deng, Z. Wang, Friction reduction of water based lubricant with highly dispersed functional MoS₂ nanosheets, *Colloid. Surface. Physicochem. Eng. Aspect.* 562 (2019) 321–328.
- [43] A.P. Gaur, S. Sahoo, M. Ahmadi, S.P. Dash, M.J.-F. Guinel, R.S. Katiyar, Surface energy engineering for tunable wettability through controlled synthesis of MoS₂, *Nano Lett.* 14 (8) (2014) 4314–4321.
- [44] V. Ramakrishnan, C. Alex, A.N. Nair, N.S. John, Designing metallic MoO₂ nanostructures on rigid substrates for electrochemical water activation, *Chem–A Eur. J.* 24 (68) (2018) 18003–18011.
- [45] A. Bee, R. Massart, S. Neveu, Synthesis of very fine maghemite particles, *J. Magn. Magn Mater.* 149 (1–2) (1995) 6–9.
- [46] A. Vasudev, A. Kaushik, S. Bhansali, Electrochemical immunosensor for label free epidermal growth factor receptor (EGFR) detection, *Biosens. Bioelectron.* 39 (1) (2013) 300–305.
- [47] B.R. Wiston, M. Ashok, Electrochemical performance of hydrothermally synthesized flower-like α -nickel hydroxide, *Vacuum* 160 (2019) 12–17.
- [48] N. Elgrishi, K.J. Rountree, B.D. McCarthy, E.S. Rountree, T.T. Eisenhart, J. L. Dempsey, A practical beginner's guide to cyclic voltammetry, *J. Chem. Educ.* 95 (2) (2017) 197–206.
- [49] S. Konopka, B. McDuffie, Diffusion coefficients of ferri-and ferrocyanide ions in aqueous media, using twin-electrode thin-layer electrochemistry, *Anal. Chem.* 42 (14) (1970) 1741–1746.



Electrochemical biosensor utilizing dual-mode output for detection of lung cancer biomarker based on reduced graphene oxide-modified reduced-molybdenum disulfide multi-layered nanosheets

Ritika Khatri¹, Nitin K. Puri^{1,a)}

¹Nanomaterials Research Laboratory, Department of Applied Physics, Delhi Technological University, Delhi 110042, India

^{a)}Address all correspondence to this author. e-mail: nitinkumarpuri@dtu.ac.in

Received: 13 December 2021; accepted: 23 March 2022

Here, we present an electrochemical biosensor for sensitive, specific, and rapid detection of lung cancer biomarker, neuron-specific enolase by utilization of rGO-modified r-MoS₂ multi-layered nanosheets as a matrix. Layered structures along with the synergetic effect of r-MoS₂ and rGO allow easy grafting of two materials into one another. This empowers the sensor to have a heterogeneous rate transfer constant of 1.29×10^{-3} cm/s and an electroactive surface area of 27.83 mm². Electrochemical impedance spectroscopy and cyclic voltammetry are used as dual modes for the detection of NSE, and the sensor exhibits a wide linear detection range. The sensor is found to be reproducible with a relative standard deviation of less than 5% along with an invariant response towards other endogenous interfering species found in human serum. The investigations done in this study will further help us to fabricate a device for rapid and early detection of lung cancer.

Introduction

Cancer poses a serious life threat to the human race [1]. Among different types of cancers, lung cancer is found to be the major cause of cancer mortality in men, while it is the second major cause of cancer-related deaths in women with the first major cause being breast cancer [1]. Smoking, use of tobacco, and air pollution are found to be some of the major reasons for lung cancer, and only 10 to 20% of people are found to survive after 5 years of diagnosis in most of the countries [1]. To ensure effective and timely treatment and, thus, to alleviate the contribution of lung cancer towards a high rate of mortality across the world, early detection of this cancer is critically important. Conventional techniques that are being used for the detection of cancer, i.e., computed tomography (CT), chest radiography, biopsy, and magnetic resonance imaging (MRI) are accompanied by many disadvantages like limited availability, heavy machinery involved, the skill required for their operations, high cost, etc., which make it very challenging to use them in true essence for early and easy detection of lung cancer. Thus, an alternative and non-cumbersome strategy is required for early detection, to suppress the elevation of cancerous cells in the body at the initial

stage. Electrochemical immunosensors have steadily gained ground in the last decade, all thanks to a large number of advantages which they proffer like a fast response, real-time monitoring, the minimal requirement for pre-processing of the sample, high sensitivity, low sample requirement, and high specificity to name a few [2, 3]. Since the over-expression of cancer protein biomarkers can be closely related to the development or occurrence of cancer, therefore, sensitive and specific detection of these biomarkers at an early stage can reduce the mortality rate.

Neuron-specific enolase (NSE) is found to be expressed in high concentration in patients suffering from small cell lung cancer (SCLC), which makes it a highly specific and sensitive biomarker [4, 5]. A concentration value greater than 12 ng/mL is found in serum for the target biomarker (NSE) in the case of 69% of patients diagnosed with small cell lung cancer (SCLC) [6]. SCLC has a poor prognosis in comparison to other types of lung cancer which necessitates its specific detection at an early stage [5]. Since NSE is overexpressed in serum in case of malignant proliferation of cells leading to SCLC [7], therefore, NSE can be used for diagnosis, prognosis, progression of the disease, and follow-up of SCLC (treatment efficacy) [8]. SCLC has two

clinical stages namely limited-stage disease (LD), and another one is an extensive-stage disease (ED) [7]. The serum NSE level is raised to 13.8 ng/mL and 59 ng/mL in LD and ED patients, respectively [6]. Further, it can be used to check if a patient is responding to cancer treatment or not [6]. Several appreciable reports are available for the detection of NSE using electrochemical techniques. For instance, Han et al. reported the use of gold (Au) nanoparticles-functionalized graphene-based biosensor for detecting NSE in the range 0.001 to 100 ng/mL [4]. Yin et al. utilized the synergistic effect of multi-walled carbon nanotubes (MWCNTs) with metal nanoparticles like Au and palladium (Pd) for realizing an electrochemical biosensor in the linear detection range of 0.001 to 100 ng/mL for NSE [9]. Zhang and co-workers employed another carbon-based nanomaterial that is reduced graphene oxide along with polyaniline (PANI) on a gold electrode for detection of NSE in a linear range of 0.5 pg/mL to 100 ng/mL with an Ag incubation time of 40 min [10]. Wang et al. used polyresorcinol nanocomposite with Au and Platinum (Pt) for detecting NSE, with an optimized incubation time of 50 min [11]. Fu and co-workers synthesized catalysts based on Pt nanoflowers and obtained a pseudo-linear relationship between the log of NSE concentrations and cyclic voltammetry currents [12]. However, the commercial realization of these platforms is impeded by the high cost of metal nanoparticles like gold, palladium, platinum, etc., or usage of gold electrode for fabrication of biosensor, beating the essence of making an electrochemical biosensor. These previous reports along with the biosensing parameters are reported in Table S1 (see Supplementary File). We found that our bioelectrode detected NSE using 2 electrochemical techniques and is found to exhibit less incubation time for attachment of NSE as well as a wide linear detection range in comparison to other bioelectrodes reported in the literature. Table S1 also shows that still, a considerable room is available for the development of new biosensors and exploration of different nanomaterials and substrates to reduce the cost and simultaneously have great electrochemical parameters with enriched activity for early detection of NSE.

MoS₂ is a widely explored material for various applications including biomarker-based biosensing due to its layered structure, a high value of heterogeneous rate transfer constant along with large electroactive surface area [13, 14]. However, the non-availability of any pristine functional groups limits its capability to attach biomolecules onto it, therefore, causing unspecific interaction with analytes. The absence of any dangling bonds promotes physisorption in place of chemisorption, which may be suited when fast response and recovery are required. However covalent linkages are more suitable when biomolecules are immobilized and tested in buffer saline solutions [15, 16]. Thus, the use of MoS₂ in its pristine form is hindered in biosensors. However, an enriched surface-to-volume ratio and its synergistic

effect with most of the materials including polymers, carbon nanomaterials, metal nanoparticles, metal oxides, etc. provide leeway in its surface modification and chemical functionalization [14]. Hence, the incorporation of functional groups can provide reactive sites for covalent linkage with biomolecules in turn enhancing the sensitivity and specificity. Reduced graphene oxide (rGO) which has abundant functional groups like hydroxylate and carboxylate can provide sites for covalent linkages of biomolecules, providing an alternative for functionalization of MoS₂ and harnessing the sensitivity and specificity of device [17]. The utilization of bare rGO as an electrode material is prohibited by the fact that the layers tend to stick together and cause aggregation to reduce the free energy [18]. Both MoS₂ and rGO are 2D nanomaterials which impart them the capability to load more and more biomolecules onto them owing to their high surface-to-volume ratio. Thus, a new gateway is provided to the potential use of various nano-composites like MoS₂-rGO for the detection of various protein biomarkers. There are innumerable reports available on utilization of rGO-modified MoS₂-based matrix as a sensing platform for detection of many potential biomarkers, various organic as well as inorganic molecules [13, 19–21]. However, there is no such report available on the employment of rGO-modified r-MoS₂ multi-layered nanosheets-based matrix utilizing dual modes for electrochemical detection of NSE.

r-MoS₂ corresponds to reduced-MoS₂, which indicates that MoS₂ nanostructures formed are of pure crystalline phase without any intercalated ammonia between MoS₂ nanosheets. Due to excess ammonia released during the synthesis process, ammonia intercalates MoS₂ nanosheets and renders them low stability and low crystallinity [22–25]. Therefore, r-MoS₂-rGO shows better performance than MoS₂-rGO or MoS₂-GO, because of decreased spacing in between the layers, of MoS₂ due to removal of intercalated ammonia facilitating the fast transfer of electrons [22]. Here, r-MoS₂ is used as a supporting matrix to hold the biomolecules and facilitate the smooth transfer of electrons between the electrolyte and electrode, while rGO provides the functional groups for covalent attachment of biomolecules on the surface of the supporting matrix. A few reports are available on the utilization of r-MoS₂ or r-MoS₂-rGO for various electrochemical applications, and the devices have been found to display better performance in the case of r-MoS₂ or r-MoS₂-rGO [23, 26–29].

Therefore, in this work, we explored for the first-time employment of rGO-modified r-MoS₂ multi-layered nanosheets-based matrix for electrochemical detection of NSE, a potential lung cancer biomarker. Scheme S1 (see supplementary file) shows layers of r-MoS₂ bridged by rGO which provides immobilization sites to biomolecules and also acts as conducting channels. Dual-mode output is realized by electrochemical impedance spectroscopy (EIS) and cyclic voltammetry (CV)

electrochemical techniques, which are used to assess the performance of the bioelectrode. The r-MoS₂-rGO-based bioelectrode is found to demonstrate a good sensitivity, a wide linear range of detection, a low incubation time for attachment of NSE, colossal reproducibility, stability, as well as specificity against various other endogenous interferents found in human serum. Since both the cut-off values for LD and ED lie well within the linear detection range of the fabricated bioelectrode, therefore, it can be useful for early detection as well as detection of SCLC at advanced stages.

Results and discussion

Characterization

Structural study using X-ray diffraction (XRD)

Figure 1 shows the XRD pattern of synthesized graphene oxide (GO) and r-MoS₂-rGO. GO shows a diffraction peak centered at 12.73° which confirms the successful formation of graphene oxide by modified Hummer's method [30]. The peak at 12.73° corresponds to a spacing of 0.69 nm in between the layers, which is large in comparison to graphite, which has an interlayer spacing of 0.34 nm ($2\theta = 26.57^\circ$). An increase in interlayer spacing in GO indicates the presence of oxygen-containing functional groups like ketonic and enolic groups [31, 32]. Using the interlayer spacing and the crystallite size obtained from XRD data, the estimated number of layers in GO is found to be ~7. The disappearance of the peak around 12.73° in r-MoS₂-rGO indicates the reduction of GO to rGO [33]. Peaks observed in Fig. 1(b) at 13.91°, 33.27°, 39.62°, and 58.57° are found to be matching with JCPDS Card No. 37-1492 of MoS₂. The absence of any additional peaks indicates the incorporation of only rGO into r-MoS₂, without any impurities being formed. A peak around 26.6° corresponding to rGO could not be observed, which indicates that rGO is uniformly

dispersed into layers of r-MoS₂ [34, 35] without altering the crystal structure of r-MoS₂ [30].

Confirmation of layered structure using Raman spectroscopy

Figure 2 shows the Raman spectra of GO and rGO-modified r-MoS₂. Raman spectrum of GO shows the D band at 1343.69 cm⁻¹ and the G band at 1583.12 cm⁻¹. The I_D/I_G value, which corresponds to the ratio of the intensity of the D and G peaks, is calculated to be 0.99. The D peak corresponds to defect peak which arises due to intervalley scattering, or disorder, while the G peaks arise from in-plane stretching of the C-C bonds present in graphitic structure [34, 36]. Besides the D and G bands, two overtones are also observed corresponding to 2D and D + G peaks at 2697.25 and 2895.71 cm⁻¹, respectively. r-MoS₂-rGO shows two peaks corresponding to E_{2g}¹ and A_{1g} modes of MoS₂ at 380.77 and 405.97 cm⁻¹, respectively. The separation between E_{2g}¹ and A_{1g} modes can be used to identify the number of layers in MoS₂ [22]. A separation of 25.2 cm⁻¹ in our case pertains to multilayers of r-MoS₂ in r-MoS₂-rGO. In addition to these peaks, the D and G bands corresponding to rGO are also observed at 1348.92 cm⁻¹ and 1584.16 cm⁻¹. Also, the I_D/I_G value is found to be ~1.03 in r-MoS₂-rGO. An increase in value of I_D/I_G for r-MoS₂-rGO in comparison to GO indicates the creation of new graphitic domains which are smaller in size in comparison to those present in GO before reduction [37]. Also, an increase in I_D/I_G value from 0.99 to 1.03 implies a successful reduction of GO in r-MoS₂-rGO [38].

Identification of functional groups using Fourier transform infrared spectroscopy (FTIR)

The FTIR spectra of GO and rGO-modified r-MoS₂ are shown in Fig. 3. Absorption peaks which are seen in case of GO are assigned to OH stretching (3436 cm⁻¹), C=O carbonyl (1705 cm⁻¹), aromatic C=C (1624 cm⁻¹), -C-O carbonyl (1366 cm⁻¹), epoxy -C-O (1262 cm⁻¹), -C-OH- (1235 cm⁻¹), and C-O alkoxy (1098 cm⁻¹) [39,

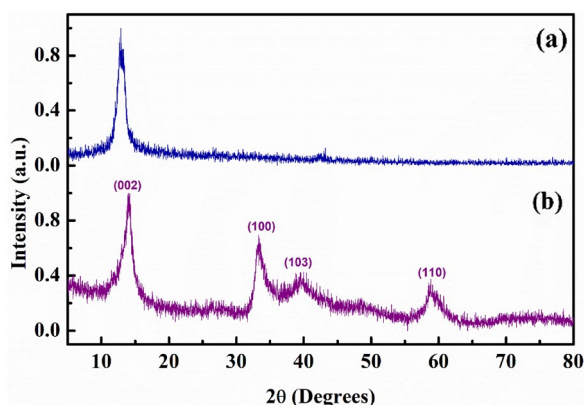


Figure 1: XRD spectra of (a) GO and (b) rGO-modified r-MoS₂.

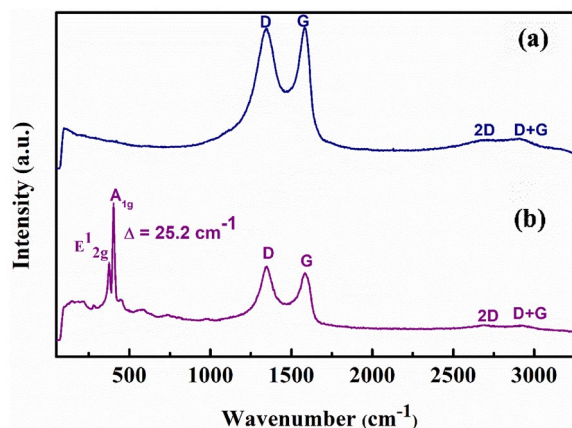


Figure 2: Raman spectra of (a) GO and (b) rGO-modified r-MoS₂.

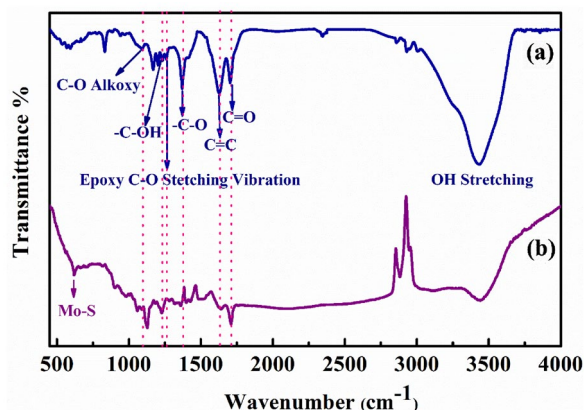


Figure 3: FTIR spectra of (a) GO and (b) rGO-modified r-MoS₂.

40]. In the FTIR spectrum of r-MoS₂-rGO, a peak corresponding to Mo-S vibrations is observed at 619 cm⁻¹ [41]. A decrease in the peak intensity of all the oxygen-containing functional groups as well as the disappearance of some groups like epoxy and alkoxy -C-O indicates a successful reduction of GO into rGO [42, 43] in r-MoS₂-rGO. Simultaneously the presence of all the other functional groups also shows successful grafting of rGO into multilayers of r-MoS₂ [44, 45].

Morphological study using scanning electron microscopy (SEM)

Figure 4 shows the morphology obtained for GO as well as rGO-modified r-MoS₂. Figure 4(a) shows large, crinkled sheets pertaining to GO, with large lateral length and surface area. At low magnification [Fig. 4(b) and (c)], nano-units comprising layers of rGO, as well as various irregularly shaped flowers of MoS₂, can be observed. Further, at higher magnifications [Fig. 4(d) and (e)], flowers of MoS₂ can be seen consisting of numerous layers and nano rod-like structures of rGO are also visible. rGO layers have a natural tendency to scroll and curl up, because of the thermodynamic stability which accompanies bending [46, 47]. The average length for rGO nanorods is calculated to be 1.66 μm by plotting a histogram [Fig. 4(f)]. This type of interconnected bridging network formed between rGO and r-MoS₂ can provide conduction pathways for rapid transportation of electrons and can be greatly beneficial for the formation of electrochemical sensors. The consonance of the multi-layered nature of both GO and r-MoS₂ as affirmed by XRD and Raman, probably leads to unstinted grafting of rGO into the r-MoS₂ matrix. This also indicates the synergetic nature of both materials.

Elemental analysis using energy dispersive X-ray analysis (EDX)

Elemental analysis of GO and r-MoS₂-rGO nanocomposite is done using EDX on different areas of the sample. Figure S1(a), S1(b), and S1(c) shows some of the selected areas, and Table S2 shows the atomic percentages of elements present in GO and

r-MoS₂-rGO. EDX data show the presence of Carbon (C) and Oxygen (O) in both GO and r-MoS₂-rGO along with Molybdenum (Mo) and Sulfur (S) content in r-MoS₂-rGO. The lower oxygen content (20.60%) in nanocomposite in comparison to GO (31.68%) indicates the reduction of GO to rGO [48].

Thermal analysis using thermogravimetric analysis (TGA)

Thermal stability of the as-prepared samples is determined by TGA in the presence of air with a heating rate of 10 °C in the temperature range from 10 to 900 °C (shown in Fig. 5). The thermal instability of GO is quite evident from Fig. 5(a) which shows a huge weight loss at 200 °C. This high weight loss could be due to the thermal decomposition of oxygen-containing functional groups present in GO [37, 39]. On the other hand, it is observed that r-MoS₂ and r-MoS₂-rGO are found to have better thermal stabilities in comparison to GO. The TGA of r-MoS₂ shows two steps of weight loss: (i) below 100 °C and (ii) between 300 to 550 °C, indicating a weight loss of 46%. r-MoS₂-rGO is found to exhibit weight loss in the range 320 to 400 °C, after which the sample is found to be stable (with a weight loss of only 17%). Due to the decrease in the number of oxygen-containing functional groups in rGO present in r-MoS₂-rGO, a sudden weight loss around 200 °C is not observed; rather the modified matrix is rendered the highest thermal stability among all three samples. All three samples undergo a weight loss below 100 °C due to the evaporation of adsorbed water molecules.

Analysis of various steps of preparation of bioelectrode using atomic force microscopy (AFM)

To assess the topography of the final bioelectrode, AFM images are recorded for various stages of preparation of bioelectrode. Figure 6 shows the topographical image of (a) r-MoS₂-rGO/ITO, (b) anti-NSE/r-MoS₂-rGO/ITO, and (c) BSA/Anti-NSE/r-MoS₂-rGO/ITO. The topography varies from large clusters in Fig. 6(a) to small globules in Fig. 6(b) to larger globules as observed in Fig. 6(c). The anti-NSE /r-MoS₂-rGO/ITO electrode is found to have a root-mean-square (rms) roughness value of 0.80 nm, due to the smooth distribution of globular antibodies onto r-MoS₂-rGO/ITO, which itself has an rms roughness value of 1.01 nm. The BSA/Anti-NSE/r-MoS₂-rGO/ITO is found to have an rms roughness value of 0.87 nm. An increase in the value of rms roughness of the bioelectrode in comparison to anti-NSE/r-MoS₂-rGO/ITO could be ascribed to attachment of BSA to block the non-specific binding sites. The observable change in topography along with the rms value of surface roughness confirms the modification at each step of preparation of bioelectrode.

Electrochemical studies

Investigation of the electrochemical performance of the as-prepared biosensor is done using various electrochemical

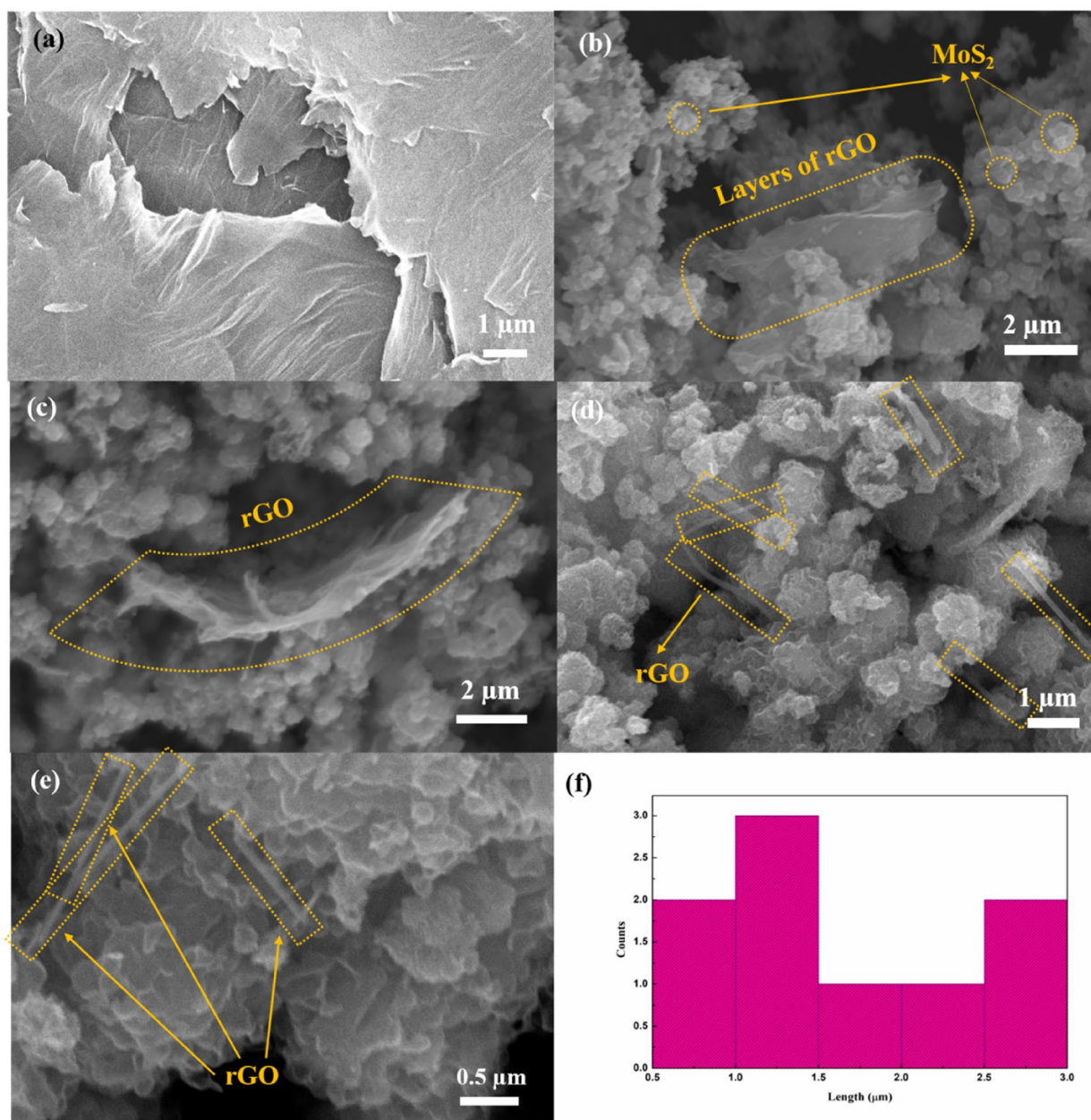


Figure 4: (a) SEM image of GO and (b, c, d, e) SEM images of rGO-modified r-MoS₂ multi-layered nanosheets (f) Histogram of length distribution of rGO in r-MoS₂-rGO.

studies. All the EIS experiments are performed at a biasing potential of 0.01 V and in the frequency range of 0.1 Hz to 100 kHz. The optimization of antibody concentration, antigen incubation time, stability, and sensitivity study of bioelectrode are done by CV in a potential bracket of -0.4 V to 1.2 V at a 50 mV/s scan rate. The EIS and CV studies are done in 0.1 M phosphate buffer saline (PBS, pH 7.4) solution containing 5 mM redox probe $[\text{Fe}(\text{CN})_6]^{3-/4-}$.

Optimization of biosensing parameters

The concentration of antibodies to be attached to the r-MoS₂-rGO matrix is optimized by varying concentrations of anti-NSE antibodies from 10 to 100 μg/mL. CV studies (Fig. S2) are carried out, and the peak current is found to decrease with the increase in concentration up to 25 μg/mL. After 25 μg/mL, a small increase in the value of current is observed for concentrations 50 and 100 μg/mL. The minimum value of current for a concentration of 25 μg/mL implies maximum attachment of

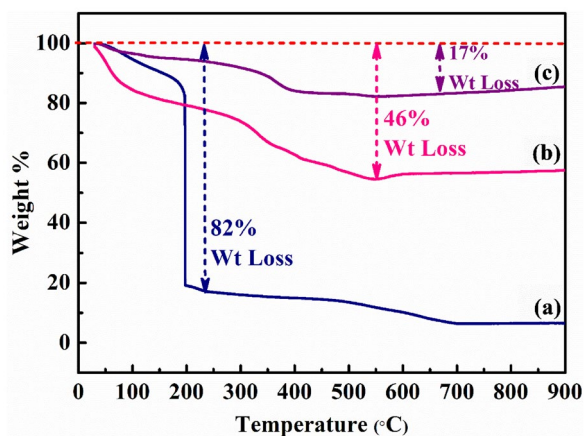


Figure 5: TGA curves of (a) GO (b) r-MoS₂ (c) rGO-modified r-MoS₂.

antibodies, while for higher concentrations (50 and 100 µg/mL), an increase in current could be due to overcrowding of antibodies resulting in lesser attachment to the surface. Thus, 25 µg/mL is finalized for attachment of anti-NSE onto the r-MoS₂-rGO/ITO electrode.

To optimize the time of incubation of NSE, 5 ng/mL of NSE is attached to the bioelectrode (BSA/Anti-NSE/r-MoS₂-rGO/

ITO). The incubation time of NSE is varied from 5 to 30 min. The CV study is conducted, and the peak current varying with the variation of incubation time is plotted in Fig. S3. It can be seen that, with the increase in time from 5 to 15 min, the current is found to be decreasing. However, after 15 min, the current becomes nearly constant indicating that the maximum attachment of NSE onto the BSA/Anti-NSE/r-MoS₂-rGO/ITO has occurred. Henceforth, 15 min is finalized as the time for incubation of NSE on the bioelectrode.

Electrochemical characterization and stability study of modified electrode

EIS technique gives the Nyquist plot between the imaginary part and the real part of the impedance, and the diameter of the semicircle, thus, obtained gives the value of charge transfer resistance (R_{ct}). To confirm the modification at various steps of preparation of the bioelectrode, EIS measurements are done at each step and the attachment is readily probed by varying Nyquist plots. Figure 7(a) shows EIS curves of r-MoS₂-rGO/ITO, anti-NSE/r-MoS₂-rGO/ITO, and BSA/Anti-NSE/r-MoS₂-rGO/ITO electrodes. The corresponding R_{ct} values are found to be 211.69 Ω, 125.38 Ω, and 147.75 Ω for r-MoS₂-rGO/ITO, anti-NSE/r-MoS₂-rGO/ITO, and BSA/Anti-NSE/r-MoS₂-rGO/ITO electrodes, respectively. The

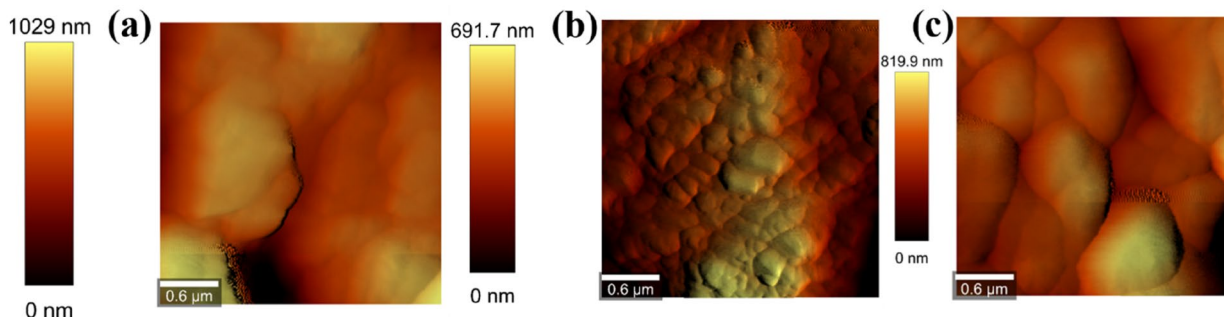


Figure 6: Topographical images taken using AFM of (a) r-MoS₂-rGO/ITO (b) anti-NSE/r-MoS₂-rGO/ITO and (c) BSA/Anti-NSE/r-MoS₂-rGO/ITO electrodes.

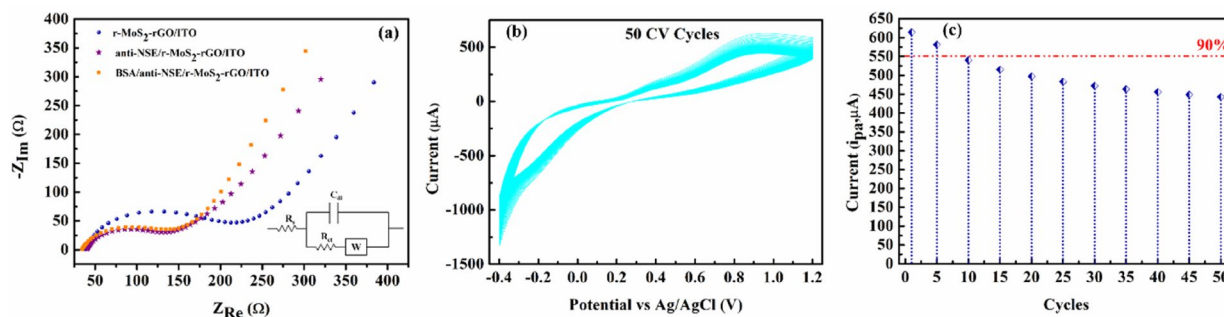


Figure 7: (a) Electrochemical response of r-MoS₂-rGO/ITO, anti-NSE/r-MoS₂-rGO/ITO and BSA/Anti-NSE/r-MoS₂-rGO/ITO electrodes, (b) Stability study of BSA/Anti-NSE/r-MoS₂-rGO/ITO bioelectrode with 50 continuous CV cycles at scan rate 50 mV/s (c) Plot of anodic peak current (i_{pa}) with respect to CV cycles.

variation in values of R_{ct} at different steps of modification confirms the attachment of moieties at the electrode surface. The R_{ct} value is found to be lowest for the Anti-NSE/r-MoS₂-rGO/ITO electrode, which may be due to the orientation of antibodies on the electrodes in such a way that the transfer of electrons between the redox probe [Fe(CN)₆]^{3-/4-} and the electrode is facilitated [49]. The value of R_{ct} for BSA/Anti-NSE/r-MoS₂-rGO/ITO electrode increases when compared to that of Anti-NSE/r-MoS₂-rGO/ITO electrode because of the insulating nature of BSA protein molecule [50]. However, the impedance offered to the flow of electrons is still balanced by the formation of an iron-binding complex between BSA and Fe present in redox probe, which leads to the formation of iron-chelates facilitating easy flow of electrons [51]. r-MoS₂-rGO_ITO electrode is found to exhibit maximum resistance to the flow of electrons which might be due to the presence of negatively charged carboxyl groups (COO⁻), on the r-MoS₂-rGO matrix which repels the flow of electrons from the electrolyte to the electrode. The inset of Fig. 7(a)

anti-NSE/r-MoS₂-rGO/ITO, and BSA/Anti-NSE/r-MoS₂-rGO/ITO electrodes, and corresponding values of α are obtained to be 0.71, 0.65, and 0.66, respectively. A departure in the value of α from 1 shows that the behavior of the prepared electrodes can be attributed to surface heterogeneity and not to the double-layer capacitance.

Demonstration of stability of the bioelectrode is done by scanning the BSA/Anti-NSE/r-MoS₂-rGO/ITO electrode for 50 continuous CV cycles [Fig. 7(b)]. 94% and 88% of the initial current are still retained after the 5th and 10th cycle, respectively [Fig. 7(c)]. Thus, the bioelectrode demonstrates acceptable stability till the 10th cycle. This essentially unchanged behavior of CV indicates that antibodies are stably immobilized onto the bioelectrode for 10 cycles. To acquire a better understanding of the electrochemical performance of the bioelectrode, a scan-rate-dependent study is conducted by varying the scan rate from 10 to 100 mV/s (Fig. S5). The anodic peak current (i_{pa}) is found to be varying linearly with the under root scan rate, showing that the process is diffusion-controlled [54] (Fig. S5, inset). The equation of the linearly fitted curve is given by (2)

$$i_{pa(\text{BSA/Anti-NSE/MoS}_2\text{-rGO/ITO})} = 195.29 \mu\text{A} + \left[30.55 \frac{\mu\text{A}}{\sqrt{\frac{\text{mV}}{\text{s}}}} \times \sqrt{\text{Scan rate} \frac{\text{mV}}{\text{s}}} \right], \quad (2)$$

shows the equivalent circuit used to fit the obtained experimental data. Owing to the heterogeneous nature of electrode surface, ($R_s(Q[R_{ct}W_z])$) is used as the equivalent circuit and constant phase element (CPE) denoted by Q is used in place of double-layer capacitance (C_{dl}) [52]. R_s denotes the solution resistance, which is not affected by the interfacial kinetics. The electron transfer resistance R_{ct} , Warburg impedance W_z , and CPE depend upon interfacial kinetics between the working electrode and electrolyte. Table S3 reports the values of fitted parameters.

Further, elucidation of using the CPE in place of C_{dl} is given by understanding the formulation of CPE. The representation of CPE is done as follows [53].

$$Z_{\text{CPE}} = \frac{1}{Q(j\omega)^\alpha}, \quad (1)$$

where Z_{CPE} is CPE impedance, Q is a modeling parameter, j is the imaginary number ($j = \sqrt{-1}$), ω is the angular frequency (in Hz), and α is a parameter having a value in between 0 and 1. For $\alpha = 1$, CPE behaves as a capacitor, and for $\alpha = 0$ and $\alpha = -1$, CPE behaves as a resistor and inductor, respectively [52]. The value of α can be obtained by the slope of plot between the imaginary part of impedance and frequency on a logarithmic scale [52]. Figure S4 shows the plot between the imaginary part of impedance and frequency on a logarithmic scale for r-MoS₂-rGO/ITO,

$$R^2 = 0.997.$$

Various electrochemical parameters are also calculated like electroactive surface area (A_e) and heterogeneous electron transfer constant (K_o). The value of electroactive surface area (A_e) is calculated by using the slope of Eq. (2) and Randles Sevcik equation [22, 55]:

$$i_p = 2.69 \times 10^5 n^{3/2} A_e C \sqrt{D_o v}, \quad (3)$$

where i_p is the peak current, n denotes the number of transferred electrons (which is equal to 1 for Ferro/Ferri), C denotes the concentration of redox-active species (5 mM), D_o is diffusion coefficient (0.667×10^{-5} cm²/s) [56], and v is the scan rate. Hence, the electroactive surface area is determined to be 27.83 mm². Correspondingly, K_o is determined by the equation mentioned as follows [22]:

$$K_o = \frac{RT}{n^2 F^2 A_e R_{ct} C}, \quad (4)$$

where F is Faraday's constant (96,485 C/mol), R is the universal gas constant (8.314 J/K/mol), and all the other parameters are the same as Eq. (3). And thus, using Eq. (4), the value of K_o is determined to be 1.29×10^{-3} cm/s for BSA/Anti-NSE/MoS₂-rGO/ITO bioelectrode.

Interestingly, the BSA/Anti-NSE/r-MoS₂-rGO/ITO bioelectrode is found to exhibit better electrochemical parameters in comparison to various other electrochemical biosensors

TABLE 1: Electrochemical parameters calculated for the prepared bioelectrode and its comparison to other electrochemical sensors, reported in the literature.

Platform	Biomarker detected	Electroactive surface area (A_e , in mm^2)	Heterogenous electron transfer constant (K_{or} , in cm/s)	References
EA/anti-cTnI/APTES/ WO_3 NRs/ITO	cTnI	–	4.47×10^{-5}	[57]
BSA/anti-VD/ Fe_3O_4 -PANnFs/ITO	Vitamin D_3	3.8	1.55×10^{-6}	[58]
BSA/anti-CYFRA-21-1/APTES/nYZR/ITO	CYFRA-21-1	2.58	3.77×10^{-7}	[59]
BSA/Anti-NSE/r-MoS ₂ -rGO/ITO	NSE	27.83	1.29×10^{-3}	Present work

which have been reported for detection of other biomarkers (Table 1). The superior behavior as shown by our platform may be attributed to the synergistic nature and interconnected network formed between r-MoS₂ and bridging rGO, which imparts more conduction pathways.

Analytical performance of biosensor towards detection of NSE

The analytical performance of the prepared biosensor is recorded using EIS and CV techniques. Concentration of NSE antigen is varied from 0.01 to 200 ng/mL, as shown in Fig. 8(a). Before the incubation of NSE, the bioelectrode is washed using plain pBS (pH 7.4), to remove any unbound BSA on the surface of the bioelectrode. This is followed by incubation of antigen onto the bioelectrode for an optimized time duration of 15 min. This gives sufficient time to antigen for interaction with antibodies. The impedance is found to be increasing with the increase in the concentration of the analyte. This occurs due to the immunoreaction between antibody and antigen, leading to the formation of an immunocomplex. This leads to a decrease in the redox-active surface area and decelerates the transfer of electrons from the redox probe $[\text{Fe}(\text{CN})_6]^{3-/4-}$ to the electrode surface. The change in impedance can be directly correlated to the change in concentration of NSE. Hence, a calibration curve is plotted to determine the concentration of NSE antigen [shown in Fig. 8(b)]. The calibration curve is linearly fitted using the following equation with the regression coefficient R^2 value equal to 0.96:

$$R_{ct} = 187.58\Omega + 3.80 \frac{\Omega \text{ mL}}{\text{ng}} \times \left(\text{concentration of NSE} \left(\frac{\text{ng}}{\text{mL}} \right) \right). \quad (5)$$

The sensor is found to exhibit a linear variation in the range of 1–200 ng/mL. The sensitivity of the biosensor is determined using the slope of the calibration curve, and it is found to be $3.80 \Omega \text{ ng}^{-1} \text{ mL cm}^{-2}$. The lowest value which can be detected by using the EIS technique is 1 ng/mL.

Further, an illustration of the reliability of the as-prepared bioelectrode is done by studying its response with the variation of NSE concentration using the CV technique [Fig. 8(c)]. The bioelectrode displays a linear response in the range of 0.1 to 100 ng/mL, with a sensitivity of $2.32 \mu\text{A ng}^{-1} \text{ mL cm}^{-2}$ with CV [Fig. 8(d)]. The

CV response calibration curve is linearly fitted using the following equation with the regression coefficient R^2 value equal to 0.97:

$$i(\mu\text{A}) = 636.67\mu\text{A} + 2.32 \frac{\mu\text{A mL}}{\text{ng}} \times \left(\text{concentration of NSE} \left(\frac{\text{ng}}{\text{mL}} \right) \right). \quad (6)$$

Oxygenated functional groups on r-MoS₂-rGO assist the covalent immobilization of biological entities onto the matrix. A large surface area along with the availability of oxygenated functional groups empowers the bioelectrode to exhibit a wide detection range and manifest a good sensitivity.

Reproducibility check of the bioelectrode

To check the reproducibility of the prepared BSA/Anti-NSE/r-MoS₂-rGO/ITO bioelectrode, EIS and CV response are recorded for four electrodes prepared under similar conditions (Fig. S6). All four bioelectrodes are tested for 10 ng/mL of NSE antigen. The relative standard deviation (RSD) value is found to be below 5%, which is in an acceptable range, indicating that the sensor is reproducible. The covalent binding of biomolecules onto the bioelectrode attributes to the reproducibility of the sensor.

Specificity study of the bioelectrode

The specificity of the prepared bioelectrode, BSA/Anti-NSE/r-MoS₂-rGO/ITO is investigated against different interferents which are also present in human serum, for instance, Cardiac Troponin I (cTnI, 0.1 ng/mL), Myoglobin (mB, 85 ng/mL), C-reactive protein (CRP, 10 $\mu\text{g/mL}$), Urea (0.1 mg/mL), Sodium Chloride (NaCl, 6.2 mg/mL), etc. The concentrations are taken in physiological ranges of these interferents in the serum of a human being. The bar graph in Fig. S7 shows the R_{ct} and CV current values of BSA/Anti-NSE/r-MoS₂-rGO/ITO when incubated with different interferents for 15 min. The negligible change in R_{ct} and CV current of the bioelectrode with the interferents shows insignificant cross-linking between BSA/Anti-NSE/r-MoS₂-rGO/ITO bioelectrode and interferents. Correspondingly, a huge difference in R_{ct} [Fig. S7(a)] and CV current [Fig. S7(b)] value for NSE shows the interaction between

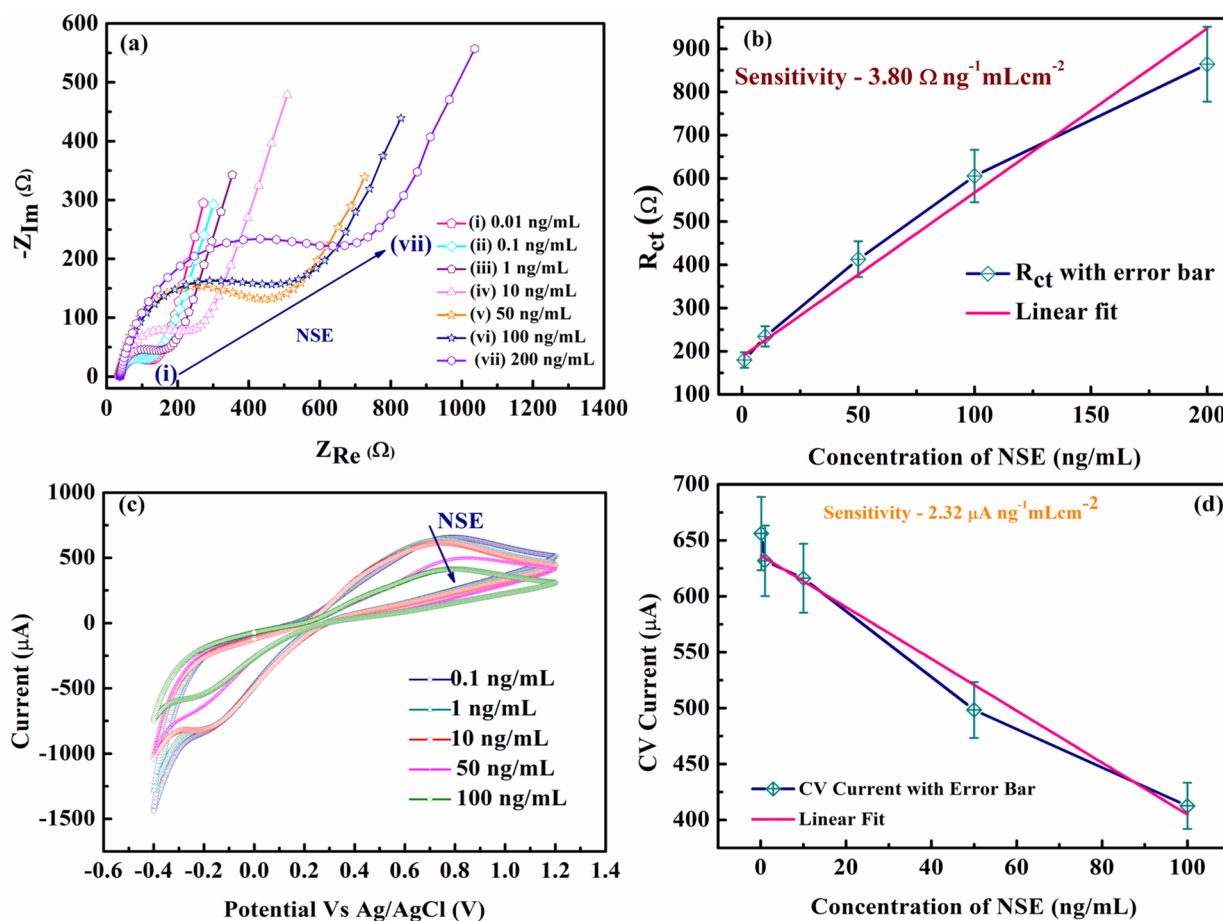


Figure 8: (a) EIS response of BSA/Anti-NSE/r-MoS₂-rGO/ITO bioelectrode as a function of concentration of NSE, (b) Calibration plot between R_{ct} and concentration of NSE, (c) CV response of BSA/Anti-NSE/r-MoS₂-rGO/ITO bioelectrode as a function of concentration of NSE, (d) Calibration plot between CV current and concentration of NSE.

NSE and anti-NSE antibodies, which shows the specificity of the bioelectrode towards NSE.

Conclusions

A sensitive, specific, fast, and economical biosensor is prepared by utilizing the synergistic effect of r-MoS₂ and rGO for the detection of a potential lung cancer biomarker. Layered structures of these 2D nanomaterials allow easy grafting of rGO into r-MoS₂. Electrochemical parameters like heterogeneous rate transfer constant and electroactive surface area are determined to be 1.29×10^{-3} cm/s and 27.83 mm², respectively. The superior performance of the prepared bioelectrode is owed to the bridged interconnected network between r-MoS₂ and rGO, which provides more conduction pathways. A large surface area empowers the bioelectrode to exhibit a wide detection range and demonstrate a good sensitivity. It is found that the availability of oxygenated functional groups onto r-MoS₂-rGO assists

covalent immobilization of biological moieties onto the matrix which makes it specific as well as reproducible. This study also proposes the use of r-MoS₂-rGO based matrix for the preparation of biosensors for detection of other biomarkers too by using their respective antibodies.

Experimental details (synthesis and characterization)

Materials and solutions

The monoclonal anti-NSE antibody, Neuron-specific enolase (NSE), N-(3-Dimethylaminopropyl)-N'-ethyl carbodiimide hydrochloride (EDC), N-Hydroxysuccinimide (NHS), Bovine Serum Albumin (BSA), Ammonium Molybdate Tetrahydrate (NH₄)₆Mo₇O₂₄·4H₂O are the products bought from Sigma-Aldrich. While Thiourea (CH₄N₂S) is purchased from SRL. Some Chemicals are procured from Thermo Fisher Scientific like Hydrazine Hydrate, Sodium Chloride, and Potassium Bromide. Concentrated Hydro Chloric Acid is bought from RFCL

limited. Other chemicals including Acetonitrile, Potassium Hexacyano Ferrate(II) Trihydrate/Potassium Ferrocyanide ($K_4Fe(CN)_6 \cdot 3H_2O$), Potassium Hexacyano Ferrate (III)/Potassium Ferri Cyanide ($K_3Fe(CN)_6$), di Sodium Hydrogen diphosphate dihydrate ($Na_2HPO_4 \cdot 2H_2O$), and Sodium di Hydrogen Phosphate dihydrate ($NaH_2PO_4 \cdot 2H_2O$) are all purchased from Merck. A Millipore Milli-Q system (Bedford, MA, USA) is used to obtain Milli-Q water for the preparation of the solutions which are used for various experiments. Potassium Permanganate ($KMnO_4$) and Orthophosphoric Acid (H_3PO_4) are purchased from Fisher Scientific. Tris Hydrochloride (Tris-HCl), Magnesium Sulfate ($MgSO_4$), and Potassium Chloride (KCl) which serves as a buffer for dilution of NSE are purchased from loba Chemie and Thermo Fisher Scientific.

The prepared buffers are kept at 4 °C after preparation and brought to room temperature (RT) before usage.

Characterization of samples and instrumentation

Various characterization tools are used to confirm the formation of samples. A Bruker D8 Advance facility is used to record the XRD pattern of samples. A WITec Raman spectrometer producing a wavelength of 532 nm is used to record Raman spectra. SEM and elemental analysis are done using Jeol Japan mode and Zeiss EVO 18. The FTIR spectroscopy measurements are done using Perkin Elmer spectrum two. A Perkin Elmer 4000 thermogravimetric analyzer is used to study the thermal stability of prepared samples. WITec alpha 300 RA is used for AFM. A Metrohm Potentiostat/Galvanostat (Multi Autolab M204) along with NOVA software is used for recording all the electrochemical measurements.

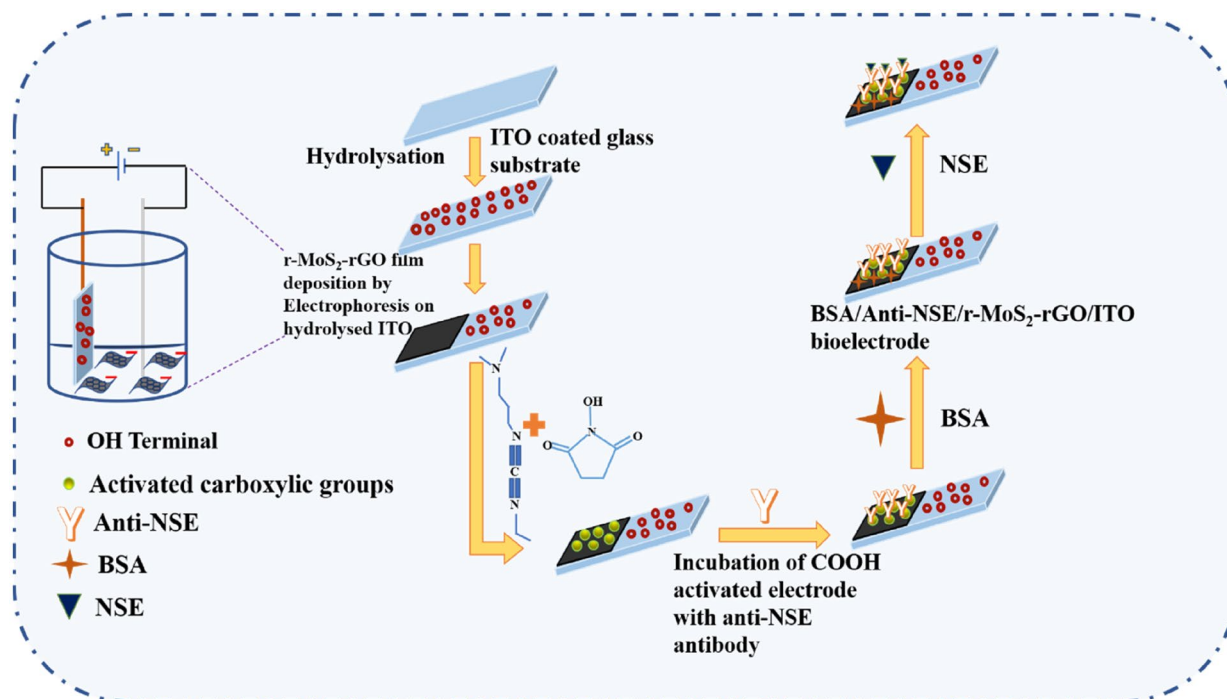
In situ preparation of rGO-modified r-MoS₂ multi-layered nanosheets

GO powder is prepared by improved Hummer's method [60]. In brief, a 9:1 combination of H_2SO_4 and H_3PO_4 is added to 1 g of graphitic flakes. After, 15 min, 12 g of $KMnO_4$ is added to the reaction mixture in small steps, and these reaction products are stirred at 50 °C for 12 h. After 12 h the reaction is quenched, by adding ice and 2 mL of H_2O_2 . The suspension mixture is then washed with de-ionized (DI) water until its pH becomes 7. The obtained solid precipitate is filtered out and kept for drying in an oven at 90 °C, overnight. Then, 40 mg of the as-obtained dried powder of GO is dispersed in 20 mL of DI water and kept for ultrasonication for 1 h. After 1 h, this dispersion is added into the process of synthesis of r-MoS₂, reported elsewhere [22]. Briefly, appropriate amounts of ammonium molybdate tetrahydrate and thiourea are dissolved in DI water, and 2 mL of hydrazine hydrate is added to this reaction mixture. A pH value of 5 is maintained using dilute HCl and then dispersion

of GO is added and this reaction mixture is left for stirring for 30 min. Then, the reaction mixture is put in a hydrothermal autoclave and maintained at 230 °C for 24 h. Obtained black precipitates are washed using DI water and ethanol and are dried subsequently in a vacuum oven. The reduction of GO to rGO occurs during reaction [61] due to the release of H_2S gas by thiourea, and henceforth, rGO is introduced into the r-MoS₂ matrix in an in-situ way. Also, the addition of hydrazine hydrate aids the reduction of GO to rGO, along with the reduction of $(NH_4)_2MoS_4$ [62]. Scheme S2 (see Supplementary File) shows the preparation steps of rGO-modified r-MoS₂ multi-layered nanosheets in a pictorial way.

Preparation of electrochemical immuno-sensing platform for detection of lung cancer biomarker

The electrochemical immuno-sensing platform is prepared by depositing r-MoS₂-rGO on pre-hydrolyzed indium Tin Oxide (ITO) coated glass substrates by electrophoretic deposition (EPD) technique. Before deposition, a uniform dispersion (1 mg/mL) of r-MoS₂-rGO is prepared in acetonitrile by ultrasonication. An assembly constituting of Platinum (Pt) as an auxiliary electrode and Copper (Cu) as a connector to attach the working electrode (WE) is taken. ITO is attached at Cu as our WE, and these 2 electrodes are placed 1 cm apart in a glass cell. Prepared dispersion is poured in the glass cell, and films are formed on a geometrical area of $1 \times 1 \text{ cm}^2$ by applying an optimized potential of 40 V for 120 s. The prepared films are left for air-drying overnight. The as-prepared r-MoS₂-rGO/ITO electrode is loaded with an optimized concentration (25 µg/mL) of anti-NSE antibodies. Before immobilization of antibodies, freshly prepared 0.4 M EDC (coupling agent) and 0.1 M NHS (intermediate stabilizer) are aliquoted, which are used for activating COOH groups on the r-MoS₂-rGO matrix. Thereafter, 20 µL of antibodies of NSE are uniformly spread onto r-MoS₂-rGO/ITO electrode, which is then incubated in a humid chamber for 5 h. Following this period, the anti-NSE/r-MoS₂-rGO/ITO electrode is washed with plain PBS buffer (pH 7.4) to remove unbound anti-NSE antibodies. After this step, 10 µL of BSA is attached for 1 h, to prepare the final bioelectrode by masking any remaining active sites. Prepared BSA/anti-NSE/r-MoS₂-rGO/ITO bioelectrode is kept at 4 °C for future use. Scheme 1 shows the step-by-step preparation of bioelectrode. The covalent bonding occurs by activation of the carboxyl group ($-COOH$) present on the matrix of r-MoS₂-rGO by EDC and NHS and formation of strong carbamide (CO-NH) bond with amino (NH_2) group of anti-NSE antibody.



Scheme 1: Step-by-step preparation of BSA/Anti-NSE/r-MoS₂-rGO/ITO bioelectrode and detection of NSE.

Acknowledgments

Authors are highly obliged to Hon'ble Vice-Chancellor, Delhi Technological University, Delhi, India for promoting research and providing appropriate infrastructure and facilities.

Data availability

Data related to the manuscript content will be made available upon request.

Declarations

Conflict of interest On behalf of all authors, the corresponding author states that there is no conflict of interest.

Supplementary Information

The online version contains supplementary material available at <https://doi.org/10.1557/s43578-022-00546-w>.

References

1. F. Bray, J. Ferlay, I. Soerjomataram, R.L. Siegel, L.A. Torre, A. Jemal, Global cancer statistics 2018: GLOBOCAN estimates of incidence and mortality worldwide for 36 cancers in 185 countries. *CA: A Cancer J Clin* **68**(6), 394 (2018)
2. H. Singh, J. Bernabe, J. Chern, M.J.J.M.R. Nath, Copper selenide as multifunctional non-enzymatic glucose and dopamine sensor. *J. Mater. Res.* **36**(7), 1413–1424 (2021)
3. H. Wang, S. Wu, T. Cao, B. Zhao, J. Ruan, J. Cao, Z. Tong, X.J.J.M.R. Zhang, Self-assembly behavior of layered titanium niobate and methylene blue cation and electrochemical detection of dopamine. *J. Mater. Sci.* **36**, 1437 (2021)
4. J. Han, Y. Zhuo, Y.-Q. Chai, Y.-L. Yuan, R. Yuan, Novel electrochemical catalysis as signal amplified strategy for label-free detection of neuron-specific enolase. *Biosens. Bioelectron.* **31**(1), 399 (2012)
5. G. Yang, Z. Xiao, C. Tang, Y. Deng, H. Huang, Z. He, Recent advances in biosensor for detection of lung cancer biomarkers. *Biosens. Bioelectron.* **141**, 111416 (2019)
6. D. Carney, D. Ihde, M. Cohen, P. Marangos, P. Bunn Jr., J. Minna, A.J.T.L. Gazdar, Serum neuron-specific enolase: a marker for disease extent and response to therapy of small-cell lung cancer. *The Lancet* **319**(8272), 583 (1982)
7. C.-M. Xu, Y.-L. Luo, S. Li, Z.-X. Li, L. Jiang, G.-X. Zhang, L. Owusu, H.-L.J.B. Chen, Multifunctional neuron-specific enolase: its role in lung diseases. *Biosci. Rep.* **39**(11), BSR20192732 (2019)
8. A. Kalkal, S. Kadian, S. Kumar, G. Manik, P. Sen, S. Kumar, G.J.B. Packirisamy, Ti3C2-MXene decorated with nanostructured silver as a dual-energy acceptor for the fluorometric neuron specific enolase detection. *Biosens. Bioelectron.* **195**, 113620 (2022)
9. S. Yin, L. Zhao, Z. Ma, Label-free electrochemical immunosensor for ultrasensitive detection of neuron-specific enolase based on enzyme-free catalytic amplification. *Anal. Bioanal. Chem.* **410**(4), 1279 (2018)

10. Q. Zhang, X. Li, C. Qian, L. Dou, F. Cui, X. Chen, Label-free electrochemical immunoassay for neuron specific enolase based on 3D macroporous reduced graphene oxide/polyaniline film. *Anal. Biochem.* **540**, 1 (2018)
11. H. Wang, Z. Ma, Amperometric immunoassay for the tumor marker neuron-specific enolase using a glassy carbon electrode modified with a nanocomposite consisting of polyresorcinol and of gold and platinum nanoparticles. *Microchim. Acta* **184**(9), 3247 (2017)
12. X. Fu, R. Huang, J. Wang, X. Feng, Platinum nanoflower-based catalysts for an enzyme-free electrochemical immunoassay of neuron-specific enolase. *Anal. Methods* **5**(16), 3803 (2013)
13. A. Mohammadi, E. Heydari-Bafrooei, M.M. Foroughi, M. Mohammadi, Electrochemical aptasensor for ultrasensitive detection of PCB77 using thionine-functionalized MoS₂-rGO nanohybrid. *Microchem. J.* **155**, 104747 (2020)
14. A. Sinha, B. Tan, Y. Huang, H. Zhao, X. Dang, J. Chen, R. Jain, MoS₂ nanostructures for electrochemical sensing of multidisciplinary targets: a review. *TrAC Trends Anal. Chem.* **102**, 75 (2018)
15. C. Anichini, W. Czepa, D. Pakulski, A. Aliprandi, A. Ciesielski, P. Samori, Chemical sensing with 2D materials. *Chem. Soc. Rev.* **47**(13), 4860 (2018)
16. K. Kalantar-zadeh, J.Z. Ou, Biosensors based on two-dimensional MoS₂. *ACS Sens.* **1**(1), 5 (2016)
17. V. Georgakilas, J.N. Tiwari, K.C. Kemp, J.A. Perman, A.B. Bourlino, K.S. Kim, R. Zboril, Noncovalent functionalization of graphene and graphene oxide for energy materials, biosensing, catalytic, and biomedical applications. *Chem. Rev.* **116**(9), 5464 (2016)
18. H.-H. Huang, K.K.H. De Silva, G. Kumara, M. Yoshimura, Structural evolution of hydrothermally derived reduced graphene oxide. *Sci. Rep.* **8**(1), 1 (2018)
19. H. Yang, J. Zhou, J. Bao, Y. Ma, J. Zhou, C. Shen, H. Luo, M. Yang, C. Hou, D. Huo, A simple hydrothermal one-step synthesis of 3D-MoS₂/rGO for the construction of sensitive enzyme-free hydrogen peroxide sensor. *Microchem. J.* **162**, 105746 (2021)
20. S. Gao, Y. Zhang, Z. Yang, T. Fei, S. Liu, T.J.J.A. Zhang, Compounds: Electrochemical chloramphenicol sensors-based on trace MoS₂ modified carbon nanomaterials: Insight into carbon supports. *J. Alloys Compd.* **872**, 159687 (2021)
21. O. Jalil, C.M. Pandey, D.J.B. Kumar, Highly sensitive electrochemical detection of cancer biomarker based on anti-EpCAM conjugated molybdenum disulfide grafted reduced graphene oxide nanohybrid. *Bioelectrochemistry* **138**, 107733 (2021)
22. R. Khatri, N.K. Puri, Electrochemical study of hydrothermally synthesised reduced MoS₂ layered nanosheets. *Vacuum* **175**, 109250 (2020)
23. M.A.R. Anjum, H.Y. Jeong, M.H. Lee, H.S. Shin, J.S.J.A.M. Lee, Efficient hydrogen evolution reaction catalysis in alkaline media by all-in-one MoS₂ with multifunctional active sites. *Adv. Mater.* **30**(20), 1707105 (2018)
24. F. Wang, M. Zheng, B. Zhang, C. Zhu, Q. Li, L. Ma, W.J.S. Shen, Ammonia intercalated flower-like MoS₂ nanosheet film as electrocatalyst for high efficient and stable hydrogen evolution. *Sci. Rep.* **6**(1), 1 (2016)
25. M. Li, D. Wang, J. Li, Z. Pan, H. Ma, Y. Jiang, Z.J.R. Tian, Facile hydrothermal synthesis of MoS₂ nano-sheets with controllable structures and enhanced catalytic performance for anthracene hydrogenation. *RSC Adv.* **6**(75), 71534 (2016)
26. M. Sreeramreddygar, M. Somasundrum, W.J.N.J.C. Surarungchai, In situ polymerization and covalent functionalisation of trithiocyanuric acid by MoS₂ nanosheets resulting in a novel nanozyme with enhanced peroxidase activity. *New J Chem* **44**(15), 5809 (2020)
27. X. Xia, Z. Zheng, Y. Zhang, X. Zhao, C.J.I. Wang, Synthesis of MoS₂-carbon composites with different morphologies and their application in hydrogen evolution reaction. *Int. J. Hydrogen Energy* **39**(18), 9638 (2014)
28. M. Li, A. Addad, Y. Zhang, A. Barras, P. Roussel, M.A. Amin, S. Szunerits, R.J.C. Boukherroub, Flower-like nitrogen-co-doped MoS₂@RGO composites with excellent stability for supercapacitors. *ChemElectroChem* **8**(15), 2903 (2021)
29. H. Sun, H. Liu, Z. Hou, R. Zhou, X. Liu, J.-G.J.C.E.J. Wang, Edge-terminated MoS₂ nanosheets with an expanded interlayer spacing on graphene to boost supercapacitive performance. *Chem. Eng. J.* **387**, 124204 (2020)
30. X. Bai, Y. Du, X. Hu, Y. He, C. He, E. Liu, J. Fan, Synergy removal of Cr (VI) and organic pollutants over RP-MoS₂/rGO photocatalyst. *Appl. Catal. B* **239**, 204 (2018)
31. W.-K. Jo, S. Kumar, M.A. Isaacs, A.F. Lee, S. Karthikeyan, Cobalt promoted TiO₂/GO for the photocatalytic degradation of oxytetracycline and Congo Red. *Appl. Catal. B* **201**, 159 (2017)
32. H. Sun, S. Liu, G. Zhou, H.M. Ang, M.O. Tadé, S. Wang, Reduced graphene oxide for catalytic oxidation of aqueous organic pollutants. *ACS Appl. Mater. Interfaces.* **4**(10), 5466 (2012)
33. L. Chen, D. Ding, C. Liu, H. Cai, Y. Qu, S. Yang, Y. Gao, T. Cai, Degradation of norfloxacin by CoFe₂O₄-GO composite coupled with peroxymonosulfate: a comparative study and mechanistic consideration. *Chem. Eng. J.* **334**, 273 (2018)
34. J. Zhou, H. Xiao, B. Zhou, F. Huang, S. Zhou, W. Xiao, D. Wang, Hierarchical MoS₂-rGO nanosheets with high MoS₂ loading with enhanced electro-catalytic performance. *Appl. Surf. Sci.* **358**, 152 (2015)
35. S. Yang, X. Feng, S. Ivanovici, K. Müllen, Fabrication of graphene-encapsulated oxide nanoparticles: towards high-performance anode materials for lithium storage. *Angew. Chem. Int. Ed.* **49**(45), 8408 (2010)
36. H. Wang, J.T. Robinson, X. Li, H. Dai, Solvothermal reduction of chemically exfoliated graphene sheets. *J. Am. Chem. Soc.* **131**(29), 9910 (2009)
37. S. Stankovich, D.A. Dikin, R.D. Piner, K.A. Kohlhaas, A. Kleinhammes, Y. Jia, Y. Wu, S.T. Nguyen, R.S. Ruoff, Synthesis of

- graphene-based nanosheets via chemical reduction of exfoliated graphite oxide. *Carbon* **45**(7), 1558 (2007)
38. J. Zhang, L. Zhao, A. Liu, X. Li, H. Wu, C. Lu, Three-dimensional MoS₂/rGO hydrogel with extremely high double-layer capacitance as active catalyst for hydrogen evolution reaction. *Electrochim. Acta* **182**, 652 (2015)
 39. L. Lin, S. Zhang, Effective solvothermal deoxidization of graphene oxide using solid sulphur as a reducing agent. *J. Mater. Chem.* **22**(29), 14385 (2012)
 40. T. Yang, L.-H. Liu, J.-W. Liu, M.-L. Chen, J.-H. Wang, Cyanobacterium metallothionein decorated graphene oxide nanosheets for highly selective adsorption of ultra-trace cadmium. *J. Mater. Chem.* **22**(41), 21909 (2012)
 41. R. Vinoth, I.M. Patil, A. Pandikumar, B.A. Kakade, N.M. Huang, D.D. Dionysios, B. Neppolian, Synergistically enhanced electrocatalytic performance of an N-doped graphene quantum dot-decorated 3D MoS₂-graphene nanohybrid for oxygen reduction reaction. *ACS Omega* **1**(5), 971 (2016)
 42. G. Sun, X. Zhang, R. Lin, J. Yang, H. Zhang, P. Chen, Hybrid fibers made of molybdenum disulfide, reduced graphene oxide, and multi-walled carbon nanotubes for solid-state, flexible, asymmetric supercapacitors. *Angew. Chem.* **127**(15), 4734 (2015)
 43. S. Kumar, V. Sharma, K. Bhattacharyya, V. Krishnan, Synergetic effect of MoS₂-RGO doping to enhance the photocatalytic performance of ZnO nanoparticles. *New J. Chem.* **40**(6), 5185 (2016)
 44. N. Kumar, S. Kumar, R. Gusain, N. Manyala, S. Eslava, S.S. Ray, Polypyrrole-promoted rGO-MoS₂ nanocomposites for enhanced photocatalytic conversion of CO₂ and H₂O to CO, CH₄, and H₂ products. *ACS Appl. Energy Mater.* **3**(10), 9897 (2020)
 45. E.G. da Silveira Firmiano, A.C. Rabelo, C.J. Dalmaschio, A.N. Pinheiro, E.C. Pereira, W.H. Schreiner, E.R. Leite, Supercapacitor electrodes obtained by directly bonding 2D MoS₂ on reduced graphene oxide. *Adv. Energy Mater.* **4**(6), 1301380 (2014)
 46. Y.-L. Chen, Z.-A. Hu, Y.-Q. Chang, H.-W. Wang, Z.-Y. Zhang, Y.-Y. Yang, H.-Y.J.T.J.P.C.C. Wu, Zinc oxide/reduced graphene oxide composites and electrochemical capacitance enhanced by homogeneous incorporation of reduced graphene oxide sheets in zinc oxide matrix. *J Phys. Chem. C* **115**(5), 2563 (2011)
 47. G. Wang, X. Shen, J. Yao, J.J.C. Park, Graphene nanosheets for enhanced lithium storage in lithium ion batteries. *Carbon* **47**(8), 2049 (2009)
 48. L. Zhang, W. Fan, W.W. Tjiu, T. Liu, 3D porous hybrids of defect-rich MoS₂/graphene nanosheets with excellent electrochemical performance as anode materials for lithium ion batteries. *RSC Adv.* **5**(44), 34777 (2015)
 49. V.K. Singh, S. Kumar, S.K. Pandey, S. Srivastava, M. Mishra, G. Gupta, B. Malhotra, R. Tiwari, A. Srivastava, Fabrication of sensitive bioelectrode based on atomically thin CVD grown graphene for cancer biomarker detection. *Biosens. Bioelectron.* **105**, 173 (2018)
 50. S. Kumar, S. Kumar, S. Tiwari, S. Srivastava, M. Srivastava, B.K. Yadav, S. Kumar, T.T. Tran, A.K. Dewan, A. Mulchandani, Biofunctionalized nanostructured zirconia for biomedical application: a smart approach for oral cancer detection. *Adv. Sci.* **2**(8), 1500048 (2015)
 51. M. Kukkar, A. Sharma, P. Kumar, K.-H. Kim, A. Deep, Application of MoS₂ modified screen-printed electrodes for highly sensitive detection of bovine serum albumin. *Anal. Chim. Acta* **939**, 101 (2016)
 52. J.-B. Jorcin, M.E. Orazem, N. Pébère, B.J.E.A. Tribollet, CPE analysis by local electrochemical impedance spectroscopy. *Electrochim. Acta* **51**(8-9), 1473 (2006)
 53. B. Hirschorn, M.E. Orazem, B. Tribollet, V. Vivier, I. Frateur, M.J.J.T.E.S. Musiani, Constant-phase-element behavior caused by resistivity distributions in films: I. Theory **157**(12), 452 (2010)
 54. M. Farrokhnia, G. Amoabediny, M. Ebrahimi, M. Ganjali, M.J.T. Arjmand, Ultrasensitive early detection of insulin antibody employing novel electrochemical nano-biosensor based on controllable electro-fabrication process. *Talanta* **238**, 122947 (2021)
 55. O. Jalil, C.M. Pandey, D.J.M.A. Kumar, Electrochemical biosensor for the epithelial cancer biomarker EpCAM based on reduced graphene oxide modified with nanostructured titanium dioxide. *Microchim. Acta* **187**(5), 1 (2020)
 56. X. Xi, D. Wu, W. Ji, S. Zhang, W. Tang, Y. Su, X. Guo, R.J.A.F.M. Liu, Manipulating the sensitivity and selectivity of OEECT-based biosensors via the surface engineering of carbon cloth gate electrodes. *Adv. Funct. Mater.* **30**(4), 1905361 (2020)
 57. D. Sandil, S.C. Sharma, N.K. Puri, Protein-functionalized WO₃ nanorods-based impedimetric platform for sensitive and label-free detection of a cardiac biomarker. *J. Mater. Res.* **34**(8), 1331 (2019)
 58. D. Chauhan, P.K. Gupta, P.R. Solanki, Electrochemical immunosensor based on magnetite nanoparticles incorporated electrospun polyacrylonitrile nanofibers for Vitamin-D₃ detection. *Mater. Sci. Eng. C* **93**, 145 (2018)
 59. S. Kumar, N. Gupta, B.D. Malhotra, Ultrasensitive biosensing platform based on yttria doped zirconia-reduced graphene oxide nanocomposite for detection of salivary oral cancer biomarker. *Bioelectrochemistry* **140**, 107799 (2021)
 60. D.C. Marcano, D.V. Kosynkin, J.M. Berlin, A. Sinitskii, Z. Sun, A. Slesarev, L.B. Alemany, W. Lu, J.M. Tour, Improved synthesis of graphene oxide. *ACS Nano* **4**(8), 4806 (2010)
 61. M. Saraf, K. Natarajan, A.K. Saini, S.M. Mobin, Small biomolecule sensors based on an innovative MoS₂-rGO heterostructure modified electrode platform: a binder-free approach. *Dalton Trans.* **46**(45), 15848 (2017)
 62. Y. Li, H. Wang, L. Xie, Y. Liang, G. Hong, H. Dai, MoS₂ nanoparticles grown on graphene: an advanced catalyst for the hydrogen evolution reaction. *J. Am. Chem. Soc.* **133**(19), 7296 (2011)

PAPER



Cite this: *New J. Chem.*, 2022, 46, 7477

Electrochemical studies of biofunctionalized MoS₂ matrix for highly stable immobilization of antibodies and detection of lung cancer protein biomarker

Ritika Khatri and Nitin K. Puri *

To address the issue of the lack of stable immobilization of antibodies on the biosensing matrix for repeated cycles of measurement, MoS₂ biofunctionalized with chitosan (CS) is prepared to serve as a biosensing matrix. The electrochemical performance of the CS/MoS₂ matrix towards the detection of neuron-specific enolase (NSE), a lung cancer biomarker, is also investigated. Unlike other complex matrices involving various steps of modification, the matrix studied herein involves only 2 steps of modification without the use of any label, amplifying its appeal for biosensing applications. The fabricated immunoelectrode is found to exhibit remarkable cyclic stability, with a sensitivity of 3.35 $\mu\text{A ng}^{-1} \text{mL cm}^{-2}$ and a wide linear detection range of 0.1–100 ng mL^{-1} . Also, the sensor is found to be fast, specific, reproducible, regenerable up to 4 cycles, and has a shelf life of 6 weeks. The stability study of our fabricated immunoelectrode revealed that the cumulative effect of CS and MoS₂ ensures the stable immobilization of biomolecules on the immunoelectrode for 50 cyclic voltammetry (CV) cycles. The results of this study suggest that the proposed matrix will be promising in the fabrication of devices for early monitoring of protein biomarkers.

Received 31st January 2022,
Accepted 16th March 2022

DOI: 10.1039/d2nj00540a

rsc.li/njc

1. Introduction

Electrochemical biosensors have gained momentum in the development of point-of-care devices owing to their ease of miniaturization, the requirement of small sample volumes, their rapid response, and low requirement for power.^{1,2} They use electron mediators to translate the events of analyte binding into a detectable electrical signal. The preparation of an electrochemical biosensor requires the fabrication of a suitable immobilization matrix that can hold the bio-recognition elements efficiently and effectively.³ Nanostructured materials have been proved as a good choice to fabricate the platform for loading biological molecules for the detection of even very low levels of analyte.⁴ However, the chosen material should be able to escalate the charge-transfer process without passivating the electrode surface to maintain its performance along with increasing its effective surface area. For the fabrication of an electrochemical biosensor, it is therefore important to ensure that the bioactivity of the immobilized biomolecule is not lost through the continuous application of potential to it and repeated interaction with redox media.

In recent times, molybdenum disulfide (MoS₂) has gained great attention in electrochemical applications (*i.e.*, supercapacitors,

lithium (Li)/sodium (Na) ion batteries, the hydrogen evolution reaction (HER), sensors, *etc.*⁵) as it possesses many intriguing properties, such as a layered structure, various synthesis routes, ease of tailoring the morphology, a large surface-to-volume ratio, ease of dispersibility in aqueous solution, a fast heterogeneous electron-transfer (HET) rate, feasibility of surface functionalization and modification, and exceptional cyclic stability.^{5–9} Owing to its hydrophobicity, MoS₂ can be utilized to fabricate the immobilization platform because it provides a strong affinity for the adsorption of protein on its surface.⁶ Because of its layered structure and high surface/volume ratio, it enhances the total surface area for the immobilization of biomolecules. Owing to all these fascinating properties, MoS₂ is used to fabricate the matrix for electrochemical biosensing. Furthermore, to anchor functional groups on MoS₂ and impart biocompatibility to the matrix, chitosan (CS) is used. CS is a non-toxic biocompatible polymer, which is present in abundance, has excellent film-forming and stabilizing properties along with a polycationic nature.^{10,11} It is rich in functionalities, like amino and hydroxyl groups, on its polysaccharide chain.¹² Thus, CS is blended with MoS₂ in the presence of an ionic liquid (IL) because of its high polarity.¹³ Due to its polar nature, the IL provides a reaction atmosphere for MoS₂ and CS to interact with each other. The benefit of combining different materials is governed by the fact that both materials contribute to the properties of the final blend.¹

Nanomaterials Research Laboratory, Department of Applied Physics, Delhi Technological University, Delhi-110042, India. E-mail: nitinkumarपुरi@dtu.ac.in

In this work, the sensing behavior of biofunctionalized MoS₂ is examined by choosing the protein biomarker neuron-specific enolase (NSE) as the target analyte. NSE is considered to be a specific protein biomarker for the diagnosis of small cell lung cancer (SCLC) and is found to be present >9 ng mL⁻¹ in the case of 70% of patients diagnosed with SCLC.¹⁴ Quite a few reports are available on the detection of NSE, using different matrices with outstanding performances.^{15–18} However, achieving a high signal response along with maintaining the signal stability and the bioactivity of the platform remains a significant challenge.¹⁵ For instance, Tang *et al.*¹⁶ developed the PPy–PEDOT–Au GCE as a substrate material for the stable immobilization of immune molecules along with the maintenance of their bioactivity for the detection of NSE. They found that their platform could provide a stable environment for sensing up to 30 CV cycles. Yu and co-workers designed an electrochemical immunosensor for the detection of NSE based on graphene supported by hollow carbon balls.¹⁷ A stable trend for this immobilization matrix was found for 30 cycles of CV. Mo *et al.* fabricated an immunosensor for the simultaneous detection of NSE and CYFRA21-1 and confirmed the stability of the immunosensor for up to 15 CV cycles.¹⁸ Thus, it has been observed that after a few cycles of measurement the signal response tends to degrade. In this investigation, we explored CS/MoS₂ matrix for the stable immobilization of anti-NSE antibodies and the detection of NSE for the first time, to the best of our knowledge. The CS/MoS₂-based matrix proved to be stable, with nearly 94% of the initial signal response still retained after continuous scanning for 50 CV cycles. The bioactivity of the immobilized antibodies is ensured by the biocompatible CS, while a stable cyclic current response is maintained by the MoS₂.

The method for the synthesis and fabrication of the immunoelectrode discussed in this work is appealing because of its high yield, scalability, and simplicity, *i.e.*, without involving various modification steps, which ensures its remarkable electrochemical performance and stability. There are three major novel features of our work. First, a highly stable matrix is formed that is favorable for the immobilization of biomolecules during repeated cycles of measurement. Secondly, the platform is functionalized for the attachment of biomolecules without any harsh chemical treatment. Third, the large electroactive surface [55% of the geometric area (1 × 1 cm²)] makes it a remarkable platform for electrochemical sensing. Our sensor is found to be very fast, reproducible, specific, stable, regenerable, with a wide linear detection range and a remarkable shelf life. Considering the concentration of NSE found in the serum of SCLC patients, the sensitivity and lowest limit that can be detected using our sensor, our immunoelectrode is also expected to meet the requirements of the detection of NSE in clinical samples.

2. Experimental details

2.1 Chemicals and reagents used for synthesis, cleaning, and biosensing

The monoclonal anti-NSE antibody, neuron-specific enolase (NSE) antigen, *N*-(3-dimethylaminopropyl)-*N'*-ethyl carbodiimide

hydrochloride (EDC), *N*-hydroxysuccinimide (NHS), bovine serum albumin (BSA), ammonium molybdate tetrahydrate (NH₄)₆Mo₇O₂₄·4H₂O, and acetic acid (CH₃COOH) were purchased from Sigma-Aldrich. Thiourea (CH₄N₂S) was bought from SRL. Liquor ammonia (NH₄OH) and *N,N*-dimethylformamide (DMF) were bought from Fisher Scientific. Chitosan was purchased from HIMEDIA. 1-Butyl-3-methyl-diazolium hexafluorophosphate ([C₄mim][PF₆]) was procured from GLR innovations. Other chemicals, like hydrazine hydrate (N₂H₄), sodium chloride (NaCl), and potassium bromide (KBr), were procured from Thermo Fisher Scientific. Hydrogen peroxide (H₂O₂) was purchased from Qualigens. Concentrated hydrochloric acid (HCl) was bought from RFCL limited. Chemicals including acetonitrile, potassium hexacyanoferrate(II) trihydrate/potassium ferrocyanide (K₄Fe(CN)₆·3H₂O), potassium hexacyanoferrate(III)/potassium ferricyanide (K₃Fe(CN)₆), disodium hydrogen diphosphate dihydrate (Na₂HPO₄·2H₂O), sodium dihydrogen phosphate dihydrate (NaH₂PO₄·2H₂O), iso-propyl alcohol (IPA) and ethanol were procured from Merck. A Millipore Milli-Q system (Bedford, MA, USA) was used to obtain Milli-Q water for the preparation of the solutions used for various experiments. Tris hydrochloride (Tris–HCl), magnesium sulfate (MgSO₄), and potassium chloride (KCl), which serve as a buffer for the dilution of NSE, were purchased from Loba Chemie (Tris–HCl) and Thermo Fisher Scientific (MgSO₄ and KCl).

Before use and storage of the buffer solutions, all the glassware was autoclaved and cleaned using 70% isopropyl alcohol (IPA). All the aqueous solutions were prepared using autoclaved de-ionized (dI) water.

2.2 Characterization equipment and facilities

To record the X-ray diffraction (XRD) patterns of the samples, a Bruker D8 Advance facility was used. Raman spectra for the samples were recorded at a wavelength of 532 nm using a WITec Raman spectrometer. Scanning electron microscopy (SEM) was carried out using a Jeol (Japan) instrument. Fourier Transform Infrared (FTIR) spectroscopy measurements were carried out using a PerkinElmer spectrum two instrument. The thermal stability of the samples was recorded using a PerkinElmer 4000 thermogravimetric analyzer. To carry out thickness measurements, an Ambios XP-200 stylus profiler was used. A Metrohm Potentiostat/Galvanostat Autolab along with NOVA software was used for recording all the electrochemical measurements.

2.3 Synthesis of CS/MoS₂

MoS₂ nanostructures constituting a large number of layers were synthesized in line with our previously reported work.¹⁹ To synthesize CS/MoS₂, an IL-assisted mechanical grinding method was used. The synthesis of CS/MoS₂ was carried out according to the method adopted by Zhang *et al.*²⁰ with slight modifications for scaling up the quantity of the finally obtained product. For this, 500 mg of the above synthesized MoS₂ powder was mixed with 200 mg of CS. The mixture was ground using an agate mortar and pestle for 20 minutes. Next, a gel was formed by adding 1 mL of IL (1-butyl-3-methyl-diazolium hexafluorophosphate, [C₄mim][PF₆]) dropwise to the mortar. This mixture of MoS₂, CS,

and IL was further ground for 60 minutes. Then the obtained product was washed using acetone, acetic acid, and *N,N*-dimethylformamide (DMF) to remove excess CS and IL. Then the obtained residue was put in an oven at 100 °C for 24 hours for desolvation. Thus, the dried powder of CS/MoS₂ was collected in an Eppendorf tube for further use.

2.4 Fabrication of the immunoelectrode

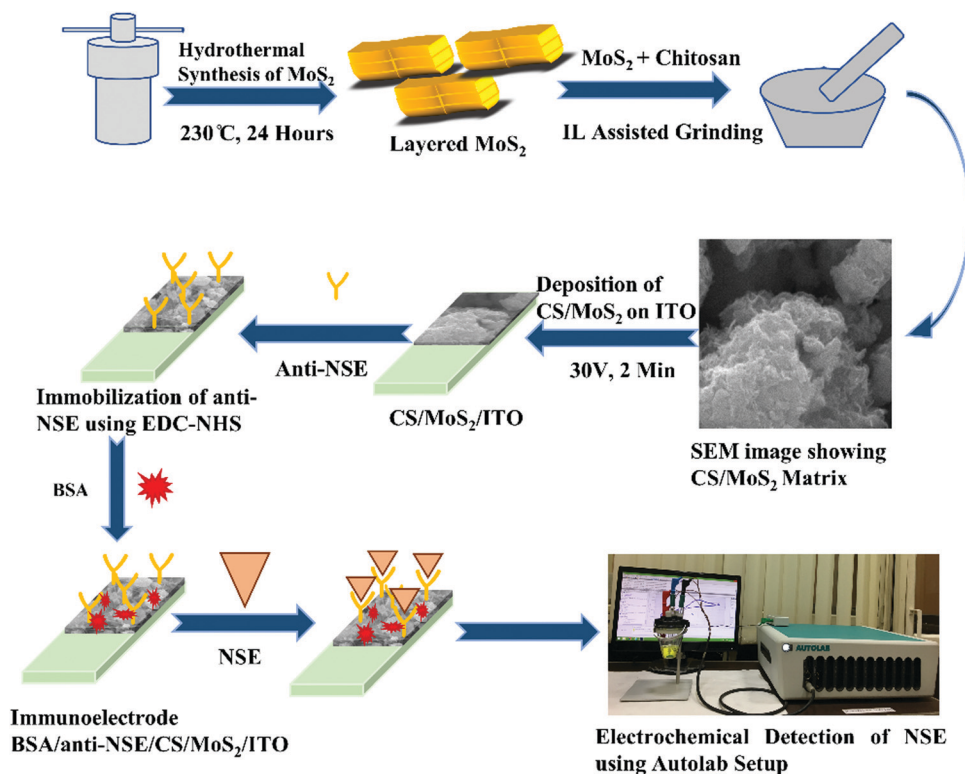
To fabricate the immunoelectrode BSA/anti-NSE/CS/MoS₂/ITO, a series of steps were followed. First, indium tin oxide (ITO) coated glass slides cut in dimensions of 3 × 1 cm² were hydrolyzed using NH₃:H₂O₂:H₂O in the ratio 1:1:5 at 80 °C for 1 hour. The hydrolyzed ITO was cleaned using water and IPA. Next, films of CS/MoS₂ were deposited on the hydrolyzed ITO using electrophoretic deposition (EPD). For this, CS/MoS₂ was well dispersed in acetonitrile at a concentration of 1 mg mL⁻¹. This solution was taken in an EPD cell containing a copper (Cu) wire and a platinum counter electrode (CE). The hydrolyzed ITO was clipped to the Cu as the working electrode (WE) and a potential of 30 V was applied for 120 seconds. The CS/MoS₂ film was formed on a geometric area of 1 × 1 cm². The film was left for overnight air-drying at room temperature. The thickness was measured at various points of the CS/MoS₂/ITO electrode and was found to vary in the range of 1.1–3 μm, indicating a non-uniform surface. For immobilization of the anti-NSE on CS/MoS₂/ITO electrode, 0.4 M EDC (used as a coupling agent), 0.1 M NHS (used as an intermediate stabilizer), and 25 μg mL⁻¹ anti-NSE were aliquoted together in

a ratio of 1:1:2. Then, 20 μL of this aliquoted solution was spread uniformly on the CS/MoS₂/ITO electrode. The anti-NSE/CS/MoS₂/ITO electrode was kept in a humid chamber for an optimized time duration of 5 hours for proper attachment of anti-NSE on CS/MoS₂/ITO electrode. Then, the anti-NSE/CS/MoS₂/ITO electrode was washed in pH 7.4 phosphate buffer saline (PBS) to remove unbound antibodies from the electrode surface. To mask the non-specific binding sites on the anti-NSE/CS/MoS₂/ITO, 10 μL of 0.1 mg mL⁻¹ BSA was drop cast to make the final immunoelectrode BSA/anti-NSE/CS/MoS₂/ITO. After 1 hour the immunoelectrode was washed in pH 7.4 PBS to remove excess BSA from the surface of the immunoelectrode. The BSA/anti-NSE/CS/MoS₂/ITO immunoelectrode was thus finally prepared and was kept at 4 °C when not in use. An illustration of the synthesis of the CS/MoS₂ matrix and the fabrication of the BSA/anti-NSE/CS/MoS₂/ITO immunoelectrode for the detection of NSE is shown in Scheme 1.

3. Results and discussion

3.1 Crystallographic study of CS/MoS₂ matrix using XRD

The primary confirmation of the formation of the CS/MoS₂ matrix and the study of its crystallographic structure was carried out using XRD (Fig. 1). The XRD spectra obtained for commercially purchased CS shows a broad diffraction peak around 20°, without the presence of any additional impurity peaks. For comparison, the XRD spectrum of MoS₂ is also shown, and both the MoS₂ and CS/MoS₂ spectra show peaks



Scheme 1 Schematic diagram illustrating the synthesis of the CS/MoS₂ matrix and fabrication of the BSA/anti-NSE/CS/MoS₂/ITO immunoelectrode for the detection of NSE.

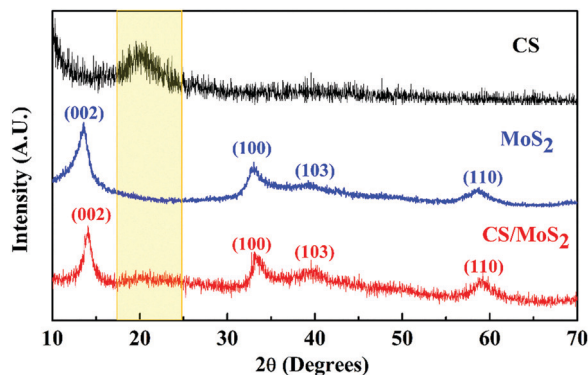


Fig. 1 XRD spectra of CS, MoS₂, and CS/MoS₂.

corresponding to the (002), (100), (103), and (110) planes of 2H-MoS₂ (JCPDS card no. 37-1492).¹⁹ Besides these peaks, a halo around 20° in the spectrum of CS/MoS₂ confirms the formation of the composite of CS and MoS₂.

3.2 Study of vibrational modes and qualitative information on the layered structure and functionalization using Raman spectroscopy

Fig. 2(a) shows the Raman spectra obtained for CS as well as CS/MoS₂ in the range of 250–3700 cm⁻¹. The appearance of the A_{1g} and E¹_{2g} vibrational modes of MoS₂ in the Raman spectrum of CS/MoS₂ (shown in Fig. 2(a) and (b)) confirm the retention of the structure of MoS₂ after the addition of CS. The A_{1g} vibrational mode that corresponds to monolayer MoS₂ is found at 402.72 cm⁻¹ (Fig. 2(b)).²¹ However, the E¹_{2g} mode is found to be red-shifted to 375.39 cm⁻¹ leading to a wavenumber separation between the two modes equal to 27.3 cm⁻¹ (Fig. 2(b)). An increase in wavenumber separation may be attributed to stacking of the layers of MoS₂ due to the incorporation of CS in the structure of MoS₂. Furthermore, the characteristic peaks of CS are observed at 893.14 cm⁻¹, 1096 cm⁻¹, 1372.67 cm⁻¹, and 2885.37 cm⁻¹, which correspond to the C–H bond of

polysaccharide in CS, with OH peaks at 3311.37 cm⁻¹ and 3376.83 cm⁻¹ (Fig. 2(a)).²² Confirmation of the functionalization of MoS₂ with CS can be drawn from the Raman spectrum of CS/MoS₂ (Fig. 2(a)), which shows a peak at 1368.61 cm⁻¹ that corresponds to the δCH of the polysaccharide chain of CS. Furthermore, a halo is observed in the range of 2500–3260 cm⁻¹, which could be due to the νCH₂ peak of CS. This study confirms the successful incorporation of CS into the structure of MoS₂.

3.3 Thermogravimetric analysis (TGA) of the CS/MoS₂ matrix

Fig. 3 shows the thermal behaviour of CS, MoS₂, and CS/MoS₂ from 30 °C to 850 °C. An initial weight loss at around 100 °C in all the samples could be attributed to moisture loss. The weight loss for CS starts at 280 °C while CS/MoS₂ starts losing some weight around 220 °C, which could be due to some remnants from the MoS₂ synthesis process.²³ The weight loss in the case of CS and CS/MoS₂ is greater in range of 280–500 °C, which can be ascribed to decomposition of the carbon skeleton at such high temperatures.²⁴ After 500 °C, 57% and 32% of the weight of MoS₂ and CS/MoS₂ are retained, respectively, while CS is completely lost. Thus, the CS/MoS₂ matrix is found to have greater thermal stability in comparison with CS. This study also implies that the incorporation of functional groups in MoS₂ reduces its thermal stability at high temperatures. However, where biosensor applications are concerned, this is not worrisome because biological testing is always done at room temperature or even lower temperatures. Hence, the successful incorporation of CS into MoS₂ can be derived from the TGA results.

3.4 Study of functional groups attached on the CS/MoS₂ matrix using FTIR spectroscopy

Confirmation of the successful functionalization of MoS₂ using CS is carried out using FTIR spectroscopy (Fig. 4). The peaks observed in CS at 1416 cm⁻¹, 1303 cm⁻¹, and 1089 cm⁻¹ correspond to the CH₂ bending, –NH stretching and C–O stretch of CS, respectively.²⁵ The peak observed at 1561 cm⁻¹ in CS is due to the bending vibration of –NH.²³ The peaks that

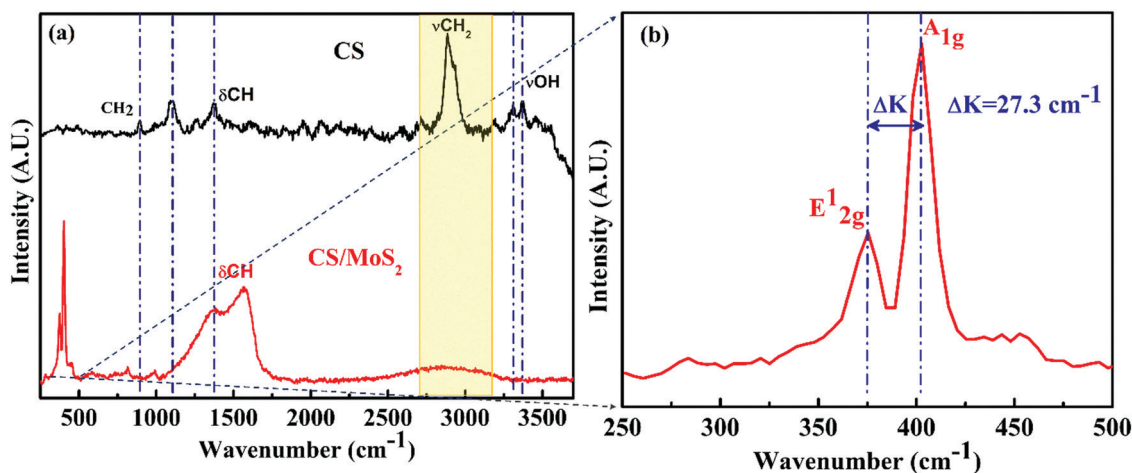


Fig. 2 (a) Raman spectra of CS and CS/MoS₂, and (b) expanded Raman spectrum of CS/MoS₂ in the range 250–500 cm⁻¹, showing the A_{1g} and E¹_{2g} modes of MoS₂ in CS/MoS₂.

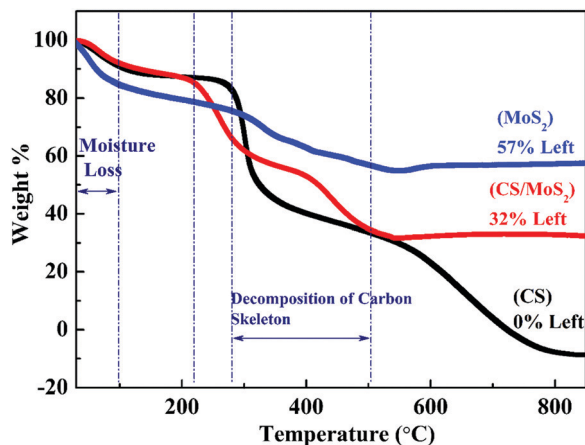


Fig. 3 TGA curves of CS, MoS₂, and CS/MoS₂.

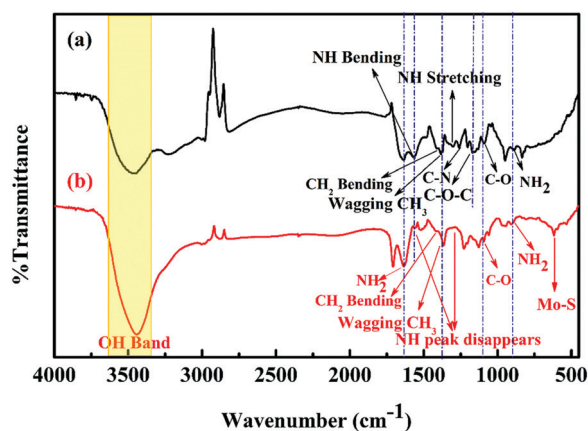


Fig. 4 FTIR curves of (a) CS and (b) CS/MoS₂.

correspond to -NH stretching (1303 cm^{-1}) and -NH bending (1561 cm^{-1}) are missing in CS/MoS₂. The disappearance of these -NH peaks in the FTIR spectrum of CS/MoS₂ could be attributed to the polycationic nature of CS, which leads to protonation of the amine group during grinding in the IL, which leads to the electrostatic interaction between the MoS₂ layers and CS.²⁴ The peaks observed in CS at 1262 cm^{-1} and 1162 cm^{-1} correspond to the C-N and C-O-C bonds in CS.²⁶ The peak observed in the range $3440\text{--}3480\text{ cm}^{-1}$ in both CS and CS/MoS₂ corresponds to the hydroxyl group (OH).²⁴ The peak observed in both CS and CS/MoS₂ at 1371 cm^{-1} corresponds to wagging CH₃.²⁷ Furthermore, peaks corresponding to NH₂ are observed in both CS and CS/MoS₂ at 895 cm^{-1} ²⁸ and 1625 cm^{-1} ,²⁹ indicating functionalization of CS/MoS₂ with the amino group. The peak observed at 618 cm^{-1} corresponds to the Mo-S vibration.³⁰

3.5 Study of the surface morphology of the CS/MoS₂ matrix using SEM

Fig. 5(a) shows the nanostructures of MoS₂ of various sizes. Higher magnification of these nanostructures shows the large

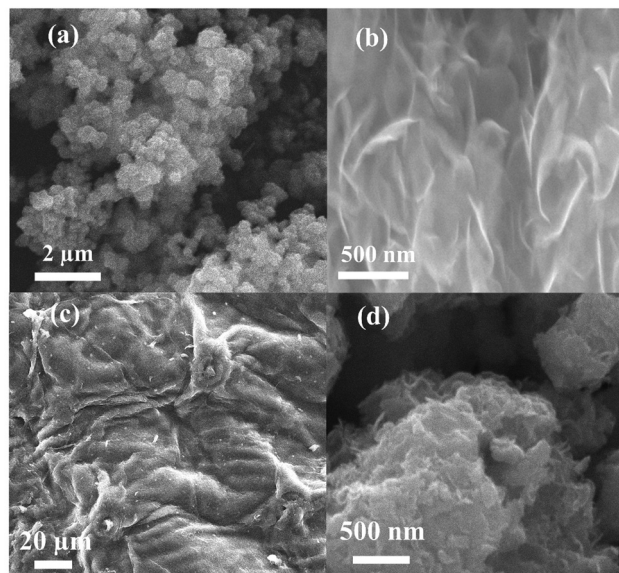


Fig. 5 SEM micrographs of (a and b) MoS₂, (c) CS and (d) CS/MoS₂.

number of layers constituting the MoS₂ sample in Fig. 5(b). Fig. 5(c) shows a large continuous membrane of CS. Evidence for the surface modification of the MoS₂ nanostructures by CS is given in Fig. 5(d), which shows that layers of MoS₂ are stacked together and encapsulated by the CS membrane, rendering a rough and uneven surface of the composite.

4 Detailed investigation of the electrochemical performance of the immunoelectrode prepared using the CS/MoS₂ matrix

4.1 Optimization of biosensing parameters

The concentration of anti-NSE to be attached to the CS/MoS₂/ITO electrode is optimized *via* attaching various concentrations of anti-NSE using EDC-NHS chemistry. Fig. 6(a) shows the current response to the varying concentration of anti-NSE ($5\text{ }\mu\text{g mL}^{-1}$, $10\text{ }\mu\text{g mL}^{-1}$, $25\text{ }\mu\text{g mL}^{-1}$, $50\text{ }\mu\text{g mL}^{-1}$, and $100\text{ }\mu\text{g mL}^{-1}$). The response is found to decrease initially until $25\text{ }\mu\text{g mL}^{-1}$, after which it becomes constant. Thus, $25\text{ }\mu\text{g mL}^{-1}$ of anti-NSE is finalized as the concentration for attachment throughout the studies.

The maximum time required for the immunoreaction to take place between NSE and anti-NSE is found through incubation of the BSA/anti-NSE/CS/MoS₂/ITO immunoelectrode with NSE for various times (Fig. 6(b)). $20\text{ }\mu\text{L}$ of 5 ng mL^{-1} of NSE is incubated on the immunoelectrode and the CV response is recorded by varying the incubation time from 0 to 5, 10, 15, 20, and 25 minutes. Initially, the current decreases until 15 minutes, after which the current becomes nearly constant. Thus, the time required for the immunoreaction to take place is found to be 15 minutes, which is used for all further studies.

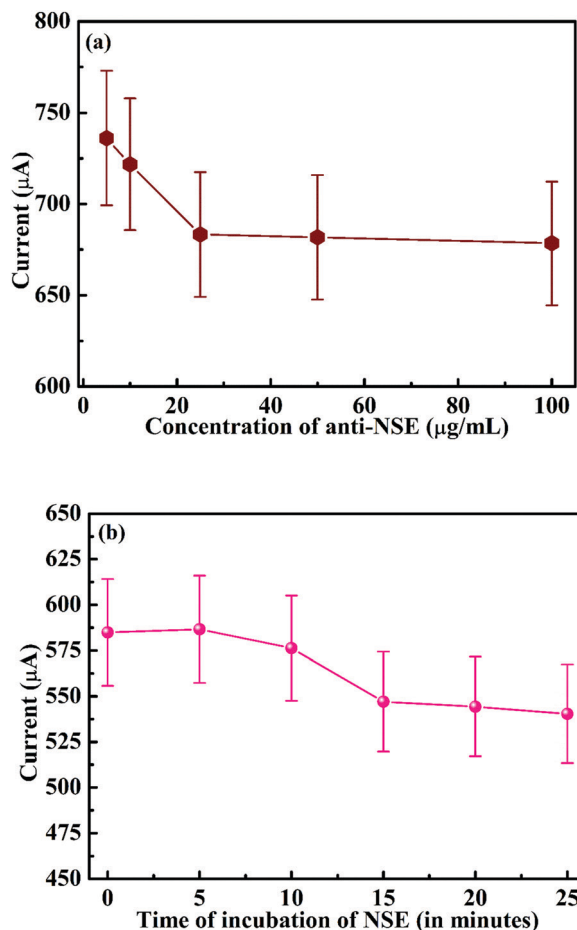


Fig. 6 (a) Current response with various concentrations of anti-NSE. (b) Current response with variation of the incubation time of NSE on the BSA/anti-NSE/CS/MoS₂/ITO immunoelectrode.

4.2 Electrochemical study of the various steps for fabrication of the immunoelectrode

Various steps for modification of the immunoelectrode are evaluated *via* recording the CV profiles at each step, in pH 7.4 PBS and at a scan rate of 50 mV s⁻¹ (Fig. 7(a)). A distinct anodic and cathodic current peak (i_{pa} and i_{pc} , respectively) is observed in each step. The maximum value of i_{pa} and i_{pc} is recorded to be 640.26 μA and -810.55 μA for the anti-NSE/CS/MoS₂/ITO electrode, followed by the BSA/anti-NSE/CS/MoS₂/ITO immunoelectrode with values of 579.35 μA and -762.63 μA, respectively. Furthermore, the minimum current values of i_{pa} and i_{pc} are found to be 436.71 μA and -579.53 μA for the CS/MoS₂/ITO electrode. The variation in peak current values for each step confirms the modification of the electrode. The sequential modification for each step of fabrication of the immunoelectrode is also confirmed using electrochemical impedance spectroscopy (EIS). EIS studies are carried out at a biasing potential of 0.01 V in the frequency range of 0.1 Hz to 100 kHz. Fig. 7(b) shows the Nyquist plots for the (i) CS/MoS₂/ITO, (ii) anti-NSE/CS/MoS₂/ITO and (iii) BSA/anti-NSE/CS/MoS₂/ITO electrodes. The results are found to complement the CV results with a minimum value of the charge-transfer resistance (R_{ct})

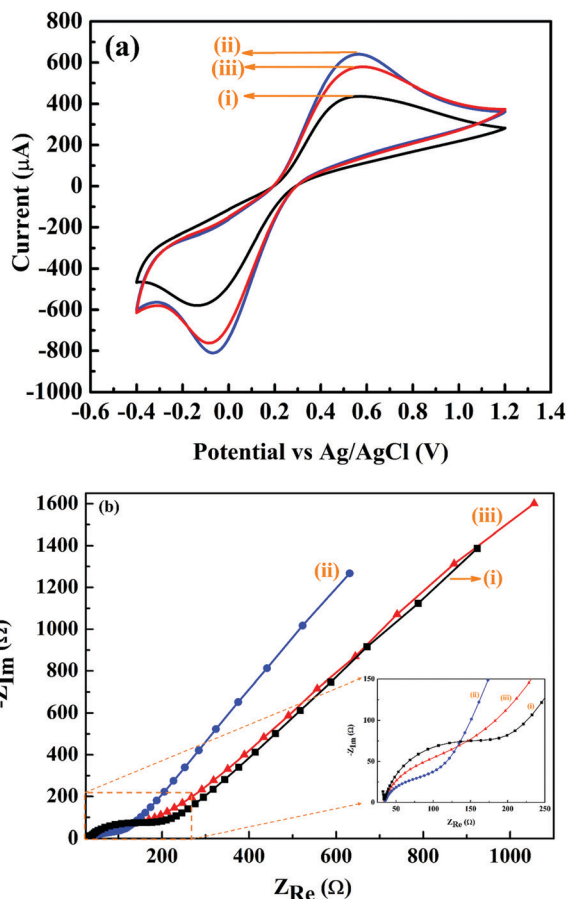


Fig. 7 (a) CV curves of the (i) CS/MoS₂/ITO, (ii) anti-NSE/CS/MoS₂/ITO and (iii) BSA/anti-NSE/CS/MoS₂/ITO electrodes. (b) EIS curves of (i) CS/MoS₂/ITO, (ii) anti-NSE/CS/MoS₂/ITO and (iii) BSA/anti-NSE/CS/MoS₂/ITO. The inset shows the magnified Nyquist plots (in the range of 25–250 Ω).

observed at 161.78 Ω for anti-NSE/CS/MoS₂/ITO. This is followed by an increase in the R_{ct} value to 245.40 Ω for BSA/anti-NSE/CS/MoS₂/ITO and the maximum value of R_{ct} is found to be 313.38 Ω for the CS/MoS₂/ITO electrode.

An increase in the value of i_{pa} and a decrease in the value of R_{ct} is observed when anti-NSE is immobilized on CS/MoS₂/ITO. This happens because of the interaction between anti-NSE and CS/MoS₂ and the spatial orientation of antibodies, which provides conduction pathways for the charge carriers at the interface.^{31,32} Furthermore, a decrease in current and an increase in R_{ct} is found after attachment of BSA onto anti-NSE/CS/MoS₂/ITO, due to the masking of non-specific sites for attachment by this blocking agent.

Fig. 8(a) displays the CV response of the prepared immunoelectrode BSA/anti-NSE/CS/MoS₂/ITO at various scan rates. The CV profile is recorded in PBS at pH 7.4 having 50 mM of [Fe(CN)₆]^{3-/4-}. An increase in i_{pa} and i_{pc} currents is observed for increasing scan rates. Furthermore, a linear variation of i_{pa} and i_{pc} with $\sqrt{\text{ScanRate}}$ (Fig. 8(b)) shows that the process of reduction and oxidation of [Fe(CN)₆]^{3-/4-} at the immunoelectrode is diffusion-controlled,^{33,34} which indicates that adsorbents when get conjugated on the electrode will inhibit

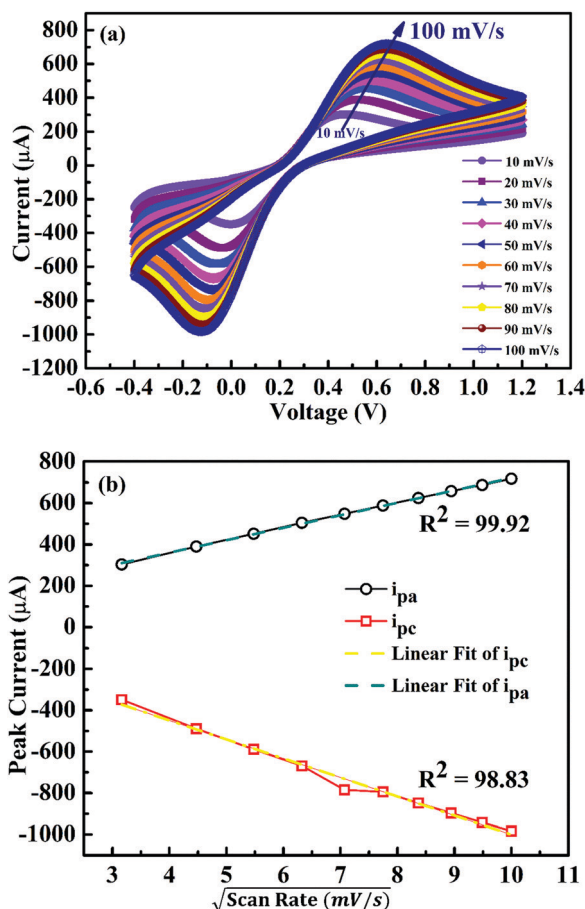


Fig. 8 (a) Scan rate study of the immunoelectrode BSA/anti-NSE/CS/MoS₂/ITO by varying the scan rate from 10 to 100 mV s⁻¹ and recording the CV profile. (b) Variation of the peak anodic current (*i*_{pa}) and peak cathodic current (*i*_{pc}) against the square root of the scan rate.

the diffusion of [Fe(CN)₆]^{3-/4-}. The linearly fitted plots as shown in Fig. 8(b) are given *via* the following equations:

$$i_{pa} = \left[\left(60.21 \mu\text{A} \times \sqrt{\frac{s}{mV}} \right) \times \sqrt{\text{Scan Rate} \left(\frac{mV}{s} \right)} \right] + 119.61 (\mu\text{A}) \quad (1)$$

$$R^2 = 99.92$$

$$i_{pc} = \left[\left(-91.84 \mu\text{A} \times \sqrt{\frac{s}{mV}} \right) \times \sqrt{\text{Scan Rate} (mV s^{-1})} \right] - 81.91 (\mu\text{A}) \quad (2)$$

$$R^2 = 98.83.$$

Evaluation of the electrochemical kinetics parameters of BSA/anti-NSE/CS/MoS₂/ITO immunoelectrode, like the electroactive surface area (*A*_e) and the HET rate transfer constant (*K*_o), is carried out as follows. The electroactive surface area (*A*_e) is determined using the Randles–Ševčík equation^{19,35}

$$i_p = 2.69 \times 10^5 n^{3/2} A_e C \sqrt{D_o \nu} \quad (3)$$

where *i*_p is peak anodic current as obtained in the CV profile of the electrode (in A), *n* is the number of electrons transferred

during the redox reaction (*n* = 1, for ferro/ferri), *A*_e is the electroactive surface area, *C* is the concentration of the redox probe (*C* = 5 mM = 5 mol cm⁻³), *D*_o is the diffusion coefficient (*D*_o = 0.667 × 10⁻⁵ cm² s⁻¹^{19,35}), and *ν* is the scan rate. The unit of the constant 2.69 × 10⁵ is $\frac{C}{mol\sqrt{V}}$.³⁶ From the plot between *i*_{pa} and *ν*^{1/2} (Fig. 8(b)) the value of the slope is obtained as 60.21 μA $\sqrt{\frac{s}{mV}}$ (from eqn (1)). By substituting all of the above values into eqn (3) the electroactive surface area is determined to be 0.55 cm² for the BSA/anti-NSE/CS/MoS₂/ITO immunoelectrode. A high value of the electroactive surface area enables the sensor to accommodate large concentrations of analyte, in turn increasing the linear detection range of the device.

The value of the electron-transfer constant (*k*_o) is determined using Nicholson's equation,³⁵ which is given as

$$\Psi = k_o \left(\frac{D_o}{D_R} \right)^{\frac{\alpha}{2}} \left(\frac{RT}{\pi n F D_o \nu} \right)^{\frac{1}{2}}. \quad (4)$$

Here, *D*_o and *D*_R are the diffusion coefficient of the oxidized and reduced electroactive species, respectively, the ratio of which is approximately equal to 1 for a symmetrical redox reaction, *α* is the transfer coefficient, *R* is the universal gas constant (8.314 J mol⁻¹ K⁻¹), *F* is the Faraday constant (96 485 C mol⁻¹), *ν* is the scan rate (50 mV s⁻¹), and the remaining parameters are the same as eqn (3) and *Ψ* is a dimensionless kinetic parameter that can be calculated using ΔE_p ³⁵ as follows

$$\Psi = \frac{-0.6288 + 0.0021 \times \Delta E_p}{1 - 0.017 \times \Delta E_p}. \quad (5)$$

Using, eqn (4) and (5), the value of *k*_o is calculated to be -4.05 × 10⁻³ cm s⁻¹ for the BSA/anti-NSE/CS/MoS₂/ITO immunoelectrode.

4.3 Stability study of the prepared immunoelectrode

The prepared immunoelectrode BSA/anti-NSE/CS/MoS₂/ITO is checked for the stability of the immobilized antibodies *via* the continuous application of potential and repeated interaction with redox media ([Fe(CN)₆]^{3-/4-}) by carrying out CV for 50 consecutive cycles. The scans are carried out at a scan rate of 50 mV s⁻¹ in the potential window of -0.4 V to 1.2 V in [Fe(CN)₆]^{3-/4-}. Essentially unchanged values of the anodic and cathodic peak current are observed as shown in Fig. 9(a). 95% and 93.66% of the initial *i*_{pa} is retained, after 15 and 50 CV cycles, respectively, while 99.45% of the initial *i*_{pc} is retained after 50 CV cycles, as shown in Fig. 9(b). The retention of a high percentage of the initial current, even after 50 CV cycles, demonstrates that our immunoelectrode has high stability. MoS₂ ensures the cyclic stability while CS in CS/MoS₂ imparts biocompatibility to the matrix, which helps the biomolecules to remain stably immobilized, after interaction with the redox media in continuous cycles of CV.

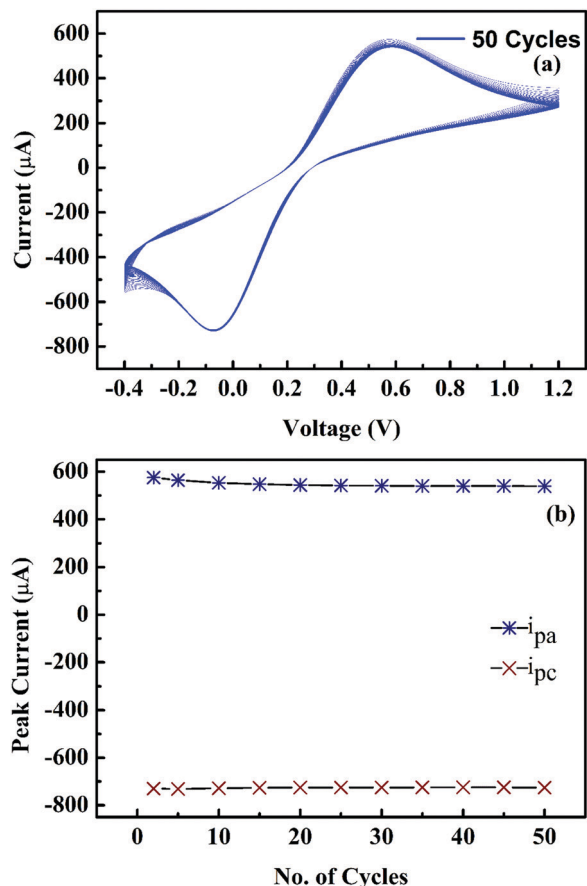


Fig. 9 (a) Consecutive scans of the immunoelectrode (BSA/anti-NSE/CS/MoS₂/ITO) for 50 CV cycles. (b) Variation of the peak anodic (i_{pa}) and peak cathodic current (i_{pc}) with the number of CV cycles.

4.4 Electrochemical performance of the immunoelectrode (BSA/anti-NSE/CS/MoS₂/ITO) and the control electrode (CS/MoS₂/ITO) towards the detection of NSE

The electrochemical detection of NSE is carried out by incubating the BSA/anti-NSE/CS/MoS₂/ITO immunoelectrode with various concentrations of NSE from 0.1 ng mL⁻¹ to 200 ng mL⁻¹. The response is recorded using CV at a scan rate of 50 mV s⁻¹. The current response is found to be inversely proportional to the concentration of NSE, which is a result of specific binding between NSE and anti-NSE. This specific binding results in the formation of an immunocomplex that impedes the diffusion of [Fe(CN)₆]^{3-/4-}. Fig. 10(a) shows the variation of the CV response of the BSA/anti-NSE/CS/MoS₂/ITO immunoelectrode when incubated with varying concentrations of NSE from 0.1 ng mL⁻¹ to 200 ng mL⁻¹. Fig. 10(b) shows the variation of i_{pa} with the concentration of NSE from 0.1 ng mL⁻¹ to 100 ng mL⁻¹. The variation is found to decrease linearly and can be fitted using the following equation with R^2 equal to 0.94:

$$y = -1.84 \mu\text{A ng}^{-1} \text{mL}^{-1} \times (\text{concentration of NSE (ng mL}^{-1}\text{)}) + 675.37 \mu\text{A} \quad (6)$$

The sensitivity of the immunoelectrode can be calculated here to be 3.35 $\mu\text{A ng}^{-1} \text{mL cm}^{-2}$ by dividing the slope of the

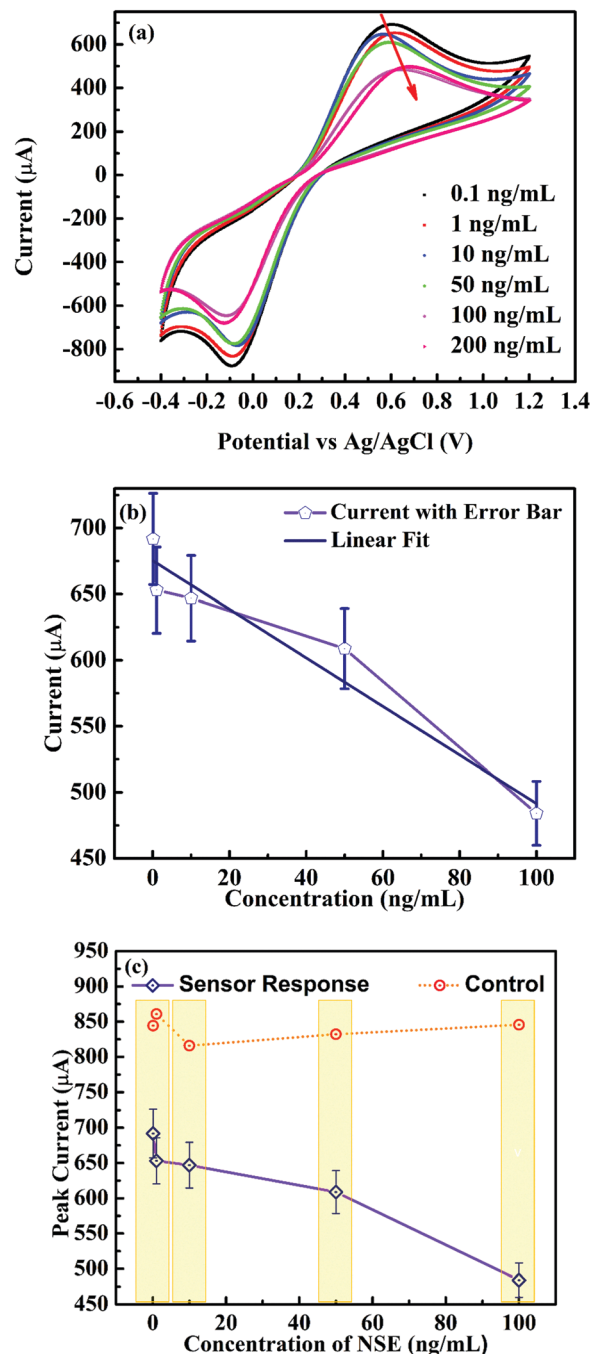


Fig. 10 (a) Electrochemical detection of NSE studied using CV with variation in the concentration of NSE from 0.1 ng mL⁻¹ to 200 ng mL⁻¹ in pH 7.4 PBS containing 50 mM [Fe(CN)₆]^{3-/4-}. (b) Calibration plot between the CV peak current and the concentration of NSE. (c) Response of the control electrode (CS/MoS₂/ITO) towards various concentrations of NSE from 0.1 to 100 ng mL⁻¹.

calibration curve by the electroactive surface area calculated for the BSA/anti-NSE/CS/MoS₂/ITO immunoelectrode.³⁷ The lowest concentration that can be detected for NSE using the prepared immunoelectrode is 0.1 ng mL⁻¹.

Fig. 10(c) shows the response of the control electrode (CS/MoS₂/ITO) towards various concentrations of NSE from 0.1 ng mL⁻¹ to

100 ng mL⁻¹. The response is recorded in a similar way to that for the BSA/anti-NSE/CS/MoS₂/ITO immunoelectrode. An invariant response towards NSE by the control electrode shows that the response of the immunoelectrode (BSA/anti-NSE/CS/MoS₂/ITO) is due to the specific interaction between NSE and anti-NSE. This interaction leads to the formation of an immunocomplex leading to a decrease in the peak current of the immunoelectrode with an increasing concentration of NSE. Thus, this study concludes that the CS/MoS₂/ITO electrode cannot interact with NSE on its own without the conjugation of anti-NSE on its surface.

4.5 Investigation of the reproducibility and specificity of the prepared immunoelectrode towards NSE

To verify the reproducibility of the prepared immunoelectrode BSA/anti-NSE/CS/MoS₂/ITO, 5 different immunoelectrodes were prepared under the same conditions and following a similar protocol. The response of these immunoelectrodes was checked for 10 ng mL⁻¹ of NSE. The immunoelectrodes exhibit an acceptable relative standard deviation (RSD) of 3.10% (Fig. 11(a)), indicating that the protocol mentioned in Section 2.4 gives reproducible immunoelectrodes.

To examine the specificity of the prepared immunoelectrode BSA/anti-NSE/CS/MoS₂/ITO towards NSE, various other commonly present interferences in human serum, like C-reactive protein (CRP, 10 µg mL⁻¹), myoglobin (mB, 85 ng mL⁻¹), cardiac troponin I (cTnI, 0.1 ng mL⁻¹), urea (0.1 mg mL⁻¹), and sodium chloride (NaCl, 6.2 mg mL⁻¹), are used. For recording the CV response, 20 µL of each of these interferences is incubated on the immunoelectrode for 15 minutes. The immunoelectrode shows an RSD value in the range of 0.27–0.94% for these other interferences, whereas a higher value of RSD equal to 7.8% is found for NSE, showing the specificity of this immunoelectrode towards NSE. Fig. 11(b) displays a bar graph depicting the response of the prepared immunoelectrode towards various other interferences in human serum including NSE (10 ng mL⁻¹). Furthermore, to examine the performance of the immunoelectrode towards the detection of NSE, when all the other common interferences are also present simultaneously, a simple control experiment is performed using the CV technique. Fig. 11(c) shows the performance of the immunoelectrode when all the other interferences, like CRP (10 µg mL⁻¹), mB (85 ng mL⁻¹), cTnI (0.1 ng mL⁻¹), urea (0.1 mg mL⁻¹), and NaCl (6.2 mg mL⁻¹), are present at their physiological concentrations at the same time without NSE (0 ng mL⁻¹, control) and along with NSE (10 ng mL⁻¹). It is observed that the immunoelectrode displays an RSD value of 0.33% in the case of the control measurement, which increases to 6.06% when NSE is also present along with all the other interferences. These results indicate the excellent specificity of the BSA/anti-NSE/CS/MoS₂/ITO electrode towards NSE. The immobilization of anti-NSE antibodies onto the immunoelectrode endows it with the requisite specificity.

4.6 Shelf life and regeneration study of the prepared immunoelectrode

The shelf life of the BSA/anti-NSE/CS/MoS₂/ITO immunoelectrode is examined *via* incubating it with 10 ng mL⁻¹ of

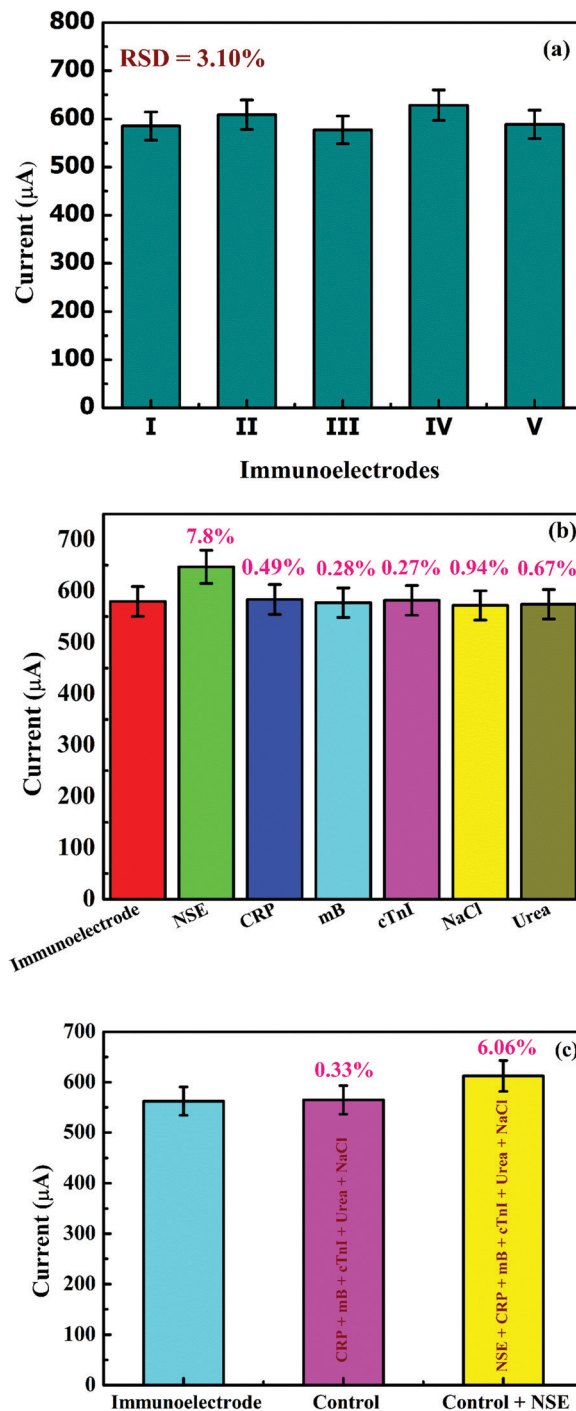


Fig. 11 (a) Reproducibility study of 5 different immunoelectrodes prepared under similar conditions. (b) Specificity study of the immunoelectrode towards various interferences commonly present in human serum. (c) Specificity study of the immunoelectrode towards NSE in the simultaneous presence of various other interferences.

NSE for 15 minutes at a regular interval of 7 days. The immunoelectrode is found to retain more than 80% of its initial response until the 6th week (Fig. 12(a)); by contrast, the response is reduced to 70% in the 7th week. Thus, the immunoelectrode displays a shelf life of up to 6 weeks.

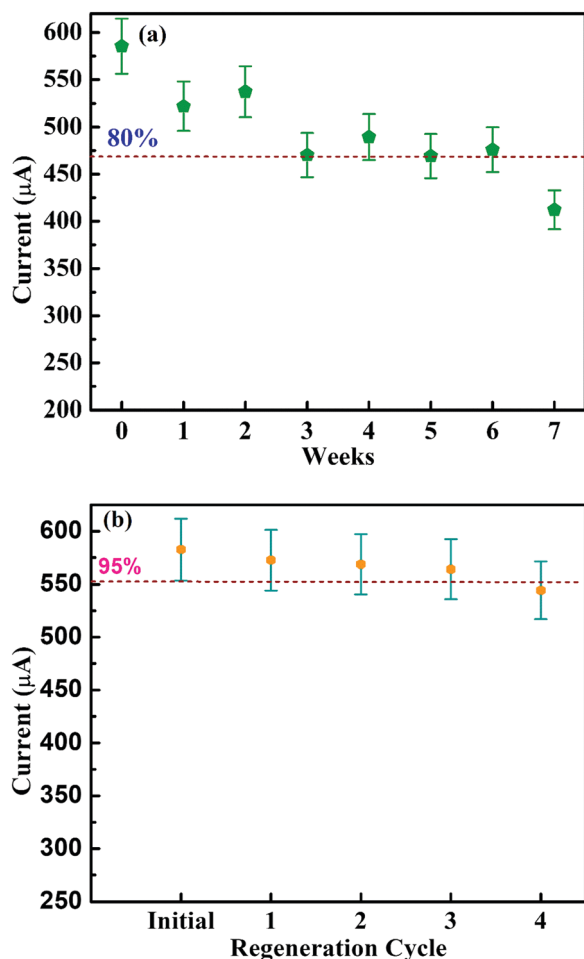


Fig. 12 (a) Shelf-life study of the fabricated immunoelectrode. (b) Regeneration study of the prepared immunoelectrode.

To check the regeneration ability of the immunoelectrode, 0.1 M of glycine HCl buffer at pH 2.5 was prepared. The immunoelectrode was first tested with 10 ng mL⁻¹ of NSE and the CV response is recorded. Then the immunoelectrode was washed in glycine HCl buffer solution followed by washing in pH 7.4 PBS buffer solution before it was tested with 10 ng mL⁻¹ of NSE. The immunoelectrode was tested for

4 cycles and was found to retain more than 90% of its initial response until the 4th cycle (Fig. 12(b)).

Table 1 shows a comparison of the platform proposed in this work with other platforms reported for the detection of NSE. The proposed immunoelectrode is found to exhibit a better performance in comparison with other immunoelectrodes, especially in terms of the response time of the immunoelectrode (incubation time of NSE). Other parameters, like the linear detection range, shelf life, and regenerability, are also found to be appreciably good.

5 Conclusions

In this work, we have developed chitosan biofunctionalized MoS₂, a simple matrix based on a two-step modification process, and tested its electrochemical performance towards the detection of NSE. Combining MoS₂ with CS provides a strategic approach to prepare a highly stable matrix, favorable for the immobilization of biomolecules with the retention of their bioactivity along with maintenance of the signal response. Also, CS provides functional groups for MoS₂ to anchor sites for the attachment of biomolecules on the matrix. Furthermore, the immunoelectrode fabricated using the CS/MoS₂ matrix exhibits a sensitivity of 3.35 µA ng⁻¹ mL cm⁻², and a wide linear detection range of 0.1–100 ng mL⁻¹. The immunoelectrode is found to be specific, reproducible, and regenerable up to 4 cycles, and it has a shelf life of up to 6 weeks. The sensor has an electroactive surface area of 0.55 cm² and a HET rate of -4.05×10^{-3} cm s⁻¹. Its excellent electrochemical performance towards the detection of NSE can be attributed to: (1) the cumulative effect of MoS₂ and CS, which imparts stability and biocompatibility to the matrix; (2) the introduction of functional groups that lead to covalent attachment between the antibodies and the matrix without the use of any harsh chemicals; and (3) the electroactive surface area, which is 55% of the geometric area. The proposed platform can further be explored for the analytical detection of various other protein biomarkers using various electrochemical techniques.

Author contributions

Ritika Khatri: conceptualization, data curation, formal analysis, investigation, methodology, and writing – original draft.

Table 1 Comparison of the analytical performance of the immunoelectrode proposed in this study with other immunoelectrodes reported earlier for the detection of NSE

Platform	Linear detection range	Shelf life (days)	Incubation time of NSE (minutes)	Regenerable	Reference
Au/PANI/3D-rGO/Ab	0.5 pg mL ⁻¹ to 10 ng mL ⁻¹	30	40	Yes (5 cycles)	3
PPD-GR-AuNPs/Ab/SPE	1 to 1000 ng mL ⁻¹	30	60	—	38
GCE/Ab/Ag/AuNPs-rGO/AP-anti-IgG	0.1 to 2000 ng mL ⁻¹	—	40	—	39
BSA/anti-NSE/polyresorcinol-Au/Pt/GCE	10 pg mL ⁻¹ to 100 ng mL ⁻¹	30	50	—	40
Au-MoS ₂ /MOF	1 pg mL ⁻¹ to 100 ng mL ⁻¹	30	40	—	41
Fc-g-Au@Pd-P(BBY) and rGO/Thi/AuPt NAs	0.0001 to 50 ng mL ⁻¹	15	—	—	42
BSA/anti-NSE/CS/MoS ₂ /ITO	0.1 to 100 ng mL ⁻¹	42	15	Yes (4 cycles)	This work

PANI, polyaniline; rGO, reduced graphene oxide; SPE, screen-printed electrode; PPD, poly(*p*-phenylenediamine); GR, graphene; Au, gold; NP, nanoparticle; Ab, antibody; GCE, glassy carbon electrode; AP, alkaline phosphatase; Ag, antigen; MOF, metal-organic framework; Fc-g, ferrocene grafted; BBY, Bismarck brown Y; Thi, thionine; Pt, platinum; NAs, nanoassemblies.

Nitin K. Puri: project administration, resources, supervision, validation, visualization, and writing – review and editing.

Conflicts of interest

There are no conflicts of interest to declare.

Acknowledgements

The authors are highly obliged to Hon'ble Vice-Chancellor, Delhi Technological University, Delhi, India for promoting research and providing appropriate infrastructure and facilities. The authors also express their gratitude to Dr Archit Dhingra for his valuable review of the manuscript. The authors would like to thank Dr Preetam Singh (Council of Scientific and Industrial Research (CSIR)-National Physical Laboratory (NPL)) and Dr Vikash Sharma (CSIR- NPL) for performing thickness measurement studies using a surface profilometer.

References

- 1 E. C. Welch, J. M. Powell, T. B. Clevinger, A. E. Fairman and A. J. A. F. M. Shukla, *Advances in Biosensors and Diagnostic Technologies Using Nanostructures and Nanomaterials, Adv. Funct. Mater.*, 2021, **31**, 2104126, DOI: 10.1002/adfm.202104126.
- 2 T. Ö. Varol, O. Hakli and U. J. N. J. o. C. Anik, *Graphene oxide-porphyrin composite nanostructure included electrochemical sensor for catechol detection, New J. Chem.*, 2020, **2021**(45), 1734–1742, DOI: 10.1039/D0NJ05475E.
- 3 Q. Zhang, X. Li, C. Qian, L. Dou, F. Cui and X. J. A. b. Chen, Label-free electrochemical immunoassay for neuron specific enolase based on 3D macroporous reduced graphene oxide/polyaniline film, *Anal. Biochem.*, 2018, **540**, 1–8, DOI: 10.1016/j.ab.2017.10.009.
- 4 M. Farrokhnia, G. Amoabediny, M. Ebrahimi, M. Ganjali and M. J. T. Arjmand, Ultrasensitive early detection of insulin antibody employing novel electrochemical nanobiosensor based on controllable electro-fabrication process, *Talanta*, 2022, **238**, 122947, DOI: 10.1016/j.talanta.2021.122947.
- 5 I. T. Bello, A. O. Oladipo, O. Adedokun and S. M. J. M. T. C. Dhlamini, Recent advances on the preparation and electrochemical analysis of MoS₂-based materials for supercapacitor applications: A mini-review, *Mater. Today Commun.*, 2020, **101664**, DOI: 10.1016/j.mtcomm.2020.101664.
- 6 X. Weng and S. J. I. s. j. Neethirajan, Immunosensor Based on Antibody-Functionalized MoS₂ for Rapid Detection of Avian Coronavirus on Cotton Thread, *IEEE Sens. J.*, 2018, **18**, 4358–4363, DOI: 10.1109/JSEN.2018.2829084.
- 7 R.-M. Kong, L. Ding, Z. Wang, J. You and F. J. A. Qu, A novel aptamer-functionalized MoS₂ nanosheet fluorescent biosensor for sensitive detection of prostate specific antigen, *Anal. Bioanal. Chem.*, 2015, **407**, 369–377, DOI: 10.1007/s00216-014-8267-9.
- 8 A. Sinha, B. Tan, Y. Huang, H. Zhao, X. Dang, J. Chen and R. J. T. T. i. A. C. Jain, MoS₂ nanostructures for electrochemical sensing of multidisciplinary targets: A review, *TrAC, Trends Anal. Chem.*, 2018, **102**, 75–90, DOI: 10.1016/j.trac.2018.01.008.
- 9 N. Kaur, R. A. Mir and O. J. J. o. A. Pandey, Electrochemical and optical studies of facile synthesized molybdenum disulphide (MoS₂) nano structures, *J. Alloys Compd.*, 2019, **782**, 119–131, DOI: 10.1016/j.jallcom.2018.12.145.
- 10 D. B. Altuntaş and F. J. M. S. Kuralay, MoS₂/Chitosan/GOx-Gelatin modified graphite surface: Preparation, characterization and its use for glucose determination, *Mater. Sci. Eng., B*, 2021, **270**, 115215, DOI: 10.1016/j.mseb.2021.115215.
- 11 M. Chen, H. Li, X. Su, R. Wu, H. Feng, X. Shi, J. Liang, J. Chen and G. J. N. J. o. C. Li, Label-free electrochemical aptasensor based on reduced graphene oxide-hemin-chitosan nanocomposite for the determination of glypican-3, *New J. Chem.*, 2021, **45**, 8608–8618, DOI: 10.1039/D1NJ00633A.
- 12 Y. Wang, B. Zhang, Y. Tang, F. Zhao and B. J. M. J. Zeng, Fabrication and application of a rutin electrochemical sensor based on rose-like AuNPs-MoS₂-GN composite and molecularly imprinted chitosan, *Microchem. J.*, 2021, **168**, 106505, DOI: 10.1016/j.microc.2021.106505.
- 13 M. Sabbaghan, A. S. Shahvelayati and K. J. S. A. P. A. M. Madankar, CuO nanostructures: optical properties and morphology control by pyridinium-based ionic liquids, *Spectrochim. Acta, Part A*, 2015, **135**, 662–668, DOI: 10.1016/j.saa.2014.07.097.
- 14 A. Roointan, T. A. Mir, S. I. Wani, K. K. Hussain, B. Ahmed, S. Abraham, A. Savardashtaki, G. Gandomani, M. Gandomani and R. J. J. o. p. Chinnappan, Early detection of lung cancer biomarkers through biosensor technology: A review, *J. Pharm. Biomed. Anal.*, 2019, **164**, 93–103, DOI: 10.1016/j.jpba.2018.10.017.
- 15 R. A. Soomro, N. H. Kalwar, A. Avci, E. Pehlivan, K. R. Hallam and M. J. B. Willander, In-situ growth of NiWO₄ saw-blade-like nanostructures and their application in photo-electrochemical (PEC) immunosensor system designed for the detection of neuron-specific enolase, *Biosens. Bioelectron.*, 2019, **141**, 111331, DOI: 10.1016/j.bios.2019.111331.
- 16 C. Tang, P. Wang, K. Zhou, J. Ren, S. Wang, F. Tang, Y. Li, Q. Liu and L. J. B. Xue, AgPt alloy/NGR as a dual signal amplification strategy for sensitive detection of Neuron-specific enolase, *Biosens. Bioelectron.*, 2022, **197**, 113779, DOI: 10.1016/j.bios.2021.113779.
- 17 X. Yu, Y. Li, Y. Li, S. Liu, Z. Wu, H. Dong, Z. Xu, X. Li and Q. J. T. Liu, An electrochemical amplification strategy based on the ferrocene functionalized cuprous oxide superparticles for the detection of NSE, *Talanta*, 2022, **236**, 122865, DOI: 10.1016/j.talanta.2021.122865.
- 18 G. Mo, X. He, D. Qin, X. Jiang, X. Zheng and B. J. A. Deng, A potential-resolved electrochemiluminescence resonance energy transfer strategy for the simultaneous detection of neuron-specific enolase and the cytokeratin 19 fragment, *Analyst*, 2021, **146**, 1334–1339, DOI: 10.1039/D0AN02106G.

- 19 R. Khatri and N. K. J. V. Puri, Electrochemical study of hydrothermally synthesised reduced MoS₂ layered nanosheets, *Vacuum*, 2020, **175**, 109250, DOI: 10.1016/j.vacuum.2020.109250.
- 20 W. Zhang, Y. Wang, D. Zhang, S. Yu, W. Zhu, J. Wang, F. Zheng, S. Wang and J. J. N. Wang, A one-step approach to the large-scale synthesis of functionalized MoS₂ nanosheets by ionic liquid assisted grinding, *Nanoscale*, 2015, **7**, 10210–10217, DOI: 10.1039/C5NR02253C.
- 21 H. Li, Q. Zhang, C. C. R. Yap, B. K. Tay, T. H. T. Edwin, A. Olivier and D. J. A. F. M. Baillargeat, From bulk to monolayer MoS₂: evolution of Raman scattering, *Adv. Funct. Mater.*, 2012, **22**, 1385–1390, DOI: 10.1002/adfm.201102111.
- 22 A. Zajac, J. Hanuza, M. Wandas and L. J. S. A. P. A. M. Dymińska, Determination of N-acetylation degree in chitosan using Raman spectroscopy, *Spectrochim. Acta, Part A*, 2015, **134**, 114–120, DOI: 10.1016/j.saa.2014.06.071.
- 23 K. Kasinathan, B. Murugesan, N. Pandian, S. Mahalingam, B. Selvaraj and K. J. I. j. o. b. m. Marimuthu, Synthesis of biogenic chitosan-functionalized 2D layered MoS₂ hybrid nanocomposite and its performance in pharmaceutical applications: in-vitro antibacterial and anticancer activity, *Int. J. Biol. Macromol.*, 2020, **149**, 1019–1033, DOI: 10.1016/j.ijbiomac.2020.02.003.
- 24 J. Wang, W. Zhang, Y. Wang, W. Zhu, D. Zhang, Z. Li and J. J. P. Wang, Enhanced exfoliation effect of solid auxiliary agent on the synthesis of biofunctionalized MoS₂ using grindstone chemistry, *Part. Part. Syst. Charact.*, 2016, **33**, 825–832, DOI: 10.1002/ppsc.201600114.
- 25 H. Wang, P. Cheng, J. Shi, D. Wang, H. Wang, J. Pezoldt, M. Stich, R. Chen, P. A. van Aken and W. J. G. C. Huang, Efficient fabrication of MoS₂ nanocomposites by water-assisted exfoliation for nonvolatile memories, *Green Chem.*, 2021, **23**, 3642–3648, DOI: 10.1039/D1GC00162K.
- 26 M. Zhao, Z. Huang, S. Wang and L. J. C. E. J. Zhang, Ultrahigh efficient and selective adsorption of Au (III) from water by novel Chitosan-coated MoS₂ biosorbents: Performance and mechanisms, *Chem. Eng. J.*, 2020, **401**, 126006, DOI: 10.1016/j.cej.2020.126006.
- 27 Z. Feng, X. Liu, L. Tan, Z. Cui, X. Yang, Z. Li, Y. Zheng, K. W. K. Yeung and S. J. S. Wu, Electrophoretic deposited stable chitosan@ MoS₂ coating with rapid in situ bactericidal ability under dual-light irradiation, *Small*, 2018, **14**, 1704347, DOI: 10.1002/smll.201704347.
- 28 O. Akakuru, H. Louis, P. Amos, O. Akakuru, E. Nosike and E. J. B. P. Ogulewe, The chemistry of chitin and chitosan justifying their nanomedical utilities, *Biochem. Pharmacol.*, 2018, **7**, 2167-0501.1000241, DOI: 10.4172/2167-0501.1000241.
- 29 D. Sandil, S. Srivastava, B. Malhotra, S. Sharma and N. K. J. J. o. A. Puri, Biofunctionalized tungsten trioxide-reduced graphene oxide nanocomposites for sensitive electrochemical immunosensing of cardiac biomarker, *J. Alloys Compd.*, 2018, **763**, 102–110, DOI: 10.1016/j.jallcom.2018.04.293.
- 30 R. Vinoth, I. M. Patil, A. Pandikumar, B. A. Kakade, N. M. Huang, D. D. Dionysios and B. J. A. O. Neppolian, Synergistically enhanced electrocatalytic performance of an N-doped graphene quantum dot-decorated 3D MoS₂-graphene nanohybrid for oxygen reduction reaction, *ACS Omega*, 2016, **1**, 971–980, DOI: 10.1021/acsomega.6b00275.
- 31 A. K. Singh, T. K. Dhiman, G. Lakshmi and P. R. J. B. Solanki, Dimanganese trioxide (Mn₂O₃) based label-free electrochemical biosensor for detection of Aflatoxin-B₁, *Bioelectrochemistry*, 2021, **137**, 107684, DOI: 10.1016/j.bioelechem.2020.107684.
- 32 V. K. Singh, S. Kumar, S. K. Pandey, S. Srivastava, M. Mishra, G. Gupta, B. Malhotra, R. Tiwari and A. J. B. Srivastava, Fabrication of sensitive bioelectrode based on atomically thin CVD grown graphene for cancer biomarker detection, *Biosens. Bioelectron.*, 2018, **105**, 173–181, DOI: 10.1016/j.bios.2018.01.014.
- 33 Y. Guo, Y. Shu, A. Li, B. Li, J. Pi, J. Cai, H.-h. Cai and Q. J. J. o. M. C. B. Gao, Efficient electrochemical detection of cancer cells on in situ surface-functionalized MoS₂ nanosheets, *J. Mater. Chem. B*, 2017, **5**, 5532–5538, DOI: 10.1039/C7TB01024A.
- 34 M. Rezki, N. L. W. Septiani, M. Iqbal, S. Harimurti, P. Sambegoro, D. R. Adhika and B. J. J. o. M. C. B. Yulianto, Amine-functionalized Cu-MOF nanospheres towards label-free hepatitis B surface antigen electrochemical immunosensors, *J. Mater. Chem. B*, 2021, **9**, 5711–5721, DOI: 10.1039/D1TB00222H.
- 35 X. Xi, D. Wu, W. Ji, S. Zhang, W. Tang, Y. Su, X. Guo and R. J. A. F. M. Liu, Manipulating the Sensitivity and Selectivity of OECT-Based Biosensors via the Surface Engineering of Carbon Cloth Gate Electrodes, *Adv. Funct. Mater.*, 2020, **30**, 1905361, DOI: 10.1002/adfm.201905361.
- 36 A. A. Aljabali, J. E. Barclay, J. N. Butt, G. P. Lomonosoff and D. J. J. D. t. Evans, Redox-active ferrocene-modified Cowpea mosaic virus nanoparticles, *Dalton Trans.*, 2010, **39**, 7569–7574, DOI: 10.1039/C0DT00495B.
- 37 A. Kaur, S. Rana, A. Bharti, G. R. Chaudhary and N. J. M. A. Prabhakar, Voltammetric detection of vitamin D employing Au-MoS₂ hybrid as immunosensing platform, *Microchim. Acta*, 2021, **188**, 1–14, DOI: 10.1007/s00604-021-04862-6.
- 38 J. Amani, M. Maleki, A. Khoshroo, A. Sobhani-Nasab and M. J. A. b. Rahimi-Nasrabadi, An electrochemical immunosensor based on poly p-phenylenediamine and graphene nanocomposite for detection of neuron-specific enolase via electrochemically amplified detection, *Anal. Biochem.*, 2018, **548**, 53–59, DOI: 10.1016/j.ab.2018.02.024.
- 39 Z. Wei, J. Zhang, A. Zhang, Y. Wang and X. J. M. Cai, Electrochemical detecting lung cancer-associated antigen based on graphene-gold nanocomposite, *Molecules*, 2017, **22**, 392, DOI: 10.3390/molecules22030392.
- 40 H. Wang and Z. J. M. A. Ma, Amperometric immunoassay for the tumor marker neuron-specific enolase using a glassy carbon electrode modified with a nanocomposite consisting of polyresorcinol and of gold and platinum nanoparticles, *Microchim. Acta*, 2017, **184**, 3247–3253, DOI: 10.1007/s00604-017-2287-z.

- 41 H. Dong, S. Liu, Q. Liu, Y. Li, Y. Li and Z. J. B. Zhao, A dual-signal output electrochemical immunosensor based on Au-MoS₂/MOF catalytic cycle amplification strategy for neuron-specific enolase ultrasensitive detection, *Biosens. Bioelectron.*, 2022, **195**, 113648, DOI: 10.1016/j.bios.2021.113648.
- 42 Y. Chen, X.-Y. Ge, S.-Y. Cen, A.-J. Wang, X. Luo and J.-J. J. S. Feng, Ultrasensitive dual-signal ratiometric electrochemical aptasensor for neuron-specific enolase based on Au nanoparticles@ Pd nanoclusters-poly (bismarck brown Y) and dendritic AuPt nanoassemblies, *Sens. Actuators, B*, 2020, **311**, 127931, DOI: 10.1016/j.snb.2020.127931.